UNIVERSITÀ DEGLI STUDI DI ROMA
"LA SAPIENZA"

Dottorato di ricerca in Astronomia
XXIV ciclo

Theoretical models of the spectrophotometric properties of atmosphereless bodies surfaces in the Solar System

Dott. Mauro CIARNIELLO

Coordinatore del corso di dottorato:
Prof. Roberto Capuzzo Dolcetta

Relatore:
Dott. Fabrizio Capaccioni
INAF-IASF, Roma

Anno Accademico 2010-2011

Contents

List of Figures

List of Tables

Introduzione

Nel contesto delle missioni spaziali il remote sensing rappresenta uno degli strumenti più potenti per l'osservazione di oggetti planetari. Esso permette di determinare le proprietà chimico-fisiche sia della superficie che dell'atmosfera attraverso l'analisi spettrale e fotometrica. Tuttavia, i dati prodotti nel telerilevamento per essere interpretati necessitano di modelli fisici che descrivano l'interazione tra la luce e i mezzi osservati. Diversi modelli sono stati sviluppati (Lumme and Bowell, 1981; Drossart, 1993; Shkuratov et al., 1999b; Mishchenko et al., 1999) che dipendono da diversi parametri a loro volta correlati alle proprietà fisiche degli oggetti investigati.
Il vantaggio di questi modelli di scattering è quello di essere analitici e ciò semplifica notevolmente l'analisi dei dati. Tuttavia per conservare l'analiticità è necessario fare delle assunzioni e approssimazioni che non sono del tutto soddisfatte nei mezzi reali, e ciò deve essere preso in considerazione nella discussione dei risultati ottenuti.
Inoltre il processo di inversione che dai dati acquisiti permette la determinazione delle caratteristiche del target presenta diverse difficoltà e può condurre a soluzioni non univoche. Da questo punto di vista testare i modelli attraverso misure di laboratorio sotto condizioni note che permettano di caratterizzare il relativo peso dei parametri utilizzati (per esempio misurando indipendentemente l'abbondanza di contaminanti e la dimensione delle particelle dei mezzi in esame) è di fondamentale importanza per determinarne le capacità interpretative. Un altro approccio di investigazione dei dati da remote sensing è rappresentato dal confronto di questi con simulazioni numeriche dei processi di scattering in mezzi particolati (Stankevich and Shkuratov, 2004; Shkuratov et al., 2005; Mishchenko et al., 2007). Sebbene questo approccio sia in principio rigoroso, richiede lunghi tempi computazionali dato che si devono trattare grandi numeri di particelle per simulare dei mezzi reali.
Il presente lavoro è incentrato principalmente sullo studio dei processi di scattering su superfici planetarie senza atmosfera attraverso l'applicazione della soluzione analit-

ica dell'equazione del trasferimento radiativo derivata da Hapke (Hapke, 1993; Hapke et al., 1998; Hapke, 2002, 2008; Hapke et al., 2009). La teoria di Hapke è riassunta nel capitolo 2. Il modello di Hapke è stato ampiamente applicato allo studio delle regoliti (Mallama et al., 2002; Buratti et al., 2004) e per correggere dati fotometrici a condizioni geometriche standard di illuminazione e osservazione. La mia analisi parte dallo studio delle proprietà spettrofotometriche degli oggetti ghiacciati nel sistema di Saturno, così come sono osservati da VIMS (Visual Infrared Mapping Spectrometer) a bordo della sonda Cassini. Una descrizione dello strumento è data nel capitolo 1.
La missione Cassini-Huyghens, lanciata il 15 Ottobre 1997, ha raggiunto Saturno dopo sette anni di crociera, il 30 Giugno 2004. Questa è il risultato di una collaborazione tra le agenzie spaziali di Stati Uniti (NASA), Europa (ESA) e Italia (ASI),e dopo la fine del periodo nominale (Giugno 2008) è stata estesa per una prima volta fino a Settembre 2010 (Cassini Equinox mission) e per una seconda volta fino a Settembre 2017 (Cassini Solstice mission). Nei suoi sette anni di attività Cassini ha investigato l'interno e l'atmosfera di Saturno, il suo campo magnetico, il sistema di anelli ed i satelliti: Titano per primo (la sonda Huyghens è atterrata sulla luna nel Gennaio 2005) e poi i corpi ghiacciati.
Come accennato sopra, lo studio delle lune ghiacciate è il punto di partenza di questo lavoro, con l'analisi di Rhea ed Encelado (capitoli 3 e 4 rispettivamente). Per entrambi i satelliti sono stati analizzati sia lo spettro che la curva di fase applicando il modello di Hapke. L'analisi spettrale ha permesso di definire la composizione superficiale (dimensione dei grani e abbondanza di contaminanti), mentre lo studio fotometrico ha fornito indicazioni sulla porosità del materiale, sulla rugosità a larga scala e sulle proprietà di scattering della regolite.
Modelli composizionali della superfice sono stati prodotti, in via preliminare, anche per le lune Dione, Mimas e Tethys (capitolo 4) e per glia anelli maggiori di Saturno (C, B, Divisione di Cassini e A, capitolo 5), utilizzando lo stesso paradigma di Rhea ed Encelado.
Nel capitolo 6 sono presentati i risultati che riguardano misure di laboratorio su minerali di interesse planetario (pirosseni con diverse abbondanze di Ferro). Con questo studio ci si prefigge di determinare la dipendenza delle segnature spettrali dalla dimensione dei grani che compongo la miscela e dalla geometria dell'osservazione. Anche in questo caso il modello di Hapke è stato adottato per descrivere la funzione di fase dei campioni e per determinarne le proprietà fotometriche delle particelle. Viene inoltre

introdotta una applicazione del modello di Hapke che permette di derivare le costanti ottiche dei minerali a partire dalla misura della riflettanza in varie condizioni osservative. Infine nel capitolo 7, viene introdotto un approccio di tipo statistico che, utilizzando un metodo Montecarlo, permette di simulare lo scattering in mezzi particolati. Questo modello è in grado di studiare in dettaglio gli effetti dello scattering multiplo. In generale il modello proposto permette di simulare sia la diffusione all'interno di superfici solide porose (mezzi seminfiniti) che in sospensioni come potrebbero essere gli anelli di Saturno o una chioma cometaria e si presta pertanto ad interessanti sviluppi. Nel capitolo 7 sono riportati i risultati di alcuni test preliminari.

Introduction

In space missions remote sensing represents one of the most powerful tools for the observations of planetary objects. It allows to infer physical and chemical properties both of surfaces and atmospheres by spectroscopic and photometric analysis. However data produced by remote sensing observations need to be interpreted by physical models which describe the interaction between light and observed media. Many models have been developed (Lumme and Bowell, 1981; Drossart, 1993; Shkuratov et al., 1999b; Mishchenko et al., 1999) which depends on several parameters that are related to physical properties of the targets. The inversion process from acquired data to target properties through one of these physical models is often challenging and can lead to non-unique solutions. From this point of view the test of these models with measurements of laboratory samples under very well controlled conditions (for example medium composition and grain size), is crucial to constrains their capabilities. The advantage of these scattering models is to be analytical, and this greatly simplifies the data analysis. Analyticity however often relies on assumptions which are not fully satisfied in real media, and these must be taken into account in the discussion of the results we obtain.

Another approach to investigate remote sensing data is represented by the comparison with numerical simulations of the scattering processes in particulate surfaces (Stankevich and Shkuratov, 2004; Shkuratov et al., 2005; Mishchenko et al., 2007) . Though this approach is in principle rigorous, it requires long computational time as we deal with a very large number of particles, which is the case of real media.

In this work I mainly focused on the investigation of scattering processes on planetary surfaces without atmosphere through the application of the analytical solution of the radiative transfer equation given by Hapke (Hapke, 1993; Hapke et al., 1998; Hapke, 2002, 2008; Hapke et al., 2009) (Hapke theory is summarized in chapter 2). The Hapke model has been widely applied to the study of regoliths (Mallama et al., 2002; Buratti

et al., 2004) as well as to correct photometric data to standard lighting and viewing geometry (Domingue et al., 2009). My analysis starts from the study of spectrophotometric properties of the icy objects in the Saturn's system, as observed by the VIMS (Visual Infrared Mapping Spectrometer) onboard the Cassini spacecraft. A description of the instrument is given in chapter 1.
The Cassini-Huygens mission, launched 15th October 1997, reached Saturn after seven years of cruise, on the 30th of June 2004. The mission, which is the result of the collaboration of U.S (NASA), European (ESA) and Italian (ASI) space agencies after the end of the nominal period (June 2008) has been extended for the first time to September 2010 (Cassini Equinox mission) and for the second time through September 2017 (Cassini Solstice mission). In its seven years of activity Cassini has investigated Saturn's interior and atmosphere,its magnetic field, the rings system and the satellites of the planet: Titan at first (the Huygens probe landed on the moon on January 2005) and then the icy moons.
As written above, the study of the icy moons is the starting point of this work, with the investigation of Rhea and Enceladus (chapter 3 and 4, respectively). For the two satellites both the spectrum and the phase curve have been analyzed applying the Hapke model. The spectral analysis allowed to model the surface composition (grain size and amount of contaminant), while the photometric investigation has constrained the porosity and the large scale characteristics of the surface, as well as it has given indication on the scattering properties of the regolith.
Preliminary surface composition models have been produced also for the moons Dione, Mimas and Tethys (chapter 4) and the major Saturn's rings (C, B, Cassini Division and A, chapter 5) , using the same paradigm adopted for Rhea and Enceladus.
In chapter 6 results about lab measures and interpretation of spectra of pyroxenes of planetary interest are presented. Correlation of spectral signatures with grain size and geometry is investigated. Even in this case the Hapke model has been adopted to describe the phase function of the pyroxenes and to constrain the photometric properties of the particles. An application of the Hapke model to retrieve optical constants of the samples is described.
Finally, in chapter 7, a statistical approach that simulates scattering in particulate media by means of a Montecarlo method is introduced. This model allows to study in detail the effects of the multiple scattering. In general, the proposed routine is able to simulate the diffusion both in solid porous surfaces (semi-infinite media) and

suspensions like the rings of Saturn or a cometary coma, and provides interesting developments. In chapter 7 the results of some preliminary tests are shown.

Chapter 1

VIMS

VIMS (Visual Infrared Mapping Spectrometer) is an imaging spectrometer that works in the 0.3 - 5.1 μm wavelength range, onboard the Cassini spacecraft. Unlike the normal (point) spectrometers it produces bidimensional images of the target in 352 bands. VIMS data allow to study the distribution of materials on the surface of Saturn's satellites and of the rings and the structure and composition of Saturn and Titan atmospheres (Brown et al., 2004; McCord et al., 2004). The opportunity to join spectral analysis with imaging under various geometric conditions (variable illumination and emission angles) allows a detailed study of radiative processes, which in the case of objects without atmosphere, permits an accurate investigation of regolith physical properties.
VIMS is composed by the Optical Pallet Assembly (OPA) and the Main Electronics Assembly (ME) (Miller et al., 1996) (see fig.1.1). The OPA includes two imaging spectrometers (VIS and IR) and their electronics. The VIS and IR channels cover respectively the 300 - 1050 nm and 800 - 5100 nm range. The two hyper-spectral images are acquired in pushbroom by the VIS channel which uses a 2D focal plane array; in whiskbroom by the IR channel which adopt a 1D linear detector. In fig. 1.2 it is shown how the two channels work.

The VIS channel detector is a CCD and the image is acquired through a slit, which aligned at the focal plane of the telescope. The product of the acquisition is a column of pixels orthogonally oriented respect to the spacecraft motion. The image is decomposed by a diffraction grating in its spectral components and it is projected on the CCD along

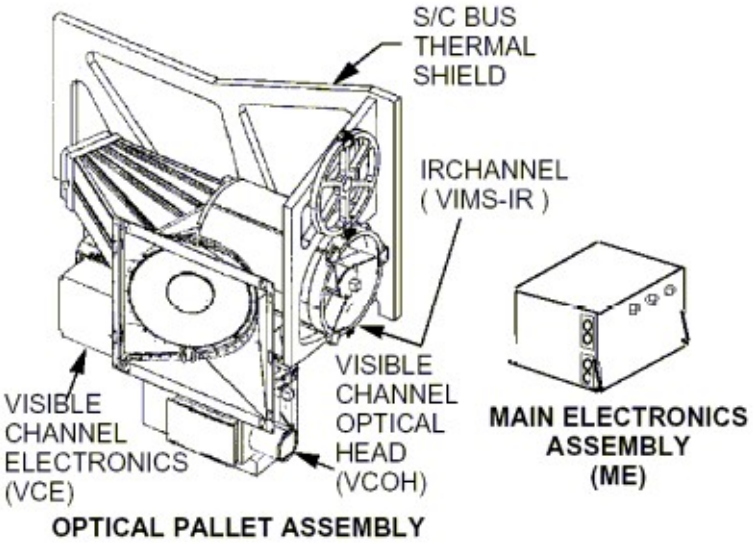

Figure 1.1: VIS and IR channels and main electronics (MS) of Cassini-VIMS.

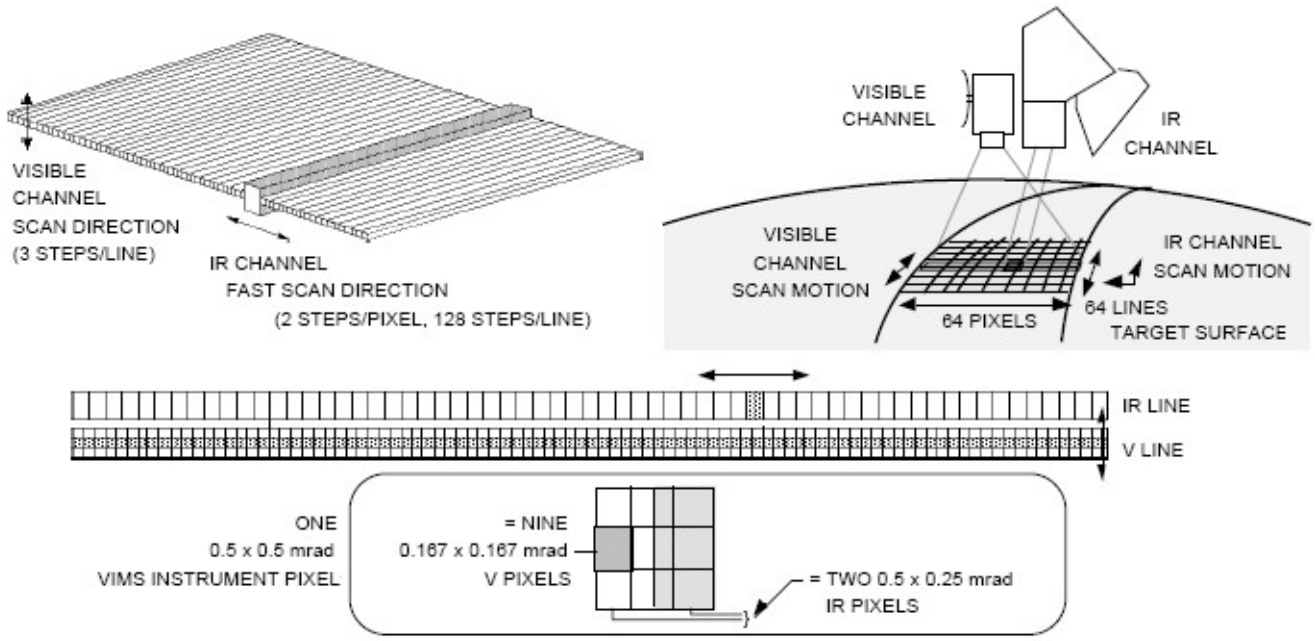

Figure 1.2: Scanning process of both VIS and IR channel and production of the nominal pixel.

a direction orthogonal to the slit ("bands" direction). The slit defines the "samples" direction. After each acquisition the CCD is read and then the instrument moves to the next column. The columns, acquired according to the temporal sequence ("lines" direction), form the bidimensional image. The final output of the acquisition process is then an hyper-spectral cube where the spectrum of each pixel is stored along the third dimension (fig. 1.3). An example of a spectrum measured by VIMS is in fig. 1.4.

The IR channel also produces an hyper-spectral cube identical to the visible but in a different wavelength range. However the IR uses a linear array of detectors and so it can acquire the spectrum of one pixel at a time. This implies that during the VIS acquisition the IR channels scans the image along the samples direction. Once the VIS has acquired a column of pixel and the IR has scanned the entire column both the channels move to the next line. These operative modes are respectively named push-broom (VIS) and whisk-broom (IR). The typical output image size is a square of 64×64 pixels with an IFOV (Istantaneus Field Of View) of 500 $\mu rad \times 500$ μrad each (nominal mode). Each pixel doesn't correspond to a physical pixel on the focal plane because the instrument sums the signal of many pixels (binning, see fig. 1.2). In the case of VIS channel the total signal is given by the sum of 3 pixels along the sample and 3 pixel along the lines, producing a 3×3 pixels square on the CCD. Each pixel is 167 $\mu rad \times 167$ μrad. The IR has rectangular pixels which cover 250 μrad along the samples and 500 μrad along the lines. The nominal pixel is the obtained summing two pixel along the samples direction. Along the bands direction 5 pixels are summed, giving a nominal spectral resolution of 7.3 nm for the VIS, and 16.6 nm for the IR. The visible channel has 96 bands ad the infrared 256.

1.1 VIMS-VIS

The visible channel (Reininger et al., 1994; Miller et al., 1996) is composed by the Visible Channel Optical Head (VCOH) and an electronics unit called the Visible Channel Electronics (VCE). The optical head (fig. 1.5) consists of the telescope and spectrometer. The telescope in mounted on an aluminum optical bench, and the other components are also made of aluminum in order to make the entire system athermal.

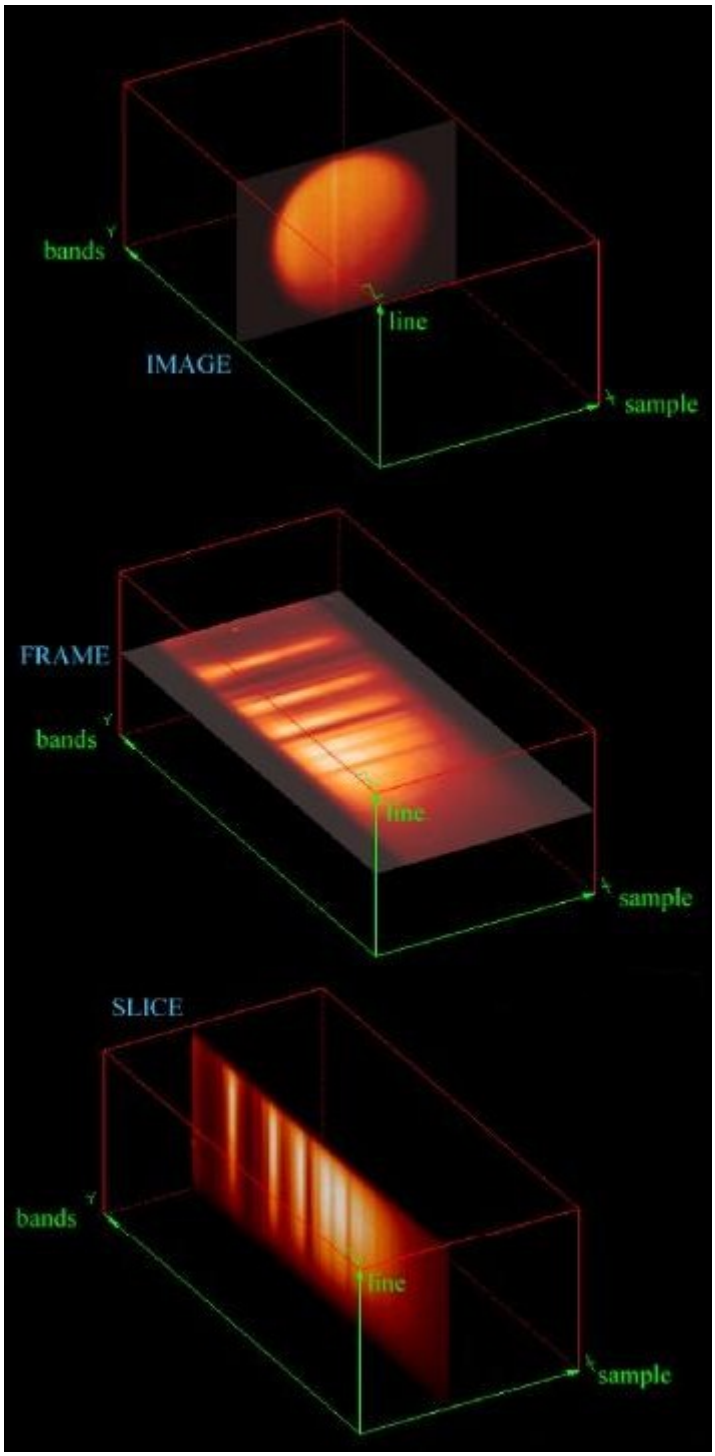

Figure 1.3: Hyper-spectral cube sections: image, frame and slice.

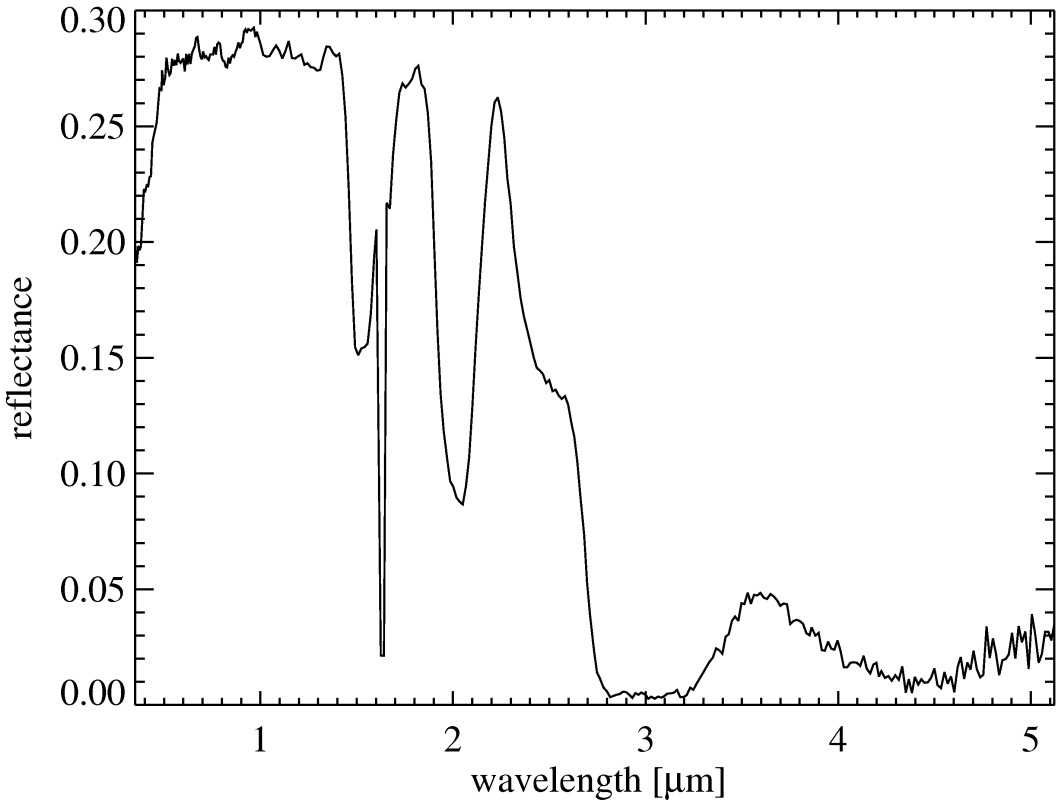

Figure 1.4: Spectrum of Rhea (a satellite of Saturn), measured by VIMS. The bands of water ice at 1.5, 2 and 3 μm are visible. The dropoff of reflectance towards UV indicates the presence of contaminants. Signal at 1.59 μm is is absorbed by the gap of the order sorting filter. The other order-sorting filters are at 2.96 and 3.86 μm but produce a weaker effect.

The scan unit supports the primary mirror with ultra-sensitive flexural pivots while the spectrometer is mounted on the telescope slit plane. The latter consists of the Focal Plane Assembly (FPA), which is packaged in kovar, the proximity electronics and a passive cooling system. Inside the FPA there are the optical window and the CCD. The FPA is connected to the cold finger of the passive cooling system.

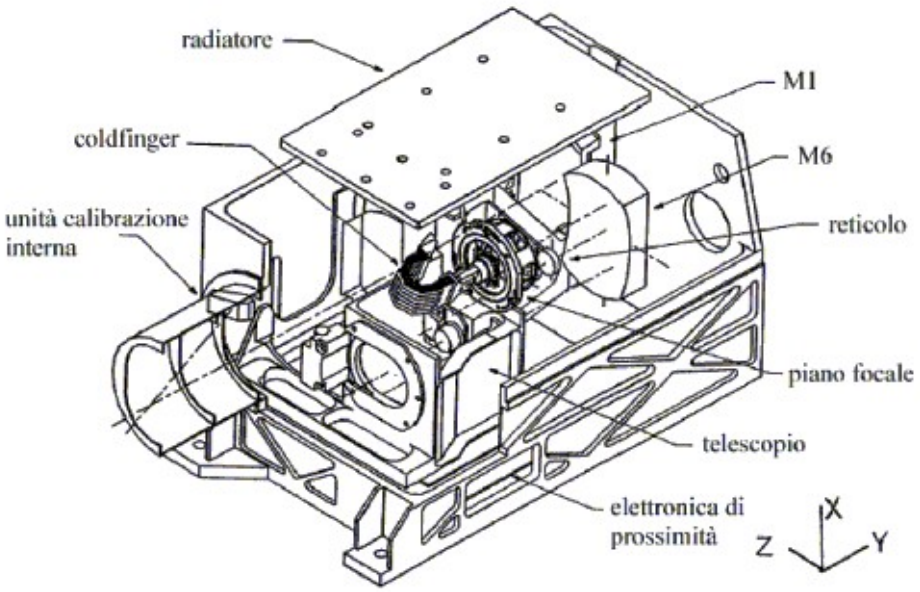

Figure 1.5: VIMS-VIS optical head (Galileo Avionica).

The optical system (fig. 1.6) is composed of a Shafer telescope $f/3.2$, an Offner grating spectrometer and the calibration unit. A light ray entering in the system is reflected by the primary mirror M1 (scanning mirror) to the folding mirror M2. The flipped image hits the secondary mirror M3 and it is sent to relay Offner mirror M4 and then to M5. Another reflection on M4 sends the beam towards the slit ($24\ \mu m \times 6\ mm$) which is at the entry of the spectrometer. The image of the slit is then reflected by M6 on the convex grating, diffracted and collected again by M6 to be sent on the CCD. On the latter a bidimensional image which contains a series of monochromatic images of the slit is recorded.

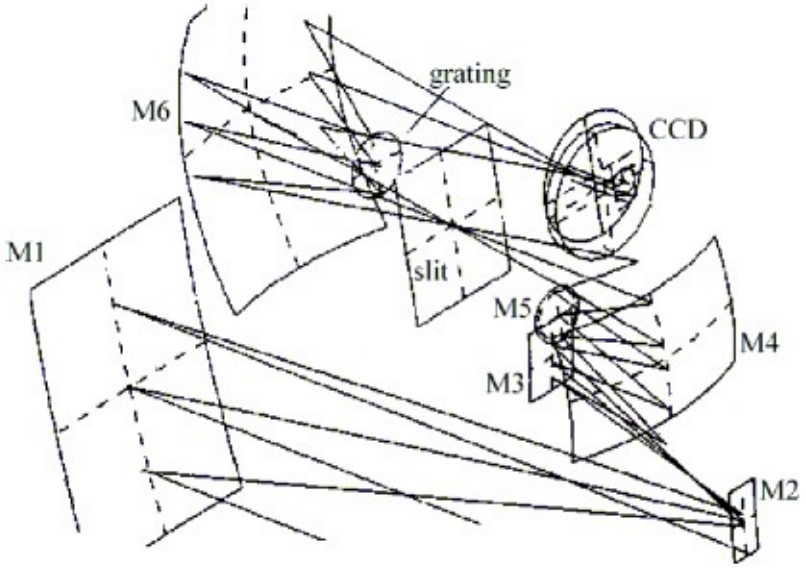

Figure 1.6: Optical system design and ray-tracing (Galileo Avionica).

1.1.1 Shafer telescope

The Shafer telescope (fig. 1.7) is obtained coupling an Offner relay to an inverted Burch telescope (Shafer, 1978). The Burch telescope uses two concentric spherical surfaces, with a primary mirror smaller than the secondary, which is obscured. This solution produces a curved image field without spherical aberration, astigmatism and coma. The inverted Burch telescope is still anastigmatic and has the primary mirror (M1) larger than the secondary (M3), however it generates a virtual image behind the secondary mirror. In order to obtain a real image it is necessary to couple the inverted Burch telescope to a relay Offner which is composed by two spherical concentric off-axis mirrors (M4 and M5). The coupling is done through a folding mirror (M2). This kind of telescope is diffraction limited. Indeed, in an optical system $f/3.2$ free of aberrations the 97% of the energy of light at 1 μm is distributed in the focal plane in a diameter of 25 μm, which is about the size of the CCD pixels (24 μm, Reininger et al. (1994)). The principal characteristics of the system are summarized in table 1.1.

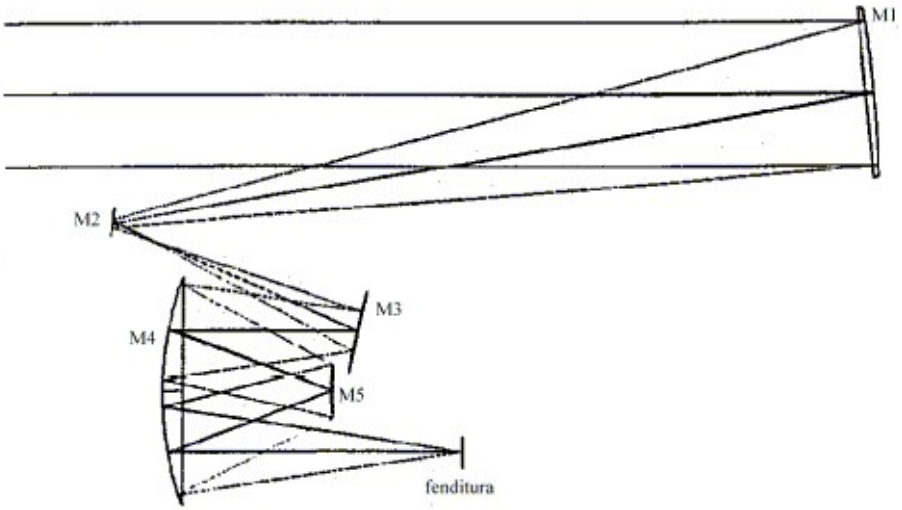

Figure 1.7: Shafer telescope ray-tracing (Galileo Avionica).

Table 1.1: VIS telescope features

Entrance pupil	$45mm$
Effective focal length	143.2 mm
Throughput ($A\Omega$)	4.42×10^{-7} cm^2ster
Slit size	24 μm $\times$ 6 mm

1.1.2 Offner spectrometer

The Offner spectrometer (fig. 1.8) has a very simple design and it is composed by the M6 mirror, the grating and the slit. Light from the slit is reflected by the M6 mirror and sent to the grating, which diffracts the light back to M6 and then on the CCD. On the focal plane the spectrum has a dispersion of 60.81 nm/mm. The main element of the spectrometer is the diffraction grating. It has a convex shape and is made of NG5 glass. The groove pattern on the grating is oriented parallel with respect to the slit and has a density of 350 $grooves/mm$. The grooves are organized in 5 concentric annular (Rowland configuration) with two alternate groove depth (fig. 1.9).

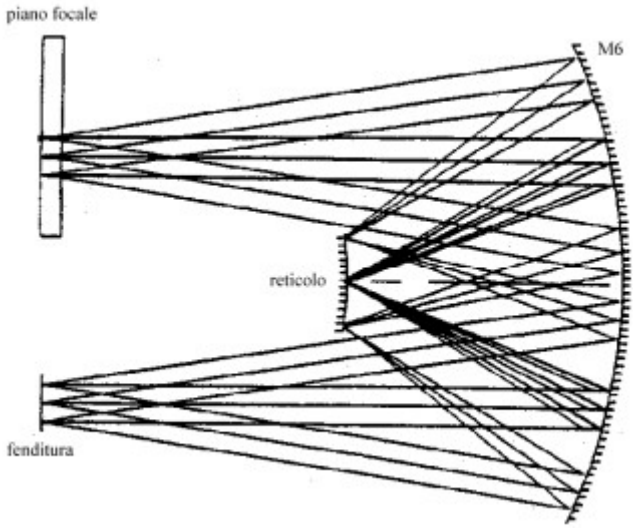

Figure 1.8: Offner spettrometer: ray-tracing, for rays entering the slit at an height of $+3$, 0 and -3 mm respect to the optical axis, is drawn.

The 68% of the grating is covered with grooves $H_1 = 285$ nm deep while the remaining 32% has $H_2 = 420$ nm. This solution allows to compensate the CCD response which is lower in ultraviolet and infrared domains. In fig. 1.10 the efficiency of the grating is shown, for a variation of $\pm 2.5\%$ of the areas with different groove depth.

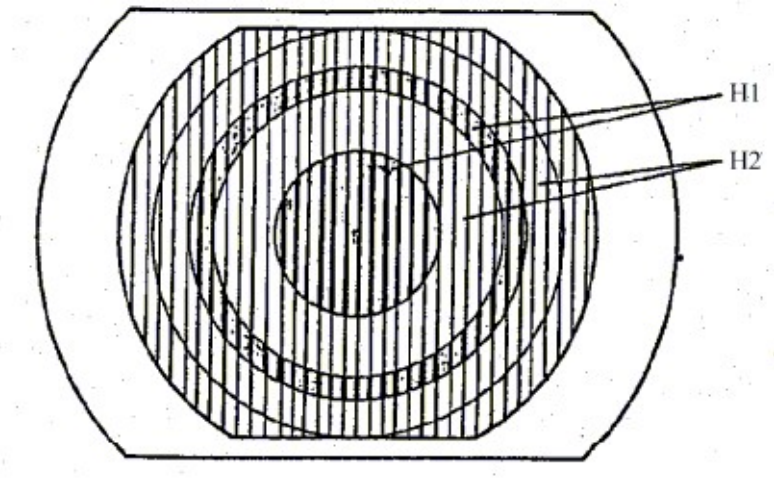

Figure 1.9: Grating grooves pattern (Zeiss).

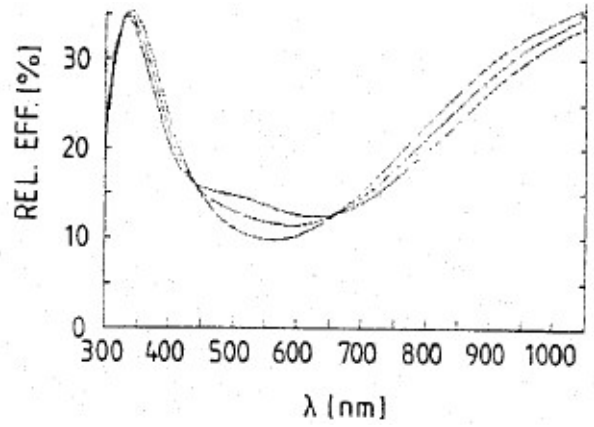

Figure 1.10: Grating efficiency vs wavelength (Zeiss)

If we analyze the dispersion equation of the grating,

$$p(\sin(\theta_1) + \sin(\theta_2)) = m\lambda \tag{1.1}$$

where p is the groove spacing, θ_1 and θ_2 the incidence and emission angles respectively, m the order (in our case -1) and λ the wavelength, we find that the m order of λ overlaps the $m+1$ of $\lambda/2$, and then, even if the $m+1$ order is much less intense than the m one it is necessary to use order sorting filters to avoid signal contamination.

1.1.3 Focal Plane Assebmly (FPA)

The FPA is composed by the CCD and the optical window (fig. 1.11).

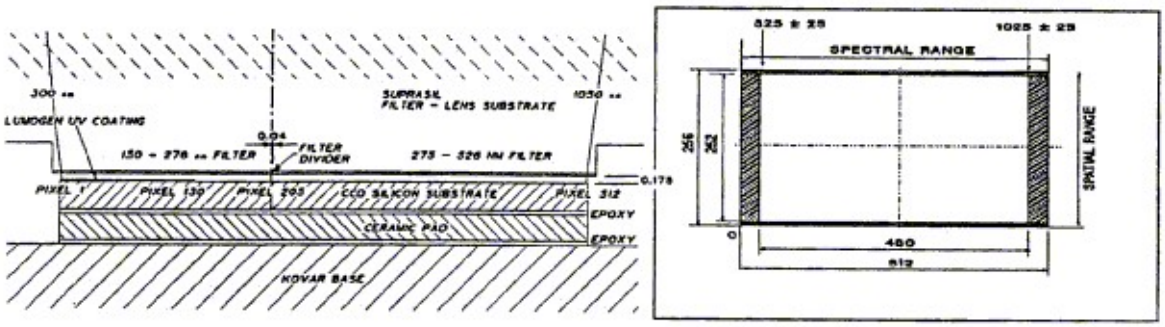

Figure 1.11: *Left panel*: section of the VIMS-VIS focal plane. *Right panel*: schematic representation of the CCD (Galileo Avionica).

The CCD of VIMS-VIS is a chip produced by Loral, front illuminated, built with NMOS technique on three silica levels and cooled at $-40°C$. The chip has 512×512 pixels of 24 $\mu m \times 24$ μm. Only half of the pixels (rows 257-512) is sensitive to light (256×512) while the others (rows 1-256) are covered by an aluminum sheet and used as a reading and storing data area, avoiding the necessity of a mechanic shutter. The CCD is oriented such that the short edge of the sensitive region is parallel to the slit of the spectrometer. The chip is mounted on a insulating ceramic layer (BeO_2) so that the kovar structure of the FPA acts like a Faraday cage to isolate the focal plane.

The suprasil optical window has a ring of Indium that closes tight the CCD. It is placed at 178 μm from the latter to avoid photonic backscattering. The inner part which corresponds to the CCD columns of the 300-490 nm spectral region is covered with Lumogen. Indeed the CCD has low sensitivity at this wavelengths (UV-Blue) but Lumogen, when hit by photon in this range, emits photons with longer wavelengths (where CCD is more sensitive). This device grants good signal even at high frequencies. On the optical window there are two high pass filters at 276 nm and 576 nm to avoid contamination from second and third order. The junction between the two filters is 40 μm wide and generates a black region on the CCD at 559 μm. The interior of the FPA is filled with Argon that prevents Lumogen sublimation.

1.2 VIMS-IR

Similarly to VIS channel the IR has two subassemblies: an infrared imaging spectrometer and its Signal Processing Electronics (SPE). The IR channel design recalls the one of the Galileo NIMS (Near Infrared Mapping Spectrometer) which has been modified to improve performances (Miller et al., 1996) (fig. 1.12). In the following list the major improvements are summarized:

- New FPA.
- Two directions scanning mechanism of the secondary mirror.
- Fixed triple-blazed grating (instead of the scanning double-blazed grating of NIMS).
- New in-flight calibration system.
- New design of the radiator.

The optical subassembly consists of a 23 cm diameter Richtey-Chretien telescope ($f/3.5$), a Dahl-Kirkham collimator of the spectrometer ($f/3.5$) and a flat field camera ($f/1.86$).

1.2.1 The telescope

In fig. 1.13 the optical design of NIMS, which has been adopted for the VIMS IR channel, is shown. As we can see the beam is sent from the primary mirror to the

secondary which scans along two orthogonal directions (samples and lines) by means of 4 voice-coil actuators and 2 LVDT (Linear Variable Displacement Transformers) that sense the mirror position (fig. 1.14). The mirror is supported at its center on a weight-balanced aluminum dish to which the voice coils, a monolithic gimbal ring, and the LVDTs are attached. The image from the secondary mirror arrives to the slit of 0.2 mm × 0.4 mm size. In table 1.2 the telescope features are summarized.

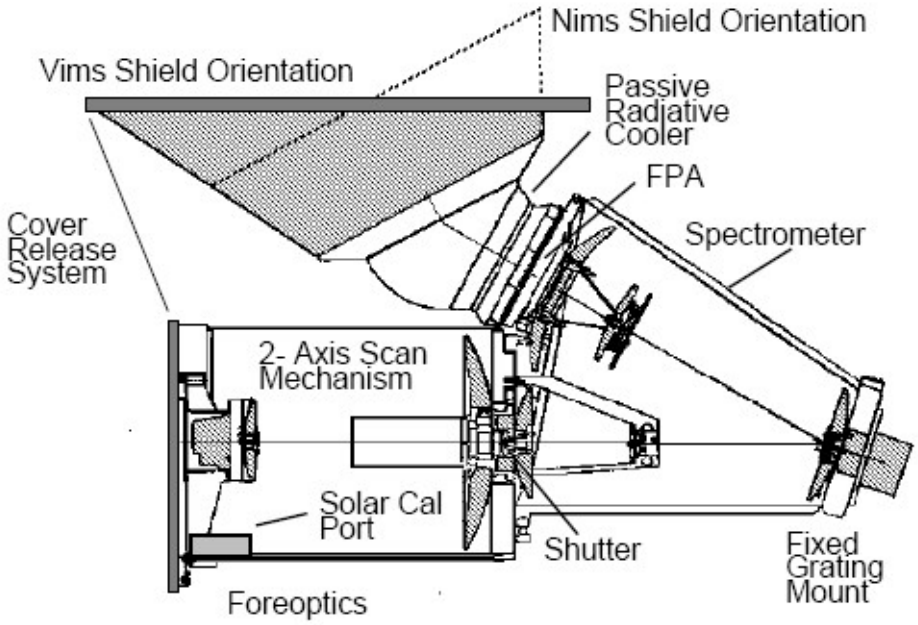

Figure 1.12: IR channel.

Table 1.2: IR telescope features

Effective focal length	426 mm
Throughput ($A\Omega$)	4.37×10^{-5} $cm^2 ster$
Slit size	0.2 mm × 2.4 mm

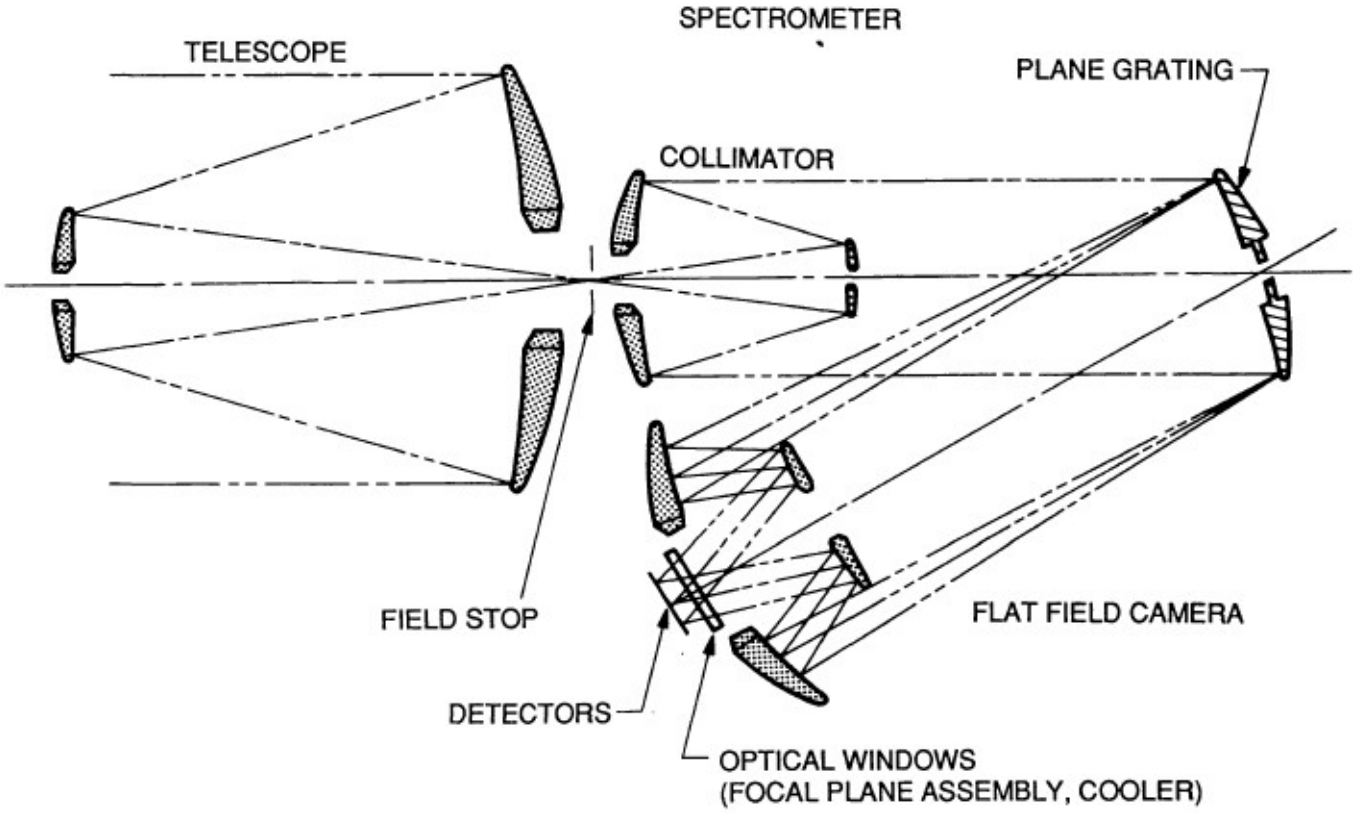

Figure 1.13: Optical design of the NIMS experiment. This one has been adopted for the IR channel of VIMS.

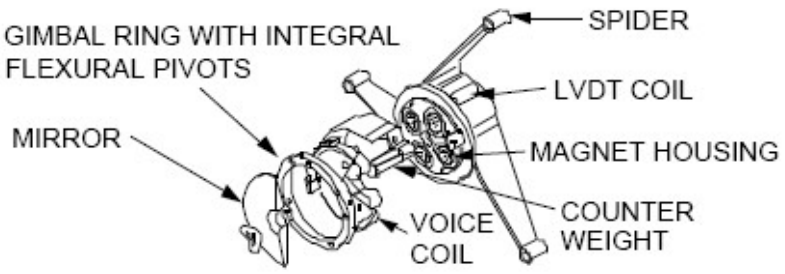

Figure 1.14: Scanning system of the secondary mirror (IR).

1.2.2 The spectrometer

As written above, the spectrometer has a fixed triple-blazed grating. This choice allows to compensate the steep intensity decrement of the solar spectrum at larger wavelengths. The three blaze wavelengths are 1.3, 3.25 and 4.25 μm which respectively cover 20, 40 and 40 % of the grating. The groove density is 27.67 $rows/mm$.

1.2.3 FPA

The FPA (fig. 1.15) consists of a linear array with 256 photodiodes read out by a couple of multiplexers whose signal is processed by the SPE. One reads out odd photodiodes and the other one even. The system is mounted on a kovar structure that connects the FPA and the radiator, allowing the focal plane to work in a temperature range of 60-77 K. Above the detector sensitive area there are four order sorting filters. The filters are configured in 4 segments which cover respectively the ranges 0.8 - 1.63 μm, 1.55 - 3.0 μm, 2.91 - 3.88 μm and 3.86 - 5.12 μm, caring that the gaps between the segments do not correspond to wavelengths of scientific interest. Each detector is 200 μm $\times$ 130 μm with a spacing of 123 μm between the centers of contiguous photodiodes.

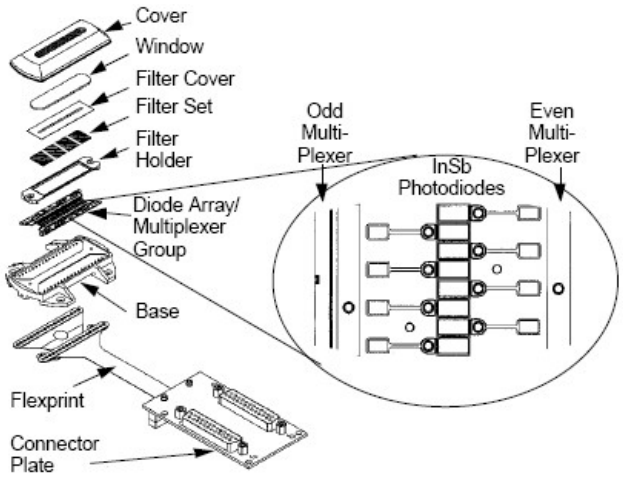

Figure 1.15: IR channel FPA.

Chapter 2

Bidirectional reflectance

In fig. 2.1 reflectance profiles of three bodies in the solar system without atmosphere (the Moon, Oberon and 69 Hesperia) is reported as a function of the phase angle. Phase angle represents the angular separation between the incident and emitted light. This kind of profiles are described by the bidirectional reflectance equation which is shown above:

$$\begin{aligned} r(i,e,g) &= \frac{w(\lambda)}{4\pi}\frac{\mu_0}{\mu+\mu_0}[p(g)B_{SH}(g)+H(\mu_0)H(\mu)-1]B_{CB}(g,\lambda) \\ B_{SH} &= 1+B_{S0}B_S(g) \\ B_{CB} &= 1+B_{C0}B_C(g). \end{aligned} \tag{2.1}$$

This formula relates the reflectance of the medium with the observation geometry that depends on the incidence and emission angle (i and e) through $\mu = \cos e$ and $\mu_0 = \cos i$ and the phase angle (g). The equation takes into account for the single scattering (which depends on the phase function $p(g)$) and the multiple scattering (the term $H(\mu)H(\mu_0)$) mechanisms and gives explanation of Shadow Hiding Opposition Effect (SHOE) and Coherent Backscattering Opposition Effect (CBOE) respectively represented by B_{SH} and B_{CB}. The spectral properties of the eq. 2.1 are determined mostly by the single scattering albedo w, which depends on the composition of the investigated medium and depends on the wavelength λ. Another parameter which explicitly depends on λ is the one which describes the CBOE, B_{CB}. In the next sections it will be shown how to derive this expression and a detailed description of each term of the equation will be given. We'll follow the description given in Hapke (1993), starting

from the basic concepts of the scattering theory and gradually introducing all the quantities that characterize the phenomenon. Further developments given in Hapke (2002, 2008) and Hapke et al. (2009) will be introduced when needed.

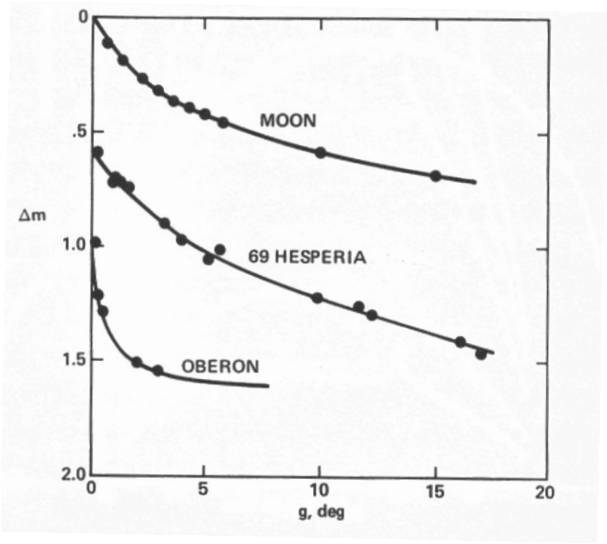

Figure 2.1: Reflectance vs. phase angle for three bodies of the solar system: the Moon, Oberon (satellite of Uranus) and the asteroid 69 Hesperia. Adapted from Hapke (1993).

2.1 Scattering from a spherical particle

In this section we discuss light scattering from a perfect sphere but as a first step it's necessary to introduce concepts and physical quantities that we'll be used throughout the chapter.

2.1.1 Fundamental quantities

The first fundamental quantity we need to introduce is the radiance $I(\mathbf{r}, \Omega)$ which is the power in the $\mathbf{r}$ position that passes through the unit area perpendicular to the propagation direction Ω, in the unit solid angle along Ω itself $[Watt/m^2/ster]$. Radiance refers to not collimated light and should not be confused with irradiance J, which is the power per unit area of a collimated ray $[Watt/m^2/ster]$ (fig. 2.2). In the following sections light incident on a particle will be implicitly considered as irradiance J while

emitted light as radiance I.

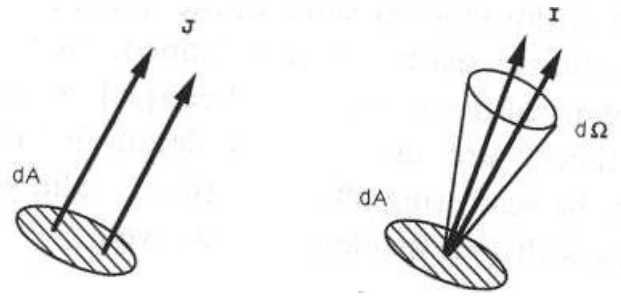

Figure 2.2: Irradiance and radiance (Hapke, 1993).

Now consider fig. 2.3 where it is shown the scattering geometry for a perfect sphere. The particle of refractive index $m = n + ik$ is illuminated by irradiance J and the radiation is emitted as radiance I with an angle θ (scattering angle) respect to the incident light. The phase angle is g, as written above.

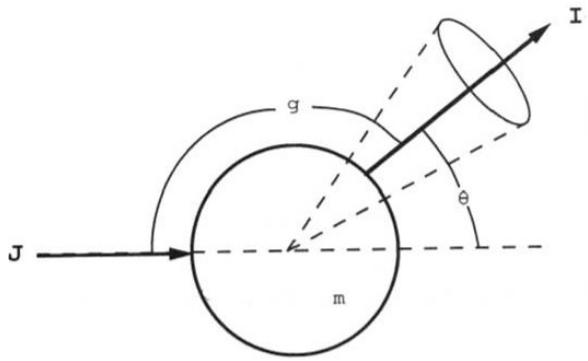

Figure 2.3: Scattering geometry (Hapke, 1993).

Only part of the radiation interacts with the particle, a fraction of this is absorbed while the rest is scattered in another direction. The fraction of light interacting with the particle is P_E. Now we can define the *extinction cross section* as

$$\sigma_E = P_E/J. \tag{2.2}$$

The fraction of extinguished radiation which is absorbed is P_A while the one that is scattered is P_S ($P_E = P_A + P_S$). We can then define the *scattering cross section* as

$$\sigma_S = P_S/J \tag{2.3}$$

and the *absorption cross section*

$$\sigma_A = P_A/J. \tag{2.4}$$

Obviously $\sigma_E = \sigma_S + \sigma_A$. For each cross section we can determine an efficiency given by the ratio of the cross section itself and the geometric cross section of the particle σ. Then

$$Q_E = \sigma_E/\sigma \tag{2.5}$$

$$Q_S = \sigma_S/\sigma \tag{2.6}$$

$$Q_A = \sigma_A/\sigma \tag{2.7}$$

where $Q_E = Q_A + Q_S$. These quantities can be combined to produce two fundamental parameters in the scattering theory: the particle *single scattering albedo* and the *espat function*. The first one is the ration between the scattered power P_S and the extinguished power P_E

$$w = P_S/P_E = \sigma_S/\sigma_E = Q_S/Q_E, \tag{2.8}$$

while the second one is the ratio between the absorbed power P_A and the scattered power P_S:

$$W = Q_A/Q_S = \frac{1-w}{w}. \tag{2.9}$$

These relations describe how much of the light incident on the particle is effectively intercepted and if it is absorbed or scattered. However, in the case of scattering, these quantities don't give any information about the direction of the scattered radiation and so we need to define a new parameter, the particle *phase function* $p(g)$, that describes how much of the scattered light is emitted in the direction indicated by g. We can

proceed as follows. The scattered power, as stated above, is $P_S = J\sigma Q_S$. The power coming from the Ω_0 direction and scattered in the unit solid angle along the direction Ω is $(dP_S/d\Omega)(\Omega, \Omega_0)$. Again g is the angle between Ω_0 and Ω. Then the phase function $p(g)$ can be defined with the following equation:

$$\frac{dP_S}{d\Omega}(\Omega_0, \Omega) = J(\Omega_0)\sigma Q_S \frac{p(g)}{4\pi}. \tag{2.10}$$

If we integrate the eq. 2.10 over the entire solid angle we must obtain again P_S so it must be true the normalization condition $\int_{4\pi} p(g)d\Omega = 4\pi$. For a particle which scatters light isotropically we have $p(g) = 1$.

2.2 Mie theory

Scattering from a spherical particle has been treated e rigorously solved by Gustav Mie (Mie, 1908) . The solution is analytic and is given as infinite series: the bigger the particle the higher the number of terms to be taken into account to give a sufficiently accurate result. In these section we are going to summarize the main properties of the MIe solution, which is the starting point for the description of the scattering process in real irregular particles.
The solution depends on two main parameters: the imaginary refractive index of the particle $m = n + ik$ and his size parameter $X = 2\pi a/\lambda = \pi D/\lambda$ where $D = 2a$ is the diameter. The solution can be analyzed defining three scattering regimes:

- particle size much smaller than wavelength: $X \ll 1$
- particle size comparable to wavelength: $X \approx 1$
- particle size much larger than wavelength: $X \gg 1$

Before describing in detail the three regimes is useful to show what happens to extinction efficiencies when the particle size changes, referring to fig. 2.4 and fig. 2.5. In fig. 2.4 it is shown Q_E for a particle with size parameter X and refractive index $m = n$ as a function of $(n-1)X$. If the imaginary part of the refractive index k is 0 there is no absorption and $Q_A = 0$. For small X the extinction efficiency is proportional to X^4, then, when the maximum is reached at $(n-1)X = 2$, Q_E begins to decrease with small

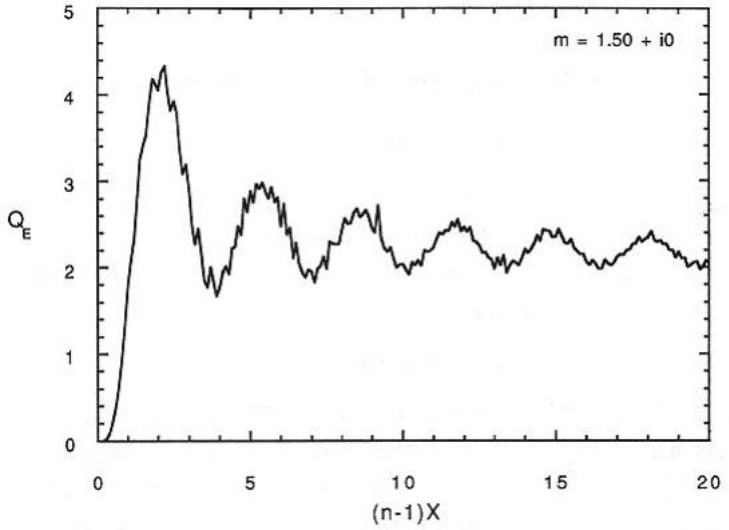

Figure 2.4: Extinction efficiency of a sphere with refractive index $m = 1.50 + i0$ and size parameter X vs. $(n-1)X$ (Hapke, 1993).

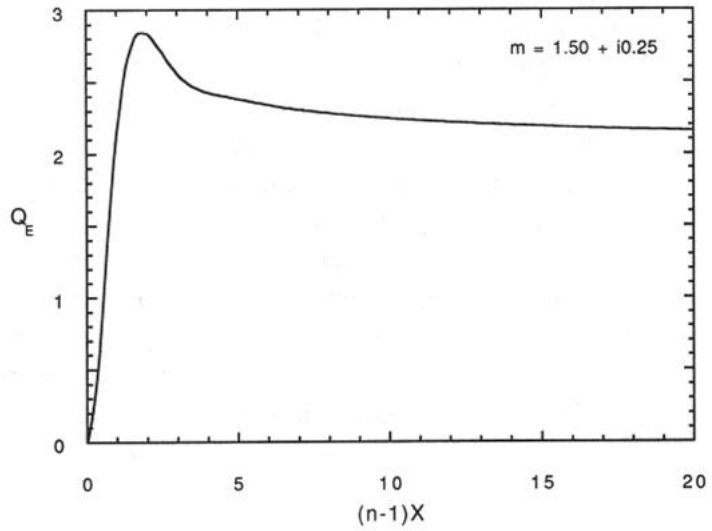

Figure 2.5: Extinction efficiency of a sphere with refractive index $m = 1.50 + i0.25$ and size parameter X vs. $(n-1)X$ (Hapke, 1993).

oscillations superimposed on larger ones, tending to the value 2. In fig. 2.5 it is shown the same situation for a particle with $m = 1.50 + i0.25$ which implies $Q_A \neq 0$. In this case, for small X, Q_E grows linearly, reaches the maximum at $(n-1)X = 2$ and slowly decrease towards 2, without oscillations, that are dumped by the absorption. Values of Q_E larger than 1 mean that the particle affects a portion of the wavefront larger than the geometric cross section, due to diffraction mechanisms.
Let's see now what happens in the three scattering regimes listed above. The $X \ll 1$ domain is indicated as Rayleigh scattering and the Mie solution gives the following expression for the particle phase function $p(g) = \frac{3}{4}(1 + cos^2 g)$ (fig. 2.6). In this case the particle phase function is symmetric and doesn't show a strong forward scattering which is the tendency to emit radiation at large phase angles ($g \approx 180°$).
The $X \approx 1$ is named resonance region. In this case the particle size is of the same order of the wavelength. The shape of particle phase function is different form case to case depending on particle properties (D and m), however to have an idea of what $p(g)$ looks like we can refer at fig. 2.7. As we can see, both in the case of absorbing ($k = 0.25$) and non-absorbing ($k = 0$) particle the particle phase function doesn't change so much end shows a strong forward scattering.
The last regime, $X \gg 1$, is the geometric optic domain. In fig. 2.8 the particle phase functions for $k = 0.25$ and $k = 0$ are shown. The behaviors are fairly different in the two cases, indeed the non absorbing particle has a phase function much more indented and rich of substructures than the absorbing particle with $k0.25$, and shows a depression in the $30° - 90°$ region. Nonetheless both the phase functions have a strong forward scattering.

The case of particle size much larger than the wavelength of incident radiation can be treated in the approximation of geometric optics considering the contributes of three scattering mechanisms: diffraction, specular reflection and refraction inside the particle. This approach is still analytical and gives an approximate closed solution, comparable with the rigorous Mie solution. The geometric optics approach allow us to investigate how each different scattering process affects the final shape of $p(g)$ (fig. 2.9). The back scattering lobe is dominated by rays that undergo internal reflections inside the particle and come back. In the central gap the only contribute is from Fresnel reflection on the particle surface, while at large g the phase function shows strong forward scattering

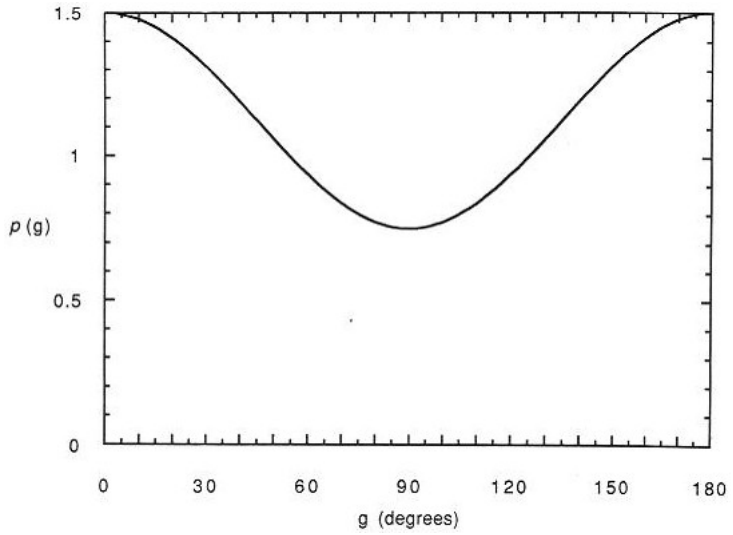

Figure 2.6: Phase function for a particle with $X \ll 1$ (Hapke, 1993).

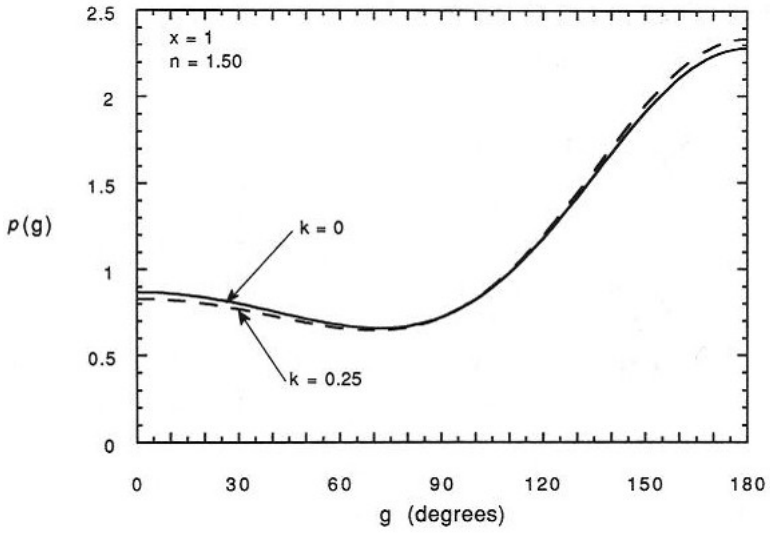

Figure 2.7: Phase function for a particle with $X = 1$ (Hapke, 1993).

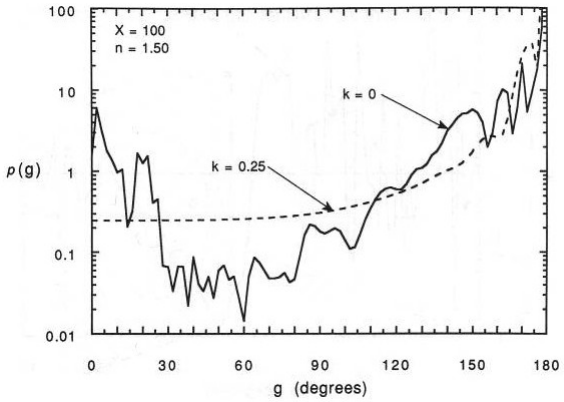

Figure 2.8: Phase function for a particle with $X = 100$ (Hapke, 1993).

due to diffraction, summed to the contribute of refracted rays that have passed through the particle once. If we compare this particle phase function with the one form MIe solution we can see that they have a good agreement.
The solutions shown here are valid for spherical particles. In the case of real irregular particles there are not analytical solutions and the problem is treated with empirical or approximate relations or with a numerical approach. In the course of this work we'll deal with irregular particles, however we'll always approximate them to spherical grains characterized by an equivalent radius (not a physical one) given by $a = \sqrt{\sigma/\pi}$ where σ is the area of the average shadow cast by particles if illuminated randomly from all the directions.

2.3 Radiative transfer equation

In this section we derive the equation of radiative transfer. The fundamental assumption we make in this framework is that the medium has inhomogeneities and that they emit radiation independently and not coherently. If the medium was made of regular particles uniformly distributed they theory would not be applicable.
Consider a radiance field $I(s, \Omega)$, in the s position which propagates into the direction Ω ($I(s, \Omega)$ generally depends on wavelength but we don't explicitly indicate this in order to maintain a synthetic notation). Take an infinitesimal cylinder in s with base area dA and height ds oriented along Ω (fig. 2.10). Through the base of the cylinder,

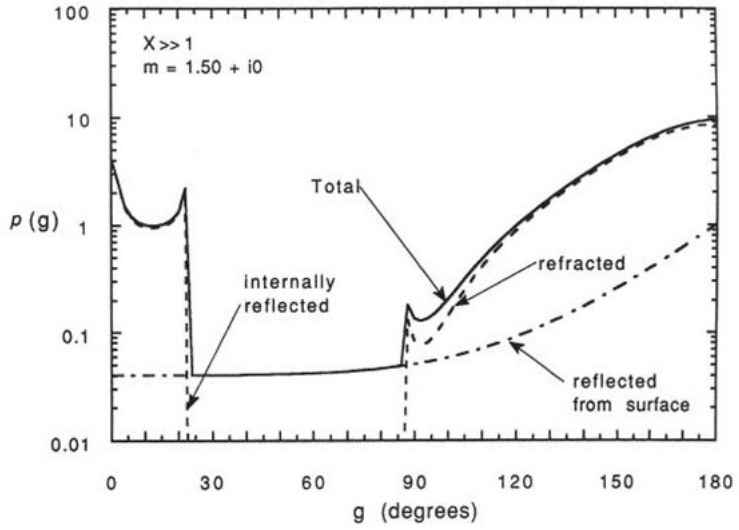

Figure 2.9: Phase function computed in approximation of geometric optics for particle much larger than the wavelenght. The various contributes to the final shape are shown (Hapke, 1993).

which has volume $dsdA$, and in the infinitesimal solid angle $d\Omega$ along the Ω direction passes the power $I(s,\Omega)dAd\Omega$. In the same way, for the superior base of the cylinder we have:

$$I(s+ds,\Omega)dAd\Omega = [I(s,\Omega) + \frac{\partial I(s,\Omega)}{\partial s}ds]dAd\Omega, \tag{2.11}$$

This means in and out radiations differ for the quantity $(\partial I/\partial s)dsdAd\Omega$. This radiance difference is due to three fundamental processes: scattering, absorption and emission. Absorption can be joined to scattering in a unique process named extinction. Now we are going to analyze each one of these mechanisms.

Extinction. The extinction process is characterized by the medium extinction coefficient $E(s,\Omega)$. It is defined by the following expression, where ΔP_E is the decrement of the power which passes through the volume element due to extinction:

$$\Delta P_E = -E(s,\Omega)I(s,\Omega)dsdAd\Omega. \tag{2.12}$$

If we consider extinction as the only mechanism at work we could write $\Delta P_E = (\partial I/\partial s)dsdAd\Omega = dIdAd\Omega$ and then, substituting in eq. 2.12 end integrating we

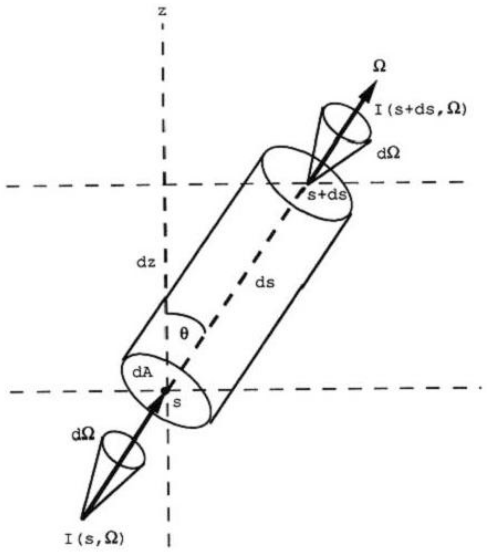

Figure 2.10: Radiation passing through an infinitesimal volume of the medium (Hapke, 1993).

obtain:

$$I(s) = I(0)e^{-\int_0^s E(s')ds'}. \tag{2.13}$$

As stated above extinction includes absorption and scattering, so we can split the extinction coefficient:

$$E(s,\Omega) = K(s,\Omega) + S(s,\Omega) \tag{2.14}$$

where $K(s,\Omega)$ and $S(s,\Omega)$ are respectively the volume absorption and scattering coefficients.

Scattering. Scattering can both increase or decrease the radiation field exiting the volume element, moreover it can changes the direction of light coming from Ω' into Ω and vice versa. This process is characterized by the volume angular scattering coefficient $G(s,\Omega',\Omega)$ defined by the following equation, where ΔP_S is the power that is scattered in the direction Ω from the direction Ω':

$$\Delta P_S = \frac{1}{4\pi} G(s,\Omega',\Omega) I(s,\Omega') ds dA d\Omega d\Omega'. \tag{2.15}$$

If we integrate this quantity over all the Ω' directions the entire power scattered in Ω is obtained. The integral of the volume angular scattering coefficient is named

volume scattering coefficient $S(s,\Omega)$ and it is given the following relation:

$$S(s,\Omega) = \frac{1}{4\pi}\int_{4\pi} G(s,\Omega',\Omega)d\Omega'. \tag{2.16}$$

Emisson. The emission mechanism is described by the volume emission coefficient $F(s,\Omega)$, which is the power emitted per unitary solid angle along the direction Ω in the position s:

$$\Delta P_F = F(s,\Omega)dsdAd\Omega. \tag{2.17}$$

The only processes that can contribute to the emission in a particulate medium are the single scattering $F_S(s,\Omega)$ and the thermal emission ($F_T(s,\Omega)$):

$$F(s,\Omega) = F_S(s,\Omega) + F_T(s,\Omega). \tag{2.18}$$

Single scattering is the scattering of the irradiance that directly hits the medium. At the depth s the irradiance coming form Ω_0 that has not been extinguished is

$$J\delta(\Omega-\Omega_0)e^{-\int_s^\infty E(s',\Omega)ds'}. \tag{2.19}$$

This radiation undergoes one scattering and can be considered as a source of diffuse radiance, contributing to the volume emission coefficient with the quantity

$$\begin{aligned} F_S(s,\Omega) &= \int_{4\pi} J\delta(\Omega'-\Omega_0)e^{-\int_s^\infty E(s',\Omega)ds'}G(s,\Omega',\Omega)d\Omega' \\ &= JG(s,\Omega_0,\Omega)e^{-\int_s^\infty E(s',\Omega)ds'}. \end{aligned} \tag{2.20}$$

We are not giving a description of thermal emission process because it is not important for our future purposes. Now if we sum all the contributes to the radiance variation we obtain:

$$\Delta P_S + \Delta P_E + \Delta P_F = (\frac{\partial I}{\partial s})dsdAd\Omega \tag{2.21}$$

and if we divide for $dsdAd\Omega$ we have

$$\frac{\partial I(s,\Omega)}{\partial s} = -E(s,\Omega)I(s,\Omega) + \frac{1}{4\pi}\int_{4\pi} I(s,\Omega')G(s,\Omega',\Omega)d\Omega' + F(s,\Omega). \tag{2.22}$$

Referring to fig. 2.10 we can easily verify the relation $ds = dz/\cos\theta$. With this substitution it is possible to express the derived formulas as a function of z. This is the best choice because in common application the investigated media are horizontally stratified. Moreover, in many situations, the functions E, S and K do not depend on the propagation direction and so we can eliminate their dependence on Ω. After these consideration we can substitute s with z and divide eq. 2.22 for $E(z)$ obtaining:

$$\frac{cos\theta}{E(z)}\frac{\partial I(z,\Omega)}{\partial z} = -I(z,\Omega) + \frac{S(z)}{E(z)}\frac{1}{4\pi}\int_{4\pi} I(z,\Omega')\frac{G(z,\Omega',\Omega)}{S(z)}d\Omega' + \frac{F(z,\Omega)}{E(z)}. \tag{2.23}$$

Now let's define a new quantity, the *optical depth* τ, as

$$\tau = \int_s^\infty E(s')ds'\cos\theta = \int_z^\infty E(z')dz' \tag{2.24}$$

whence

$$d\tau = -E(s)ds\cos\theta = -E(z)dz. \tag{2.25}$$

Optical depth is an adimensional number which expresses the vertical depth in unit of $1/E$. Light which penetrates vertically in the medium from above unto the height which corresponds to τ is reduced for a factor of $e^{-\tau}$ and the same is for the light propagating from z to the top.
Now let there be the single scattering albedo

$$w(z) = \frac{S(z)}{E(z)}, \tag{2.26}$$

the particle phase function

$$p(z,\Omega',\Omega) = \frac{G(z,\Omega',\Omega)}{S(z)} \tag{2.27}$$

and the source function

$$\begin{aligned}\mathcal{F}(z,\Omega) &= \frac{F(z,\Omega)}{E(z)} \\ &= J[e^{-\int_s^\infty E(s')ds'}]\frac{G(z,\Omega_0),\Omega}{E(z)} + \mathcal{F}_T(z,\Omega) \\ &= Je^{-\tau/\cos i}w(\tau)p(\tau,\Omega_0,\Omega) + \mathcal{F}_T(\tau,\Omega) \end{aligned} \tag{2.28}$$

where i is the angle between the incident radiation and the vertical and $\mathcal{F}_T = F_T/E$. With these definitions we can write the equation of radiative transfer in the following way:

$$\begin{aligned}-\cos\theta\frac{\partial I(\tau,\Omega)}{\partial\tau} = -I(\tau,\Omega) + \frac{w(\tau)}{4\pi}\int_{4\pi} I(\tau,\Omega')p(\tau,\Omega',\Omega)d\Omega' \\ +J\frac{w(\tau)}{4\pi}p(\tau,\Omega_0,\Omega)e^{-\tau/\cos i} + \mathcal{F}_T(\tau,\Omega).\end{aligned} \tag{2.29}$$

2.3.1 Radiative transfer equation in a medium of well-separated particles

In the deriving of the equation of radiative transfer we defined the functions E, S and K without giving an explicit expression. In this section we give one analyzing what happens to the radiation which passes through a medium made of particles randomly distributed and separated by a distance which is larger than the wavelength and their size. Consider a slab of material whose volume is $dsdA$ (fig. 2.11), made of identical particles.

If N is the number of particles per unitary volume, σ the cross section and Q_E the extinction coefficient, we can write for the intercepted and extinguished power the following expression:

$$\Delta P_E = JN\sigma Q_E dsdAd\Omega. \tag{2.30}$$

We made the implicit assumption that no particle shields another because dA is much larger than σ and ds is sufficiently small. If we compare the eq. 2.30 with eq. 2.12 it is possible to conclude that

$$E = N\sigma Q_E. \tag{2.31}$$

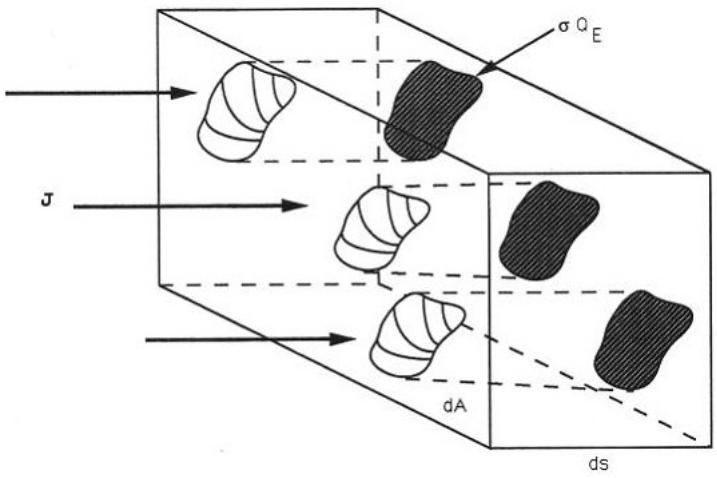

Figure 2.11: Extinction from particles in a slab (Hapke, 1993).

If the medium is made of different types of particles that are indicated by the index $\jmath$ we should write

$$E = \sum_{\jmath} N_{\jmath}\sigma_{\jmath}Q_{E\jmath} = N\langle\sigma Q_E\rangle, \tag{2.32}$$

where $N = \sum_{\jmath} N_{\jmath}$ e $\langle\sigma Q_E\rangle = (\sum_{\jmath} N_{\jmath}\sigma_{\jmath}Q_{E\jmath})/N$.

In an analogue way it is possible to define

$$S = \sum_{\jmath} N_{\jmath}\sigma_{\jmath}Q_{S\jmath} \tag{2.33}$$

and

$$K = \sum_{\jmath} N_{\jmath}\sigma_{\jmath}Q_{K\jmath}. \tag{2.34}$$

Then if the particle phase function is $p(g)_{\jmath}$ we have for the angular scattering coefficient

$$G(g) = \sum_{\jmath} N_{\jmath}\sigma_{\jmath}Q_{S\jmath}p(g)_{\jmath}. \tag{2.35}$$

2.3.2 The filling factor

The expression we derived in the previous section are not valid in medium where the particles are not well-separated (Ishimaru and Kuga, 1982; Kortum, 1969). This can be understood with the following considerations.
Suppose to have a medium composed of one type of particles and constant N. The transmission of such a slab of thickness s, $t(s) = I(s)/I(0)$, is given by

$$t(s) = e^{-Es} \tag{2.36}$$

where $Es = N\sigma a Q_E(s/a)$ and the average particle radius $a = \sqrt{\sigma/\pi}$. The particle volume is $\mathcal{V} \approx (4/3)\pi a^3 = (4/3)\sigma a$. Let's define filling factor the quantity $\phi = N\mathcal{V} = (4/3)N\sigma a$. This means that

$$t(s) = e^{-\frac{3}{4}\phi Q_E(s/a)}. \tag{2.37}$$

If $\phi \to 1$ all the lights should be blocked and then $t \to 0$. However, even if we put $Q_E = 1$, for a slab of thickness a the eq. 2.37 gives $t(a) = e^{-3/4} \neq 0$. This shows that it's necessary to investigate the dependence of the efficiencies on the filling factor. Consider now a slab of thickness δz, larger than the size of its particles and of large lateral extent. The total volume of the slab is V, N is the number of particles per unit volume and $\mathcal{N} = NV \gg 1$ the total number. The particles, not necessarily identical, are randomly distributed and indicated by the subscript $\jmath$. Each particle has a volume $\mathcal{V}_\jmath \ll V$, cross section $\sigma_\jmath$ and extinction efficiency $Q_{E\jmath}$. The shadow cast by the single particle are treated as circular because are relative to the average cross section, that is circular by definition. We can define the transmission $t(\delta z, \theta)$ as the probability for a light-ray incident with an angle θ respect to the vertical to penetrate through the slab without encountering a particle (fig. 2.12). This is equal to the probability that the cylinder that has as axis the light-ray, base area $\sigma_\jmath Q_{E\jmath}$ and volume $\sigma_\jmath Q_{E\jmath}\delta z \sec\theta$ is free of particles. To estimate this probability let's do the following reasoning (to simplify the computation we put $Q_E = 1$, but at the end this assumption will be removed). Imagine to remove all the particles from the slab and then to replace them one at a time in random position. The volume available for the center of the first particle ($\jmath = 1$) we place is $V - \mathcal{V}_1$, therefore the probability that this one is not in the

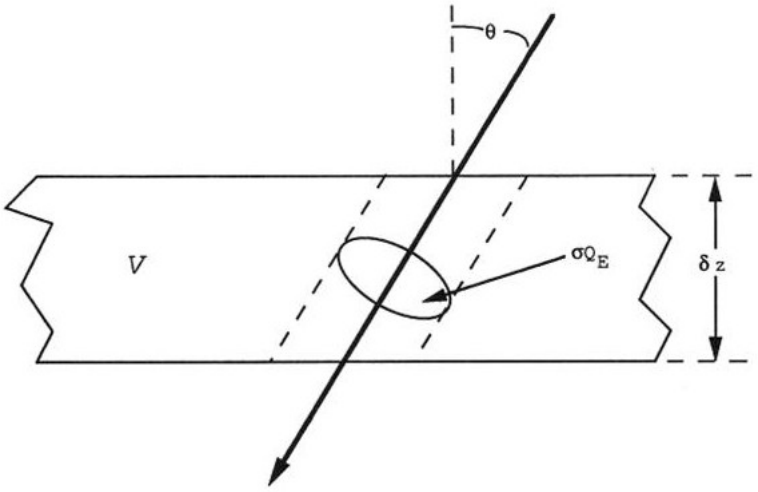

Figure 2.12: Light-ray that passes through a slab of infinitesimal thickness δ (Hapke, 1993).

cylindrical volume $\sigma_1 \delta z \sec\theta$ is

$$\Delta t_1 = 1 - \frac{\sigma_1 \delta z \sec\theta}{V - \mathcal{V}_1}. \tag{2.38}$$

If we place the second particle the available volume is $V - \mathcal{V}_1 - \mathcal{V}_2$ and the probability is

$$\Delta t_2 = 1 - \frac{\sigma_2 \delta z \sec\theta}{V - \mathcal{V}_1 - \mathcal{V}_2}. \tag{2.39}$$

For the jth particle we obatin

$$\Delta t_j = 1 - \frac{\sigma_j \delta z \sec\theta}{V - \sum_{l=1}^{j} \mathcal{V}_l}. \tag{2.40}$$

The probability that none of the particles blocks the ray is given by the product of the probability of each particle:

$$\Delta t = \prod_{j=1}^{\mathcal{N}} (1 - \frac{\sigma_j \delta z \sec\theta}{V - \sum_{l=1}^{j} \mathcal{V}_j}). \tag{2.41}$$

Assume that V is sufficiently large and that $V - \sum_{l=1}^{j} \mathcal{V}_l \gg \sigma_j \delta z \sec\theta$. This means that each factor making up Δt is close to 1 but it doesn't imply that transmission is

large. Then it is true the following approximation

$$\Delta t = e^{-\Delta\tau \sec\theta} \tag{2.42}$$

and

$$\Delta\tau = \frac{\delta z}{V}\sum_{\jmath=1}^{\mathcal{N}} \frac{\sigma_\jmath}{1-(1/V)\sum_{l=1}^{\jmath}\mathcal{V}_l}. \tag{2.43}$$

This computation takes in account only for one order of slab loading, however there are $N!$ combinations of the order in which the particles can be placed in the slab. If we average all the combinations and permutations we obtain (the computation is not shown here):

$$\Delta t(\delta z,\theta) = e^{\frac{N\langle\sigma\rangle\delta z\sec\theta}{\phi}\ln(1-\phi)}, \tag{2.44}$$

where

$$\langle\sigma\rangle = \sum_{l=1}^{\mathcal{N}}\sigma_l/\mathcal{N} \tag{2.45}$$

is the average particles cross section,

$$\langle\mathcal{V}_l\rangle = \sum_{l=1}^{\mathcal{N}}\mathcal{V}_l/\mathcal{N} \tag{2.46}$$

the average volume and

$$\phi = N\langle\mathcal{V}_l\rangle \tag{2.47}$$

the filling factor. If we consider a continuous sequence of layers of infinitesimal thickness the transmission is the product of terms like the one of eq. 2.44 and the result is:

$$t(z,\theta) = e^{\sec\theta\int_0^z \frac{N\langle\sigma\rangle}{\phi}\ln(1-\phi)dz'}. \tag{2.48}$$

Then if we remove the $Q_{E_\jmath} = 1$ assumption we have to substitute $\langle\sigma\rangle$ with $\langle\sigma Q_E\rangle$, whence:

$$t(z,\theta) = e^{\sec\theta\int_0^z \frac{N\langle\sigma Q_E\rangle}{\phi}\ln(1-\phi)dz'}. \tag{2.49}$$

From the comparison of eq. 2.49 with eq. 2.13we find a more general expression for

the volume extinction coefficient:

$$E = -\frac{N\langle\sigma Q_E\rangle}{\phi}\ln(1-\phi) \tag{2.50}$$

which, in the limit $\phi \ll 1$, gives the eq. 2.32, while, when $\phi \to 1$, makes the medium totally opaque and $E \to \infty$. Analogues expression can be found for S and K. Referring to eq. 2.50 ,it is possible to introduce a new quantity, named effective particles density $N_E = -N\frac{\ln(1-\phi)}{\phi}$.

For completeness it is useful to report the expression of all the coefficients that appear in the radiative transfer equation, for the case of a medium composed by different types of particles $\jmath$ with a corresponding particles number for unit volume $N_\jmath$:

$$\begin{aligned}
E &= N_E\langle\sigma Q_E\rangle = -\frac{\ln(1-\phi)}{\phi}\sum_\jmath N_\jmath\sigma_\jmath Q_{E\jmath}, && (2.51)\\
S &= N_E\langle\sigma Q_S\rangle = -\frac{\ln(1-\phi)}{\phi}\sum_\jmath N_\jmath\sigma_\jmath Q_{S\jmath}, && (2.52)\\
K &= N_E\langle\sigma Q_A\rangle = -\frac{\ln(1-\phi)}{\phi}\sum_\jmath N_\jmath\sigma_\jmath Q_{A\jmath}, && (2.53)\\
N &= \sum_\jmath N_\jmath, && (2.54)\\
\langle\sigma Q_E\rangle &= (\sum_\jmath N_\jmath\sigma_\jmath Q_{E\jmath})/N, && (2.55)\\
\langle\sigma Q_S\rangle &= (\sum_\jmath N_\jmath\sigma_\jmath Q_{S\jmath})/N, && (2.56)\\
\langle\sigma Q_A\rangle &= (\sum_\jmath N_\jmath\sigma_\jmath Q_{A\jmath})/N. && (2.57)\\
& && (2.58)
\end{aligned}$$

The filing factor is

$$\phi = N\langle\mathcal{V}\rangle = \sum_\jmath N_\jmath\mathcal{V}_\jmath, \tag{2.59}$$

$$\langle\mathcal{V}\rangle = \sum_\jmath N_\jmath\mathcal{V}_\jmath/N. \tag{2.60}$$

Because the particles are randomly oriented the volume scattering coefficient doesn't

depend on the direction of incident and emergent light, but only on the phase angle, so:

$$G(g) = N_E\langle\sigma Q_S p(g)\rangle = -\frac{\ln(1-\phi)}{\phi}\sum_{\jmath} N_\jmath\sigma_\jmath Q_{S\jmath}p_\jmath(g). \tag{2.61}$$

Concerning the single scattering albedo we have

$$\begin{aligned} w = S/E = \langle\sigma Q_S\rangle/\langle\sigma Q_E\rangle &= (\sum_{\jmath} N_\jmath\sigma_\jmath Q_{S\jmath})/(\sum_{\jmath} N_\jmath\sigma_\jmath Q_{E\jmath}) \\ &= (\sum_{\jmath} N_\jmath\sigma_\jmath Q_{E\jmath}w_\jmath)/(\sum_{\jmath} N_\jmath\sigma_\jmath Q_{E\jmath}) \end{aligned} \tag{2.62}$$

where $w_\jmath = Q_{S\jmath}/Q_{E\jmath}$ is the single scattering albedo of the $\jmath$ particles. The phase function of the medium is

$$\begin{aligned} p(g) = G(g)/S &= [\sum_{\jmath} N_\jmath\sigma_\jmath Q_{S\jmath}p_\jmath(g)]/[\sum_{\jmath} N_\jmath\sigma_\jmath Q_{S\jmath}] \\ &= [\sum_{\jmath} N_\jmath\sigma_\jmath Q_{E\jmath}w_\jmath p_\jmath(g)]/[\sum_{\jmath} N_\jmath\sigma_\jmath Q_{E\jmath}w_\jmath], \end{aligned} \tag{2.63}$$

and last thing remained to define is the espat function:

$$\begin{aligned} W = (1-w)/w = K/S &= [\sum_{\jmath} N_\jmath\sigma_\jmath(Q_{E\jmath} - Q_{S\jmath})]/[\sum_{\jmath} N_\jmath\sigma_\jmath Q_{S\jmath}] \\ &= [\sum_{\jmath} N_\jmath\sigma_\jmath Q_{E\jmath}(1-w_\jmath)]/[\sum_{\jmath} N_\jmath\sigma_\jmath Q_{E\jmath}w_\jmath]. \end{aligned} \tag{2.64}$$

2.4 Bidirectional reflectance of a semi-infinite medium

In this section we solve the radiative transfer equation for a semi-infinite medium. The result we obtain is the *reflectance* of the medium, which is the ration between radiance scattered by the surface and the incident irradiance.

Before we start, let us define the geometry of the problem, referring to fig. 2.13. The irradiance J hits the area element of the surface ΔA with an angle i respect to the vertical indicated by the vector $\mathbf{N}$. The observer receives the radiance I which is emitted with an angle e. The angle between incidence and emission direction is the phase angle g. The two planes that contains the vertical and the incidence and emission directions, respectively, are the incidence and emission planes. The plane

which contains both the incidence and emission directions is the scattering plane. The angle between the incidence and emission planes is ψ. In the common notation we have:

$$\begin{aligned} \mu &= \cos e \\ \mu_0 &= \cos i. \end{aligned} \tag{2.65}$$

2.4.1 Radiance received by a detector observing a semi-infinite medium

In the observation of horizontally stratified media it's necessary to understand which is the relation between the radiance filed in the medium and the radiation received by the detector. To answer this question we apply the radiative transfer equation, referring to fig. 2.14. Imagine a particulate medium with a random distribution of particles and the only condition that the density N is 0 when $z \to \infty$ or $\tau \to 0$. Below the $\tau = 0$ limit the particles are characterized by $E(z)$, $S(z)$, $K(z)$, $G(z, \Omega', \Omega)$ and $F(z, \Omega)$. The space above $\tau = 0$ is empty, excepting for the irradiance J source which illuminates the medium. The sensitive area of the detector is Δa and the acceptance solid angle is $\Delta\omega$. The light entering the detector is like if it is emitted by an area ΔA, given by the intersection between the acceptance cone and the medium surface. Actually the radiance is determined by all the particles in $\Delta\omega$. In the case that the particles numerical density is a step function the apparent surface is the top of the medium, while, for different particles distributions we consider as apparent surface the $\tau = 1$ level. Now consider a volume element $dV = R^2 \Delta\omega dR$, inside the cone $\Delta\omega$, at altitude z and distance R from the detector. This volume element is in a radiance field $I(z, \Omega')d\Omega'$. The power per unit solid angles scattered toward the detector along the Ω direction is $(dV/4\pi) \int_{4\pi} G(z, \Omega', \Omega)d\Omega'$. We have to add the power emitted by the volume dV, $F(z, \Omega)dV$. The solid angle under which the detector is seen by the infinitesimal volume is $\Delta a/R^2$, while the attenuation undergone by the radiation before exiting the medium is $e^{-\tau/\mu}$. After these considerations we can compute the radiation

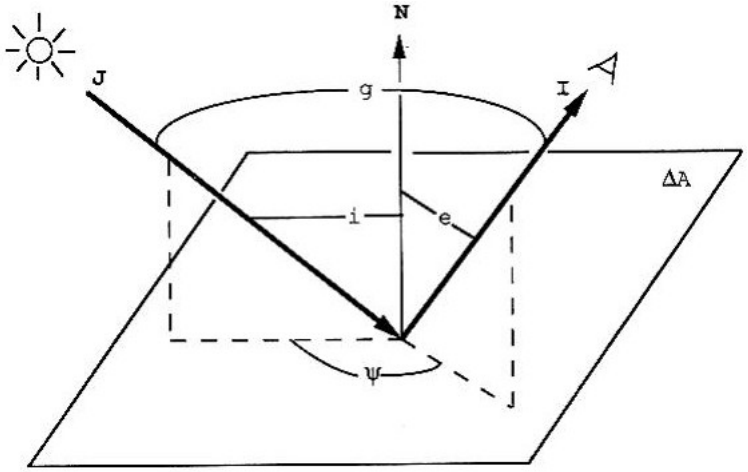

Figure 2.13: Bidirectional reflectance geometry (Hapke, 1993).

on the detector emitted by the volume dV:

$$\begin{aligned} dP_D &= \left[\frac{1}{4\pi}\int_{4\pi} G(z,\Omega',\Omega)I(z,\Omega')d\Omega' + F(z,\Omega)\right] dV\frac{\Delta a}{R^2}e^{-\tau/\mu} \\ &= \left[\frac{1}{4\pi}\frac{S(z)}{E(z)}\int_{4\pi}\frac{G(z,\Omega',\Omega)}{S(z)}I(z,\Omega')d\Omega' + \frac{F(z,\Omega)}{E(z)}\right] R^2\Delta\omega\frac{E(z)dz}{\mu}\frac{\Delta a}{R^2}e^{-\tau/\mu} \\ &= -\Delta\omega\Delta a\left[\frac{w(\tau)}{4\pi}\int_{4\pi} p(\tau,\Omega',\Omega)I(\tau,\Omega')d\Omega' + \mathcal{F}(\tau,\Omega)\right] e^{-\tau/\mu}\frac{d\tau}{\mu}, \end{aligned} \tag{2.66}$$

where $dz = \mu dR = -d\tau/E$. To obtain the total power on the detector we must integrate dP_D over all the volume contained in $\Delta\omega$, i.e. from 0 to $\tau = \infty$. In order to have the radiance we must divide this quantity for the detector solid angle and area, then we have:

$$I_D = \frac{1}{\Delta\omega\Delta a}\int_{\tau=\infty}^{0} dP_D = \int_0^{\infty}\left[\frac{w(\tau)}{4\pi}\int_{4\pi} p(\tau,\Omega',\Omega)I(\tau,\Omega')d\Omega' + \mathcal{F}(\tau,\Omega)\right] e^{-\tau/\mu}\frac{d\tau}{\mu}. \tag{2.67}$$

From the radiative transfer equation we see that the factor in square brackets is

$$\begin{aligned} &\left[\frac{w(\tau)}{4\pi}\int_{4\pi} p(\tau,\Omega',\Omega)I(\tau,\Omega')d\Omega' + \mathcal{F}(\tau,\Omega)\right] \\ &= -\left[\mu\frac{\partial I(\tau,\Omega)}{\partial\tau} - I(\tau,\Omega)\right] = -\mu e^{\tau/\mu}\frac{\partial}{\partial\tau}[I(\tau,\Omega)e^{-\tau/\mu}]. \end{aligned} \tag{2.68}$$

Imposing that $I(\tau, \Omega)$ remains finite when $\tau \to 0$ we have:

$$I_D = -\int_{\tau=0}^{\infty} \partial[I(\tau,\Omega)e^{-\tau/\mu}] = -[I(\tau,\Omega)e^{-\tau/\mu}]|_0^{\infty} = I(0,\Omega). \tag{2.69}$$

What comes out is that the radiance measured by the detector is the radiance which leaves the surface in the direction of the detector itself.

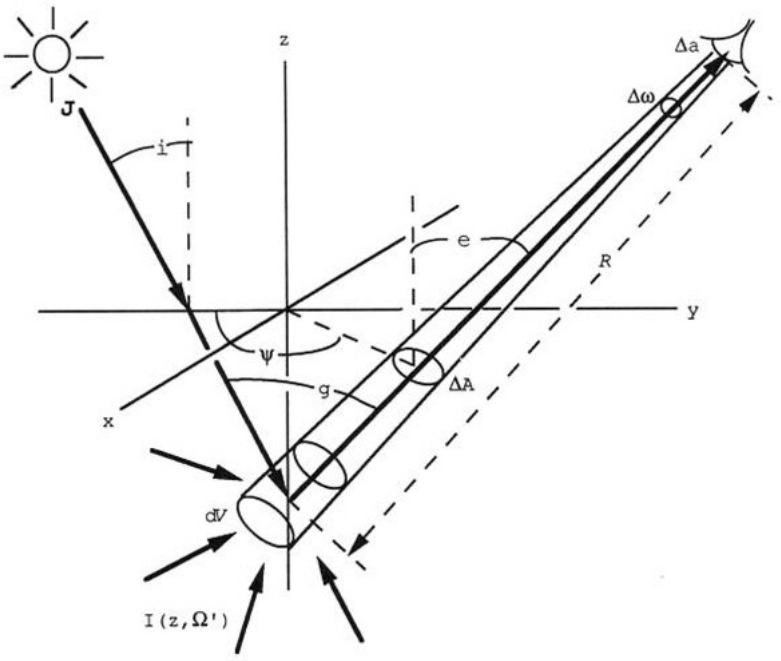

Figure 2.14: Scattering geometry for an horizontally stratified particulate medium (Hapke, 1993).

2.4.2 Lambert surfaces

Luminosity measures very often are expressed as the ratio of the radiance emitted by the medium and the one of a Lambert surface, if both illuminated by the same irradiance. A Lambert surface emits radiation without any dependence on the emission e and azimuth ψ angles. So the radiance is proportional to $J\mu_0$, and because the reflectance is the ratio between the emitted radiance and incident irradiance, we can

write $r_L(i) = K_L \cos i$. Then the total emitted power from a unit Lambert surface is:

$$P_L = \int_{2\pi} I(i)\mu d\Omega = \int_{e=0}^{\pi/2} \int_{\psi=0}^{2\pi} JK_L \cos i \cos e \sin e de d\psi = \pi J K_L \mu_0. \tag{2.70}$$

The $\mu = \cos e$ term in the first integral is due to the fact that the radiance $I(i)$ is defined as power per unit solid angle and unit surface. The unit surface is orthogonal respect to the propagation direction, and it is $\cos e$ times the real Lambertian unit surface. $J\mu_0$ represents the incident power per unit surface and we define *Lambert albedo* the quantity $A_L = P_L/J\mu_0 = K_L\pi$ and then $K_L = A_L/\pi$. Finally the Lambert reflectance is:

$$r_L(i) = \frac{A_L}{\pi}\mu_0. \tag{2.71}$$

2.4.3 Bidirectional reflectance for a medium composed by particles with isotropic phase function

The computing of the bidirectional reflectance by means of the radiative transfer equation requires approximation methods. Moreover if we deal with anisotropic scatterers the computing becomes cumbersome and difficult, while is largely simplified in the case of isotropic single particle phase function. Because of this here it is preferred to derive the bidirectional reflectance for isotropic scatterers adopting an alternative approach, which is the method of the *embedded invariance*, which on the other side provide an exact analytic solution. The basic consideration of this approach is that the reflectance properties of a semi-infinite medium don't change if we add a layer of material with infinitesimal thickness on top of the medium itself. We'll proceed investigating all the interaction that light undergoes in the added layer. Because of the *embedded invariance* (Ambartsumian, 1958) the sum of the various contributes must be 0 and from the corresponding equation we derive the bidirectional reflectance. As stated above we deal with isotropic particles $p(g) = 1$, so the solution is independent of ψ. Later it will be shown how to extend the result to anisotropic scatterers.

2.4.4 The embedded invariance method

Consider a semi-infinite medium and add on top of this a subtle layer of the same material of thickness Δz and optical depth $\Delta\tau$. The added layer gives raise to 5 processes in the scattered light whose effect is proportional to $\Delta\tau$ (fig. 2.15, 2.16 and 2.17). Higher order processes are neglected.

(a). Light passing through the layer is partially extinguished before and after the reflection on the reference surface (fig. 2.15). The radiation is reduce respectively of a factor $e^{-\tau/\mu_0}$ and $e^{-\tau/\mu}$, and the emerging radiance is

$$I = Je^{-\Delta\tau\left(\frac{1}{\mu_0}+\frac{1}{\mu}\right)}r(i,e) \simeq j\left[1-\Delta\tau(\frac{1}{\mu_0}+\frac{1}{\mu})\right], \tag{2.72}$$

and the corresponding variation is

$$\Delta I_a = -J\Delta\tau\left(\frac{1}{\mu_0}+\frac{1}{\mu}\right)r(i,e). \tag{2.73}$$

(b). Light is suddenly scattered-back by the added layer (fig. 2.15), b). The intercepted power is scattered by all the particles inside a cylinder with base Q_S and height $\Delta z/\mu$, and the radiance increment is:

$$\Delta I_b = JN\sigma Q_S\frac{\Delta z}{\mu}\frac{1}{4\pi} = J\frac{w}{4\pi}\frac{\Delta\tau}{\mu}. \tag{2.74}$$

(c). The radiation is scattered down by the added layer (fig. 2.16, c). It is like a further light source and a fraction of this is sent back to the detector. For the light scattered by the layer we have $J(w/4\pi)(\Delta\tau/\mu_0')$, where $\mu_0' = \cos i'$ (i' is the angle that scattered light forms with the vertical). If we consider a solid angle increment $d\Omega_{i'} = \sin i' di' d\psi_{i'}$ we obtain for the radiance $dI_{i'} = J(w/4\pi)(\Delta\tau/\mu_0')d\Omega_{i'}$ where $\psi_{i'}$ is the azimuth between the scattered ray and the one coming out. If we integrate over

all the direction $\Omega_{i'}$ the quantity $dI_{i'}r(i',e)$ we have all the light sent to the detector.

$$\begin{aligned}\Delta I_c &= \int_{\Omega_{i'}} r(i',e)dI_{i'} = \int_{\psi_{i'=0}}^{2\pi}\int_{i'=0}^{\pi/2} r(i',e)J\frac{w}{4\pi}\frac{\Delta\tau}{\mu_0'}\sin i'di'd\psi_{i'} \\ &= J\frac{w}{2}\Delta\tau\int_{\mu_0'=0}^{1} r(\mu_0',\mu)\frac{d\mu_0'}{\mu_0'}. \end{aligned} \tag{2.75}$$

We neglect extinction during the crossing of the added layer for the light scattered back by the reference surface because it introduces an additive term proportional to $(\Delta\tau)^2$.
(d). The same as (c), with the difference that light undergoes scattering leaving the medium:

$$\begin{aligned}\Delta I_d &= \int_{\Omega_{e'}} r(i,e')dI_{e'} = \int_{\psi_{e'=0}}^{2\pi}\int_{e'=0}^{\pi/2} r(i,e')J\frac{w}{4\pi}\frac{\Delta\tau}{\mu}\sin e'de'd\psi_{e'} \\ &= J\frac{w}{2}\frac{\Delta\tau}{\mu}\int_{\mu'=0}^{1} r(\mu_0,\mu')d\mu', \end{aligned} \tag{2.76}$$

where $\mu' = \cos e'$.
(e). Light passing through the superior layer is reflected from the surface and sent back again by added layer (fig. 2.17). This light represents a further illuminating source. Then the medium scatters light a fraction of radiation $Jr(i,e'')d\Omega_{e''}$ in the direction e'', with azimuth angle $\psi_{e''}$. This light, when encounters the top layer, illuminates a cylindrical volume which sends back to the lower medium a fraction $dI_{ie} = dI_{e''}(w/4\pi)(\Delta\tau/\mu_0'')d\Omega_{i''}$, with $\mu_0'' = \cos i''$. An amount $dI_{ie}r(i'',e)$ is scattered again and leaves the medium with an emission angle e. Integrating over all the available directions $\Omega_{e''}$ and $\Omega_{i''}$ we have:

$$\begin{aligned}\Delta I_e &= \int_{\Omega_{e''}}\int_{\Omega_{i''}} r(i'',e)dI_{ie} \\ &= \int_{\psi_{e''=0}}^{2\pi}\int_{e''=0}^{\pi/2}\int_{\psi_{i''=0}}^{2\pi}\int_{i''=0}^{\pi/2}[Jr(i,e'')\frac{w}{4\pi}\frac{\Delta\tau}{\mu_0''}r(i'',e) \\ \times \sin e''de''d\psi_{e''}\sin i''di''d\psi_{i''}]. \end{aligned} \tag{2.77}$$

The integration of eq. 2.77 gives:

$$\Delta I_e = Jw\pi\Delta\tau \left[\int_{\mu_0''}^{1} r(\mu_0'',\mu)\frac{d\mu_0''}{\mu_0''}\right] \cdot \left[\int_{\mu''=0}^{1} r(\mu_0,\mu'')d\mu''\right]. \tag{2.78}$$

Now we are ready to sum all the contributes of the five processes, and for the *embedded invariance* principle the results must be 0, so we can write:

$$\begin{aligned}\left(\frac{1}{\mu_0}+\frac{1}{\mu}\right) r(\mu_0,\mu) &= \frac{w}{4\pi\mu} + \frac{w}{2}\int_{\mu_0'=0}^{1} r(\mu_0',\mu)\frac{d\mu_0'}{\mu_0'} + \frac{w}{2}\int_{\mu'=0}^{1} r(\mu_0,\mu')d\mu' \\ + \quad w\pi &\left[\int_{\mu_0''}^{1} r(\mu_0'',\mu)\frac{d\mu_0''}{\mu_0''}\right] \cdot \left[\int_{\mu''=0}^{1} r(\mu_0,\mu'')d\mu''\right].\end{aligned} \tag{2.79}$$

Because μ_0'' and μ'' are dummy variables we can substitute them respectively with μ_0' and μ'. Then, if we multiply eq. 2.79 for $4\pi\mu/w$, we obtain:

$$\begin{aligned}\frac{4\pi}{w}\frac{\mu_0+\mu}{\mu_0} r(\mu_0,\mu) &= 1 + 2\pi\mu\int_{\mu_0'=0}^{1} r(\mu_0',\mu)\frac{d\mu_0'}{\mu_0'} + 2\pi\int_{\mu'=0}^{1} r(\mu_0,\mu')d\mu' \\ + \quad 4\pi^2\mu &\int_{\mu_0'=0}^{1} r(\mu_0',\mu)\frac{d\mu_0'}{\mu_0'} \cdot \int_{\mu'=0}^{1} r(\mu_0,\mu')d\mu' \\ = \quad &\left[1 + 2\pi\mu\int_{\mu_0'=0}^{1} r(\mu_0',\mu)\frac{d\mu_0'}{\mu_0'}\right] \cdot \left[1 + 2\pi\int_{\mu'=0}^{1} r(\mu_0,\mu')d\mu'\right].\end{aligned} \tag{2.80}$$

Now if we impose

$$\mathcal{P}(\mu_0,\mu) = \frac{4\pi}{w}\frac{\mu_0+\mu}{\mu_0} r(\mu_0,\mu) \tag{2.81}$$

the eq. 2.80 becomes:

$$\mathcal{P}(\mu_0,\mu) = \left[1 + \frac{w}{2}\mu\int_0^1 \frac{\mathcal{P}(\mu_0',\mu)}{\mu_0'+\mu}d\mu_0'\right] \cdot \left[1 + \frac{w}{2}\mu_0\int_0^1 \frac{\mathcal{P}(\mu_0,\mu')}{\mu_0+\mu'}d\mu'\right]. \tag{2.82}$$

The function $\mathcal{P}$ is symmetric respect to the interchange of μ with μ_0 and the two terms in square brackets are respectively functions of μ and μ_0. Then it is possible to define both of them with the function $H(x)$ where $x = \mu$ gives the first term and $x = \mu_0$ the second. With this substitution the eq. 2.82 can be rewritten as $\mathcal{P}(\mu_0,\mu) = H(\mu_0)H(\mu)$

and $H(x)$ solves the integral equation:

$$H(x) = 1 + \frac{w}{2} x H(x) \int_0^1 \frac{H(x')}{x + x'} dx'. \tag{2.83}$$

From eq. 2.81 we can finally explicit the bidirectional reflectance of a semi-infinite medium made of isotropic scatterers:

$$r(i, e, g) = \frac{w}{4\pi} \frac{\mu_0}{\mu + \mu_0} H(\mu_0) H(\mu). \tag{2.84}$$

Now we can wonder it is possible to extend this solution to anisotropic scatterers. Exact solutions for single particle phase functions of the form $p(g) = 1 + \cos^2 g$ o $p(g) = 1 + b \cos g$ have been found, but they are very complex and of little convenience in usual applications. On the other side it should be noted that the solution strongly depends on particle phase function only in the case of single scattering, while, in the multiple scattering the directional effects due to an anisotropic phase function tend to be averaged and the final result is close to the one due to isotropic scatterers. in fig. 2.18 the component of radiance which undergoes multiple scattering is plotted for the following particle phase functions: $p(g) = 1$, $p(g) = 1 \pm \cos g$ and $p(g) = \frac{3}{4}(1 + cos^2 g)$ (Rayleigh scatterers). The two cases $p(g) = 1 \pm \cos g$ are extreme, because they treat strongly anisotropic phase functions, and are far form the result obtained with $p(g) = 1$. However when we deal with symmetric phase functions, as the one of Rayleigh particles, the behavior is close to the one of isotropic scatterers. We can conclude that in the equation of bidirectional reflectance it is possible to treat the multiple scattering as if the particles were isotropic scatterers, computing explicitly the contribute of single scattering with an anisotropic phase function. Now let's go back to eq. 2.67. We can neglect the term $\int_{4\pi} p(\tau, \Omega', \Omega) I(\tau, \Omega') d\Omega'$ if we ignore multiple scattering. From eq. 2.28 we have for the source function the following expression $\mathcal{F}(\tau, \Omega) = J e^{-\tau/\mu_0} w(\tau) p(\tau, g)$, if the thermal contribute is not considered. So, for the radiance concerning single scattering only, we have:

$$I_{Ds} = J \frac{1}{4\pi} \frac{1}{\mu} \int_0^\infty w(\tau) p(\tau, g) e^{-(1/\mu_0 + 1/\mu)\tau} d\tau. \tag{2.85}$$

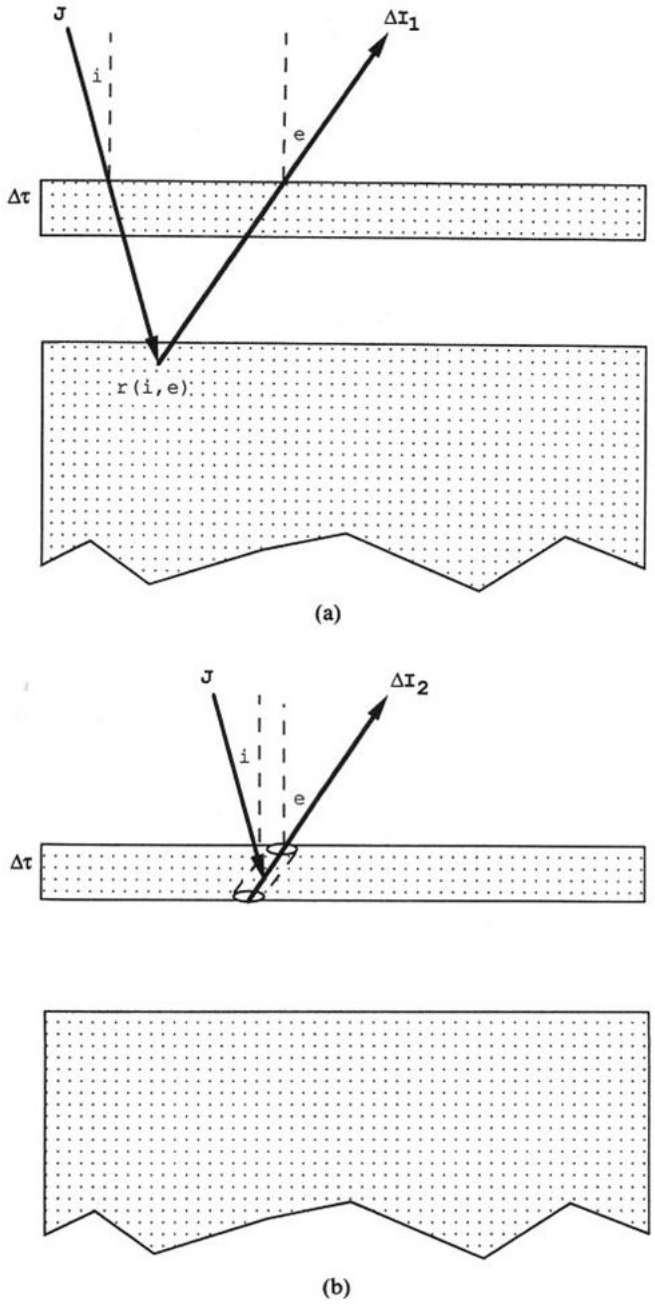

Figure 2.15: Representation of the effects induced on the scattered radiation by adding a layer of optical depth $\Delta\tau$ above a semi-infinite medium (Hapke, 1993). Case *(a)* and *(b)*.

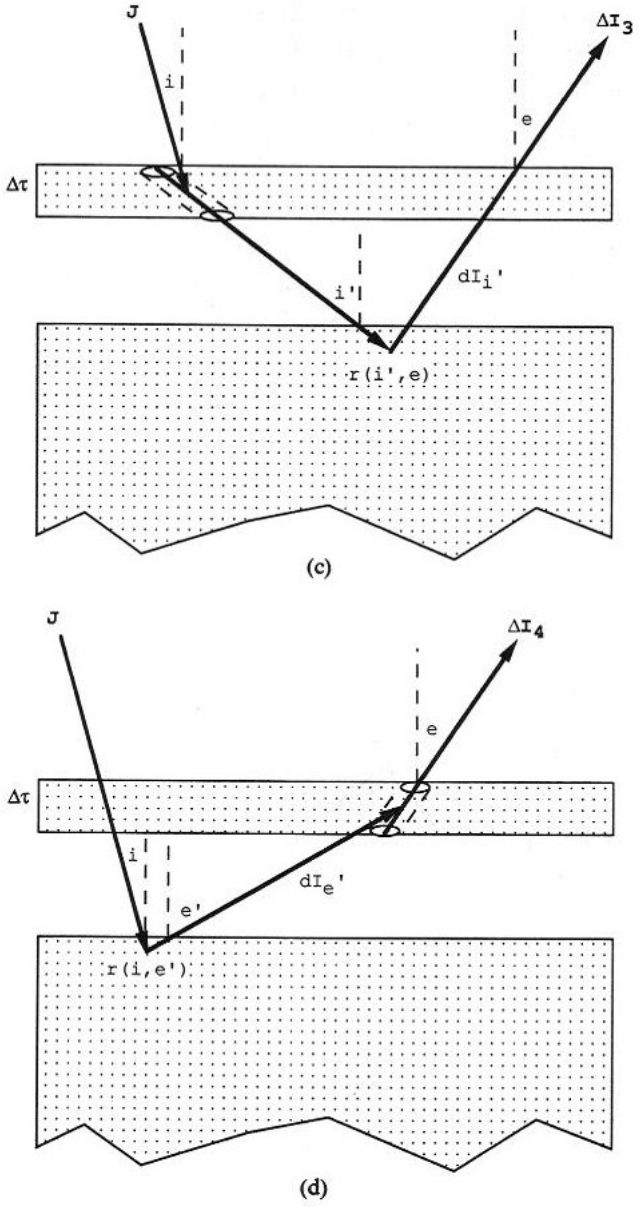

Figure 2.16: Representation of the effects induced on the scattered radiation by adding a layer of optical depth $\Delta\tau$ above a semi-infinite medium (Hapke, 1993). Cases *(c)* and *(d)*.

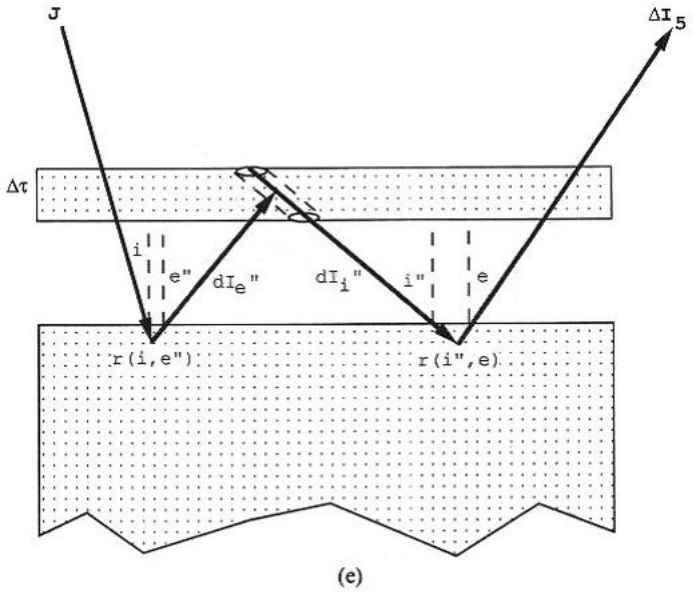

Figure 2.17: Representation of the effects induced on the scattered radiation by adding a layer of optical depth $\Delta\tau$ above a semi-infinite medium (Hapke, 1993).Case *(e)*.

If p and w are independent of τ the integration gives

$$I_{Ds} = J\frac{w}{4\pi}\frac{\mu_0}{\mu_0+\mu}p(g). \tag{2.86}$$

In the case of only multiple scattering, with isotropic scatterers, the contribute to the radiance is:

$$I_{Dm} = J\frac{w}{4\pi}\frac{\mu_0}{\mu+\mu_0}[H(\mu_0)H(\mu)-1]. \tag{2.87}$$

Joining the two terms we obtain the following expression for the bidirectional reflectance:

$$r(i,e,g) = \frac{w}{4\pi}\frac{\mu_0}{\mu+\mu_0}[p(g)+H(\mu_0)H(\mu)-1]. \tag{2.88}$$

At this point it is important to understand which is the field of applicability of the derived equation, in relation to the approximations we made. When we deal with regoliths and similar particulate media, the irregular particles shape and their closeness, which neglects the diffraction, should make the phase function isotropic. If we try to extend this equation to media composed of isolated particles, in which the diffraction is

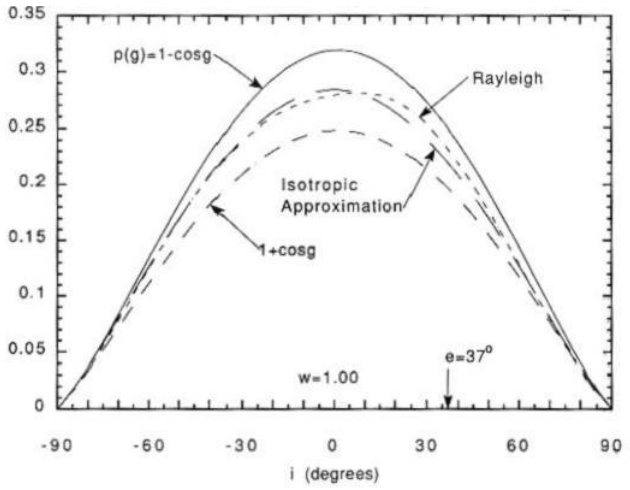

Figure 2.18: Component of the radiance which undergoes multiple scattering, for particles with $w = 1$, and various particle phase function, at emission angle $e = 37°$ (Hapke, 1993).

important, we commit an error. Another interesting consideration concerns the single scattering albedo w. Low w values produce a better agreement between observation and previsions from eq. 2.88, because they depress multiple scattering, and so the result is less dependent on the isotropic scattering assumption.
Apart form these intrinsic limitations, the bidirectional reflectance equation we derived doesn't take into account for a peculiar phenomenon, the opposition effect, that we'll be investigated later in this chapter.

Single particle phase function

In the equation of bidirectional reflectance the scattering properties of the single particle are described by the phase function $p(g)$. It depends on the physical characteristics of the particle itself and the parameter which the most affects its shape is the size parameter X. When $X \gg 1$ the simple form of the phase function adopted for small particles (Reyleigh scatterers) cannot be used. In this case the common approach is to use empirical formulations that depend on one or more parameters, which determine the phase function behavior. One of the most adopted phase function is the one derived by Heyney and Greenstein (1941):

$$p(g) = \frac{1 - \xi^2}{(1 + 2\xi \cos g + \xi^2)^{3/2}} \tag{2.89}$$

This formulation depends on the ξ parameter which is the asymmetry factor and is given by $-\langle cosg \rangle$. Positive values of ξ correspond to a forward-scattering phase function, while negative values to a back-scattering one (fig. 2.19). An improvement of this

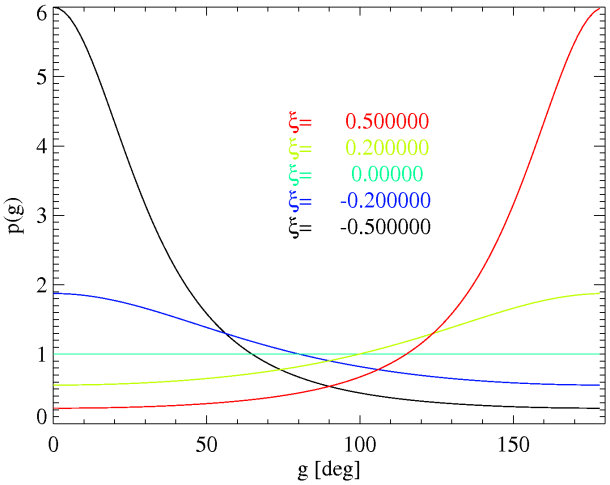

Figure 2.19: Henyey-Greenstein phase function for different ξ values.

phase function is the double Heyney-Greenstein phase function:

$$p(g) = \frac{1+v}{2}\frac{1-b^2}{(1-2b\cos g + b^2)^{3/2}} + \frac{1-v}{2}\frac{1-b^2}{(1+2b\cos g + b^2)^{3/2}} \tag{2.90}$$

It is the combination of two Heyney-Greenstein phase function which are respectively forward-scattering and back-scattering. The ξ parameter is changed in b, that can assume only positive values in the $[0;1)$ range and determines the width of both back-scattering and forward-scattering lobes (the larger b the narrower the lobes). The v parameter affects the height of the back lobe respect to the forward ($v > 0$ predominantly back-scattering, $v < 0$ predominantly forward-scattering).

The H function

In the expression of the bidirectional reflectance the multiple scattering term contains the H functions. Even called Chandrasekhar functions, they solve the integral equation 2.83, but their analytical expression is not known. Tabulated values of the H function are tabulated in several places (Chandrasekhar, 1960) but in common applications it is

preferred to deal with approximate analytic expressions. In this section we report two widespread approximate formulations, skipping the details concerning their derivation. The first one, that comes out from an approximate solution of the radiative transfer equation, is

$$H(x) =\simeq \frac{1+2x}{1+2\gamma x} \tag{2.91}$$

The eq. 2.91 differs from the exact solution by less than the 4% everywhere (fig. 2.20). As we can see the H functions are almost linear over most of its range, but the approximation with a linear function gives worse result than the eq. 2.91. An excellent approximation is obtained if we substitute a linear approximation of H in the integral in eq. 2.83. If we explicit $H(x)$, with a little algebra, it is possible to obtain the following expression:

$$H(x) \approx \left[1 - wx\left(r_0 + \frac{1-2r_0x}{2}\ln\frac{1+x}{x}\right)\right]^{-1} \tag{2.92}$$

where $r_0 = \frac{1-\gamma}{1+\gamma}$. The eq. 2.92 differs from the exact solution by less the 1%.

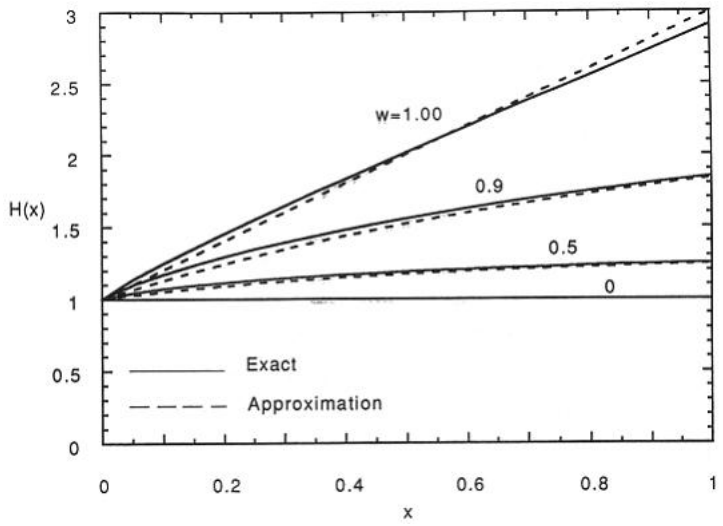

Figure 2.20: Comparison of the approximate solutions of $H(x)$ (dashed line) to the exact one (solid line). The only visible approximate solution is given by eq. 2.91 because the eq. 2.92 is indistinguishable from the exact one (Hapke, 1993).

2.4.5 Opposition effect

When a particulate medium is observed at small phase angles a steep luminosity increment occurs with the decrease of the phase angle itself (fig. 2.21). This phenomenon is due to two mechanisms that are named Shadow Hiding Opposition Effect (SHOE) and Coherent Backscattering Opposition Effect (CBOE). In the following sections we describe this processes and the corresponding corrections to introduce in the bidirectional reflectance equation.

Figure 2.21: Oppsition effect on the surface of the Moon: the sun is behind the observer.

Shadow Hiding Opposition Effect

In media made of particles larger than the wavelength of the incident radiation the particles on top cast their shadow on the ones below. When the surface is observed at large phase angles the shadows are visible, but when we move to smaller and smaller phase angle a larger and larger fraction of the shadow is hidden by the casting particle itself. What happens is that, at low phase angles, the light which has been able to reach a given particle can travel along the same path in the opposite direction to reach the observer. This cannot happen for large g observations. This process clearly depends on single scattering. To quantify the effect due to SHOE we must compute the probability that a given ray, after being scattered by a particle, can escape the medium without interacting whit other particles. Consider the term of single scattering described in eq.

2.85 and rewrite it as:

$$I_{Ds} = J\frac{1}{4\pi}\frac{1}{\mu}\int_0^\infty w(\tau)p(\tau,g)t_i(\tau,\mu_0)t_e(\tau,\mu)d\tau, \tag{2.93}$$

where $t_i(\tau,\mu_0) = e^{-\tau/\mu_0}$ and $t_e(\tau,\mu) = e^{-\tau/\mu}$. The t_i represents the probability that an incident ray reaches the optical depth τ, that is the probability that in the cylindric volume along the direction μ_0, with vertical axis coincident with the direction observer-**P** (**P** is the point where the scattering occurs) and section $\pi\langle a_E\rangle^2$ there are no particles. We remind that $\langle a_E\rangle$ is the average extinction radius $\langle a_E\rangle = \sqrt{\langle\sigma Q_E\rangle/\pi}$. It is useful to write again the definition of the optical depth $\tau = \int_z^\infty E(z')dz'$, where $E(z) = N_E(z)\langle\sigma Q_E\rangle$, with $N_E = -N\frac{\ln(1-\phi)}{\phi}$ effective numerical particles density. In an similar way we define t_e, which is about emitted rays. In eq. 2.93 the product t_it_e represents the total probability that a ray, arrived in z can escape the medium without any further interaction. The probabilities t_i and t_e are independent of one each other for large phase angles, but for small g values the two cylinders partially overlap, and so in the computing of the interaction probability one term is counted twice (fig. 2.22). From this point of view the opposition effect becomes fairly intuitive. If we observe at null phase angle, a ray that reaches the depth z has already walked the path that will walk in the emission process, and so the probability to escape the medium without new interactions is larger. This explains the luminosity increase. To quantify the phenomenon we need to compute the overlapping fractions of the two cylindric volumes. We can write:

$$t_it_e = e^{-(\tau/\mu_0+\tau/\mu-\tau_c)}, \tag{2.94}$$

where τ_c is linked to the overlap region with volume $\mathcal{V}_c$ by the relation

$$\tau_c = \int_{\mathcal{V}_c} N_E(z)d\mathcal{V}. \tag{2.95}$$

This means that τ_c is the effective number of particles in the volume $\mathcal{V}_c$. When $g = 0$ the two cylinders match perfectly and then $\tau_c = \tau/\mu_0$. The eq. 2.93 then becomes

$$I_{Ds}(e,e,o) = -J\frac{w}{4\pi}p(0)\frac{1}{\mu}\int_\infty^0 e^{-\tau/\mu}d\tau = J\frac{w}{4\pi}p(0). \tag{2.96}$$

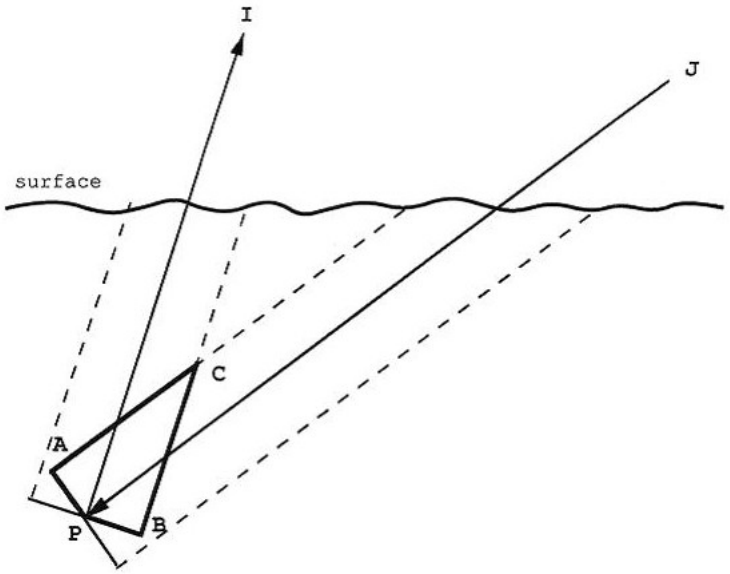

Figure 2.22: Overlap region $\mathcal{V}_c$ section represented by the polygon **APBC** (Hapke, 1993).

The result is exactly twice the one we obtain from the equation which describes the single scattering 2.86, that doesn't take into account for the shadow hiding, at $g = 0$. To compute the contribute of opposition effect at each g we must determine which is the dependence of the overlap region on the phase angle. The calculation is cumbersome so here it is reported an approximate solution.
The volume $\mathcal{V}_c$ is the intersection between the two cylinders described above, and its section in the scattering plane is the polygon **APBC**, which can represent as made of by two right triangles with common hypotenuse $\mathbf{PC} = \langle a \rangle \csc(g/2)$ and sides $\langle a \rangle$ and $\langle a \rangle \cot(g/2)$. Let z_1 be the projection of the hypotenuse on the vertical axis. This depends on q and q_0 which are the distances between **C** and the intersection of entering and escaping rays with the plane containing **C** respectively:

$$\begin{aligned} q^2 &= \frac{z_1^2}{\mu^2} + \langle a_E \rangle \csc^2 \frac{g}{2} - 2\frac{z_1 \cos(g/2)}{\mu} \langle a_E \rangle \csc \frac{g}{2} \\ &= (\frac{z_1}{\mu} - \langle a_E \rangle \cot \frac{g}{2})^2 + \langle a_E \rangle^2, \\ q_0^2 &= \frac{z_1^2}{\mu_0^2} + \langle a_E \rangle \csc^2 \frac{g}{2} - 2\frac{z_1 \cos(g/2)}{\mu_0} \langle a_E \rangle \csc \frac{g}{2} \\ &= (\frac{z_1}{\mu_0} - \langle a_E \rangle \cot \frac{g}{2})^2 + \langle a_E \rangle^2. \end{aligned} \tag{2.97}$$

Because for small g it is $\cot(g/2) \gg 1$ we can neglect the term $\langle a_E \rangle$ and write

$$\begin{aligned} q &\simeq \pm[z_1/\mu - \langle a_E \rangle \cot(g/2)] \\ q_0 &\simeq \pm[z_1/\mu_0 - \langle a_E \rangle \cot(g/2)]. \end{aligned} \tag{2.98}$$

where the + sign is for q and $-$ is for q_0 if $e > i$, while it is the opposite for $e < i$. For small g both q and q_0 are small, even if each term of their expressions is large. Because of this, their difference is small too and we can write:

$$|q - q_0| \simeq z_1/\mu + z_1/\mu_0 - 2\langle a_E \rangle \cot(g/2) \simeq 0 \tag{2.99}$$

quindi

$$z_1 \simeq \langle \mu \rangle \langle a_E \rangle \cot(g/2), \tag{2.100}$$

with $\langle \mu \rangle = \frac{2\mu\mu_0}{\mu_0+\mu}$. At any altitude z' between z and z_1 an horizontal cut of $\mathcal{V}_c$ consists of the common area between two overlapping ellipses. The thickness of this area in the direction perpendicular to the scattering plane is much less sensitive to z' than is the width in the parallel direction. Hence the volume $\mathcal{V}_c$ can be approximated by a volume of constant thickness u and section parallel to the scattering plane equal to a triangle with the same area of the polygon **APBC** $\langle a_E \rangle^2 \cot(g/2)$ and same projection z_1. From this considerations:

$$\mathcal{V}_c \simeq u\langle a_E \rangle^2 \cot(g/2). \tag{2.101}$$

The portion of $\mathcal{V}_c$ above z' is $\mathcal{V}(z') = \mathcal{V}_c[1-(z'-z)/z_1]^2$ whence differentiating respect to z' we obtain $d\mathcal{V} = -(2u\langle a_E \rangle/\mu)[1-(z'-z)/z_1]dz'$. Then for τ we have:

$$\tau_c = \int_{\mathcal{V}_c} N_E(z') d\mathcal{V} \simeq -\int_z^{z+z_1} N_E(z') \frac{2u\langle a_E \rangle}{\langle \mu \rangle} (1 - \frac{z'-z}{z_1} dz'). \tag{2.102}$$

The right thickness u is given assuming that $\tau_c = \tau/\mu$ when $g = 0$, $\langle \mu \rangle = \mu = \mu_0$ and $z_1 \to \infty$, that is

$$\int_z^\infty N_E(z') \frac{2u\langle a_E \rangle}{\langle \mu \rangle} = \frac{1}{\mu} \int_z^\infty E(z') dz' = -\frac{1}{\mu} \int_z^\infty N_E(z') \langle \sigma Q_E \rangle dz'. \tag{2.103}$$

It gives $u = \langle \sigma Q_e \rangle / 2 \langle a_E \rangle = \pi \langle a_E \rangle / 2$ and we have:

$$\tau_c = -\frac{1}{\langle \mu \rangle} \int_{\tau(z)}^{\tau(z+z_1)} (1 - \frac{z' - z}{z_1}) d\tau(z'). \tag{2.104}$$

Integrating the expression above we obtain for τ_c:

$$\tau_c = \tau / \langle \mu \rangle + \tau' / \langle \mu \rangle, \tag{2.105}$$

where

$$\tau' = -\frac{1}{z_1} \int_z^{z+z_1} \tau(z') dz'. \tag{2.106}$$

If we put this expression in eq. 2.94 we have:

$$\tau/\mu_0 + \tau/\mu - \tau_c = (\tau + \tau')/\langle \mu \rangle. \tag{2.107}$$

and single scattering term becomes:

$$I_{Ds}(i, e, g) = J \frac{w}{4\pi} p(g) \int_0^\infty e^{-(\tau+\tau')/\langle \mu \rangle} \frac{d\tau}{\mu}. \tag{2.108}$$

Equations 2.107 and 2.108 can be easily computed for a step distribution of particle sizes

$$N_E(z) = \begin{cases} 0 & \text{se } z \geq 0 \\ N_E = constant & \text{se } z < 0 \end{cases} \tag{2.109}$$

and it gives

$$I_{Ds}(i, e, g) = J \frac{w}{4\pi} p(g) \frac{\mu_0}{\mu + \mu_0} [1 + B_S(g)]. \tag{2.110}$$

where $B_S(g)$ is

$$\begin{aligned} B_S(g) &= \sqrt{4\pi/y} e^{1/y} [erf(\sqrt{4/y}) - erf(\sqrt{1/y})] + e^{-3/y} - 1, \\ y &= 2\frac{\langle \mu \rangle}{\tau_1} = 2\frac{\tan(g/2)}{N_E \langle \sigma Q_E \rangle \langle a_E \rangle} \end{aligned} \tag{2.111}$$

$erf(x)$ is the error function or gaussian with x argument and $\tau_1 = N_E \langle \sigma Q_E \rangle z_1$ is the optical depth at z_1. This expression for $B_S(g)$ is analytic but anyway hard to be computed because of the error function. In practical application it is preferred to use

an approximate expression which gives an error less than 3% (fig. 2.23) given by

$$B_S(g) \simeq (1+y)^{-1} = \left(1 + \frac{1}{h_s}\tan\frac{g}{2}\right), \tag{2.112}$$

with

$$h_s = \frac{1}{2}N_E\langle\sigma Q_E\rangle\langle a_E\rangle = -\frac{1}{2}N\langle\sigma Q_E\rangle\langle a_E\rangle\frac{\ln(1-\phi)}{\phi} = \frac{1}{2}E\langle a_E\rangle. \tag{2.113}$$

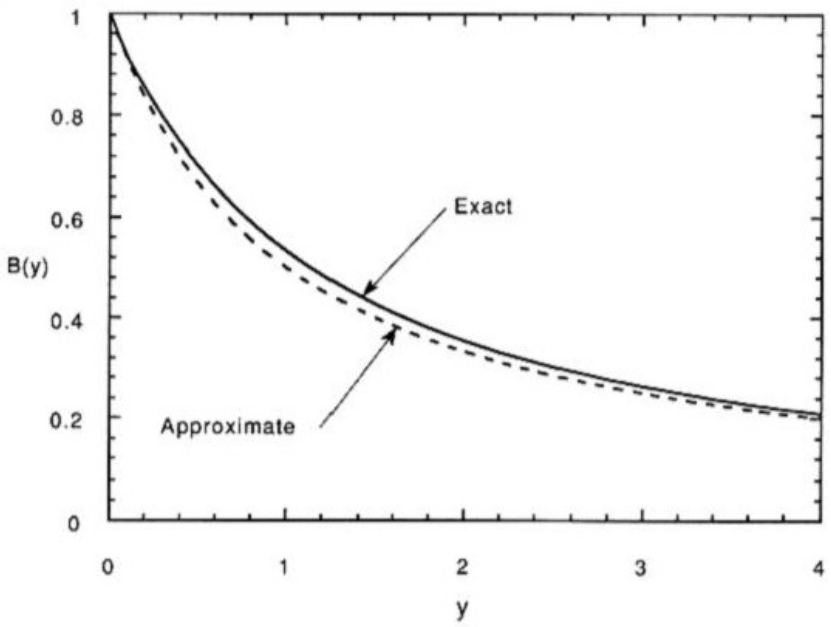

Figure 2.23: Comparison between the exact (solid line) and approximate (dashed line) expressions of the function $B(y)$ (Hapke, 1993).

An important thing to be considered is the opposition effect angular width. An easy calculation shows that an angular width $\Delta g = 2h_S$ correspond to half of the maximum of the opposition peak. The determination of h_S is crucial because constrains the porosity of the medium and can be performed through the analysis of the opposition effect peak. Computations executed assuming power law grain size distribution and filling factor $\phi = 0.5$ give $h_S = 0.065$ that corresponds to $\Delta g = 7°$, an angular width commonly observed in the analysis of regoliths.

One last consideration is about opposition effect amplitude. In the derivation of the shadow hiding we considered the single scattering process implicitly assuming that

the ray was emitted by the particle from the incidence point. However we must even consider when the scattering is not a specular reflection and the light leaves the particle from a point which is not the incidence point. In this case the probability that the emitted ray travels the same path of the incident ray, without interactions with other particles, is lower. To include this effect it's necessary to multiply $B_S(g)$ for an empirical quantity B_{S0} comprised between 0 and 1, which determines the amplitude of the SHOE and depends on the contribute of specular reflection to the back-scattering lobe of the particle phase function.

Coherent Backscattering Opposition Effect

If the grain size is lower than the wavelength, i. e. $X \leq 1$, the particle doesn't cast an effective shadow and the SHOE cannot be observed. However if $X \approx 1$ another mechanisms arises, the coherent backscattering opposition effect (CBOE). In this regime light can be treated as a wave and interference effects can be considered, but at the same time multiple scattering is described by means of geometric optics. The CBOE is due to the process described below: two partial waves of a common wavefront incident on a medium interact with some particles (multiple scattering) traveling the same path, but in opposite directions (fig. 2.24). If the two waves emerge from the medium in places whose distance is small respect to the wavelength, interference can occur. If the interference is constructive, i. e. when the phase between the two waves is 0, the luminosity increases of 4 times, producing a reflectance peak. We will not show here how to compute the function which describes the CBOE, but the angular width of the effect will be derived. See fig. 2.24 and consider a plane wave incident on the medium with wave vector $\vec{k_i}$ interacting with a particle in the $\vec{x_1}$ position. The wave undergoes multiple scattering and emerges from the medium with wave vector $\vec{k_f}$ after the last scattering in $\vec{x_N}$ (solid line). At the same time let us consider the same path in opposite direction (dashed line). The two emerging rays, γ and $-\gamma$, can interfere, constructively or not, depending on the optical path difference which determines their relative phase given by $e^{(\vec{k_i}+\vec{k_f})\cdot(\vec{x_N}-\vec{x_1})}$. When $g = 0$ we have $\vec{q} = \vec{k_i} + \vec{k_f} = 0$ and the interference is constructive. If we define θ as the angle comprised between $\vec{k_i}$ and $\vec{k_f}$, the coherence condition is given by $\vec{q} \cdot (\vec{x_N} - \vec{x_1}) = (2\pi/\lambda)\theta|\vec{x_N} - \vec{x_1}| \approx (2\pi/\lambda)\theta\ l < 1$, where l represents the photon average free path length. From the above relation we can easily compute the CBOE peak width which is $\Delta g \simeq \lambda/2\pi l$. This is proportional to

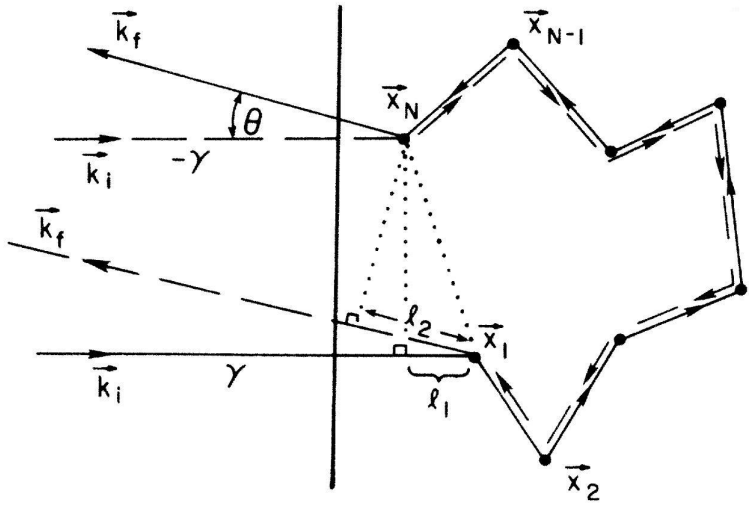

Figure 2.24: Schematic representation of CBOE (MacKintosh and Sajeev, 1988).

the wavelength. A detailed computation allows to derive the function which describes the CBOE and it is given by (Hapke, 2002):

$$\begin{aligned} B_C(g) &= \frac{1+\frac{1-e^{-(1/h_C)\tan(g/2)}}{(1/h_C)\tan(g/2)}}{2[1+(1/h_C)\tan(g/2)]^2} \\ h_C &= \frac{\lambda}{4\pi\Lambda} \\ \Lambda &= [N\langle\sigma Q_S\rangle(1-\langle\cos\theta\rangle)] \end{aligned} \tag{2.114}$$

where $\langle\cos\theta\rangle$ is the average cosine of the scattering angle. Also for CBOE we can define a multiplicative term B_{C0} that determines the effect amplitude. As written in the above equation the photon average free path length l is now better represented by the quantity Λ, and using the eq. 2.115 the CBOE peak width $\Delta g = 0.36\lambda/(2\pi\Lambda)$ can be derived . Taking into account for the SHOE, which acts only on the single scattering term, and for the CBOE, the final expression for the bidirectional reflectance is:

$$\begin{aligned} r(i,e,g) &= \frac{w}{4\pi}\frac{\mu_0}{\mu+\mu_0}[p(g)B_{SH}(g)+H(\mu_0)H(\mu)-1]B_{CB}(g) \\ B_{SH} &= 1+B_{S0}B_S(g) \\ B_{CB} &= 1+B_{C0}B_C(g). \end{aligned} \tag{2.115}$$

Scattering efficiency Q_s

If we look at eq. 2.115 we can see that the bidirectional reflectance depends on the single scattering albedo w parameter. It represents the fraction of light, extinguished by the particle, which is scattered. This quantity is related to the optical constants of the medium and the particle size, which determine the absorption properties of the grain. In this section we show a method to compute an analytic approximation of the scattering efficiency Q_s once that the optical constants and the grain size are known. It coincides to the particle single scattering albedo in close-packed media where the effect of diffraction is negligible. The possibility to correlate w to the physical properties of the medium allows to use the bidirectional reflectance equation for the analysis of spectral data, in order to infer the surface composition.
The model we are going to describe is applicable to particles much larger of the wavelength and when the incident light is unpolarized. The derivation is performed by replacing the spherical particle by a slab with appropriate optical properties. The equivalent-slab model is schematically represented in fig. 2.4.5. Let us call the total fraction of incident light specularly reflected into all directions from the outer surface of a sphere S_e. This represent the reflection coefficient of the equivalent slab for externally incident light. A fraction $1-S_e$ enters the slab and it is attenuated by absorption by a factor Θ. After the first passage a quantity S_i of light is internally reflected. The process continues as shown in fig. 2.4.5. The total fraction of light emerging from the particle is then

$$\begin{aligned} Q_s &= S_e + (1-S_e)\Theta(1-S_i) + (1-S_e)\Theta S_i\Theta(1-S_i) \\ &\quad +(1-S_e)\Theta S_i\Theta S_i\Theta(1-S_i) + \cdots \\ &= S_e + (1-S_e)(1-S_i)\Theta\left[1 + (S_i\Theta) + (S_i\Theta)^2 + \cdots\right] \\ &= S_e + (1-S_e)\frac{(1-S_i)}{(1-S_i\Theta)}\Theta. \end{aligned} \tag{2.116}$$

Now we need to derive the three quantities S_e, S_i and Θ. The detailed derivation is in Hapke (1993) and we report here only the results. For the light specularly reflected by the spherical surface we have

$$S_e = \int_0^{\pi/2} \left[R_\perp(\theta) + R_\parallel(\theta)\right] \cos\theta \sin\theta d\theta. \tag{2.117}$$

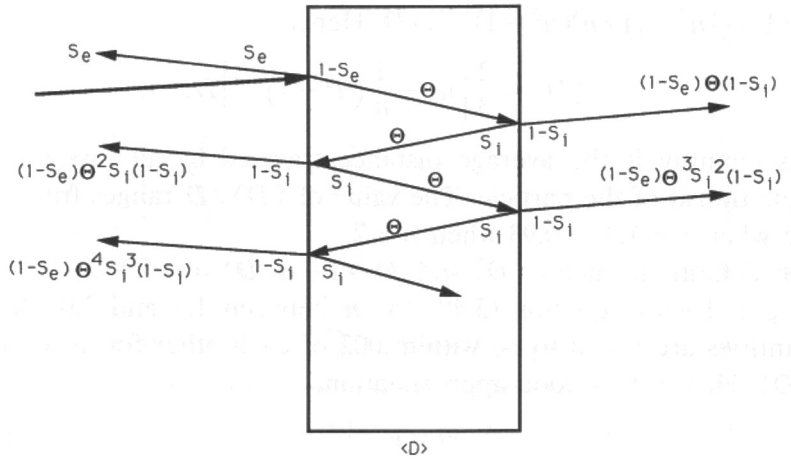

Figure 2.25: Slab model (Hapke, 1993).

where $R_\perp(\theta)$ and $R_\parallel(\theta)$ are the Fresnel reflectivities for light polarized perpendicular and parallel to the scattering plane respectively.:

$$R_\perp = \left[\frac{\cos\theta - n\cos\theta'}{\cos\theta + n\cos\theta'}\right]^2 \tag{2.118}$$

$$R_\parallel = \left[\frac{n\cos\theta - \cos\theta'}{n\cos\theta + \cos\theta'}\right]^2 \tag{2.119}$$

Because of the spherical shape of the particle $S_e = S_i$. In fact the angle at which a ray enters the sphere (θ') is the same at which it is incident on the inner side of the sphere. The expression for the internal-transmission factor Θ is:

$$\Theta = 2\int_0^{\pi/2} e^{-4kX\cos\theta'}\sin\theta\cos\theta d\theta. \tag{2.120}$$

From the Snell's law, $\sin\theta\cos\theta d\theta = n^2\sin\theta'\cos\theta' d\theta'$. Also, $4kX = \alpha D$ where α is the absorption coefficient and $D = 2a$ is the particle diameter. Hence,

$$\Theta = 2n^2\int_0^{\Theta'_c} e^{-4kX\cos\theta'}\sin\theta'\cos\theta' d\theta'. \tag{2.121}$$

where $\theta'_c = \sin^{-1}(1/n)$. The integration of eq. 2.121 gives:

$$\Theta = \frac{2n^2}{(\alpha D)^2}\left[e^{-\alpha D(1-1/n^2)^{1/2}}\left[1+\alpha D(1-1/n^2)^{1/2}\right] - e^{-\alpha D}[1+\alpha D]\right]. \qquad (2.122)$$

Another approach to obtain an analytical description of the scattering properties of large spherical particles is represented by the geometric optics (we will not discuss further this subject). It produces result that are very close to to the ones obtained with the rigorous Mie theory. However what it is interesting is that the slab model is in very good agreement with the result of geometric optics and this makes this approach very useful and preferable because of its simplicity (see fig. 2.4.5).

The success of slab model suggests to extend it to irregular particles much larger than wavelength. The eq. 2.116 will be preserved, but each single term needs a new derivation. As written above the term S_e represents the exterior-surface reflection. If the particle is convex (this means that its surface is without structures that can cast shadows) and the surface smooth, the external reflection is the same of a spherical particle, because the random distribution of the facets composing the surface is the same of a sphere. An issue can be represented by surface roughness. If the scale of the roughness is smaller than the wavelength the asperities on the surface can be treated as Rayleigh scatterers. However the efficiency of Rayleigh scattering is proportional to $(size/\lambda^4)$ and this contribute can be neglected (Berreman, 1970; Zerull and Giese, 1974). Exceptions are when the complex refractive index is in the the region of anomalous dispersion or when k is very large, as for metals. In this case both scattering and absorptions can be extremely large and the effect of surface roughness can't be ignored. The case in which surface roughness scale is larger than the wavelength is more complicated, but several studies (Torrance and Sparrow, 1967; O'Donnell and Mendez, 1987) show that even in this regime the external reflection is quasi-specular.
Thus, to a first approximation we can assume that scattering from an irregular particle can be treated as specular and the expression of S_e is the same as eq. 2.117. A convenient approximation which is accurate for $k^2 \ll 1$ and $1.2 \leq n \leq 2.2$ is

$$S_e \approx \frac{(n-1)^2+k^2}{(n+1)^2+k^2} + 0.05 \qquad (2.123)$$

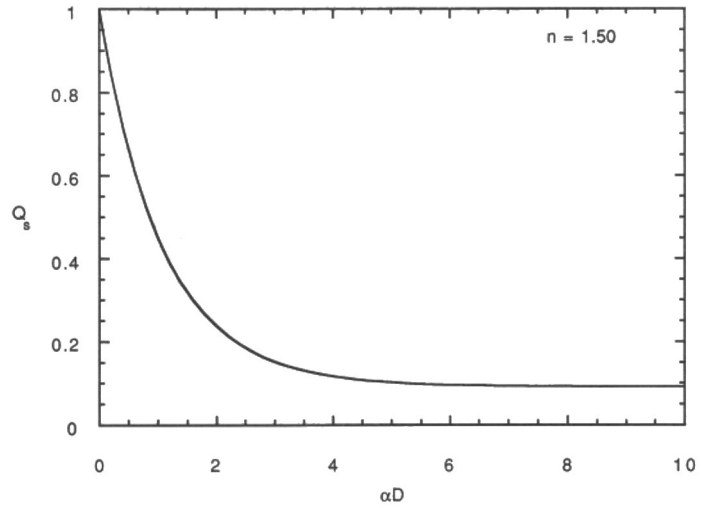

Figure 2.26: Scattering efficiency of a large sphere vs. αD calculated according to the slab model and from geometric optics: the two curves are indistiguishable (Hapke, 1993).

For a irregular particle the term S_i is not the same as S_e because the angle at which a given ray is incident on the inside of the sphere is not correlated with the angle at which it enters the sphere. A reasonable expression for the internal reflection coefficient is then given by the average of the Fresnel reflection coefficients over all angles:

$$S_i = \int_0^{\pi/2} \left[R_\perp(\theta') + R_\parallel(\theta')\right] \cos\theta' \sin\theta' d\theta'. \tag{2.124}$$

In eq. 2.124 θ' refers to the incidence angle of the interior rays. In calculating the expression for S_i we need to consider only the case $k \ll 1$, otherwise the particle is opaque and transmission is negligible. In this case we can proceed as follows. If we consider eq. 2.119 and fig. 2.4.5 it can be seen that the sum of the reflectivities is nearly constant and equal to the value in $\theta' = 0$ when $0 < \theta' < \theta'_c$. θ_c is the critical angle, i. e. the largest angle at which a refracted ray can cross the separation surface between two media with $n_1 < n_2$. θ_c is given by the following relation:

$$n_1 = n_2 \sin\theta_c \tag{2.125}$$

When $\theta = \theta'_c$ both the parallel and perpendicular reflectivities arise abruptly to

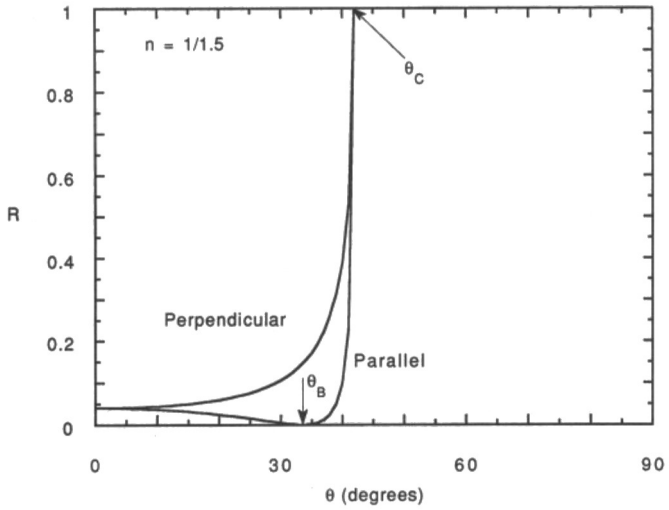

Figure 2.27: Fresnel reflection for $m = 1.50 + i0$ vs. the angle of incidence (Hapke, 1993).

1 and are equal to 1 for $\theta'_c < \theta' < \pi/2$. Then, with a good approximation we can conclude that

$$S_i \approx 2\left[\int_0^{\theta'_c}\left(\frac{n-1}{n+1}\right)^2 \cos\theta' \sin\theta' d\theta' + \int_{\theta'_c}^{\pi/2} \cos\theta' \sin\theta' d\theta'\right] \tag{2.126}$$

Carrying out the integration gives:

$$S_i \approx 1 - \frac{4}{n(n+1)^2} \tag{2.127}$$

The determination of the transmission factor Θ is not trivial. Here we report only the result of the so-called internal scattering model. In this model the spherical particle is approximated with a slab and the equation of radiative transfer is solved using the method of the two stream approximation. The result is:

$$\Theta = \frac{r_i + e^{-\sqrt{\alpha(\alpha+s)}\langle D\rangle}}{1 + r_i e^{-\sqrt{\alpha(\alpha+s)}\langle D\rangle}} \tag{2.128}$$

In the above expression $\langle D\rangle$ is related to the particle diameter d by the following relation $\langle D\rangle = 2d/3$, while s represents internal scattering coefficient. The physical meaning of s is similar to α. The intensity of traveling radiation is reduced by a factor

e^{-1} after a distance $1/s$ because of internal scattering on scatterers (e.g. impurities) inside the particle.

Chapter 3

Hapke modeling of Rhea surface properties through Cassini-VIMS spectra

The Cassini spacecraft completed its initial four-year mission to explore the saturnian system in June 2008. Since then it entered in the extended mission phase (Cassini-Huygens Equinox Mission), which lasted until September 2010 and later went through the extend-extended mission (Cassini Solstice Mission) that will stop on september 2017. During all these years the VIMS (Visual and Infrared Mapping Spectrometer) instrument on board Cassini extensively observed the saturnian moons. VIMS collected both resolved and disk-integrated spectra of the moons in a wide range of observing conditions (solar phase angle and hemispheric coverage). While high spatial resolution observations of the satellites are essential to obtain compositional maps of the objects, the disk integrated observations are very useful to study the global properties of the surfaces and to point out correlations as well as differences among the various satellites. The full disk observations constitute of a huge database with more than 1400 observations, obtained over a wide range of phase angles, for a total of 126000 spectra, covering the full VIMS spectral range. For a detailed description of the database see Filacchione et al. (2007, 2010) (in the following referred to as F2007 and F2010 respectively). Spectrophotometry is a very powerful diagnostic tool in remote sensing to study the composition and the physical properties of the surfaces of objects under investigation. The amount of solar radiation, as a function of the wavelength, scattered

from a surface towards the observer under varying observing conditions (incidence, emergence and phase angles) is a nonlinear function of several parameters such as the composition of the materials making up the surface, their grain size, the porosity and surface roughness of the interacting surface layers. To retrieve quantitative information on these fundamental parameters of the surfaces, we need a multiple scattering model which provide approximate solutions to the radiative transfer in a particulate medium. The Hapke IMSA model (Isotropic Multiple Scattering Approximation), described in chapter 2 is the one we chose to perform our analysis. It is an analytic two stream approximate solution to the radiative transfer equation and it has been applied successfully to perform photometric corrections of imaging data (Hudson and Ostro, 1999; Domingue et al., 2009), to investigate physical properties of regoliths (Mallama et al., 2002; Buratti et al., 2004) and to estimate surface compositions of planetary surfaces (Cruikshank et al., 2001, 2005; Poulet et al., 2002). In F2007 and F2010 the authors have adopted an empirical method of spectral analysis to reduce the dimensionality of the spectra by mapping high dimensional data into a lower dimension while preserving the main features of the original spectra. This led to the definition of a number of "Spectrophotometric Indicators" which are specifically tuned to infer physical properties of water ice-rich surfaces. For instance spectral slopes in the visible range are a useful indicator of the degree of purity of water ice with respect to the presence of contaminants, thus two of the selected indicators are the slopes in the blue range of the spectrum ($350 - 550nm$) and in the NIR (near infrared) range ($550 - 1000nm$). In the IR range the most prominent features are the water ice absorption bands; consequently the authors have selected the depth of the 1.25, 1.5, 2.0 and 3.0 μm water ice bands as additional indicators. The systematic analysis performed in F2007/F2010 on the basis of these indicators indeed pointed out several compositional trends within the satellites system and raised several questions which have not yet received a satisfactory answer. For instance:

- the correlation among Phoebe, Iapetus and Hyperion. The origin of the material that causes the albedo dichotomy of Iapetus has been the subject of a long standing debate (Buratti and Hicks, 2003; Spencer and Denk, 2010; Tosi et al., 2010). However Clark et al. (2008); Clark and et al. (2011) showed that the visible colors and UV absorber are consistent with a single source with varying abundance of the contaminants. Key to solution of the problem was the discovery of Rayleigh scattering from small particles Clark et al. (2008). From the VIMS

data the spectral behavior in the VIS-NIR range shows similarities between Iapetus and Hyperion; while the IR spectra point out a strong correlation between the features observed on Iapetus and Phoebe.

- The Band Depth at 1.5 μm versus Band Depth at 2.0 μm trend is the result of the combined effect of ice contamination, due to "darkening agents" as well as variable grain sizes, but the relative contribution of the two effects could not be ascertained. However Clark et al. (2011); Clark and et al. (2011) show that the 1.5 and 2.0 μm ice band depth ratio is affected by the amount of sub-micron sized ice grains in the regolith.

- The symmetry of the 2-micron ice bands is unusual, being asymmetric toward longer wavelengths in spectra of the icy saturnian satellites (Clark et al., 2008) and in other icy objects (see review by Clark et al. (2011)). Clark and et al. (2011) showed that this asymmetry could be due to the presence of sub-micron ice grains and modeled the spectra using Hapke theory modified to include the diffraction component from those particles.

From this point of view the analysis performed in F2007 and F2010 represent a valuable empirical study to describe the global properties of the surfaces of the moons, however quantitative estimates on the nature (composition and physical properties) of the regolith require a full radiative transfer model. We have then set ourselves to work to this task (Ciarniello et al., 2010c,d), and this chapter describes the results we have obtained applying a radiative transfer model to the complete data set of Rhea's full disk observations.
Rhea (fig. 3.1), with a radius of $764 \pm 1.1 km$ (Thomas et al., 2006), is the second largest moon of Saturn; it orbits in the E ring with mean semimajor axis of 527070 km (see *http://ssd.jpl.nasa.gov* and reference therein); its mass is $M = (2.306481 \pm 0.000059) \times 10^{21} kg$, which corresponds to a density of $1232.8 \pm 5.4 kgm^{-3}$ (Iess et al., 2007) and geometric albedo of the satellite is 0.83 at 0.51 μm (Pitman et al., 2010). We have selected Rhea as the starting point for this analysis since it has the largest coverage in solar phase angle and thus allows to thoroughly test the model. Our approach is based on a two steps analysis: first a spectral fit is performed to retrieve the abundances of contaminants and regolith grain size, then these properties are used to compute single-scattering albedo at each wavelength, whose values are adopted in the Rhea's phase

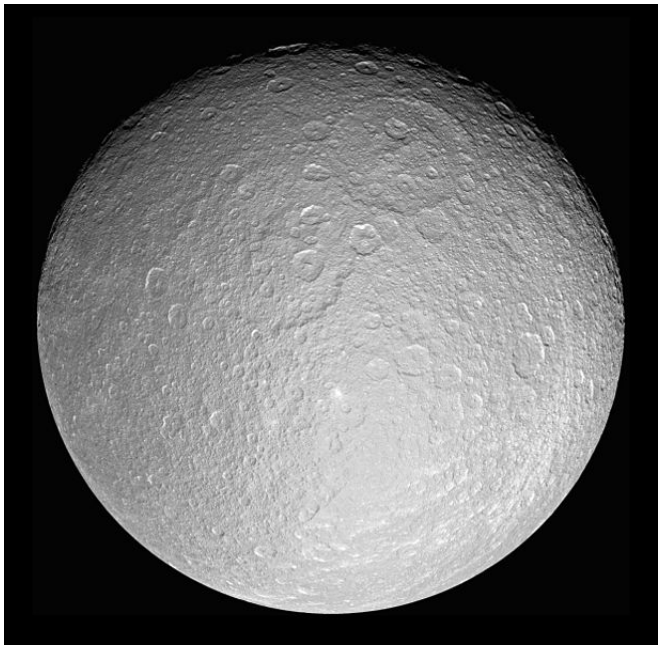

Figure 3.1: Rhea. Image courtesy of NASA-CICLOPS-ISS team.

function fit for the whole VIMS spectral range. In section 3.1 we have described the method applied to model the phase curves and the spectra. In section 3.2 the selected dataset is described as well as the reduction data procedure. In sections 3.3 and 3.4 spectral and phase function fits respectively are analyzed. Section 3.5 concerns the feedback of phase function fit to the spectrum fit.

3.1 Hapke model FDR (full-disk reflectance)

Hapke model has been widely used to describe both solar phase curve and spectral properties of various objects in the solar system (Buratti, 1985; Bowell et al., 1989; Domingue et al., 1995; Domingue and Verbiscer, 1997). In this paper we refer to Hapke (1993) in order to describe the spectrophotometric properties of Rhea. For our analysis we have chosen full-disk images of the satellite and the formula we have applied to describe the object full-disk reflectance (FDR) as a function of the phase angle g is

straightforward derived by Eq. 10.40, p.275 in Hapke (1993) :

$$FDR(g) = \int_{A(i,v)} r(i,e,g)S(i,e,g)\mu d\Omega = \left\{\frac{1}{8}\left[1-\sin\left(\frac{g}{2}\right)\tan\left(\frac{g}{2}\right)\ln\left(\cot\left(\frac{g}{4}\right)\right)\right]\times\{[(1+B(g))\,p(g)-1]\,w+ \right. \tag{3.1}$$
$$\left. +4r_0(1-r_0)\} + \frac{4}{3}r_0^2\left[\frac{\sin(g)+(\pi-g)\cos(g)}{2\pi}\right]\right\}K(g,\bar{\theta})$$

This equation just represents the sum of the reflectances $r(i,e,g)$ of each point on the surface $A(i,v)$ which is both viewed by the instrument and illuminated by the Sun, depending on the incidence and emission angles (i,e), and the phase angle. Each term is weighted by the cosine of the emission angle $\mu = \cos(e)$ which correctly projects the emitting area on the plane orthogonal to the emission direction, and by the term $S(i,e,g)$ which describes the large scale surface roughness (craters, depressions and other reliefs). Two mechanisms contribute to the emission process: single scattering and multiple scattering. The first one depends on the single-particle phase function $p(g)$, which describes how the light interacting with a particle is scattered. Actually the single-particle phase function is an average on a small but statistically significant given volume of particles. We modeled it assuming a double lobed Henyey-Greenstein (Heyney and Greenstein, 1941; Domingue and Verbiscer, 1997) phase function (see sec.2.4.4, eq. 2.90) depending on two parameters b and v: the first one describes the angular width of both forward and back scattering lobes, while the second one describes their relative amplitude. Another term which depends on single scattering is the one that takes into account for the opposition effect (OE), $B(g)$. It describes the observed non-linear increase in reflectance towards small phase angles. In this work we use the mathematical formulation developed to treat shadow hiding opposition effect SHOE, which depends on the parameters B_0 and h, respectively the amplitude and the angular width of the effect. Actually B_0 can assume values in the 0-1 range, however we allow B_0 to be greater than 1 in order to consider even coherent backscattering (CB), another mechanism contributing to OE (Roush, 1994). We choose not to model explicitly the CBOE in order to have fewer free parameters. The last term to be described is $K(g,\bar{\theta})$, which is the full disk correction due to large scale surface roughness. Its value is always less than 1 and decreases with increasing roughness parameter, which is an average

slope of the facets composing the surface. Spectral information is included in the single-scattering albedo $w(\lambda)$. This parameter represents the fraction of light interacting with the particle (light can be absorbed, scattered or diffracted) that undergoes only scattering. Its value is in the range 0-1 and strictly depends on optical constants of the medium grain size and shape. Similarly to the case of single-particle phase function, the value of the single-scattering albedo is an average over a small but statistically significant volume of particles, and it is calculated as the ratio of the scattering and extinction efficiencies Q_S and Q_E. In close-packed particulate media with spherical grains much larger than the wavelength (which is the assumption we made in our analysis) the IMSA model assumes that diffraction is negligible such that extinction efficiency is 1 (the cross section of the particle is equal to the geometrical cross section) and single-scattering albedo is equal to the scattering efficiency Q_S that can be directly calculated in the Hapke model once that optical constants of end-members, type of mixing and grain size are fixed.

We have investigated three types of mixing: areal, intimate and intraparticle.

Areal mixing (fig. 3.2a) is obtained averaging the reflectance of different patches of surface covered with different materials:

$$r_{tot} = \sum_i p_i r_i \tag{3.2}$$

where r_i is the reflectance of i'th component and p_i is the fraction of total surface covered.

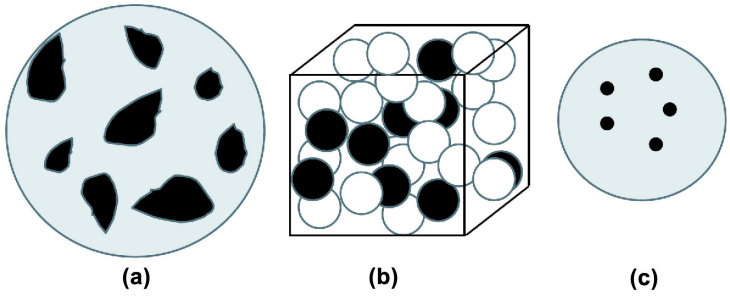

Figure 3.2: Schematic representations of two-component mixtures: areal (a), intimate (b) and intraparticle (c). In (a) the circle represents the field of view of the observing instrument, while in (c) the circle represents a single grain. Ciarniello et al. (2011a).

Intimate mixing (fig. 3.2b) describes a medium in which particles of different composition are mixed together: this kind of mixing is obtained through a weighted average of single-scattering albedos of the different types of grains:

$$w_{tot} = \frac{\sum_i p_i \sigma_i w_i}{\sum_i p_i \sigma_i} \tag{3.3}$$

where σ_i is the geometrical cross section of the i'th particle type and p_i is the volume percentage of each component.

Intraparticle mixing (fig. 3.2c) describes media in which inclusions of contaminants are embedded in a matrix of different optical properties. This kind of mixing is obtained with the Maxwell-Garnett rule (Maxwell-Garnett, 1904; Mallet et al., 2005; Grundy, 2009):

$$\epsilon_{eff} = \epsilon_1 + 3\epsilon_1 p_2 \frac{(\epsilon_2 - \epsilon_1)}{[\epsilon_2 + 2\epsilon_1 - p_2(\epsilon_2 - \epsilon_1)]} \tag{3.4}$$

where ϵ_1 and ϵ_2 are the complex dielectric constants of the matrix and of the embedded material respectively, p_2 is the fraction of contaminant and ϵ_{eff} is the effective complex dielectric constant of the particle. The dielectric constant is related to optical constants by the following relation:

$$m = \sqrt{\epsilon} = n + ik \tag{3.5}$$

Once the medium optical constants and particle diameter a_m are fixed it is possible, following the Hapke's model (see sec. 2.4.5, eq. 2.116), to compute the scattering efficiency Q_s which, as stated above, is equal to the single scattering parameter w, in close-packed media.

3.2 Observation and data reduction

Our dataset is composed of 140 observations acquired by VIMS in the period January 2005-January 2008. Since Rhea exhibits a marked dichotomy between leading and trailing hemisphere (Verbiscer and Veverka, 1989; Buratti et al., 1998) we have selected only images in which the illuminated and observed area was more than 60% on the leading side, in order to study homogeneous regions of the satellite. With this limitation the total number of observations reduces to 111 with solar phase angles ranging from 0.08° to 109.8°. VIMS collected full-disk images of the satellite acquired at different

spacecraft-target distance D both in normal and high-resolution modes. Accordingly, the satellite image size in the instrument field of view can cover from a few tens to some hundreds of pixels. In order to produce phase function curves of the satellite at each wavelength we developed an IDL procedure that sums up the reflectances (I/F) of observed-illuminated pixels in the image, correcting them by the multiplicative factor $\delta\epsilon D^2/R^2$ (where R is Rhea's radius and $\delta\epsilon$ is the solid angle subtended by the pixel). This factor represents the solid angle increment on the satellite surface times the emission angle cosine. The relation between observed data and FDR is:

$$\int_{A(i,v)} r(i,e,g)S(i,e,g)\mu d\Omega \approx \sum_j \left(\frac{I}{F}\right)_j \frac{\delta\epsilon D^2}{R^2} \tag{3.6}$$

where the subscript j identifies each single pixel.

In fig. 3.3 Rhea full-disk normalized spectra acquired at various phase angles are plotted (for a discussion about VIMS calibration uncertainties refer to McCord et al. (2004)). All the spectra exhibit typical features of water ice (1.51, 2.2 and 3.1 μm absorption bands), however towards the UV region the shape of the spectrum strongly departs from the flat behavior of water ice producing a strong reddening. This feature has been explained with the presence of organic contaminants as suggested by Cruikshank et al. (1998) and Poulet et al. (2002). However there is no clear additional signature in the IR, and this constrains the amount of contaminants to be at most few percent (Clark and Owensby, 1981). Clark et al. (2008) gave alternative explanations, including UV absorption by other compounds and very small grains (nano-phase) of opaque minerals such as hematite. Clark and et al. (2011) model the shape of the UV absorber with combinations of metallic iron (both large grained and nano-sized particles) and nano-phase hematite. A feature centered at 0.9 μm is present in all the spectra. This seems to be an artifact due to the data calibration process. However, the presence of this feature does not affect the global slope in VIS-IR region and does not introduce any offset between the two channels, and thus does not alter the results of the following analysis. The spectra show a certain dependence on observing geometry. The slope in VIS-NIR (around 1 μm) region and the band depth at 1.5 and 2.05 μm slowly increase with increasing phase angle, while this trend is reversed at 3.5 μm. This peculiar behavior can be partially explained by varying the relative contributions of single and multiple scattering at different wavelengths (related to different values of the single-scattering albedo w as we will discuss later) and to a variation of single-particle phase

function along the spectrum (even in this case related to w).

In fig. 3.4 Rhea's normalized full-disk phase functions at various wavelengths are plotted. The coverage is fairly complete across the whole range, except for the $20° - 40°$ interval. The shape of the phase function is not constant with wavelength, because, as discussed before, the reflectance has a dependance with the solar phase. As discussed in Hapke (1993), phase induces changes on the continuum level, spectral slopes (reddening effect) and absorption band properties. In particular, the OE width and reflectance at intermediate phase angles show a lot of variability while the differences decrease towards larger phase angles.

3.3 Spectral fit

The first step of our investigation is the interpretation of Rhea spectra in terms of physical characteristics of the surface involved in the scattering process. The principal properties that determine the observed spectral properties are the composition (in this case water ice + contaminants) and the grain size. The presence of certain end-members is directly correlated with spectral signatures (absorption bands), while the grain size basically affects the depth of the bands as well as the IR slope (Clark and Lucey, 1984; Emery et al., 2005). In Hapke's model the spectral behavior is described by the single-scattering albedo w, whose value at each wavelength can be calculated once the end-members, their relative abundances, mixing mode and grain size distribution have been fixed. The single-scattering albedo cannot be directly compared to the observed spectra, because the reflectance at each wavelength depends on single scattering, which relies on the single-particle phase function, and multiple scattering, which involves w in a non-linear way, as shown in eq. 3.1. Moreover, at low phase angle OE must be taken into account, while at high phase angles large scale surface roughness decrease the reflectance.

We have chosen to model Rhea's surface by means of a mixture of crystalline water ice and one organic contaminant. We used separately tholin from Khare et al. (1993), Triton tholin (McDonald et al. (1994), optical constants from Cruikshank (personal communication)), Titan tholin (McDonald et al. (1994); Khare et al. (1984), optical constants from Cruikshank (personal communication)) and hydrogenated amorphous

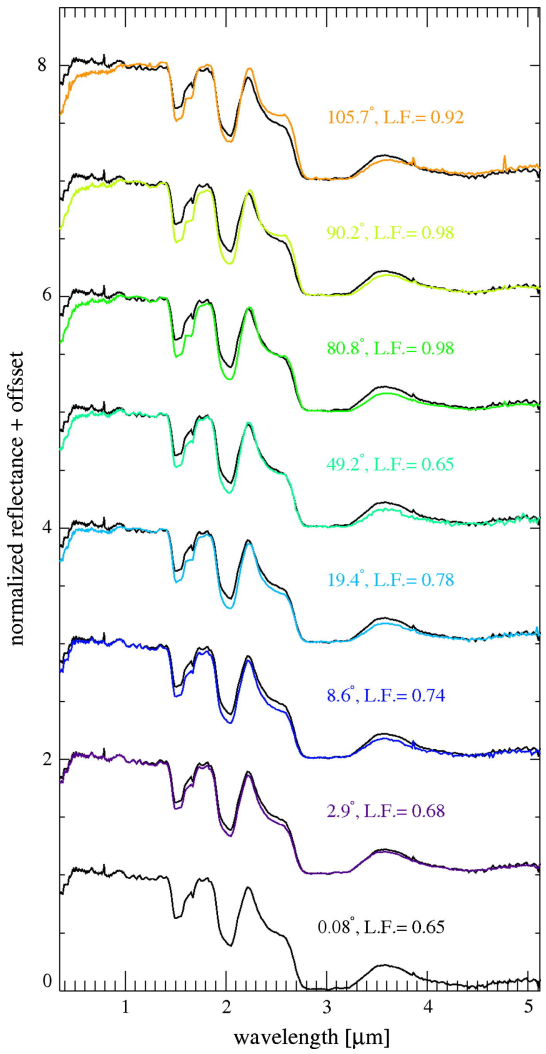

Figure 3.3: VIMS full-disk spectra of Rhea acquired at different phase angles, normalized at 1 μm. An offset is added for clarity. The spectrum at each phase angle is compared to the spectrum at 0.08° (black curve). The leading fraction L. F. of each spectrum is reported. Ciarniello et al. (2011a).

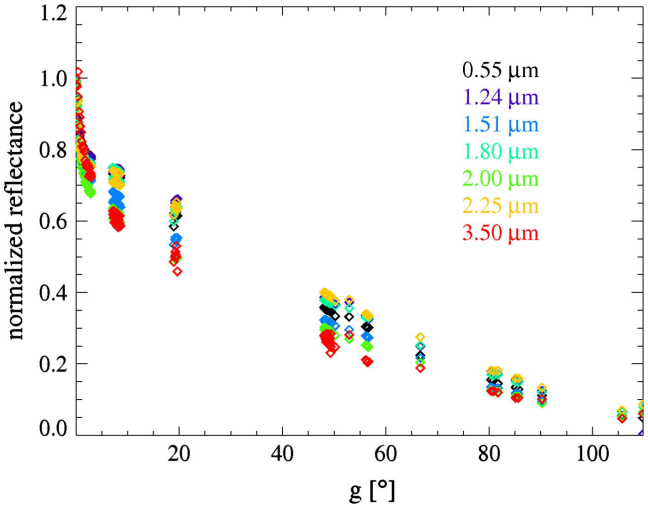

Figure 3.4: Rhea's full-disk phase functions at various wavelengths. All the curves are normalized to the value at minimum phase angle (0.08°). Ciarniello et al. (2011a).

carbon (ACH2) from Zubko et al. (1996). Optical constants for crystalline water ice are those derived by Warren (1984) (0.35-1.25 μm, 266.15 K), Mastrapa et al. (2008) (1.25-2.5 μm, 120 K), Mastrapa et al. (2009) (2.5-3.20 μm, 120 K) and Clark and et al. (2011) (3.20-5.12 μm, 120 K). We investigated areal mixing, intimate mixing and intra-particle mixing. In order to investigate spectral behavior of different mixtures without superimposing any grain size effect we studied only monodisperse particle diameter distribution (particles are all equal in size). This may lead to a non-unique solution, but as we shall see, provides information on the single particle phase function as a function of single particle albedo. The other parameter fixed by the fitting procedure is the volume fraction of water ice p, with $pc = 1 - p$ being the amount of contaminants. In order to retain a minimum number of parameters we decided to perform the spectral fit at high phase angle (90°) thus avoiding the OE surge. To remove the contribution of large scale surface roughness K we fitted normalized spectra (normalization was performed at 1 μm). This choice also allows to minimize the geometrical effects of single-particle phase function which at this stage is assumed isotropic, but may further reduce the uniqueness of the solution.

3.3.1 Optical constants

Summary plots of optical constants vs. wavelength used in this work are shown in fig. 3.5, 3.6 In the VIS-NIR range optical constants from Warren (1984) pertain to ice at -7 $°C$, whose temperature is too high if compared to Rhea's surface at 77 K (Pitman et al., 2010). However these values match reasonably well with the ones derived by Mastrapa et al. (2008) at 120 K. Optical constants in the 3.2-5.1 μm range are from Clark and et al. (2011) and have been computed starting from Mastrapa's values at the same wavelengths. The temperature difference between Rhea's surface and ice for which optical constants are determined introduces a tolerable error in our calculations, because it only minimally affects the results concerning grain size and contamination. The organic compounds, listed above, used to contaminate water ice, all have the effect of producing a red spectrum towards the UV (fig.3.6). Tholin from Khare et al. (1993) have been produced by plasma irradiation in an iced 6 : 1 mixture of H_2O and C_2H_6 at 77 K. Titan and Triton tholin are instead obtained in gaseous phase by irradiation of 0.9 : 0.1 and 0.999 : 0.001 N_2/CH_4 mixtures. ACH2 is obtained by arc discharge between carbon electrodes in H_2 atmosphere.

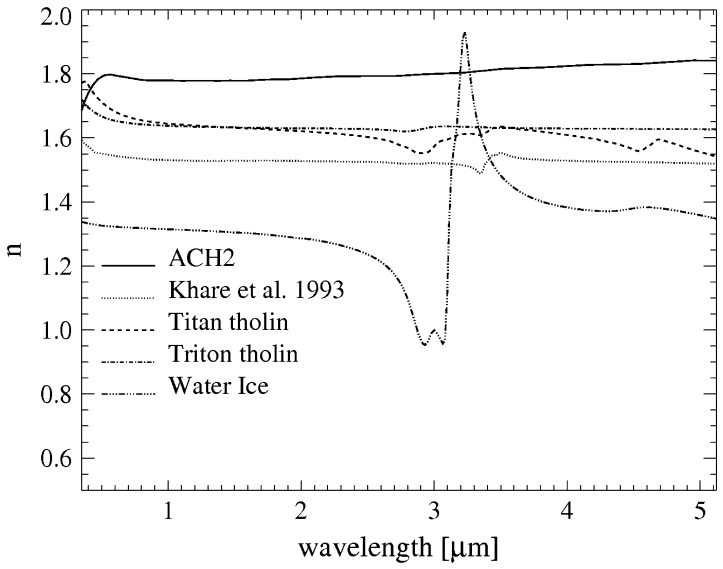

Figure 3.5: Real part (n) of the refractive index for water ice and four organic contaminants: hydrogenated amorphous carbon (ACH2), tholin from Khare et al. (1993), Titan tholin and Triton tholin. Ciarniello et al. (2011a).

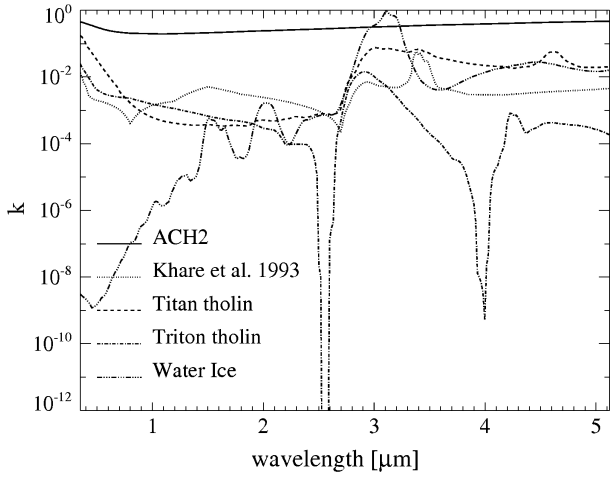

Figure 3.6: Imaginary part (k) of the refractive index for water ice and four organic contaminants: hydrogenated amorphous carbon (ACH2), tholin from Khare et al. (1993), Titan tholin and Triton tholin. Ciarniello et al. (2011a).

3.3.2 Areal mixing

We fitted observed spectra with different areal mixtures of two components where the main end-member is always water ice and the second is one among the selected organic contaminants. In areal mixing, the two different types of surface are characterized by different single-scattering albedo, and a beam of light interacts only with particles of the same composition. The resulting spectrum is a linearly-weighted average of the reflectances relative to the different regions. This kind of mixing is inefficient to produce the observed reddening towards UV. As an example we examine the cases of ACH2 and tholin (Khare et al., 1993). In the case of ACH2 the problem is mainly due to the fact that contaminant spectrum is not red enough to produce a sensible effect. It just reduces the reflectance across the whole spectrum without producing any absorption in the UV region, where water ice is strongly non-absorbing. In the normalized spectra this corresponds to an increment of reflectance of the darker wavelengths. This is shown in fig. 3.7 (left panel) where the results of five simulations with different abundances of ACH2 are plotted. The case of tholins (fig. 3.7, right panel) is different because their spectra are not as flat as ACH2 far from UV region. In order to produce an effective feature towards short wavelengths many unobserved features need to be introduced in other regions of the spectrum. The outcome of this simulations that the strong UV downturn observed in the Rhea spectrum it is not compatible with mixtures including

compounds expected to be found on its surface. As an example, the best fit obtained with an areal mixture of water ice and Titan tholin is plotted in fig. 3.8 (top left panel). The results are similar using other types of contaminants. The fit, fairly good in IR, is completely lost in UV-VIS where a plateau is formed at the shortest wavelengths, missing the observed spectral downturn. Results for areal mixtures fits are summarized in table 3.1.

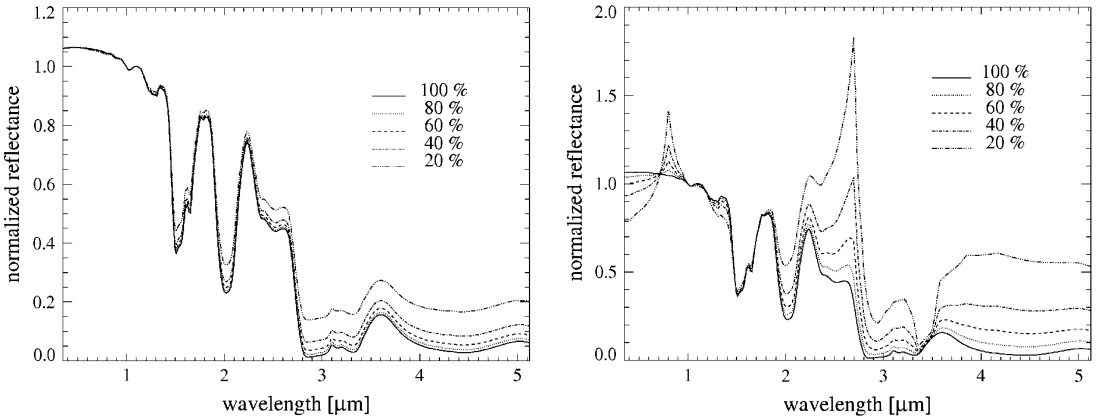

Figure 3.7: Simulated spectra of areal mixtures of water ice and ACH2 (left panel) and of water ice and Tholin from Khare et al. (1993) (right panel). The percentage of water ice is indicated. Spectra are normalized at 1 μm. Grain size is 50 μm. Ciarniello et al. (2011a).

3.3.3 Intimate mixing

Similar to the case of areal mixtures we obtained fits to Rhea's spectrum considering intimate mixtures of water ice and the available contaminants. In an intimate mixture, particles of different composition are in close contact (Clark, 1999), so this kind of mixing is also named "salt and pepper" (Poulet et al., 2003). A single ray of light entering the medium in a given position interacts both with water ice particles and contaminant particles. A small volume containing a statistically significant number of particles behaves as if it had an effective single-scattering albedo given by the average of the albedo of the single particles. This kind of mixing is expected to be more efficient than areal mixing because at this stage spectral signatures (e.g. reddening) affect the effective single-scattering albedo and are stretched in higher order terms (w^2, w^3, . .

.) involved in the resulting reflectance, while in the case of areal mixtures, spectra of contaminants are only linearly combined. As a result, in intimate mixing, the darker component dominates the spectra signature (Clark, 1999). However, intimate mixing alone is still unable to reproduce the observed reddening of Rhea's spectrum for all the contaminants analyzed. Fig. 3.8(top right panel) shows the best fit obtained with an intimate mixture of water ice and Titan tholin. As with the result of the areal mixture the fit is acceptable in the IR but no reddening is produced towards the UV. The results of the fits are summarized in table 3.2.

3.3.4 Intraparticle mixing

In this approach we consider the surface covered by identical particles of water ice with small inclusion of contaminants. The single particle behaves as if it had effective optical constants derived from a combination, given by the Maxwell-Garnett equation, of optical constants of ice and inclusions. For small amount of contaminants (which is the case of this work) the Maxwell-Garnett equation gives results similar to those obtained by a weighted average of the optical constants (Cuzzi and Estrada, 1998). This kind of mixing is the most efficient means of producing reddening because it exaggerates spectral differences, working directly with the complex refractive indices. As shown in fig. 3.8(bottom left panel), intraparticle mixing produces the required UV reddening with every contaminant considered in this work, although the type of reddening change from one contaminant to another. Extremely low concentrations of ACH2 (0.01%) are able to introduce UV reddening, but the resulting spectrum falls too quickly towards short wavelengths before 1 $\mu m$and it is not steep enough below 0.4 μm. Titan tholin produces good fits at the shortest wavelengths but it is not sufficiently absorbing towards 1 μm. Tholin from Khare et al. (1993) shows a good agreement below 0.5 μm but has an unobserved feature at 0.8 μm. The best fit (fig. 3.8, bottom right panel) is obtained with Triton tholin which reproduces even the change of slope in the spectrum around 0.5 μm. The particle size varies depending on the chosen contaminant. However, if we discard the results given by Titan tholin which produces the worst fit in the IR where the spectrum is more sensitive to grain size, we find that the particles diameter is limited to the range 40-50 μm. This diameter can be considered as an average size of particles, once we assume a monodisperse grain size distribution. Some discrepancies between the final fit and observed spectrum due

to particle size are discussed in the next section where the best spectral fit is shown. Results for intraparticle mixtures fits are summarized in table 3.3.

3.3.5 Best spectral fit

Considering the results presented in previous sections the best way to reproduce the spectral properties of Rhea is to assume an intraparticle mixture of $99.60 \pm 0.05\%$ water ice and $0.40 \pm 0.05\%$ Triton tholin, with a grain diameter of $38.0 \pm 0.5 \mu m$ (fig. 3.8, bottom right panel). Uncertainty on the derived values is related to the procedure we applied to perform the fit, as explained in Appendix A. Despite the small number of free parameters and end-members, the simulation fits well the observed spectrum. With such a low amount of tholin as a contaminant in the ice, other tholin absorption bands have a small effect on the infrared spectrum where ice is more absorbing. VIS reddening as well as water ice bands are very well reproduced. The secondary absorption band of crystalline water ice at 1.65 lm, which is shown in simulated spectrum, cannot be confirmed in VIMS data because in the wavelength range 1.60-1.66 μm the measured signal is affected by the presence of an order sorting filter on the detector. Consequently, the measured signal in that region is replaced by an interpolated value. One of the stronger discrepancies is in the peak at 2.2 μm. This problem is shown in all the mixtures that have been analyzed, so it does not depend on the spectral properties of the contaminant but is instead most probably due to the chosen grain size distribution. In the case of monodisperse grain size distribution all the particles are equal and the contribution from smaller particles (with particle size similar or smaller than the wavelength), which certainly are present in a real distribution of sizes, is not considered. It must be noted that Hapke's model is developed in the geometric optics domain, so normally does not deal with grain size smaller than the wavelength. Clark and et al. (2011) have extended the Hapke model to include the diffractive scattering and absorption effects from sub-micron particles. Adopting a distribution of sizes which includes smaller particles it might be possible to reproduce the peak at 2.2 μm. Another part of the spectrum where the fit is lost for all the mixtures we deal with, is given by the absorption band at 3 μm. In simulated spectra the 3.1 μm Fresnel peak is always visible, while in the measured spectra it completely disappears. The absence of the Fresnel peak cannot be completely attributed to the relative abundance of amorphous vs. crystalline ice, as in amorphous ice the Fresnel peak does not fully disappear as

shown by Mastrapa et al. (2009). Moreover ground-based telescopic spectra of Rhea also attest to the crystalline nature of H_2O dominating its surface (Cruikshank et al., 2005; Emery et al., 2005). The absence of the Fresnel peak in Rhea's spectra (as in the case for the others icy bodies of the saturnian system) is probably due again to a grain size effect. In large particles light at 3 μm is almost completely absorbed, given the high value of k and the longer path that light travels inside the grain. This implies that when we deal with big grains the light scattered by the particles is the one coming from surface reflections (that involves n) and which generates the Fresnel peak. Scattered light from smaller particles is the result of both surface reflection and internal reflection, thus the Fresnel peak is minimized. Since in our analysis the grain size is around 40 μm and the contribution from small particles is neglected, the resulting spectrum exhibits an evident peak at $3.1\mu m$. An intraparticle mixture of water ice and Triton tholin was adopted in Cruikshank et al. (2005) where a fit of Rhea spectrum was performed applying the Shkuratov model. It is interesting to note that both approaches require a comparable amount of embedded contaminant (0.4% in this work, 0.2% in Cruikshank et al. (2005)) and they both reproduces the reddening in the UV, even if the adopted spectral models and the surface modeling are different. It reinforces the idea that intraparticle mixing is the best approach to explain the UV feature and that Triton tholin is a reasonable candidate as the water ice contaminant.

Table 3.1: Areal mixture fits

Contaminants	a_m (μm)	p	pc	res^a
ACH2	29	1	0	3.2
Triton tholin	30	0.9932	0.0068	3.2
Titan tholin	57	0.59	0.41	1.87
Khare et al. (1993)	29	0.9973	0.0027	3.2

[a] Sum of fit residuals

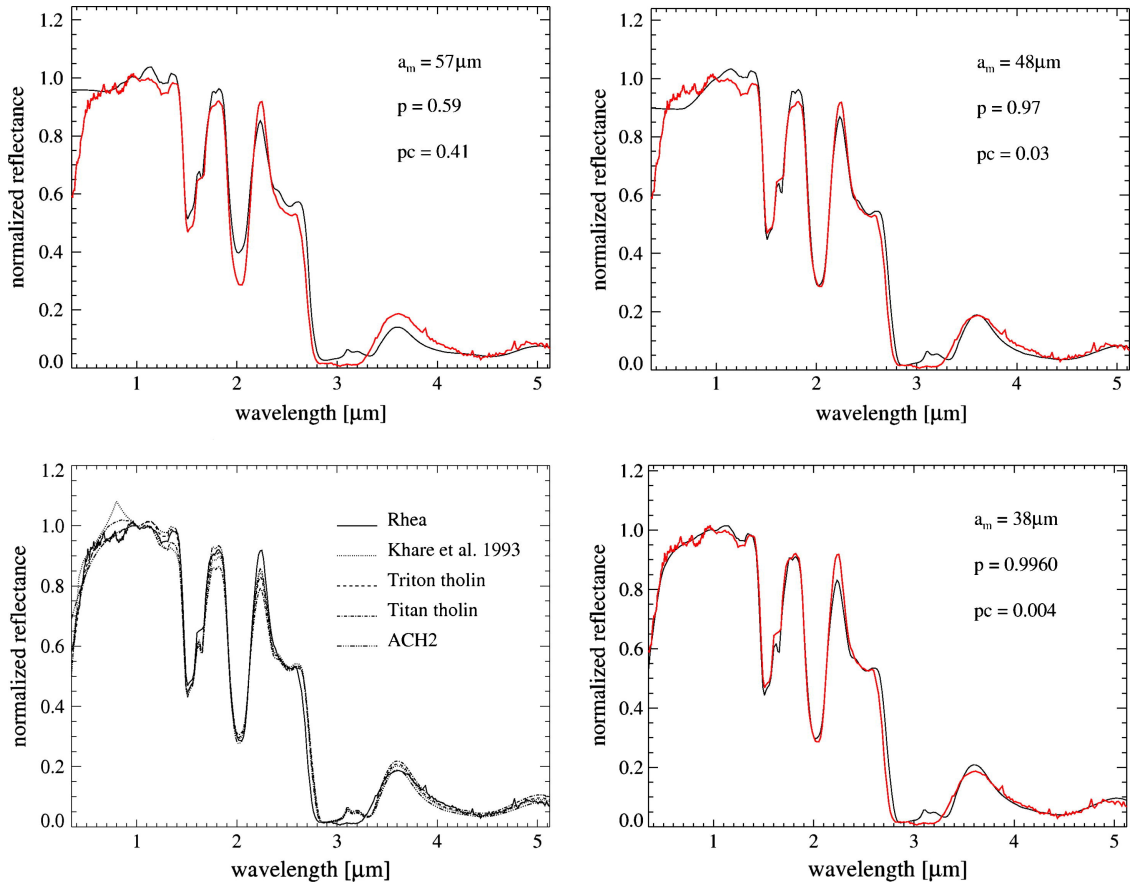

Figure 3.8: *Top left panel*: areal mixture best fit. It is obtained with water ice and Titan tholin. The percentages of water ice (p) and contaminant (pc) and the grain size are indicated. Observed spectrum is in red. Spectra are normalized at 1 μm. *Top right panel*: intimate mixture best fit. It is obtained with water ice and Titan tholin. The percentages of water ice (p) and contaminant (pc) and the grain size are indicated. Observed spectrum is in red. Spectra are normalized at 1 μm. *Top left panel*: summary plot of intraparticle mixtures fits. Rhea spectrum is the continuum line. All the mixtures are water ice + contaminant. Spectra are normalized at 1 μm. Grain sizes and compounds abundances are in table 3.3. *Top right panel*: intraparticle mixture best fit. It is obtained with water ice and Triton tholin. The percentages of water ice (p) and contaminant (pc) and the grain size are indicated. Observed spectrum is in red. Spectra are normalized at 1 μm. Ciarniello et al. (2011a).

Table 3.2: Intimate mixture fits

Contaminants	a_m (μm)	p	pc	res^a
ACH2	60	0.96	0.04	2.2
Triton tholin	49	0.98	0.02	1.6
Titan tholin	48	0.97	0.03	1.1
Khare et al. (1993)	54	0.96	0.04	1.6

[a] Sum of fit residuals

Table 3.3: Intraparticle mixture fits

Contaminants	a_m (μm)	p	pc	res^a
ACH2	49	0.9999	0.0001	0.36
Triton tholin	38	0.996	0.004	0.31
Titan tholin	32	0.9996	0.0004	0.54
Khare et al. (1993)	42	0.992	0.008	0.62

[a] Sum of fit residuals

3.4 Phase function fit

Results from the spectral fit allow us to determine the mixture (type of contaminant and mixing modality) and the grain size. The knowledge of these two parameters enables us to compute single-scattering albedo w which determines the spectral behavior of the observed surface. This quantity is involved in eq. 3.1, which in our approach depends on five parameters (apart from w). The possibility to fix the single-scattering albedo reduces the complexity of phase function fit procedure and allows the decoupling of spectral effect from photometric ones. A phase function fit at each wavelength available in VIMS range has been performed, using the surface model given by the best spectral fit that is represented by an intraparticle mixture of water ice and Triton tholin (99.6-0.04 %), with 38 μm grain size. Parameters relative to the OE (B_0, h) are allowed to vary along the spectrum because, as we mention in sec 3.1, we want to take into account the CBOE as well which can depend on wavelength. Even the single-particle phase function (b, v) parameters can vary with wavelength because the single-scattering albedo has spectral variation and modifies the scattering properties of the grain. The large-scale surface roughness parameter ($\bar{\theta}$) is constant across the spectrum because

it accounts only for geometric effects due to surface morphology. Details on the fit procedure are in Appendix A. In table 3.4 the best phase function fit variables for each VIMS channel are reported. As we deal with particles that are in average larger than the wavelength, we do not expect a direct correlation between the values of parameters obtained by the fit and the wavelength itself. On the other hand, the single-scattering albedo, which determines the contribution of scattering in the light extinction process, plays a fundamental role for the photometric properties at a given wavelength. This implies that the estimated parameters should be correlated with the single-scattering albedo rather than with the wavelength.

Table 3.4: Full-disk phase function best fits.

Band	$\lambda(\mu m)$	w	B_0	h	v	b	θ	res
0	0.35054	0.881	0.8	0.00447	0.9	0.3	33	0.074
1	0.35895	0.897	0.8	0.00224	0.2	0.4	33	0.104
2	0.36629	0.910	1.0	0.00112	0.2	0.4	33	0.062
3	0.37322	0.919	0.8	0.00447	0.0	0.4	33	0.039
4	0.37949	0.926	0.8	0.00631	-0.1	0.4	33	0.041
5	0.38790	0.931	0.8	0.00224	0.1	0.4	33	0.039
6	0.39518	0.938	0.8	0.00316	0.1	0.4	33	0.055
7	0.40252	0.945	0.8	0.00447	0.0	0.4	33	0.030
8	0.40955	0.950	0.8	0.00316	0.0	0.4	33	0.018
9	0.41731	0.955	0.8	0.00631	-0.1	0.4	33	0.065
10	0.42436	0.959	0.9	0.00316	-0.1	0.4	33	0.067
11	0.43184	0.963	1.0	0.00158	-0.4	0.5	33	0.063
12	0.43919	0.967	0.9	0.00447	-0.1	0.4	33	0.038
13	0.44652	0.970	0.9	0.00112	-0.3	0.5	33	0.070
14	0.45372	0.973	1.0	0.00224	-0.4	0.5	33	0.075
15	0.46163	0.976	1.0	0.00224	-0.4	0.5	33	0.045
16	0.46841	0.978	1.0	0.00224	-0.4	0.5	33	0.058
17	0.47622	0.981	1.7	0.00040	-0.3	0.5	33	0.061
18	0.48629	0.983	1.0	0.00224	-0.4	0.5	33	0.028
19	0.48967	0.983	1.2	0.00079	-0.3	0.5	33	0.054
20	0.49777	0.984	1.2	0.00112	-0.4	0.5	33	0.018
21	0.50628	0.985	1.1	0.00158	-0.4	0.5	33	0.019
22	0.51222	0.986	1.9	0.00028	-0.3	0.5	33	0.061
23	0.51963	0.987	1.0	0.00158	-0.4	0.5	33	0.019
24	0.52766	0.987	1.3	0.00079	-0.4	0.5	33	0.019
25	0.53416	0.988	1.5	0.00056	-0.4	0.5	33	0.028
26	0.54156	0.988	1.1	0.00112	-0.4	0.5	33	0.017
27	0.54954	0.989	1.9	0.00040	-0.4	0.5	33	0.029
28	0.55614	0.989	1.8	0.00040	-0.4	0.5	33	0.025
29	0.56353	0.990	1.0	0.00316	-0.5	0.5	33	0.024
30	0.57131	0.990	1.8	0.00040	-0.4	0.5	33	0.029
31	0.57810	0.990	1.1	0.00224	-0.5	0.5	33	0.025
32	0.58548	0.991	1.2	0.00158	-0.5	0.5	33	0.025
33	0.59312	0.991	1.1	0.00224	-0.5	0.5	33	0.031
34	0.59938	0.991	1.1	0.00158	-0.5	0.5	33	0.028
35	0.60757	0.991	1.1	0.00158	-0.7	0.6	33	0.059
36	0.61505	0.992	1.2	0.00158	-0.5	0.5	33	0.026
37	0.62207	0.992	1.1	0.00158	-0.7	0.6	33	0.062
38	0.62940	0.992	1.1	0.00158	-0.5	0.5	33	0.031
39	0.63704	0.992	1.2	0.00112	-0.7	0.6	33	0.046
40	0.64408	0.992	1.3	0.00112	-0.5	0.5	33	0.040
41	0.65142	0.993	1.1	0.00158	-0.5	0.5	33	0.035
42	0.65910	0.993	1.4	0.00112	-0.5	0.5	33	0.034
43	0.66609	0.993	1.1	0.00224	-0.5	0.5	33	0.036
44	0.67342	0.993	1.0	0.00224	-0.5	0.5	33	0.054
45	0.68102	0.993	1.2	0.00158	-0.7	0.6	33	0.099
46	0.68803	0.993	1.4	0.00079	-0.7	0.6	33	0.063
47	0.69535	0.993	1.7	0.00056	-0.7	0.6	33	0.057
48	0.70288	0.993	1.5	0.00079	-0.7	0.6	33	0.068

Table 3.4 (continued)

Band	$\lambda(\mu m)$	w	B_0	h	v	b	$\bar{\theta}$	res
49	0.71000	0.994	2.0	0.00040	-0.7	0.6	33	0.046
50	0.71733	0.994	2.0	0.00040	-0.7	0.6	33	0.030
51	0.72484	0.994	1.9	0.00040	-0.7	0.6	33	0.030
52	0.73198	0.994	2.0	0.00028	-0.7	0.6	33	0.047
53	0.73930	0.994	1.9	0.00040	-0.7	0.6	33	0.032
54	0.74676	0.994	1.7	0.00040	-0.7	0.6	33	0.035
55	0.75396	0.994	2.0	0.00028	-0.7	0.6	33	0.036
56	0.76128	0.994	1.9	0.00040	-0.7	0.6	33	0.033
57	0.76874	0.994	2.0	0.00028	-0.7	0.6	33	0.049
58	0.77595	0.994	1.9	0.00040	-0.7	0.6	33	0.035
59	0.78328	0.994	2.0	0.00040	-0.7	0.6	33	0.036
60	0.79072	0.994	2.0	0.00040	-0.7	0.6	33	0.045
61	0.79793	0.995	1.9	0.00028	-0.7	0.6	33	0.066
62	0.80522	0.995	1.0	0.00891	-0.8	0.6	33	0.092
63	0.81262	0.995	1.0	0.00891	-0.8	0.6	33	0.090
64	0.81989	0.995	1.4	0.00316	-0.8	0.6	33	0.074
65	0.82721	0.995	1.3	0.00316	-0.8	0.6	33	0.075
66	0.83463	0.995	1.1	0.00631	-0.8	0.6	33	0.075
67	0.84190	0.995	1.3	0.00316	-0.8	0.6	33	0.075
68	0.84922	0.995	1.2	0.00447	-0.8	0.6	33	0.069
69	0.85663	0.996	1.1	0.00631	-0.8	0.6	33	0.074
70	0.86391	0.996	1.3	0.00316	-0.8	0.6	33	0.061
71	0.87122	0.996	1.1	0.00631	-0.8	0.6	33	0.077
72	0.87863	0.996	0.6	0.02512	-0.8	0.6	33	0.111
73	0.88589	0.996	0.9	0.01259	-0.8	0.6	33	0.092
74	0.89386	0.996	1.2	0.00631	-0.8	0.6	33	0.083
75	0.90032	0.996	1.2	0.00631	-0.8	0.6	33	0.086
76	0.90787	0.996	1.0	0.00891	-0.8	0.6	33	0.087
77	0.91518	0.996	2.0	0.00028	-0.7	0.6	33	0.065
78	0.92254	0.996	2.0	0.00028	-0.7	0.6	33	0.060
79	0.92983	0.996	1.8	0.00028	-0.7	0.6	33	0.081
80	0.93713	0.996	1.9	0.00028	-0.7	0.6	33	0.069
81	0.94445	0.996	2.0	0.00028	-0.7	0.6	33	0.062
82	0.95177	0.996	2.0	0.00020	-0.7	0.6	33	0.090
83	0.95907	0.997	2.0	0.00020	-0.7	0.6	33	0.082
84	0.96638	0.997	2.0	0.00020	-0.7	0.6	33	0.088
85	0.97382	0.997	1.3	0.00447	-0.8	0.6	33	0.083
86	0.98100	0.997	1.2	0.00631	-0.8	0.6	33	0.094
87	0.98226	0.997	1.2	0.00631	-0.8	0.6	33	0.094
88	0.99882	0.996	1.6	0.00158	-0.8	0.6	33	0.051
89	1.01479	0.996	1.9	0.00079	-0.8	0.6	33	0.070
90	1.03132	0.996	2.0	0.00056	-0.8	0.6	33	0.077
91	1.04755	0.997	2.0	0.00056	-0.8	0.6	33	0.087
92	1.06541	0.997	1.9	0.00079	-0.8	0.6	33	0.072
93	1.08183	0.997	2.0	0.00079	-0.8	0.6	33	0.066
94	1.09806	0.997	1.8	0.00112	-0.9	0.7	33	0.102
95	1.11396	0.997	1.9	0.00079	-0.9	0.7	33	0.113
96	1.13024	0.997	2.0	0.00056	-0.8	0.6	33	0.099
97	1.14695	0.997	1.9	0.00079	-0.8	0.6	33	0.062

Table 3.4 (continued)

Band	$\lambda(\mu m)$	w	B_0	h	v	b	$\bar{\theta}$	res
98	1.16370	0.997	2.0	0.00079	-0.9	0.7	33	0.109
99	1.17996	0.997	2.0	0.00056	-0.8	0.6	33	0.115
100	1.19622	0.996	1.7	0.00112	-0.8	0.6	33	0.083
101	1.21246	0.995	1.6	0.00158	-0.8	0.6	33	0.080
102	1.22859	0.995	1.5	0.00158	-0.8	0.6	33	0.084
103	1.24492	0.995	1.45	0.00191	-0.8	0.6	33	-
104	1.26166	0.994	1.4	0.00224	-0.8	0.6	33	0.099
105	1.27813	0.994	1.4	0.00224	-0.8	0.6	33	0.104
106	1.29482	0.994	1.5	0.00158	-0.8	0.6	33	0.106
107	1.31091	0.994	1.6	0.00158	-0.8	0.6	33	0.120
108	1.32695	0.995	1.6	0.00158	-0.8	0.6	33	0.084
109	1.34324	0.996	1.5	0.00224	-0.8	0.6	33	0.129
110	1.35952	0.996	1.5	0.00224	-0.8	0.6	33	0.145
111	1.37695	0.995	1.8	0.00112	-0.8	0.6	33	0.143
112	1.39326	0.995	1.6	0.00158	-0.8	0.6	33	0.167
113	1.40940	0.994	1.9	0.00056	-0.6	0.5	33	0.156
114	1.42557	0.991	1.8	0.00079	-0.6	0.5	33	0.139
115	1.44184	0.981	1.3	0.00224	-0.4	0.4	33	0.172
116	1.45841	0.956	1.2	0.00224	-0.3	0.4	33	0.201
117	1.47514	0.909	1.0	0.00447	0.0	0.3	33	0.224
118	1.49169	0.849	1.1	0.00224	0.2	0.3	33	0.198
119	1.50794	0.830	0.9	0.00316	0.3	0.3	33	0.187
120	1.52421	0.841	0.9	0.00447	0.2	0.3	33	0.175
121	1.54035	0.849	1.0	0.00316	0.2	0.3	33	0.168
122	1.55674	0.853	1.0	0.00316	0.2	0.3	33	0.172
123	1.57361	0.869	1.0	0.00447	0.2	0.3	33	0.179
124	1.59018	0.900	0.9	0.00447	0.3	0.3	33	0.195
125	1.60228	0.920	1.0	0.00224	0.3	0.3	33	0.199
126	1.62523	0.924	1.0	0.00316	0.3	0.3	33	0.187
127	1.64160	0.914	1.0	0.00224	0.5	0.3	33	0.247
128	1.65567	0.913	0.9	0.00224	0.6	0.3	33	0.273
129	1.67238	0.942	1.1	0.00158	-0.2	0.4	33	0.169
130	1.68901	0.962	1.1	0.00158	-0.2	0.4	33	0.190
131	1.70536	0.973	1.3	0.00112	-0.2	0.4	33	0.188
132	1.72175	0.980	1.1	0.00316	-0.3	0.4	33	0.199
133	1.73802	0.985	1.3	0.00316	-0.4	0.4	33	0.194
134	1.75436	0.989	2.0	0.00056	-0.6	0.5	33	0.171
135	1.77105	0.989	2.0	0.00056	-0.6	0.5	33	0.171
136	1.78771	0.988	1.6	0.00112	-0.6	0.5	33	0.183
137	1.80401	0.989	1.4	0.00158	-0.6	0.5	33	0.190
138	1.82004	0.990	1.4	0.00158	-0.6	0.5	33	0.188
139	1.83616	0.989	2.0	0.00056	-0.6	0.5	33	0.186
140	1.85288	0.987	1.8	0.00079	-0.6	0.5	33	0.198
141	1.86933	0.983	1.5	0.00112	-0.6	0.5	33	0.197
142	1.88679	0.969	1.3	0.00224	-0.4	0.4	33	0.164
143	1.90261	0.944	1.4	0.00158	-0.4	0.4	33	0.152
144	1.91916	0.904	1.3	0.00316	-0.5	0.4	33	0.157
145	1.93545	0.856	1.4	0.00224	-0.5	0.4	33	0.155
146	1.95191	0.804	1.3	0.00158	-0.4	0.4	33	0.173

Table 3.4 (continued)

Band	$\lambda(\mu m)$	w	B_0	h	v	b	$\bar{\theta}$	res
147	1.96871	0.754	1.1	0.00631	-0.2	0.3	33	0.170
148	1.98531	0.715	1.1	0.00631	-0.1	0.3	33	0.176
149	2.00167	0.693	1.0	0.00447	0.0	0.3	33	0.181
150	2.01781	0.687	1.1	0.00447	-0.1	0.3	33	0.163
151	2.03424	0.691	1.1	0.00631	-0.2	0.3	33	0.161
152	2.05091	0.699	1.1	0.00891	-0.3	0.3	33	0.180
153	2.06757	0.716	1.3	0.00447	-0.2	0.3	33	0.178
154	2.08400	0.751	1.1	0.00447	-0.1	0.3	33	0.194
155	2.10034	0.803	1.0	0.00631	-0.1	0.3	33	0.196
156	2.11667	0.858	1.1	0.00631	-0.1	0.3	33	0.198
157	2.13337	0.903	1.1	0.00631	-0.2	0.3	33	0.190
158	2.15018	0.933	1.2	0.00316	-0.2	0.3	33	0.187
159	2.16652	0.951	1.3	0.00316	-0.2	0.3	33	0.195
160	2.18288	0.963	1.2	0.00316	-0.2	0.3	33	0.201
161	2.19920	0.972	1.1	0.00447	-0.2	0.3	33	0.211
162	2.21591	0.977	1.3	0.00316	-0.2	0.3	33	0.214
163	2.23282	0.980	1.5	0.00112	-0.4	0.4	33	0.205
164	2.24952	0.978	1.5	0.00224	-0.3	0.3	33	0.216
165	2.26622	0.974	1.5	0.00158	-0.3	0.3	33	0.219
166	2.28238	0.966	1.8	0.00079	-0.5	0.4	33	0.211
167	2.29921	0.957	1.8	0.00079	-0.5	0.4	33	0.201
168	2.31612	0.945	1.6	0.00224	-0.6	0.4	33	0.182
169	2.33325	0.931	1.8	0.00079	-0.5	0.4	33	0.176
170	2.35043	0.917	1.8	0.00079	-0.5	0.4	33	0.178
171	2.36765	0.908	1.8	0.00079	-0.5	0.4	33	0.183
172	2.38472	0.904	1.3	0.00316	-0.6	0.4	33	0.198
173	2.40156	0.904	1.9	0.00079	-0.6	0.4	33	0.162
174	2.41820	0.902	1.9	0.00158	-0.7	0.4	33	0.153
175	2.43471	0.899	1.8	0.00158	-0.7	0.4	33	0.160
176	2.45097	0.894	1.8	0.00158	-0.7	0.4	33	0.155
177	2.46723	0.890	1.7	0.00158	-0.7	0.4	33	0.155
178	2.48360	0.886	1.7	0.00158	-0.7	0.4	33	0.160
179	2.50002	0.884	1.7	0.00158	-0.7	0.4	33	0.158
180	2.51659	0.882	1.9	0.00112	-0.7	0.4	33	0.182
181	2.53292	0.882	1.7	0.00447	-0.8	0.4	33	0.182
182	2.54916	0.883	1.8	0.00316	-0.8	0.4	33	0.175
183	2.56437	0.885	1.9	0.00224	-0.8	0.4	33	0.186
184	2.58176	0.887	1.8	0.00158	-0.8	0.4	33	0.236
185	2.59807	0.887	1.9	0.00447	-0.9	0.5	33	0.209
186	2.61508	0.887	2.0	0.00079	-0.9	0.5	33	0.367
187	2.63000	0.885	2.0	0.05012	-1.0	0.6	33	0.441
188	2.64650	0.880	2.0	0.02512	-1.0	0.7	33	0.572
189	2.66146	0.870	2.0	0.01259	-1.0	0.9	33	0.970
190	2.68085	0.840	2.0	0.00158	-1.0	0.9	33	1.991
191	2.69620	0.804	0.1	0.00010	-1.0	0.9	33	8.981
192	2.71205	0.749	0.1	0.00010	-1.0	0.9	33	17.550
193	2.73270	0.647	0.1	0.00010	-1.0	0.9	33	16.140
194	2.74770	0.560	0.1	0.00010	-1.0	0.9	33	24.250
195	2.76305	0.465	0.1	0.00010	-1.0	0.9	33	19.250

Table 3.4 (continued)

Band	$\lambda(\mu m)$	w	B_0	h	v	b	$\bar{\theta}$	res
196	2.78118	0.341	2.0	0.02512	-1.0	0.9	33	3.095
197	2.79889	0.222	2.0	0.03548	-1.0	0.7	33	3.932
198	2.81606	0.129	2.0	0.00010	-0.9	0.5	33	4.483
199	2.83247	0.075	2.0	0.00014	-0.7	0.4	33	3.381
200	2.84954	0.055	1.7	0.00040	-0.3	0.2	33	2.767
201	2.86609	0.052	0.7	0.00224	-0.2	0.2	33	3.846
202	2.88242	0.053	1.3	0.00040	0.4	0.1	33	2.923
203	2.89878	0.055	0.5	0.00316	-0.2	0.2	33	3.436
204	2.91540	0.058	0.6	0.00316	-0.2	0.2	33	2.360
205	2.93143	0.063	0.3	0.00112	-0.5	0.4	33	5.666
206	2.94726	0.068	0.3	0.03548	-0.5	0.3	33	2.021
207	2.96327	0.072	0.4	0.05012	-0.8	0.4	33	4.549
208	2.97720	0.075	2.0	0.00010	-0.8	0.5	33	10.940
209	3.00072	0.080	0.2	3.16000	-0.9	0.6	33	7.750
210	3.01382	0.083	0.1	0.00010	-0.9	0.6	33	7.730
211	3.02970	0.090	0.1	0.02512	-0.9	0.6	33	7.292
212	3.04806	0.103	0.2	0.00224	-0.9	0.6	33	8.658
213	3.06446	0.123	1.8	0.00010	-0.9	0.6	33	9.268
214	3.08036	0.158	1.0	0.00010	-0.9	0.6	33	19.680
215	3.09689	0.198	2.0	0.07079	-1.0	0.7	33	23.540
216	3.11213	0.200	2.0	0.14125	-1.0	0.8	33	23.520
217	3.12962	0.180	2.0	0.07079	-1.0	0.7	33	23.930
218	3.14667	0.167	2.0	0.07079	-1.0	0.7	33	22.770
219	3.16304	0.166	2.0	0.10000	-1.0	0.7	33	21.820
220	3.17974	0.171	2.0	0.07079	-1.0	0.7	33	21.760
221	3.19708	0.175	0.1	0.00010	-0.9	0.6	33	23.470
222	3.21364	0.172	0.3	0.00316	-0.9	0.6	33	12.860
223	3.23150	0.161	0.5	0.14125	-0.9	0.6	33	5.370
224	3.24806	0.147	0.4	0.02512	-0.7	0.5	33	2.214
225	3.26561	0.135	0.7	0.02512	-0.4	0.4	33	1.280
226	3.28298	0.126	1.7	0.07079	-0.4	0.3	33	1.338
227	3.29946	0.120	1.9	0.10000	0.0	0.2	33	0.708
228	3.31619	0.121	2.0	0.14125	0.1	0.2	33	0.904
229	3.33338	0.130	2.0	0.14125	0.9	0.1	33	1.021
230	3.34981	0.151	2.0	0.10000	0.9	0.1	33	1.114
231	3.36564	0.186	2.0	0.10000	0.3	0.1	33	0.774
232	3.38183	0.230	1.9	0.10000	-0.3	0.2	33	0.634
233	3.39872	0.278	1.9	0.07079	-0.4	0.2	33	0.390
234	3.41546	0.333	1.2	0.05012	-0.4	0.3	33	0.412
235	3.43178	0.372	1.4	0.05012	-0.5	0.3	33	0.499
236	3.44874	0.405	1.4	0.03548	-0.5	0.3	33	0.364
237	3.46475	0.438	0.9	0.00631	-0.4	0.4	33	0.324
238	3.48137	0.466	1.0	0.01259	-0.5	0.4	33	0.364
239	3.49795	0.490	0.9	0.00891	-0.5	0.4	33	0.265
240	3.51284	0.507	0.9	0.00631	-0.5	0.4	33	0.276
241	3.53015	0.527	0.9	0.01259	-0.6	0.4	33	0.325
242	3.54664	0.540	1.0	0.00891	-0.6	0.4	33	0.334
243	3.56274	0.549	1.1	0.00631	-0.6	0.4	33	0.320
244	3.58034	0.555	1.2	0.01778	-0.7	0.4	33	0.407

Table 3.4 (continued)

Band	$\lambda(\mu m)$	w	B_0	h	v	b	$\bar{\theta}$	res
245	3.59610	0.557	1.1	0.01778	-0.7	0.4	33	0.385
246	3.61387	0.557	1.3	0.01259	-0.7	0.4	33	0.409
247	3.63085	0.554	1.2	0.01259	-0.7	0.4	33	0.362
248	3.64853	0.548	1.2	0.01259	-0.7	0.4	33	0.413
249	3.66522	0.539	1.0	0.00447	-0.6	0.4	33	0.320
250	3.68283	0.527	1.1	0.00447	-0.6	0.4	33	0.455
251	3.69953	0.513	1.1	0.00631	-0.6	0.4	33	0.309
252	3.71743	0.497	1.0	0.00891	-0.6	0.4	33	0.499
253	3.73439	0.480	1.0	0.00891	-0.6	0.4	33	0.428
254	3.75103	0.463	1.0	0.00891	-0.6	0.4	33	0.598
255	3.76763	0.445	0.9	0.01259	-0.6	0.4	33	0.451
256	3.78444	0.428	1.3	0.01778	-0.6	0.3	33	0.506
257	3.80083	0.411	1.2	0.02512	-0.6	0.3	33	0.517
258	3.81742	0.395	1.2	0.02512	-0.6	0.3	33	0.653
259	3.83472	0.379	1.1	0.03548	-0.6	0.3	33	1.037
260	3.85141	0.364	1.1	0.01259	-0.5	0.3	33	1.814
261	3.86184	0.355	1.1	0.01778	-0.5	0.3	33	4.442
262	3.88167	0.339	0.9	0.01778	-0.4	0.3	33	1.707
263	3.89859	0.326	1.1	0.01778	-0.5	0.3	33	0.884
264	3.91478	0.316	1.1	0.03548	-0.6	0.3	33	0.945
265	3.93069	0.306	1.0	0.01778	-0.5	0.3	33	0.638
266	3.94762	0.295	1.1	0.01778	-0.5	0.3	33	0.832
267	3.96375	0.285	0.9	0.02512	-0.5	0.3	33	0.969
268	3.98015	0.276	1.0	0.01778	-0.5	0.3	33	1.140
269	3.99672	0.266	0.9	0.02512	-0.5	0.3	33	1.499
270	4.01280	0.258	1.0	0.01778	-0.5	0.3	33	1.234
271	4.02944	0.250	1.2	0.03548	-0.6	0.3	33	1.622
272	4.04730	0.240	0.9	0.02512	-0.5	0.3	33	1.489
273	4.06295	0.232	1.0	0.02512	-0.5	0.3	33	1.339
274	4.08086	0.224	0.9	0.01259	-0.4	0.3	33	1.298
275	4.09743	0.219	0.9	0.01259	-0.4	0.3	33	1.488
276	4.11450	0.215	0.9	0.02512	-0.5	0.3	33	1.574
277	4.13183	0.211	1.5	0.03548	-0.7	0.3	33	3.070
278	4.14883	0.207	1.0	0.01778	-0.5	0.3	33	2.553
279	4.16644	0.202	1.8	0.05012	-0.8	0.3	33	5.277
280	4.18299	0.197	1.0	0.03548	-0.6	0.3	33	3.191
281	4.19839	0.192	1.8	0.05012	-0.8	0.3	33	2.826
282	4.21120	0.187	1.3	0.10000	-0.8	0.4	33	3.731
283	4.22402	0.182	1.6	0.05012	-0.8	0.3	33	4.621
284	4.24220	0.178	2.0	0.10000	-0.9	0.4	33	4.633
285	4.26028	0.175	1.0	0.07079	-0.8	0.4	33	6.903
286	4.27840	0.172	1.8	0.10000	-0.9	0.5	33	9.597
287	4.29650	0.170	1.0	0.00316	-0.6	0.4	33	3.691
288	4.31470	0.167	1.6	0.14125	-0.9	0.5	33	5.715
289	4.33280	0.163	1.3	0.03548	-0.8	0.4	33	7.369
290	4.35094	0.159	1.8	0.00020	-0.8	0.6	33	14.430
291	4.36646	0.154	0.6	0.02512	-0.7	0.4	33	6.683
292	4.38295	0.151	0.8	0.01778	-0.7	0.4	33	6.203
293	4.39793	0.149	1.0	0.01778	-0.7	0.4	33	7.357

Table 3.4 (continued)

Band	$\lambda(\mu m)$	w	B_0	h	v	b	$\bar{\theta}$	res
294	4.41537	0.147	1.6	0.10000	-0.9	0.5	33	10.850
295	4.43172	0.145	0.5	0.01259	-0.6	0.4	33	5.620
296	4.44772	0.145	0.6	0.00447	-0.6	0.4	33	6.066
297	4.46573	0.146	0.8	0.02512	-0.7	0.4	33	5.962
298	4.48240	0.146	1.1	0.07079	-0.8	0.4	33	6.873
299	4.49951	0.148	1.0	0.01259	-0.6	0.3	33	5.159
300	4.51591	0.150	0.9	0.00316	-0.6	0.4	33	8.542
301	4.53379	0.153	0.3	0.01778	-0.6	0.4	33	8.965
302	4.55187	0.158	1.4	0.19953	-0.9	0.5	33	10.230
303	4.56797	0.162	1.0	0.14125	-0.8	0.4	33	5.884
304	4.58556	0.166	0.5	0.01259	-0.6	0.4	33	7.717
305	4.60290	0.170	0.8	0.02512	-0.6	0.3	33	7.812
306	4.62010	0.177	1.7	0.02512	-0.8	0.4	33	7.178
307	4.63615	0.183	0.8	0.00891	-0.6	0.4	33	5.838
308	4.65416	0.191	1.8	0.01778	-0.8	0.4	33	11.750
309	4.67034	0.197	1.3	0.01259	-0.6	0.3	33	6.434
310	4.68721	0.203	0.9	0.00891	-0.5	0.3	33	5.109
311	4.70290	0.209	0.8	0.01259	-0.6	0.4	33	5.455
312	4.71956	0.216	1.1	0.01778	-0.6	0.3	33	5.260
313	4.73706	0.225	1.2	0.01778	-0.7	0.4	33	6.444
314	4.75351	0.232	1.3	0.01259	-0.7	0.4	33	8.366
315	4.77031	0.239	1	0.02404	-0.7	0.4	33	-
316	4.78673	0.245	0.7	0.03548	-0.7	0.4	33	4.585
317	4.80349	0.253	1.6	0.14125	-0.9	0.5	33	6.520
318	4.81952	0.258	1.0	0.01259	-0.7	0.4	33	4.910
319	4.83577	0.265	0.8	0.01259	-0.7	0.4	33	4.840
320	4.85292	0.273	0.9	0.01778	-0.7	0.4	33	4.466
321	4.86940	0.279	1.2	0.00891	-0.7	0.4	33	3.701
322	4.88553	0.284	0.8	0.01778	-0.7	0.4	33	4.059
323	4.90265	0.290	1.3	0.19953	-0.9	0.5	33	6.230
324	4.91983	0.297	0.9	0.01259	-0.7	0.4	33	3.152
325	4.93685	0.301	1.0	0.00891	-0.7	0.4	33	3.745
326	4.95389	0.305	1.1	0.03548	-0.8	0.4	33	5.469
327	4.97178	0.309	1.3	0.01259	-0.8	0.4	33	7.763
328	4.98896	0.311	1.2	0.00447	-0.8	0.5	33	10.840
329	5.00576	0.313	1.0	0.02512	-0.8	0.4	33	6.575
330	5.02240	0.314	0.5	0.03548	-0.8	0.5	33	6.036
331	5.04078	0.313	1.0	0.01778	-0.8	0.4	33	7.857
332	5.05734	0.311	1.6	0.03548	-0.9	0.5	33	10.440
333	5.07402	0.309	0.9	0.00891	-0.8	0.5	33	8.624
334	5.09106	0.304	1.2	0.01778	-0.8	0.4	33	13.700
335	5.10680	0.300	0.3	0.10000	-0.8	0.4	33	9.531
336	5.12250	0.296	0.7	0.03548	-0.8	0.4	33	9.956

Notes: For bands 103 and 315 it was not possible to perform a fit because of the low S/N. In those cases we chose to assign to each parameter the average value of the corresponding ones from the previous and the following bands. The total numbers of bands is 337 instead of 352 because of the overlapping between VIS and IR channels in the NIR region.

3.4.1 Residuals

Fits are performed minimizing the residuals that are calculated for each wavelength following the formula:

$$res = \sum_i \left(\frac{r_i^m - r_i^c}{r_i^m} \right)^2 \tag{3.7}$$

where r_i^m is the measured absolute reflectance at i^{th} phase angle while r_i^c is the value computed by the fit procedure. This kind of choice aims to give equal weight to the two extremes of the full-disk phase function. Reconstructed full-disk phase functions for those wavelengths where the albedo is very low are often dominated by noise, and the corresponding fit parameters values are thought to have no physical meaning. Additionally, they produce high residuals because the model is unable to perform a satisfactory fit. For this reason we have considered for the following analysis only wavelengths with well determined full disk phase function and low value of the residuals. We found that for a residual value of 1 the full disk phase function can be considered well reproduced. From this point to the end of the paper we refer only to results relative to residuals lower than 1, unless explicitly written. In fig. 3.9 (top left panel) fit residuals for each band are plotted against the value of single-scattering albedo computed for the corresponding wavelength. As we can see the accuracy of the fits increases with larger values of the single-scattering albedo. This effect is due to two reasons. The first is that for those wavelengths corresponding to a higher value of w the signal to noise ratio is typically higher and reconstructed phase functions are more accurate. The second is that at low values of the single-scattering albedo the dominating process is single scattering. In this regime the full-disk phase function is more sensitive to single-particle phase function and worse regression accuracy indicates that the Heyney-Greenstein expression is not able to completely describe the scattering process.

3.4.2 Single-particle phase function

In fig. 3.11 the distributions of b and v parameters are plotted. In these graphs it is shown how many times a certain value of the parameter occurs in a given range of w values. According to McGuire and Hapke (1995) a clear spherical particle should have $b \approx 0.5 - 0.7$ and $v \approx -0.9$. Most of our b values are slightly lower (0.3-0.4) as it is expected for real grains that are not perfectly spherical. Moreover b values

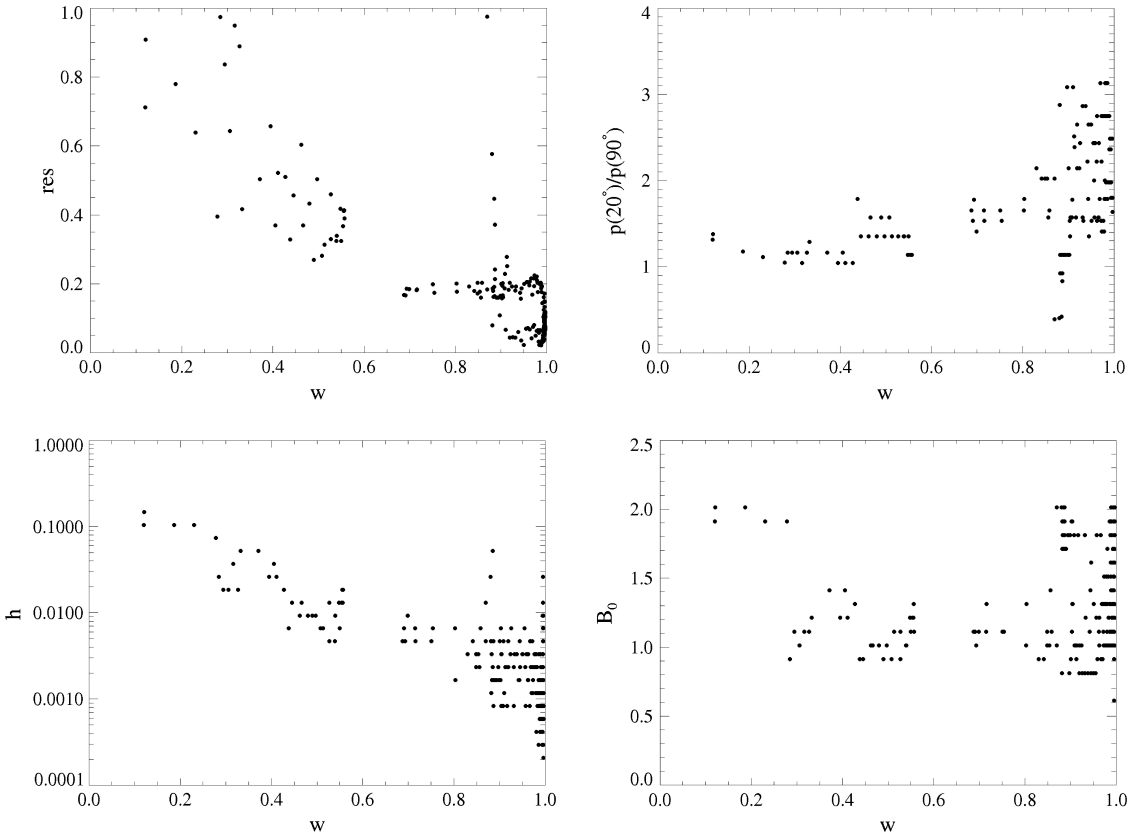

Figure 3.9: *Top left panel*: phase function fit residuals at each wavelength against the single-scattering albedo. *Top right panel*: single-particle phase function at 20 ° and 90 ° ratio for each wavelength against the single-scattering albedo. *Bottom left panel*: opposition effect width against the single-scattering albedo. *Bottom right panel*: opposition effect amplitude against the single-scattering albedo. Ciarniello et al. (2011a).

should decrease with increasing absorption and it is what we found, since the fitted values shows a positive correlation with w. Concerning the v values, they are negative for a large part but greater than -0.9 (average value is -0.5), again as expected for not perfectly spherical particles. In order to show any relation between single-particle phase function and single-scattering albedo is useful to investigate the final shape of $p(g)$. In fig. 3.9 (upper right panel), the ratio $p(20°)/p(90°)$ vs. w is shown. This choice aims to point out the trend of the single-particle phase function at intermediate phase angles, avoiding the phase angle regions where the contribution of the OE and large scale roughness become relevant. The $p(20°)/p(90°)$ ratio increases with single-scattering albedo meaning that reflectance increases at intermediate phase angles ($10° - 60°$) for more transparent particles. This behavior can be explained by the possibility for a light ray to undergo multiple internal reflections in a non-absorbing particle, producing an higher backscattering lobe respect to a darker particle, where surface reflection dominates and produces a quite flat single-particle phase function at phases $< 90°$ (Hapke, 1993, p. 77, figs. 5 and 7a). This result is better shown in fig. 3.10, where normalized full disk phase functions are plotted ordered according to increasing values of single-scattering albedo (listed along with their relative wavelengths).

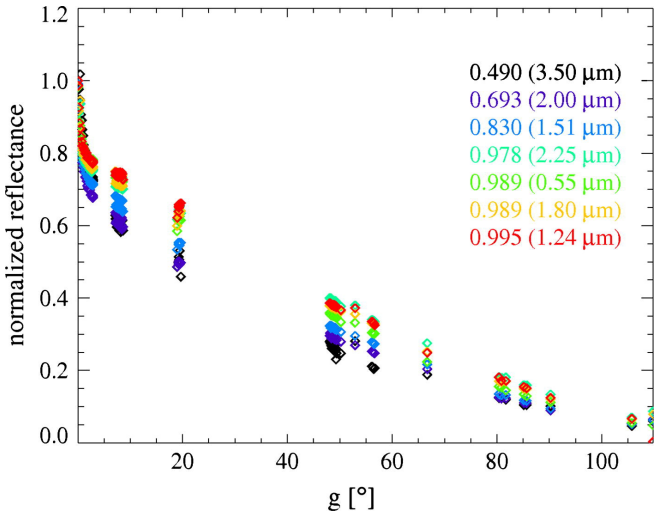

Figure 3.10: Rhea full-disk phase functions at wavelengths relative to increasing value of the single-scattering albedo. Single-scattering albedo values and corresponding wavelengths are indicated. Curves are normalized at minimum phase angle (0.08°). Ciarniello et al. (2011a).

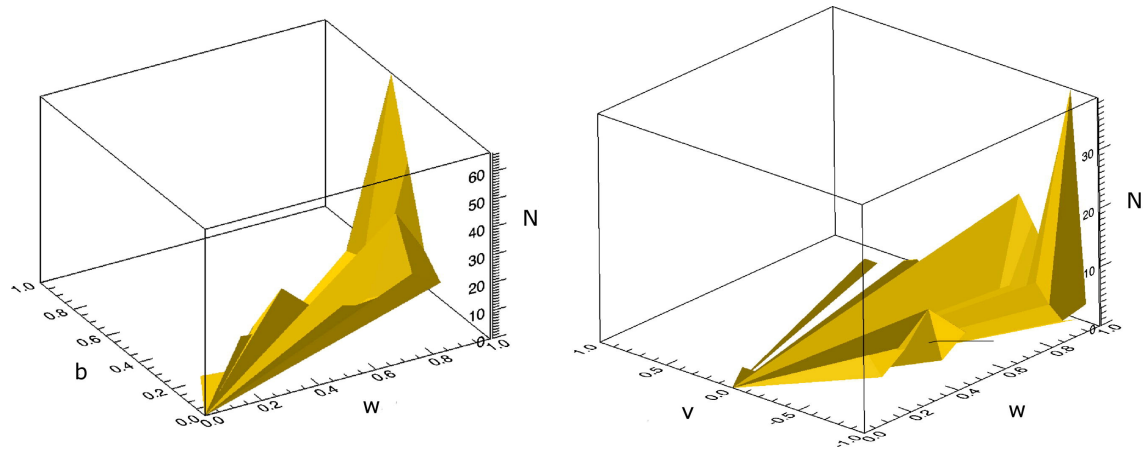

Figure 3.11: Distribution of fitted b (left panel) and v (right panel) values respect to the single scattering albedo. N represents how many times a certain value of the parameter is obtained in a given range of w values. The w range (0-1) is divided in intervals 0.1 wide. Ciarniello et al. (2011a).

3.4.3 Opposition effect

As anticipated in previous sections we choose to model the opposition effect following the results developed in Hapke (1993) which consider only shadow hiding (SHOE). This model depends on two parameters (B_0, h) which describes, respectively, the amplitude and angular width. Nonetheless, another mechanisms, coherent backscattering opposition effect (CBOE), has been recognized as contributing to the OE (Hapke et al., 1998; MacKintosh and Sajeev, 1988; Shkuratov et al., 1999a; Hapke, 2002). Given these reasons the interpretation of results concerning the OE is not trivial, because the two parameters (B_0, h) must describe the contributes of both SHOE and CBOE. The two effects have different characteristics that help us discern between them. The major difference is that angular width of SHOE does not depend on wavelength, while the CBOE does (MacKintosh and Sajeev, 1988; Hapke, 2002). The second one is that the SHOE width extends up to 10° or more while the CBOE is limited to a width of $2-3°$ at most (Hapke et al., 1998; Shkuratov et al., 1999a). Additionally we must consider that SHOE is a single-scattering effect while the CBOE develops in a multiple-scattering process. Therefore, we expect that the SHOE dominates for wavelengths corresponding to low values of w while the CBOE dominates at wavelengths where w values is close to 1.

Fig. 3.9 (bottom left panel) shows the plot h against w. The values of h spread over almost three orders of magnitude (0.0002-0.14) giving an OE half width $\Delta g \approx 2h$ ranging between 0.01° and 16°, and show a clear correlation with single-scattering albedo. At low values of w we have high h while the opposite is true when the albedo is low. This behavior reveals the presence of two competing mechanisms in the OE: the CBOE for wavelengths with high value of albedo and the SHOE for the opposite case. This fact agrees with the argument that the CBOE depends on multiple scattering and the SHOE on single scattering. Moreover, we would expect that the h values at low w would be nearly constants, since SH is independent of wavelength. What we see, in fact, is that spreading reduces considerably towards small values of w with h approaching 0.1.

In the SH regime a rough estimation of the porosity of water ice particles on the surface can be computed from the following relation (Hapke, 1993):

$$h \approx -\frac{3}{8}\ln(1-\phi) \tag{3.8}$$

where ϕ is the filling factor. The value of h we chose to use is 0.1, which is referred to low values of the single-scattering albedo, where single scattering dominate and the OE is due to SH. Moreover this value is almost constant with w, so it is independent of wavelength, which is what we expect for the SHOE. With this choice we obtain $\phi = 0.23$. However, considering that a real grain size distribution has a non-null dispersion and that the particle diameter we have measured is just an average value the filling factor can be higher. Assuming a grain size distribution of the form:

$$N(a) \propto a e^{-\frac{a}{am}} \tag{3.9}$$

we obtain $\phi = 0.35$. The derived porosity is then in the range $65 - 77\%$. These values are lower than those derived in a similar study by Domingue et al. (1995). It must be noted that in Domingue's work the analysis was performed at 0.47 and 0.55 μm, where the single-scattering albedo is close to 1 and the CBOE contribution is important, reducing h and increasing the estimated porosity. Regarding the amplitude of the opposition effect B_0 (fig. 3.9, bottom right panel) we do not find any particular trend with w, apart from the fact that values have a larger spreading for single-scattering albedo close to 1 tending to be higher respect to the rest of the spectrum. This could be an indication of the superimposition of the CB on SH, but a compensating effect

due to the unsatisfactory modeling of the single-particle phase function (backscattering region) cannot be excluded.

3.4.4 Large-scale surface roughness

The large-scale surface roughness is characterized by the $\bar{\theta}$ parameter which Hapke (1993) interprets an average slope of the surface structures. This is the only parameter that does not depend on wavelength in our fit procedure. To constrain it we performed fits of full-disk phase functions for each value of $\bar{\theta}$ in the range $10° - 35°$ and chose the one that produced the smallest residual. We found a final value of $\bar{\theta} = 33°$ (we must point out that all the values above 30° gave similar fits). The result obtained seems too high if related to common slopes of craters and other topographic structures, and exceeds the values found by Domingue et al. (1995), while is close to the one found by Buratti (1985) for Mimas. Recent experimental analysis performed by Shepard and Helfenstein (2007), has shown that the value of $\bar{\theta}$ is not only affected by subpixel topography but also, and mainly, by roughness on the scale of particles clumping which can produce fairly high slopes, related to the angle of repose of the regolith, and consistent with our determination.

Typically, in phase function fit procedures, the estimated values of single-scattering albedo and surface roughness show a certain degree of correlation, which of course has no physical meaning and reveals a degeneration in the inversion process. In our approach the evaluation of w comes from the spectral fit and it is completely independent on the determination of the roughness parameter, so the degree of degeneration of the regression is reduced making the result more reliable. However, it must be noted, as pointed out in Davidsson et al. (2009), that the treatment of surface roughness in Hapke's theory relies on the assumption of "small mean slope" ($\bar{\theta} < 10°$), which allows to obtain analytical solutions. The value we retrieved from the phase function analysis is far beyond this limit and must be considered with care. Another issue is represented by the fact that in Hapke's theory multiple scattering between the facets composing the surface is neglected which is not applicable for high albedo materials and rough surfaces. In particular, icy surfaces have high albedo and, as shown in Shepard and Helfenstein (2007), the sub-centimeters scale roughness implies fairly large slope angles (typically above 10°). This would limit the applicability of the roughness correction only to low albedo media, which is not the case of icy surface, unless the analysis is

restricted to wavelengths where strong absorption bands are located (e.g. 2.0 and 3.0 μm). In our analysis the derived $\bar{\theta}$ value produces good fits both for high and low reflectance values (e.g. 1 and 2 μm). This would imply that the effect of multiple scattering is less relevant than the "small mean slope" approximation.

3.5 Feedback on the spectral fit

The results of the phase function fits can be used to improve the spectral fit, which represented the starting point of our analysis. The spectral fit, as explained in sec. 3.3, was performed assuming an isotropic phase function and at phase angles large enough to avoid contributions from any OE. Now, for each phase angle it is possible to compute the absolute spectrum, removing the approximation of an isotropic single-particle phase function, including the OE and surface roughness. We have recalculated the spectrum at $g = 90°$, the one chosen to perform the starting spectral fit, and plotted it in fig. 3.12. The agreement between the fitted spectrum and the measured one is almost perfect throughout the VIS-NIR region. Similar fits have been performed for each spectrum (phase angle) of the dataset. As example the results relative to spectra at $g = 2.1°$ and $g = 49.4°$ are plotted in fig. 3.13. This high level of fit accuracy is possible because we deal with a large number of free parameters and this allows us to tune the reflectance at each wavelength. This represents also the limitation of this approach. In fact, any mismatches in the spectral fit due to grain size effects, as shown in sec 3.3.5 for the reflectances at 2.2 μm and 3.1 μm, or due to an incomplete knowledge of the ice optical constants, for instance, can be compensated by the contribution of the single-particle phase function. The spectral fit will be optimal but we shall be misled in the interpretation of the scattering mechanisms at work. On the other hand, the trends observed in figs. 3.9-3.11 between phase curve parameters and the single-scattering albedo points out some degree of physical correlation among those variables. For instance, it is not totally unexpected to find that brighter surfaces have a narrower width of the opposition effect than darker surfaces; the contribution of multiple scattering within the grains attenuates the shadow hiding effect limiting it to a narrow region around the zero phase condition. Also, for planetary surfaces, the slope of the linear part is larger for brighter surfaces and this is consistent with the results shown in figs. 3.9 and 3.10. In other words, we could use these correlations to give preliminary estimates of the phase curve parameters to be used in the determination

of the spectral fit; this approach can prove valuable also in case of incomplete or undersampled phase curves.

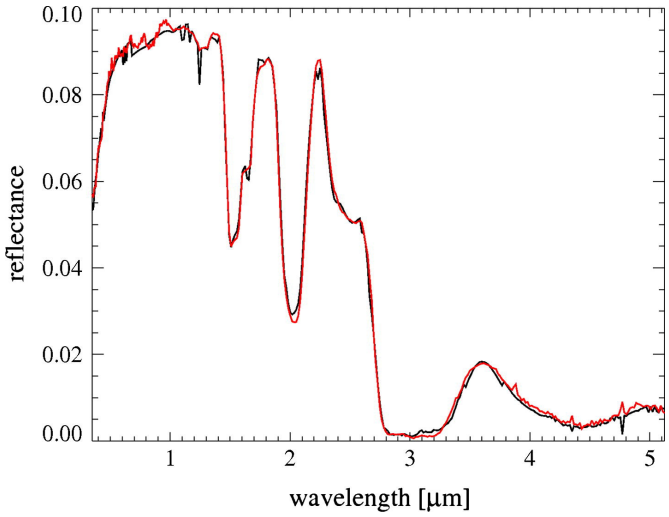

Figure 3.12: Final absolute spectral fit at $g = 90.2°$ ($p = 0.996$, $pc = 0.004$, $a_m = 38\ \mu m$, intraparticle mixture). Isotropic single-particle phase function approximation has been removed and the correction due to roughness has been introduced. Observed spectrum is red. Ciarniello et al. (2011a).

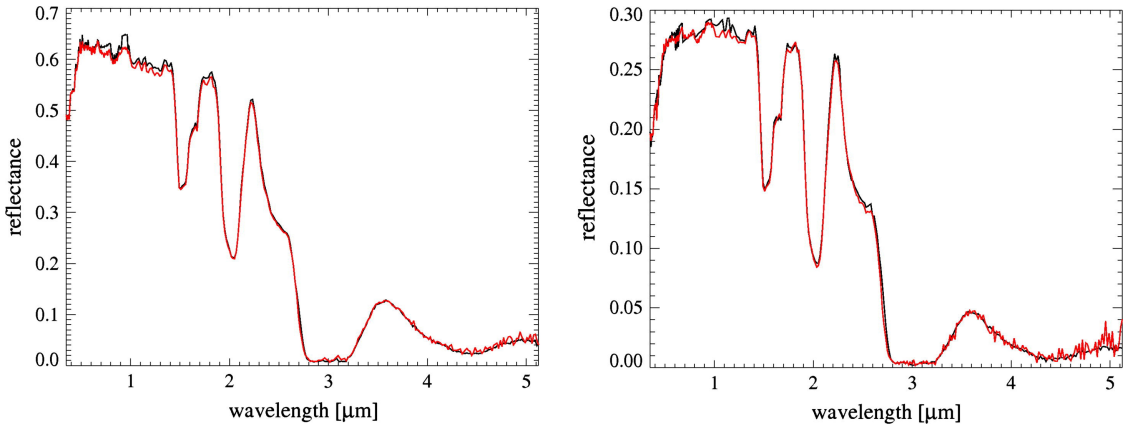

Figure 3.13: *Left panel*: final absolute spectral fit at $g = 2.1°$. *Right panel*: final absolute spectral fit at $g = 49.4°$. The two simulations are obtained with an intraparticle mixture ($p = 0.996$, $pc = 0.004$, $a_m = 38\ \mu m$). Isotropic single-particle phase function approximation has been removed and the correction due to roughness has been introduced. Observed spectrum is red. Ciarniello et al. (2011a).

Chapter 4

Hapke modeling of Enceladus and other satellites of the Saturn's system

In this section we investigate the spectrophotometric properties of Enceladus as seen by VIMS. Since we follow exactly the same approach we used for Rhea in chapter 3, here we show only the results of our analysis, referring to the Rhea's chapter for details on dataset reduction and modeling.
In sec. 4.5 we present preliminary spectral modeling of other satellites of the Saturnian system.

4.1 Enceladus

Enceladus (fig. 4.1) is the sixth largest moon of Saturn with a mean radius of 252.1 $\pm$ 0.2 km (Roatsch et al., 2009) and a mass $M = (1.08022 \pm 0.00101) \times 10^{20}$ kg (Jacobson et al., 2006) (the derived density is 1.609 $\pm$ 0.005 g/cm^3, Roatsch et al. (2009)). It orbits in the E ring which is formed by particles ejected during the plume activity on the South pole of the satellite itself (Porco et al., 2006; Spahn et al., 2006). Plumes activity, associated with internal heat production and low number of craters in the south region indicates that Enceladus is geologically active (Porco et al., 2006). Enceladus reflects almost entirely the sunlight (geometric bond albedo 0.93) and has an effective surface temperature of 46 K (Pitman et al., 2010).

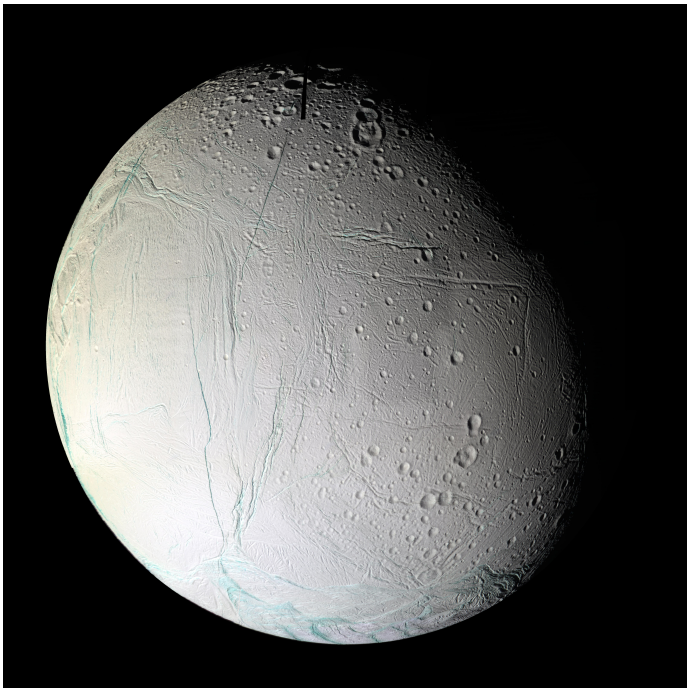

Figure 4.1: Enceladus. Image courtesy of NASA-CICLOPS-ISS team.

4.1.1 Dataset

The investigated dataset is composed by 290 full-disk images of Enceladus covering the $23° - 150°$ phase angle range. In fig. 4.2 spectra acquired at various phase angles are compared to the spectrum at minimum available phase angle (23.7°). Spectra exhibit typical features of water ice, with the absorption bands at 1.25, 1.5, 2.0, 3.0 and 4.5 μm. A peak is observed around 0.5 μm which does not correspond to features of water ice. In Clark and et al. (2011) it is addressed to Rayleigh scattering by nano-absorbers. A downturn of the spectrum is observed at short wavelength which could indicate the presence of organic (reddish) contaminants. In fig. 4.3 phase curve at various wavelength are plotted. The shape of the phase curve varies with wavelength and as it is shown in the next section it is related to the value of single-scattering albedo w.

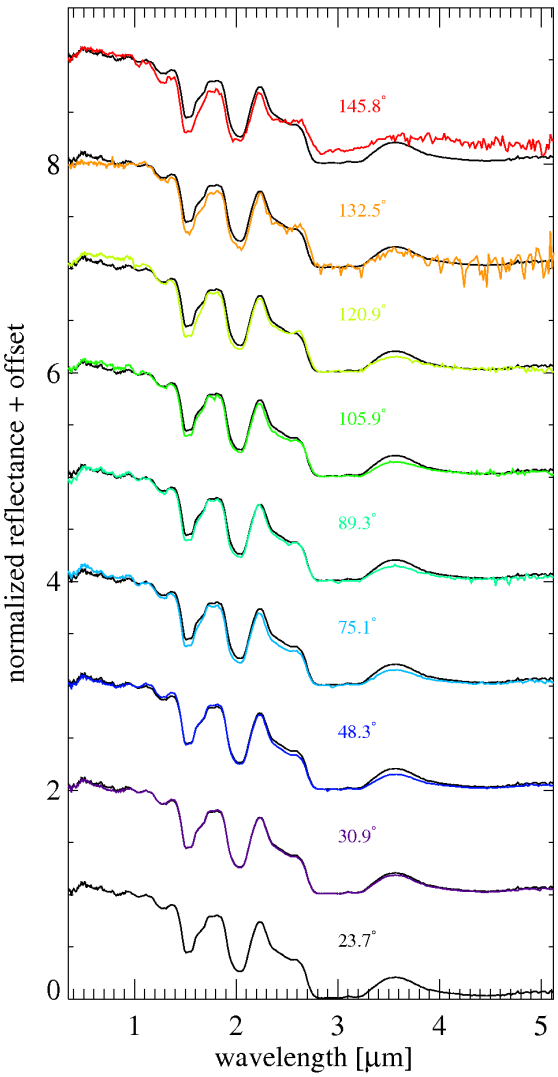

Figure 4.2: Enceladus' full-disk spectra acquired at different phase angles, normalized at 1 μm. An offset is added for clarity and the spectrum at 23.7° is overplotted on each one in order to evidence the variation with phase angle. Ciarniello et al. (2010a).

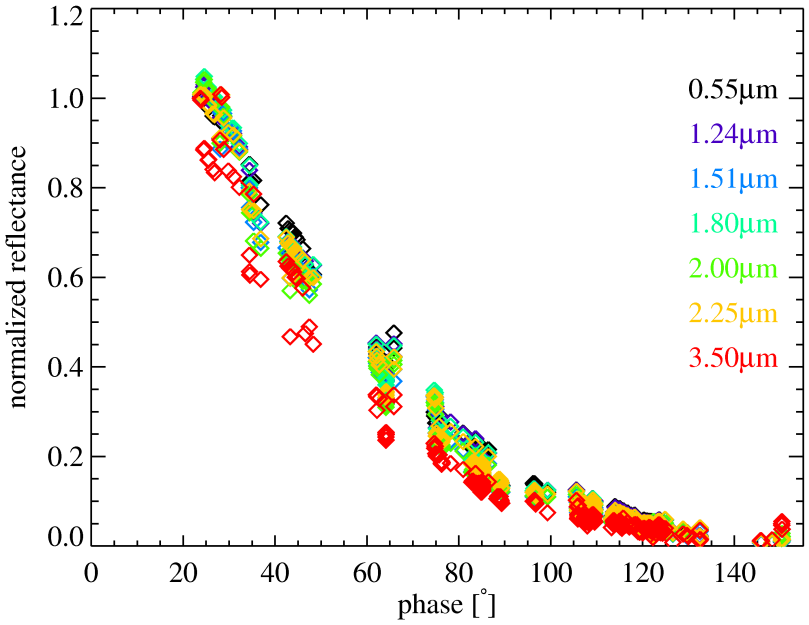

Figure 4.3: Enceladus' full-disk phase function at different wavelengths. Curves are normalized at minimum phase angle. Ciarniello et al. (2010a).

4.2 Spectral fit

In this section is described the method used to model Enceladus reflectance and a discussion about model parameters is given. Details on mixing modalities and end-members involved in the fit are in sec. 3.3, while the equations relative to radiative transfer model we used are in chapter 2, and in sec. 2.4.5.
The fit is performed applying to Enceladus the same paradigm adopetd for Rhea. We have analyzed normalized spectra (at 1 μm) in order to minimize the effect of single-particle phase function (assumed isotropic) and to eliminate the shadowing effect caused by surface roughness. Spectra at various phase angles have been fitted. The best matching is obtained at $g = 107°$ with an intraparticle mixture of water ice (99.992 %) and Triton tholin (0.008 %) with particle size of 63 μm (fig. 4.4).

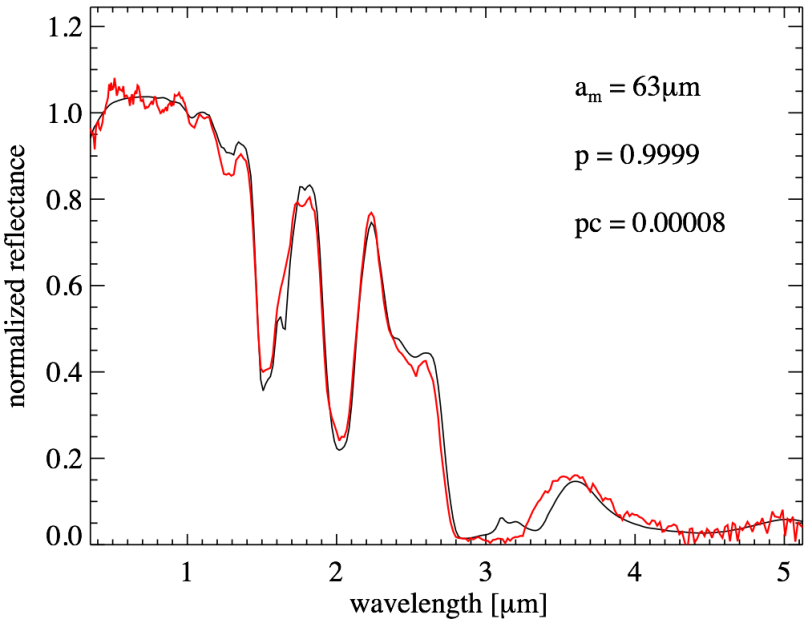

Figure 4.4: Best spectral fit. The model (black line) is an intraparticle mixture of water ice (99.992 %) and Triton tholin (0.008 %) with grain size $a_m = 63\mu m$. Ciarniello et al. (2010a).

4.3 Phase function fit

As for the Rhea case we performed a fit for the phase function (see sec. 3.4 for more details) of Enceladus for each VIMS spectral channel (337) (see fig. 4.5 and 4.6 for examples). Results are summarized in table 4.3

Table 4.1: Full-disk phase function best fits.

Band	$\lambda(\mu m)$	w	v	b	θ	res
0	0.35054	0.996	1.1	0.4	29	0.125
1	0.35895	0.996	0.5	0.5	29	0.126
2	0.36629	0.997	0.5	0.5	29	0.124
3	0.37322	0.997	0.4	0.5	29	0.120
4	0.37949	0.997	0.3	0.5	29	0.130
5	0.38790	0.998	0.4	0.5	29	0.121
6	0.39518	0.998	0.4	0.5	29	0.120
7	0.40252	0.998	0.4	0.5	29	0.121
8	0.40955	0.998	0.4	0.5	29	0.113
9	0.41731	0.998	0.3	0.5	29	0.112
10	0.42436	0.999	0.3	0.5	29	0.111
11	0.43184	0.999	0.3	0.5	29	0.117
12	0.43919	0.999	0.4	0.5	29	0.115
13	0.44652	0.999	0.4	0.5	29	0.111
14	0.45372	0.999	0.4	0.5	29	0.113
15	0.46163	0.999	0.4	0.5	29	0.114
16	0.46841	0.999	0.4	0.5	29	0.117
17	0.47622	0.999	0.9	0.4	29	0.118
18	0.48629	0.999	0.5	0.5	29	0.115
19	0.48967	0.999	0.9	0.4	29	0.115
20	0.49777	0.999	0.4	0.5	29	0.114
21	0.50628	1.000	0.5	0.5	29	0.114
22	0.51222	1.000	0.9	0.4	29	0.119
23	0.51963	1.000	0.8	0.4	29	0.116
24	0.52766	1.000	0.4	0.5	29	0.111
25	0.53416	1.000	0.4	0.5	29	0.108
26	0.54156	1.000	0.4	0.5	29	0.112
27	0.54954	1.000	0.4	0.5	29	0.111
28	0.55614	1.000	0.4	0.5	29	0.111
29	0.56353	1.000	0.3	0.5	29	0.110
30	0.57131	1.000	0.4	0.5	29	0.114
31	0.57810	1.000	0.3	0.5	29	0.112
32	0.58548	1.000	0.3	0.5	29	0.115
33	0.59312	1.000	0.3	0.5	29	0.117
34	0.59938	1.000	0.2	0.5	29	0.121
35	0.60757	1.000	0.2	0.5	29	0.114
36	0.61505	1.000	0.3	0.5	29	0.115
37	0.62207	1.000	0.2	0.5	29	0.113
38	0.62940	1.000	0.3	0.5	29	0.115
39	0.63704	1.000	0.2	0.5	29	0.116
40	0.64408	1.000	0.2	0.5	29	0.115
41	0.65142	1.000	0.2	0.5	29	0.117
42	0.65910	1.000	0.2	0.5	29	0.119
43	0.66609	1.000	0.3	0.5	29	0.120
44	0.67342	1.000	0.3	0.5	29	0.121
45	0.68102	1.000	0.2	0.5	29	0.122
46	0.68803	1.000	0.1	0.5	29	0.123
47	0.69535	1.000	0.1	0.5	29	0.121

Table 4.3 (continued)

Band	$\lambda(\mu m)$	w	v	b	$\bar{\theta}$	res
48	0.70288	1.000	0.1	0.5	29	0.123
49	0.71000	1.000	0.1	0.5	29	0.123
50	0.71733	1.000	0.1	0.5	29	0.123
51	0.72484	1.000	0.1	0.5	29	0.121
52	0.73198	1.000	0.1	0.5	29	0.129
53	0.73930	1.000	0.1	0.5	29	0.127
54	0.74676	1.000	0.1	0.5	29	0.129
55	0.75396	1.000	0.1	0.5	29	0.130
56	0.76128	1.000	0.1	0.5	29	0.129
57	0.76874	1.000	0.1	0.5	29	0.135
58	0.77595	1.000	0.1	0.5	29	0.130
59	0.78328	1.000	0.1	0.5	29	0.126
60	0.79072	1.000	0.1	0.5	29	0.135
61	0.79793	1.000	0.0	0.5	29	0.137
62	0.80522	1.000	-0.1	0.6	29	0.135
63	0.81262	1.000	-0.1	0.6	29	0.133
64	0.81989	1.000	-0.1	0.6	29	0.137
65	0.82721	1.000	-0.1	0.6	29	0.136
66	0.83463	1.000	-0.1	0.6	29	0.134
67	0.84190	1.000	-0.1	0.6	29	0.133
68	0.84922	1.000	-0.1	0.6	29	0.132
69	0.85663	1.000	-0.1	0.6	29	0.135
70	0.86391	1.000	-0.1	0.6	29	0.131
71	0.87122	1.000	0.1	0.5	29	0.137
72	0.87863	1.000	0.1	0.5	29	0.130
73	0.88589	1.000	0.1	0.5	29	0.122
74	0.89386	1.000	0.1	0.5	29	0.129
75	0.90032	1.000	0.1	0.5	29	0.125
76	0.90787	1.000	0.1	0.5	29	0.129
77	0.91518	1.000	0.2	0.5	29	0.126
78	0.92254	1.000	0.2	0.5	29	0.127
79	0.92983	1.000	0.1	0.5	29	0.129
80	0.93713	0.999	0.2	0.5	29	0.129
81	0.94445	0.999	0.2	0.5	29	0.128
82	0.95177	0.999	0.2	0.5	29	0.126
83	0.95907	0.999	0.2	0.5	29	0.126
84	0.96638	0.999	0.2	0.5	29	0.122
85	0.97382	0.999	0.2	0.5	29	0.125
86	0.98100	0.999	0.2	0.5	29	0.126
87	0.98226	0.999	0.2	0.5	29	0.125
88	0.99882	0.999	0.1	0.5	29	0.130
89	1.01479	0.998	0.0	0.6	29	0.137
90	1.03132	0.998	0.0	0.6	29	0.134
91	1.04755	0.998	0.0	0.6	29	0.136
92	1.06541	0.999	0.0	0.6	29	0.132
93	1.08183	0.999	0.1	0.5	29	0.131
94	1.09806	0.999	0.0	0.6	29	0.138
95	1.11396	0.999	0.0	0.6	29	0.138
96	1.13024	0.999	0.0	0.6	29	0.130

Table 4.3 (continued)

Band	$\lambda(\mu m)$	w	v	b	$\bar{\theta}$	res
97	1.14695	0.999	0.0	0.6	29	0.130
98	1.16370	0.998	0.2	0.5	29	0.136
99	1.17996	0.997	0.2	0.5	29	0.136
100	1.19622	0.996	0.0	0.6	29	0.137
101	1.21246	0.995	0.0	0.6	29	0.133
102	1.22859	0.994	0.0	0.6	29	0.134
103	1.24492	0.994	-0.1	0.6	29	0.147
104	1.26166	0.993	-0.1	0.6	29	0.140
105	1.27813	0.993	-0.1	0.6	29	0.141
106	1.29482	0.993	0.0	0.6	29	0.145
107	1.31091	0.992	0.0	0.6	29	0.141
108	1.32695	0.994	0.0	0.6	29	0.137
109	1.34324	0.995	0.0	0.6	29	0.138
110	1.35952	0.995	0.0	0.6	29	0.137
111	1.37695	0.994	0.0	0.6	29	0.142
112	1.39326	0.994	0.0	0.6	29	0.145
113	1.40940	0.991	0.0	0.6	29	0.150
114	1.42557	0.987	0.0	0.6	29	0.149
115	1.44184	0.970	0.2	0.5	29	0.145
116	1.45841	0.930	0.4	0.5	29	0.150
117	1.47514	0.857	0.8	0.4	29	0.169
118	1.49169	0.768	0.9	0.4	29	0.183
119	1.50794	0.741	0.9	0.4	29	0.197
120	1.52421	0.757	0.9	0.4	29	0.172
121	1.54035	0.768	0.8	0.4	29	0.160
122	1.55674	0.774	0.8	0.4	29	0.145
123	1.57361	0.798	0.8	0.4	29	0.136
124	1.59018	0.843	0.9	0.4	29	0.137
125	1.60228	0.872	0.9	0.4	29	0.131
126	1.62523	0.880	1.1	0.4	29	0.168
127	1.64160	0.864	1.2	0.4	29	0.287
128	1.65567	0.862	1.2	0.4	29	0.408
129	1.67238	0.907	1.1	0.4	29	0.180
130	1.68901	0.939	0.7	0.4	29	0.136
131	1.70536	0.957	0.7	0.4	29	0.123
132	1.72175	0.968	0.7	0.4	29	0.129
133	1.73802	0.977	0.2	0.5	29	0.122
134	1.75436	0.983	0.0	0.6	29	0.145
135	1.77105	0.983	0.0	0.6	29	0.145
136	1.78771	0.982	0.0	0.6	29	0.142
137	1.80401	0.983	0.0	0.6	29	0.142
138	1.82004	0.984	0.0	0.6	29	0.142
139	1.83616	0.983	0.0	0.6	29	0.151
140	1.85288	0.980	0.0	0.6	29	0.150
141	1.86933	0.972	0.0	0.6	29	0.155
142	1.88679	0.949	0.2	0.5	29	0.141
143	1.90261	0.910	0.2	0.5	29	0.145
144	1.91916	0.849	0.2	0.5	29	0.155
145	1.93545	0.777	0.5	0.4	29	0.177

Table 4.3 (continued)

Band	$\lambda(\mu m)$	w	v	b	$\bar{\theta}$	res
146	1.95191	0.704	0.6	0.4	29	0.145
147	1.96871	0.638	0.7	0.4	29	0.182
148	1.98531	0.588	1.2	0.3	29	0.196
149	2.00167	0.560	1.2	0.3	29	0.219
150	2.01781	0.554	1.2	0.3	29	0.198
151	2.03424	0.558	1.1	0.3	29	0.191
152	2.05091	0.568	1.1	0.3	29	0.187
153	2.06757	0.589	1.1	0.3	29	0.173
154	2.08400	0.633	1.1	0.3	29	0.155
155	2.10034	0.703	1.1	0.3	29	0.150
156	2.11667	0.781	0.6	0.4	29	0.130
157	2.13337	0.847	0.5	0.4	29	0.119
158	2.15018	0.892	0.5	0.4	29	0.133
159	2.16652	0.921	0.2	0.5	29	0.132
160	2.18288	0.940	0.2	0.5	29	0.131
161	2.19920	0.954	0.2	0.5	29	0.136
162	2.21591	0.963	0.2	0.5	29	0.137
163	2.23282	0.966	0.2	0.5	29	0.147
164	2.24952	0.964	0.2	0.5	29	0.155
165	2.26622	0.957	0.2	0.5	29	0.164
166	2.28238	0.945	0.1	0.5	29	0.179
167	2.29921	0.930	0.1	0.5	29	0.174
168	2.31612	0.912	0.0	0.5	29	0.197
169	2.33325	0.890	0.0	0.5	29	0.174
170	2.35043	0.868	0.1	0.5	29	0.163
171	2.36765	0.854	0.1	0.5	29	0.159
172	2.38472	0.848	0.1	0.5	29	0.163
173	2.40156	0.847	0.0	0.5	29	0.160
174	2.41820	0.846	0.0	0.5	29	0.184
175	2.43471	0.840	-0.1	0.5	29	0.189
176	2.45097	0.833	-0.1	0.5	29	0.190
177	2.46723	0.827	-0.1	0.5	29	0.184
178	2.48360	0.821	-0.1	0.5	29	0.185
179	2.50002	0.817	-0.1	0.5	29	0.189
180	2.51659	0.815	-0.1	0.5	29	0.210
181	2.53292	0.814	-0.2	0.5	29	0.214
182	2.54916	0.816	-0.2	0.5	29	0.212
183	2.56437	0.819	-0.2	0.5	29	0.218
184	2.58176	0.822	-0.2	0.5	29	0.234
185	2.59807	0.822	-0.2	0.5	29	0.239
186	2.61508	0.822	-0.4	0.6	29	0.246
187	2.63000	0.820	-0.4	0.6	29	0.263
188	2.64650	0.812	-0.5	0.6	29	0.286
189	2.66146	0.796	-0.5	0.7	29	0.348
190	2.68085	0.754	-0.6	0.7	29	0.341
191	2.69620	0.703	-0.7	0.7	29	0.444
192	2.71205	0.628	-0.7	0.8	29	0.437
193	2.73270	0.500	-0.8	0.7	29	0.576
194	2.74770	0.400	-0.8	0.8	29	0.664

Table 4.3 (continued)

Band	$\lambda(\mu m)$	w	v	b	$\bar{\theta}$	res
195	2.76305	0.303	-0.8	0.8	29	0.819
196	2.78118	0.193	-0.8	0.7	29	1.074
197	2.79889	0.111	-0.7	0.6	29	1.526
198	2.81606	0.068	-0.5	0.5	29	1.519
199	2.83247	0.053	-0.4	0.5	29	1.975
200	2.84954	0.051	-0.4	0.5	29	1.960
201	2.86609	0.051	-0.4	0.5	29	2.289
202	2.88242	0.053	-0.3	0.5	29	1.548
203	2.89878	0.055	-0.2	0.4	29	1.218
204	2.91540	0.058	-0.2	0.4	29	1.307
205	2.93143	0.063	-0.1	0.4	29	1.236
206	2.94726	0.068	-0.2	0.4	29	1.512
207	2.96327	0.072	-0.5	0.5	29	1.568
208	2.97720	0.076	-0.6	0.6	29	1.914
209	3.00072	0.080	-0.7	0.7	29	2.859
210	3.01382	0.083	-0.7	0.7	29	2.958
211	3.02970	0.091	-0.7	0.6	29	1.955
212	3.04806	0.104	-0.7	0.7	29	1.910
213	3.06446	0.124	-0.7	0.7	29	1.510
214	3.08036	0.159	-0.7	0.7	29	1.356
215	3.09689	0.199	-0.7	0.7	29	1.955
216	3.11213	0.201	-0.7	0.8	29	1.426
217	3.12962	0.181	-0.7	0.8	29	2.084
218	3.14667	0.168	-0.8	0.7	29	2.131
219	3.16304	0.166	-0.7	0.8	29	1.743
220	3.17974	0.171	-0.8	0.8	29	2.043
221	3.19708	0.176	-0.7	0.8	29	2.117
222	3.21364	0.173	-0.7	0.7	29	1.511
223	3.23150	0.161	-0.6	0.6	29	1.359
224	3.24806	0.148	-0.4	0.5	29	0.586
225	3.26561	0.135	0.2	0.4	29	0.394
226	3.28298	0.125	1.4	0.3	29	0.522
227	3.29946	0.119	1.2	0.4	29	1.255
228	3.31619	0.113	1.1	0.5	29	2.253
229	3.33338	0.112	1.0	0.6	29	3.164
230	3.34981	0.116	1.0	0.6	29	3.721
231	3.36564	0.130	1.0	0.6	29	3.707
232	3.38183	0.152	1.0	0.6	29	3.100
233	3.39872	0.181	1.0	0.6	29	2.493
234	3.41546	0.220	1.1	0.5	29	1.580
235	3.43178	0.249	1.1	0.5	29	1.276
236	3.44874	0.276	1.1	0.5	29	1.101
237	3.46475	0.304	1.2	0.4	29	0.806
238	3.48137	0.328	1.2	0.4	29	0.584
239	3.49795	0.350	1.2	0.4	29	0.464
240	3.51284	0.366	1.1	0.4	29	0.439
241	3.53015	0.386	1.4	0.3	29	0.352
242	3.54664	0.398	1.4	0.3	29	0.279
243	3.56274	0.407	1.4	0.3	29	0.281

Table 4.3 (continued)

Band	$\lambda(\mu m)$	w	v	b	$\bar{\theta}$	res
244	3.58034	0.413	1.4	0.3	29	0.278
245	3.59610	0.414	1.2	0.3	29	0.265
246	3.61387	0.414	1.2	0.3	29	0.259
247	3.63085	0.410	1.2	0.3	29	0.264
248	3.64853	0.404	1.2	0.3	29	0.280
249	3.66522	0.395	1.2	0.3	29	0.321
250	3.68283	0.382	1.1	0.3	29	0.283
251	3.69953	0.369	1.2	0.3	29	0.287
252	3.71743	0.353	1.2	0.3	29	0.307
253	3.73439	0.336	1.2	0.3	29	0.314
254	3.75103	0.320	1.2	0.3	29	0.368
255	3.76763	0.304	1.2	0.3	29	0.373
256	3.78444	0.288	1.2	0.3	29	0.345
257	3.80083	0.273	1.2	0.3	29	0.369
258	3.81742	0.259	1.2	0.3	29	0.368
259	3.83472	0.246	1.2	0.3	29	0.434
260	3.85141	0.233	1.2	0.3	29	0.423
261	3.86184	0.226	1.1	0.3	29	0.418
262	3.88167	0.213	1.0	0.3	29	0.471
263	3.89859	0.204	1.2	0.3	29	0.504
264	3.91478	0.196	1.2	0.3	29	0.459
265	3.93069	0.188	1.1	0.3	29	0.464
266	3.94762	0.180	1.1	0.3	29	0.589
267	3.96375	0.173	1.2	0.3	29	0.500
268	3.98015	0.166	1.2	0.3	29	0.559
269	3.99672	0.160	1.2	0.3	29	0.643
270	4.01280	0.155	1.2	0.3	29	0.587
271	4.02944	0.149	1.1	0.3	29	0.783
272	4.04730	0.143	1.2	0.3	29	0.619
273	4.06295	0.138	1.2	0.3	29	0.682
274	4.08086	0.133	1.2	0.3	29	0.652
275	4.09743	0.130	1.2	0.3	29	0.610
276	4.11450	0.128	1.1	0.3	29	0.864
277	4.13183	0.125	1.0	0.3	29	0.727
278	4.14883	0.123	1.0	0.3	29	0.904
279	4.16644	0.120	1.0	0.3	29	0.819
280	4.18299	0.117	1.0	0.3	29	0.729
281	4.19839	0.114	1.0	0.3	29	0.694
282	4.21120	0.112	0.8	0.3	29	0.839
283	4.22402	0.109	0.8	0.3	29	0.849
284	4.24220	0.107	0.7	0.3	29	1.103
285	4.26028	0.106	0.7	0.3	29	1.609
286	4.27840	0.105	0.5	0.3	29	1.470
287	4.29650	0.104	0.7	0.3	29	0.874
288	4.31470	0.102	0.2	0.4	29	1.020
289	4.33280	0.100	0.5	0.3	29	1.134
290	4.35094	0.098	0.1	0.4	29	1.903
291	4.36646	0.096	0.5	0.3	29	1.200
292	4.38295	0.095	0.2	0.4	29	1.403

Table 4.3 (continued)

Band	$\lambda(\mu m)$	w	v	b	$\bar{\theta}$	res
293	4.39793	0.094	0.1	0.4	29	1.820
294	4.41537	0.093	0.0	0.4	29	2.827
295	4.43172	0.093	0.5	0.3	29	0.982
296	4.44772	0.093	0.5	0.3	29	1.056
297	4.46573	0.093	0.1	0.4	29	1.915
298	4.48240	0.094	0.5	0.3	29	1.394
299	4.49951	0.095	0.5	0.3	29	0.955
300	4.51591	0.095	0.1	0.4	29	1.509
301	4.53379	0.097	0.5	0.3	29	2.349
302	4.55187	0.099	0.2	0.4	29	0.860
303	4.56797	0.101	0.2	0.4	29	2.599
304	4.58556	0.102	0.1	0.4	29	1.916
305	4.60290	0.104	0.4	0.4	29	0.958
306	4.62010	0.108	0.7	0.3	29	0.972
307	4.63615	0.111	0.8	0.3	29	0.632
308	4.65416	0.115	0.8	0.3	29	0.624
309	4.67034	0.118	0.7	0.3	29	1.758
310	4.68721	0.121	0.7	0.3	29	1.050
311	4.70290	0.124	0.8	0.3	29	0.809
312	4.71956	0.128	0.8	0.3	29	1.039
313	4.73706	0.133	0.4	0.4	29	3.669
314	4.75351	0.138	0.8	0.3	29	0.699
315	4.77031	0.142	0.6	0.4	29	1.076
316	4.78673	0.146	0.8	0.3	29	0.668
317	4.80349	0.150	0.8	0.3	29	0.768
318	4.81952	0.154	0.7	0.3	29	0.983
319	4.83577	0.158	0.8	0.3	29	1.112
320	4.85292	0.163	0.8	0.3	29	0.734
321	4.86940	0.167	0.7	0.3	29	0.958
322	4.88553	0.171	0.7	0.3	29	0.724
323	4.90265	0.175	0.7	0.3	29	0.749
324	4.91983	0.179	0.5	0.3	29	0.916
325	4.93685	0.182	0.4	0.4	29	0.609
326	4.95389	0.186	0.5	0.3	29	0.890
327	4.97178	0.188	0.7	0.3	29	0.672
328	4.98896	0.189	0.2	0.4	29	0.628
329	5.00576	0.191	0.2	0.4	29	0.690
330	5.02240	0.191	0.2	0.4	29	1.023
331	5.04078	0.190	0.2	0.4	29	0.689
332	5.05734	0.189	0.1	0.4	29	1.030
333	5.07402	0.187	0.2	0.4	29	0.806
334	5.09106	0.184	0.0	0.4	29	3.421
335	5.10680	0.180	0.1	0.4	29	1.098
336	5.12250	0.178	0.1	0.4	29	0.986

Notes: The total numbers of bands is 337 instead of 352 because of the overlapping between VIS and IR channels in the NIR region.

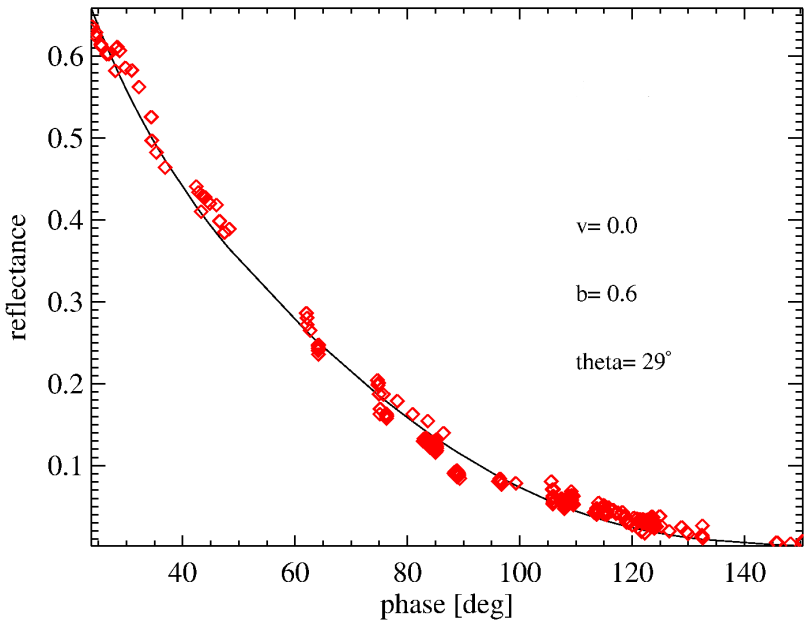

Figure 4.5: Phase function fit at 1 μm. Ciarniello et al. (2010a).

This approach enable us to point out trend of photometric parameters with wavelength. Single particle phase function properties and surface roughness (craters, reliefs, depressions etc.) can be investigated. Since in the spectral model the grain size is larger than the wavelength we expect that photometric parameters show a certain correlation with single scattering albedo, which dominates the spectral signatures. Since our data stop at $g = 23.7°$ we did not include opposition effect in our analysis.

4.3.1 Residuals

Since the Enceladus dataset seems to be noisier than the one of Rhea (in particular for high phase observations, like the ones at $g = 132.5°$ and $145.8°$ shown in fig. 4.2)we preferred to compute absolute residuals (err) in the phase function fit, in order to give

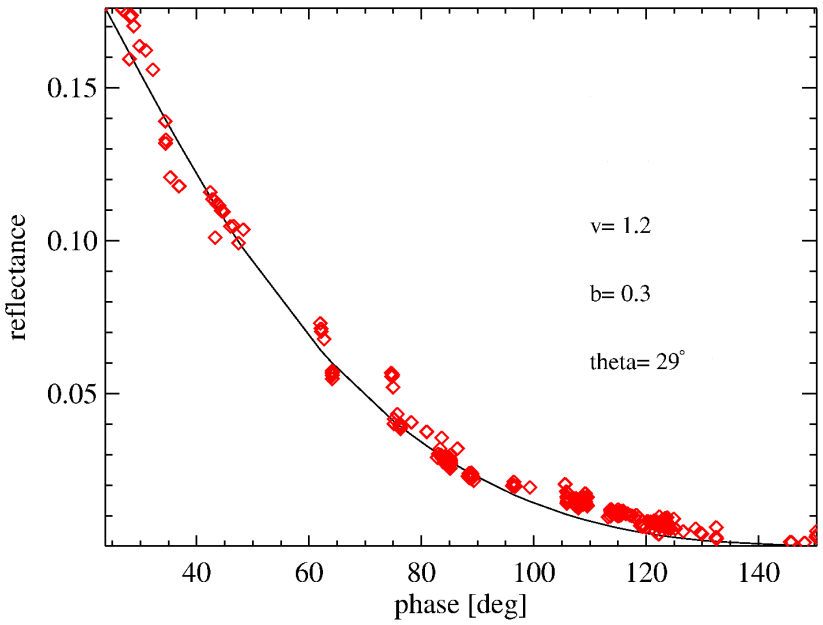

Figure 4.6: Phase function fit at 2 μm. Ciarniello et al. (2010a).

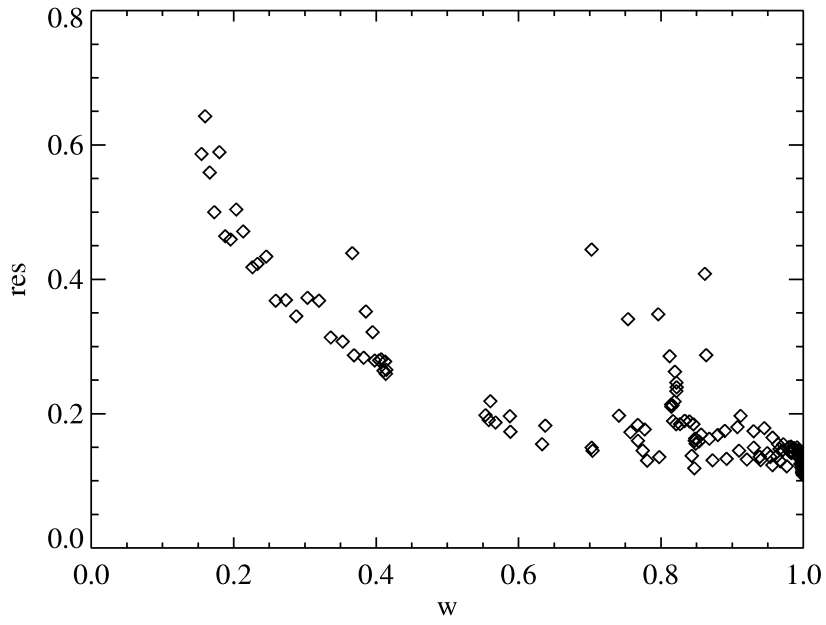

Figure 4.7: Residual vs. w. Ciarniello et al. (2010a).

a larger weight to observations with stronger signal. The equation we used is then:

$$err = \sum_i (r_i^m - r_i^c)^2 \tag{4.1}$$

where r_i^m is the measured absolute reflectance at i^{th} phase angle and r_i^c is the value computed by the fit procedure. In the region with very low signal (e.g the 3 μm band region and beyond $4\mu m$) the phase function is not well recognizable because signal to noise ratio (S/N) is particularly low and then the corresponding fit has no physical meaning. In those cases the derived parameters are not included in the following analysis.
In order to compare absolute residuals relative to different wavelengths we defined a quantity named res which is given by err divided the square of the maximum value of the reflectance at that wavelength (typically the maximum value is at $g = 23.7°$.) In this way res represents a sort of normalized residual, and later we will refer to that quantity with the word "residuals".

In fig. 4.7 phase function fit residuals (for each band) are plotted against the correspondent single scattering albedo w. The two quantities are anti-correlated. This can be due, as for the Rhea's case to:

- lower S/N for wavelength corresponding to low w leading to noisy phase function and poorer fit accuracy;
- unsatisfactory modeling of single particle phase function, whose contribution dominate for wavelengths corresponding to low w (single scattering regime).

4.3.2 Single particle phase function

In fig. 4.8 and 4.9 the b and v parameters are plotted against w. The plots show that for low w single particle phase function is back-scattering ($v < 0$) with wider lobes while for high w light transmitted through the particles increases the forward-scattering amplitude. The global effect of v and b makes $p(g)$ larger at intermediate phase angles for larger values of w. It can be seen in fig. 4.10 where the ratio $p(20°)/p(90°)$ is plotted. This behavior is shown in the observations, where full-disk phase functions

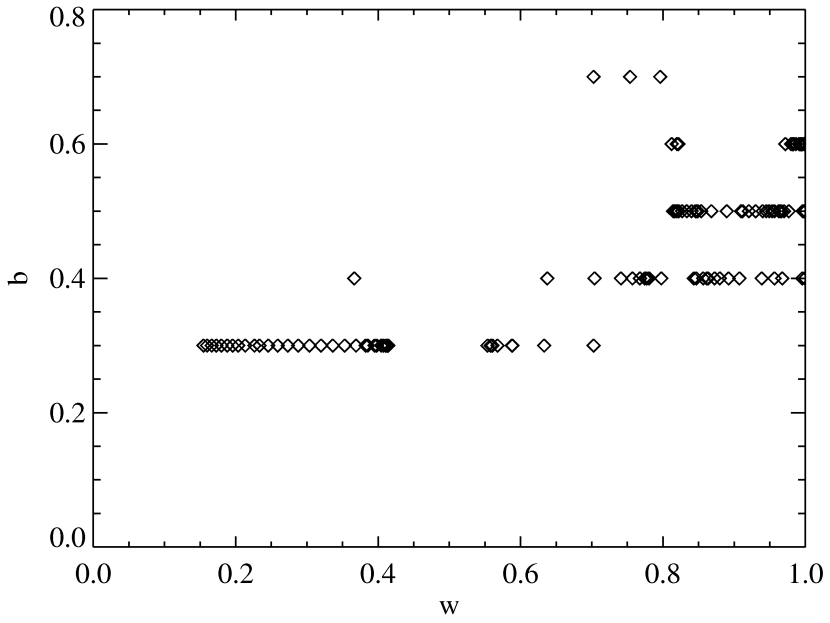

Figure 4.8: b vs. w. Ciarniello et al. (2010a).

corresponding to large values of w have larger relative reflectances in $30° - 110°$ range (4.11).

4.3.3 Large scale roughness

The best fit gives $\bar{\theta} = 29°$. This angle represents an average slope of the structures on the surface and doesn't depend on wavelength. The value is fairly high to be related to craters or reliefs, so we guess it is related to smaller scales, as the one of particles clumping (see sec.3.4.4). This result suggests that Enceladus surface is particularly porous.

4.3.4 Diffraction by small particles

Phase function at longer wavelengths show an increasing in reflectance around $g = 150°$ that can be addressed to diffraction by small particles (fig. 4.3). The angular width

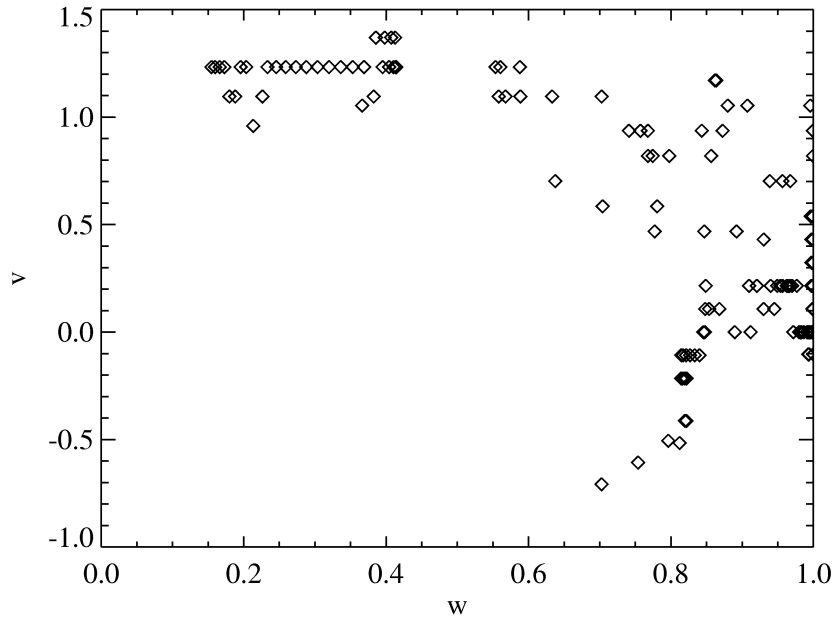

Figure 4.9: v vs. w. Ciarniello et al. (2010a).

of the diffraction pattern increases with wavelength moving the effect towards smaller phases. Given the phase angle at which the increasing of reflectance is observed and the wavelength, it is possible to estimate the size of the diffractors. In fact from the formula:

$$\sin\theta \approx 1.22\frac{\lambda}{d}, \tag{4.2}$$

which gives the angular width of the diffraction pattern (first minimum) θ as function of wavelength λ and grain size d, it is possible to infer the diameter of diffractors. For example at 2 μm the increase of reflectance reflectance is at $g \approx 150°$ which corresponds to $\theta \approx 30°$. The derived d is 5 μm, which is of the order of the size of the particles ejected by South pole plumes (Kempf et al., 2008).

4.4 Feedback on spectral fit

Values of photometric parameters for each band can be used to improve the spectral fit, removing the assumption of isotropic single particle-phase function and enabling us to

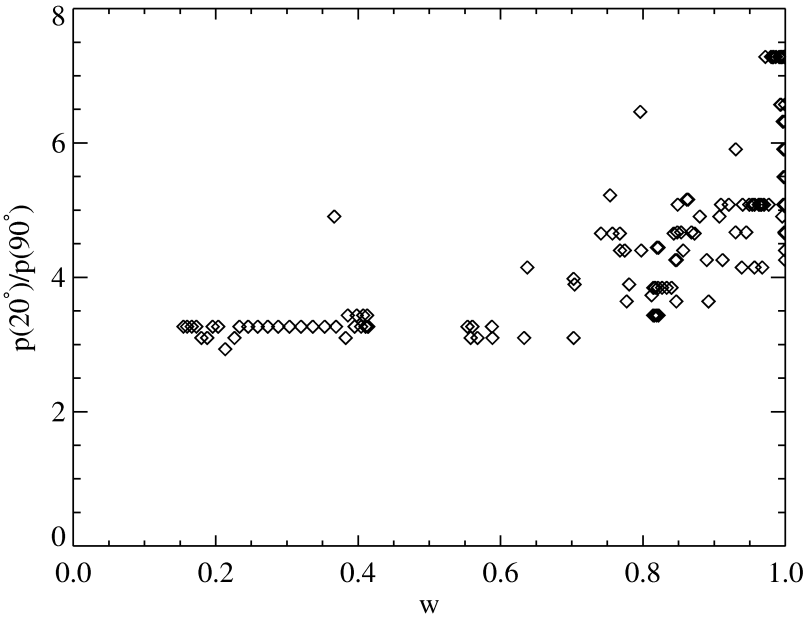

Figure 4.10: Computed single-particle phase function ratio $p(20°)/p(90°)$ vs. w. Ciarniello et al. (2010a).

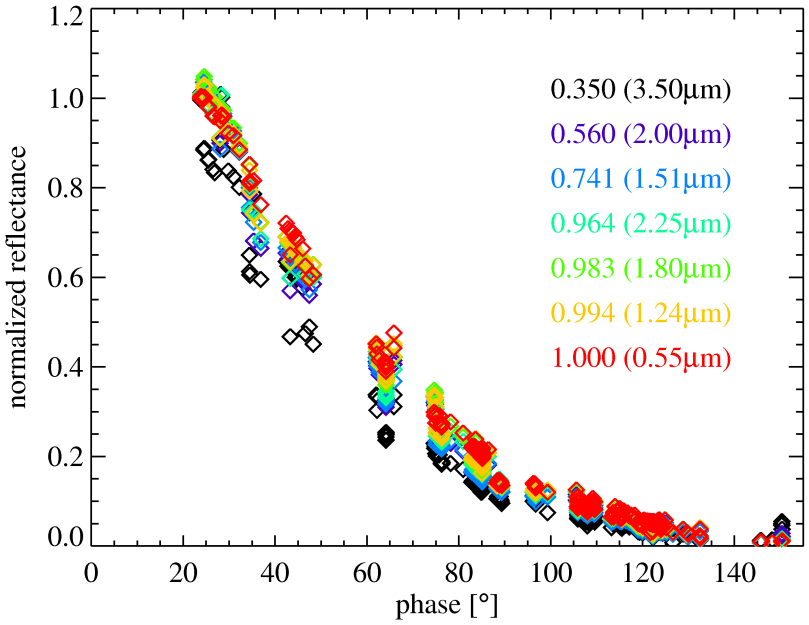

Figure 4.11: Phase functions for different single-scattering albedo w values. Curves are normalized at minimum phase angle value. Ciarniello et al. (2010a).

deal with absolute spectra. In fig. 4.12, for example, Enceladus spectrum at $g = 25.4°$ is plotted. The fit is very good on the entire wavelength range. This is possible because the photometric parameters tune the reflectance at each wavelength. However this represents a limit of the approach, because mismatches due to grain size can be compensated, misleading the understanding of the physical processes involved. On the other side the trend we found between photometric parameters and single scattering albedo has a physical meaning and suggests a way for a preliminary evaluation of parameters itself, independently from the phase function fit. The peak at 0.5 μm is well reproduced by the model, but it doesn't exclude the possibility for Rayleigh scattering of nano-absorbers (which is not explicitly modeled in this work), whose effect could be compensated in the estimation of single-particle phase function.

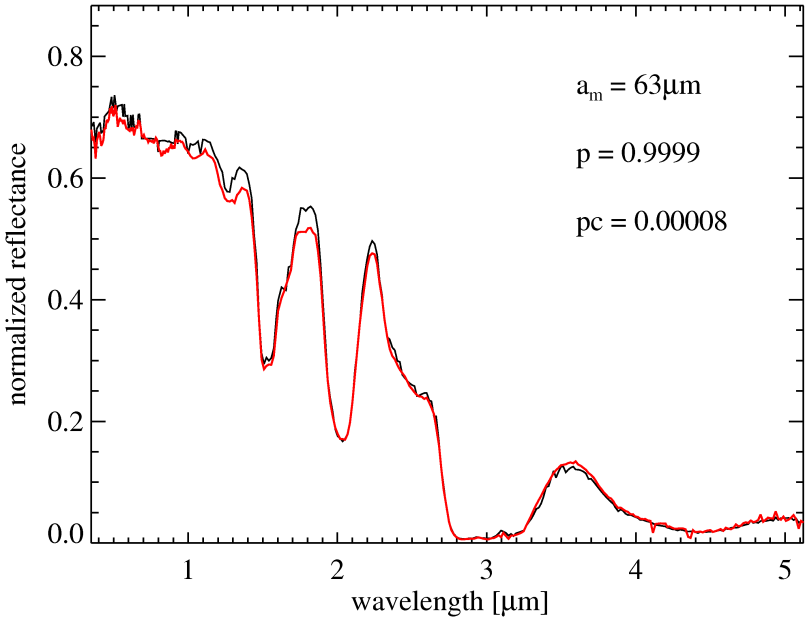

Figure 4.12: Final spectral fit at 25.4°. The model is the black line. Ciarniello et al. (2010a).

4.5 Spectral fits of other satellites

The modeling adopted to reproduce the spectral properties of Rhea and Enceladus is here applied to spectra of Mimas, Tethys and Dione acquired by VIMS. This represents a preliminary analysis aimed to point out compositional similarities and differences among the major satellites of Saturn.

4.5.1 Mimas

Mimas (fig. 4.13, left panel) is seventh-largest satellite of the Saturnian system with a mean radius of $198.2 \pm 0.4\ km$ (Roatsch et al., 2009) and a mass $M = (3.7493 \pm 0.0031) \times 10^{19}\ kg$ (Jacobson et al., 2006) (the derived density is $1.1479 \pm 0.007\ g/cm^3$, Roatsch et al. (2009)). The satellite is heavily cratered and is characterized by the presence of Herschel, a 130 km wide impact crater, placed at the equator on the center of the leading hemisphere..
The spectrum we analyzed (fig. 4.13, right panel) is relative to the leading hemisphere of the satellite and it is acquired at $g = 87.5°$. The absorption features at 1.5, 2.0 and 3.0 μm are relative to water ice, while the presence of a UV downturn indicates the presence of contaminants. The spectrum has been modeled with an intimate mixture of two type of grains: $I(pi = 98\%)$ and $C(pc = 2\%)$. I grains are an intraparticle mixture of water ice ($p = 99.9\%$) and Triton tholin ($pt = 0.1\%$), while C particles are made of amorphous carbon. The size of both I and C grains is 58 μm.

4.5.2 Tethys

Tethys (fig. 4.14, left panel) is the fifth largest satellites of the Saturnian system having a mean radius of $531.1 \pm 0.6\ km$ (Roatsch et al., 2009) and a mass $M = (6.17449 \pm 0.00132) \times 10^{20}\ kg$ (Jacobson et al., 2006) (the derived density is $0.984 \pm 0.003 g/cm^3$, Roatsch et al. (2009)). The density of the satellite indicate that it is composed almost entirely of water ice. This is confirmed by spectral properties and photometric observations: the latter indicates Tethys as the second brightest moon of the system (geometric albedo is 1.229 ± 0.005Verbiscer et al. (2007)), after Enceladus. Nonetheless a dark reddish component is present on the surface.
The spectrum we analyzed (fig. 4.14, right panel) is relative to the leading side of the

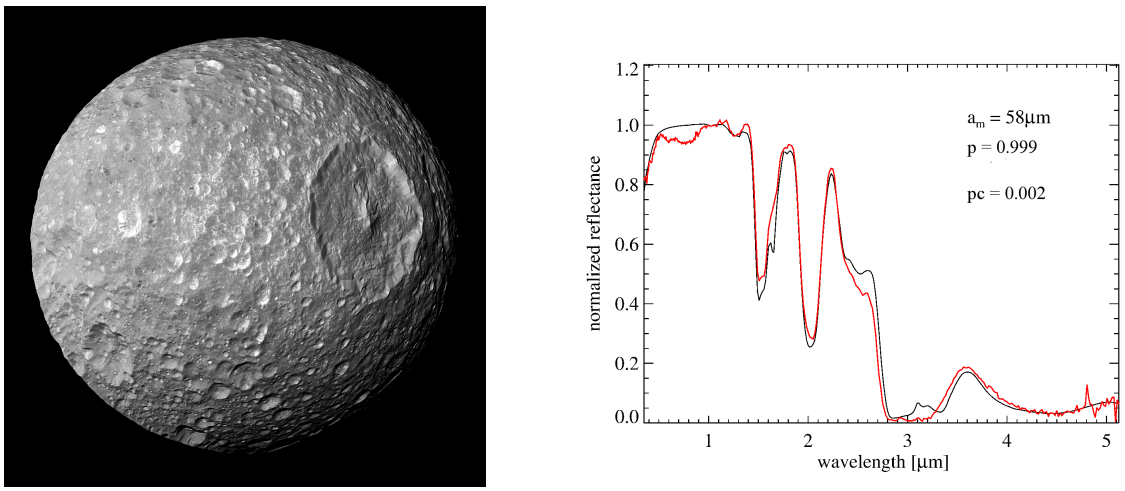

Figure 4.13: *Left panel*: Mimas. On the right the Herschel crater. Image courtesy of NASA-CICLOPS-ISS team. *Right panel*: Mimas spectrum by VIMS (red) and simulated spectrum (black). See details in the text.

satellite and it is acquired at $g = 84.9°$. The absorption features at 1.5, 2.0 and 3.0 μm are relative to water ice, while the presence of a UV downturn indicates the presence of contaminants. The spectrum has been modeled with an intimate mixture of two type of grains: $I(pi = 99.2\%)$ and $C(pc = 0.8\%)$. I grains are an intraparticle mixture of water ice ($p = 99.9\%$) and Triton tholin ($pt = 0.1\%$), while C particles are made of amorphous carbon. The size of both I and C grains is 69 μm.

4.5.3 Dione

Dione (fig. 4.15, left panel) has a mean radius of $561.4 \pm 0.4\ km$ (Roatsch et al., 2009) and a mass $M = (1.095452 \pm 0.000168) \times 10^{21}\ kg$ (Jacobson et al., 2006) (the mean density is $1.478 \pm 0.003\ g/cm^3$, Roatsch et al. (2009)). The relatively large density of the satellite indicate that a considerable fraction of the interior is made of silicate rocks. The spectrum we analyzed (fig. 4.15, right panel) is relative to the leading side of the satellite and it is acquired at $g = 84.9°$. The absorption features at 1.5, 2.0 and 3.0 μm are relative to water ice, while the presence of a UV downturn indicates the presence of contaminants. The spectrum has been modeled with an intimate mixture of two type of grains: $I(pi = 89\%)$ and $C(pc = 11\%)$. I grains are an intraparticle mixture of water ice ($p = 99.7\%$) and Triton tholin ($pt = 0.3\%$), while C particles are

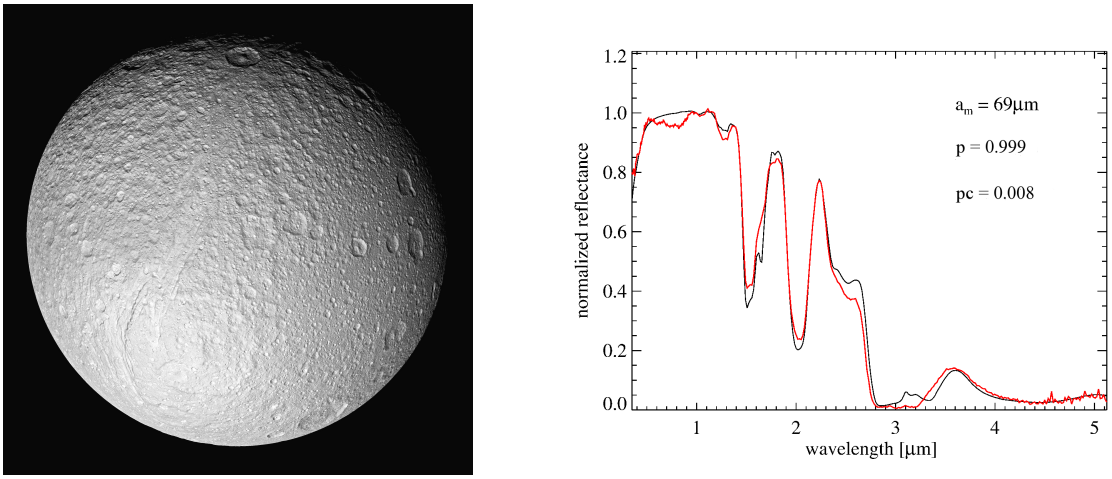

Figure 4.14: *Left panel*: Tethys. Image courtesy of NASA-CICLOPS-ISS team. *Right panel*: Tethys spectrum by VIMS (red) and simulated spectrum (black). See details in the text.

made of amorphous carbon. The size of both I and C grains is 59 μm.

4.6 Comparison of surface properties

In this section the derived spectrophotometric properties of the satellites that we investigated are compared. We start from Rhea and Enceladus for whom the photometric behavior has been studied, since the phase function of both satellites was available.
The first thing to point out is that the scattering properties, except for OE, for both the satellites, seem to be independent from wavelength, while on the other hand are strongly correlated with single scattering albedo. The phase curve for Rhea and Enceladus changes gradually shape with single scattering albedo, producing a relative increasing of reflectance at intermediate phase angle ($30° - 60°$) with increasing w (fig. 3.10 and 4.11). Moreover in both cases the single particle phase function seems to be more backscattering for larger values of w. This is shown in fig. 3.9, 3.11 (upper right panel), 4.9 and 4.10. This can be explained by the fact that when the particles are not absorbing (large w) light can undergoes multiple internal reflections that increases backscattered light. This correlation gives an hint in the modeling of the single-particle phase function of unknown media, possibly reducing the number of free parameters in the inversion process of the phase function and on the other side providing a rule in

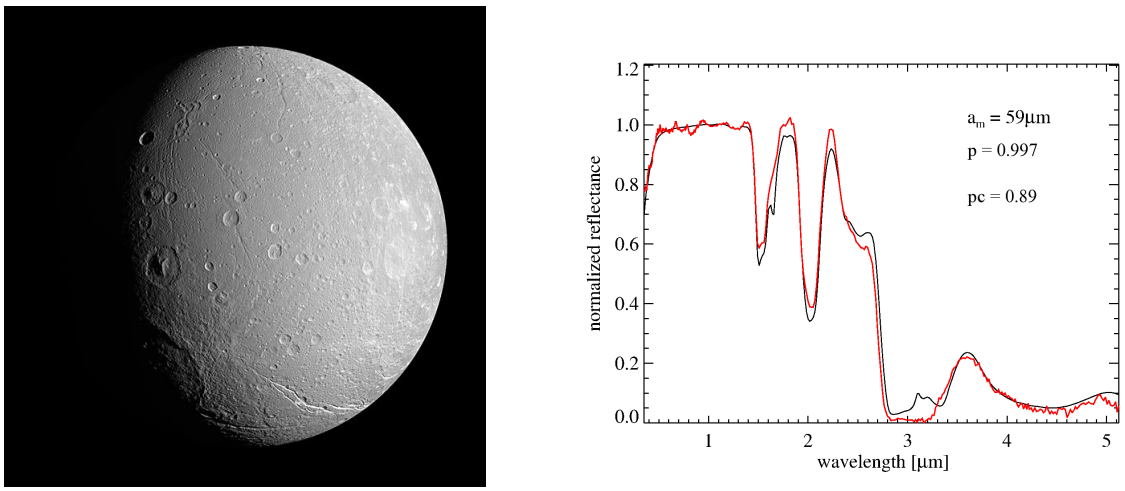

Figure 4.15: *Left panel*:Dione. Image courtesy of NASA-CICLOPS-ISS team. *Right panel*: Dione spectrum by VIMS (red) and simulated spectrum (black). See details in the text.

the photometric correction of photometric data.

The second thing that Rhea and Enceladus have in common is the large derived $\bar{\theta}$ value: 33° and 29° respectively. Both values are too large to be correlated with surface large scale roughness. In particular this is true for Enceladus that shows a more intense geological activity which renews the surface. As explained in sec.3.4.4 these large values of the slope angle indicate that the dominating roughness is at small scales ($mm - cm$) of the order of particles clumping. Moreover it must be remembered that the roughness retrieved through the Hapke model fails for $\bar{\theta}$ larger than 10°.

Move now to spectral properties of the investigated satellites. In table 4.6 the best spectral fit are reported vs. the radial distance of each satellite from Saturn. For all the moons the paradigm represented by an intraparticle mixture of water ice and Triton tholin seems to be a good explanation for the UV downturn. More contaminated objects require the addition of amorphous carbon particles to match the albedo level. Referring to table 4.6 it can be noted that the UV reddening is correlated with the orbital position of the satellites respect to Enceladus. In fact the amount of tholin requested to fit the VIMS spectra has a minimum on Enceladus. Enceladus is the source which feed the E ring by cryovolcanism activity (Porco et al., 2006) with almost pure ice particles. These particles hit the surface of the satellites which orbit in the E ring (radial distance from Saturn 180000 - 480000 km), with a flux that is maxi-

Table 4.2: Spectral fits summary.

Name	Orbital radius [km]	Grain size [μm]	Tholin	ACH2
Mimas	185000	58	0.1 %	2 %
Enceladus	238000	63	0.008 %	–
Tethys	295000	69	0.1 %	0.8 %
Dione	377000	43	0.3 %	11%
Rhea	527000	38	0.4 %	–

mum in correspondence of Enceladus position. This flux of particles provide almost uncontaminated ice on the surface of the moons. However, has shown in Schenk et al. (2011), spectral properties of moons in the E ring can be explained by interaction with energetic electrons, that are driven on the leading side of the satellites by the Saturn's magnetic field, providing energy for chemistry and tholin production (Khare et al., 1984, 1993). From this point of view space weathering of energetic particles is more efficient on satellites further from Saturn, where the flux of icy particles from the E ring is lower and the surface are not refreshed by pure ice.

Chapter 5

Hapke modeling of Saturn's rings

Following the approach described in sec. 3, here we investigate the main rings of Saturn, applying the Hapke model for a semi-infinite medium (eq. 2.115) adapted to a finite optical depth layer of particles. The Saturn's rings system is the most extensive in the Solar System (see table 5.1 and fig. 5.1). It extends from 66900 to 480000 km from Saturn's center and the main rings are (in order of distance from the planet) D,C,B,A,F,G and E (Esposito, 2006). The two densest regions are the B and A rings, which are divided by an underdense region named Cassini Division (CD). The vertical extent of the rings is $< 1\ km$ with particle sizes ranging from few centimeters to 10 meters (Esposito, 1986).

5.1 Dataset

The analyzed dataset is composed of 312 hyperspectral VIMS cubes covering the ring plane between C and F rings. The observations are performed on the lit side of the rings (reflection) and illumination conditions (incidence angle, emission angle and phase angle) as well as the ring-spacecraft distance change over the entire dataset (see table 5.2). Moreover the analyzed dataset contains both nominal and high spatial resolution cubes. In order to localize the target of each observation we have projected VIMS pixels on the standard rings reference plane. To do this we have used a SPICE-based code that allows to calculate the following 6 geometric parameters for each VIMS pixel: radial distance on the ring plane, azimuth angle on the ring plane, Cassini-ring distance,

Table 5.1: Main structures in the Saturn's rings.

Name	Inner edge (km)	Outer edge (km)	Grain size
Anello D	66900	74658	μm
Anello C	74658	91975	$mm - m$
Ringlet di Titano	77871	77896	
Maxwell gap	87491	87555	
Ringlet 1.470 R_s	88716	88732	
Ringlet 1.495 R_s	90171	90232	
Anello B	91975	117507	$cm - 10m$
Divisione di Cassini	117507	122340	$cm - 10m$
Huygens gap	117825	118185	
Anello A	122340	136780	$cm - 10m$
Encke gap	133410	133740	
Keeler gap	136510	136550	
Anello F (core)	140219		$\mu m - cm$
Anello G	166000	173200	$\mu m - mm$
Anello E	180000	480000	μm

Notes: R_s is the Saturn's radius: 60268 km.

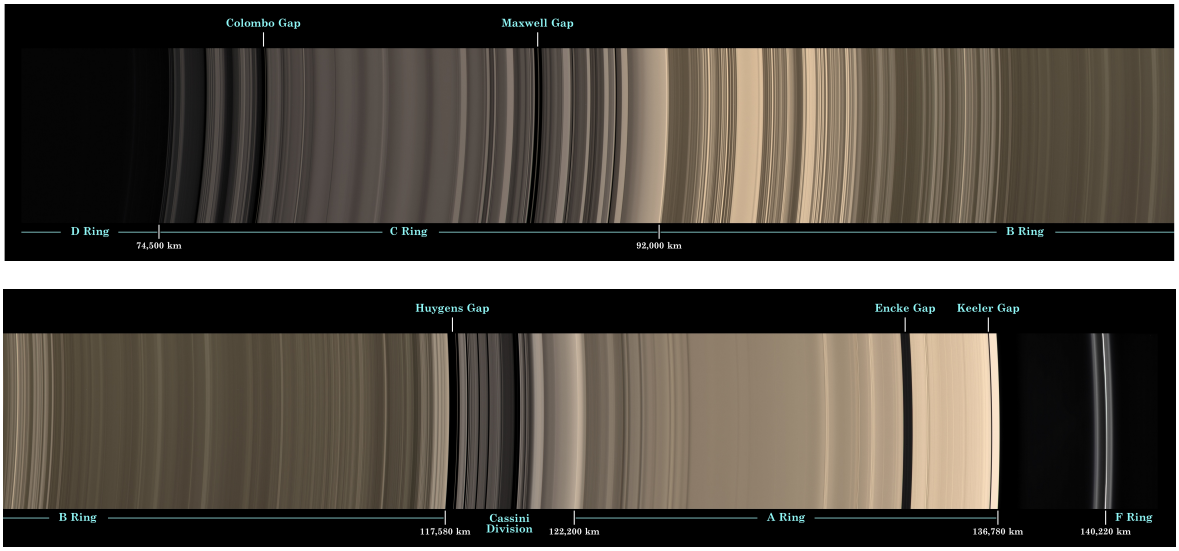

Figure 5.1: Rings mosaic from D to F ring.

incidence angle,emission angle and phase angle. In fig. 5.2 the VIMS FOV's for entire dataset reprojected on the rings are plotted, both for VIS and IR channels.

Table 5.2: Observations list.

Sequence	Session	Start Time	Stop Time	i	min e	max e	$\langle e \rangle$
S05	LATPHASE001	2004-303T17:07:57.776	2004-303T17:08:40.649	113.6°	100.4°	99.4°	101.2°
S10	LATPHASE001	2005-120T09:36:44.638	2005-120T14:22:59.119	111.8°	108.8°	107.8°	109.6°
S10	SUBML07LP001	2005-104T06:49:06.555	2005-104T09:52:03.543	112.0°	97.6°	97.4°	97.7°
S11	RDHRCOMP001	2005-140T23:45:03.243	2005-159T03:44:01.277	111.6°	104.5°	97.5°	109.9°
S13	LATPHASE001	2005-230T21:07:22.620	2005-231T03:49:46.709	110.6°	111.4°	111.0°	111.7°
S36	SUBML001	2007-353T20:21:25.366	2007-354T01:33:34.888	99.1°	100.0°	98.5°	101.6°

Sequence	Session	min g	max g	$\langle g \rangle$	min d $[km]$	max d $[km]$	$\langle d \rangle$ $[km]$
S05	LATPHASE001	134.7°	131.3°	139.0°	1058770	947013	1181170
S10	LATPHASE001	35.5°	31.9°	40.9°	1541450	1460000	1629240
S10	SUBML07LP001	31.3°	26.6°	35.5°	596623	551003	648020
S11	RDHRCOMP001	21.5°	1.6°	44.6°	326627	268793	411125
S13	LATPHASE001	26.4°	20.8°	32.3°	1056010	983677	1119700
S36	SUBML001	28.1°	19.4°	36.5°	659903	600667	709749

Notes: Sequence and session names as well as start and stop times of the observations are indicated. For the emission angle e, the phase angle g and the distance Cassini-ring d, the minimum, maximum and average values all over the sessions are reported. The incidence angle i, which corresponds to the *opening angle* of the rings (angle between the sun and the normal to the rings) is constant over the observation time scale.

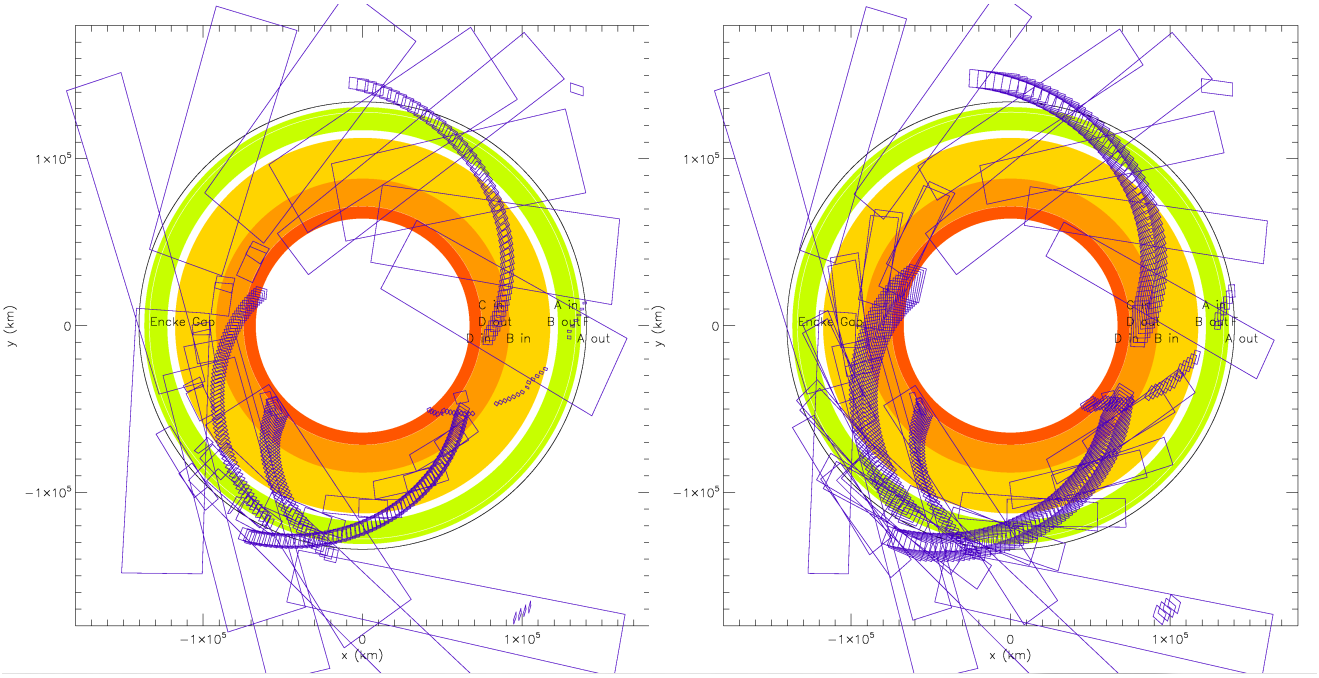

Figure 5.2: Projection of VIMS FOV (Field of View) on the rings plane. The 4 corners of the FOV for each acquisition are connected with a purple line. A ring region is shown in green, B ring in yellow, C ring in orange and D ring in red. VIS and IR cubes are on the left and right panel respectively. Ciarniello et al. (2011c).

VIS and IR channel data can show some differences due to the different instant field of view (IFOV) of the two channels in HIGH RESOLUTION mode (VIS IFOV = $167\mu rad \times 167\ \mu rad$, IR IFOV = $250\ \mu rad \times 500\ \mu rad$). In fig. 5.3 the radial distance against phase angle is plotted for pixel of the VIS channel whose maximum linear size on the ring plane is $< 3000\ km$ (For the IR channel the spatial resolution can be three times worse). For spectral analysis only pixels with VIS resolution comprised in the 500-1000 km range have been considered.

5.2 Model

Spectral analysis of Saturn rings in VIS-IR show that spectral signatures (e.g. water ice band depths) are due to particles whose size is in 10 μm -1000 μm (Poulet et al., 2002). These sizes are smaller than the typical size of the icy chunks composing the rings (10

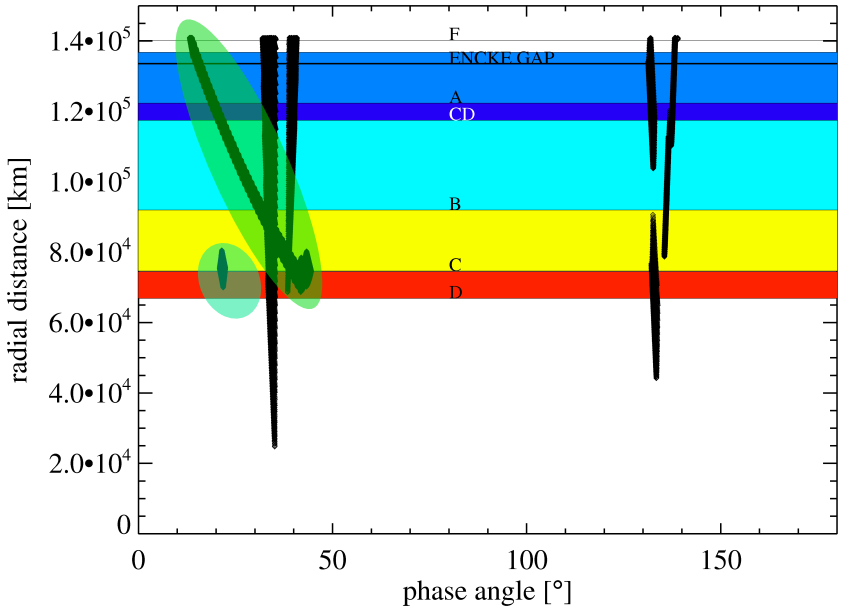

Figure 5.3: Radial distance vs. phase angles for pixels with linear size on the ring plane < 3000 km (VIS channel). Pixels with linear size in the 500-1000 km range are rimmed. Ciarniello et al. (2011c).

cm - 10 m). This means that the light measured by VIMS is mostly scattered by the fine regolith covering the rings particles. We approximate the behavior of the these icy chunks to a semi-infinite medium applying the equation of bidirectional reflectance (eq. 2.115). In order to consider the different densities of the various regions of the rings we need to multiply this equation for $(1 - e^{-(1/\mu_0+1/\mu)\tau})$ where τ is the optical depth. This term represents the probability for a light ray to interact with the rings at optical depth τ and to escape toward the observer. For the rings case we can neglect surface roughness and if we observe at $g > 15° - 20°$ (far from opposition surge) the final equation which describes the rings I/F is:

$$\frac{I}{F} = \frac{w}{4}\frac{1}{\mu_0 + \mu}[p(g) + H(\mu_0)H(\mu) - 1]\left(1 - e^{-(1/\mu_0+1/\mu)\tau}\right) \tag{5.1}$$

In this framework multiple scattering between icy chunks is neglected, while we take into account for multiple scattering of regolith on the surface of the blocks. This approach has two major limits: it doesn't take into account for small isolated particles and considers the scattering surface of the icy chunks parallel to the ring plane. The last assumption allows to use ring incidence and emission angles (fig. 5.4).

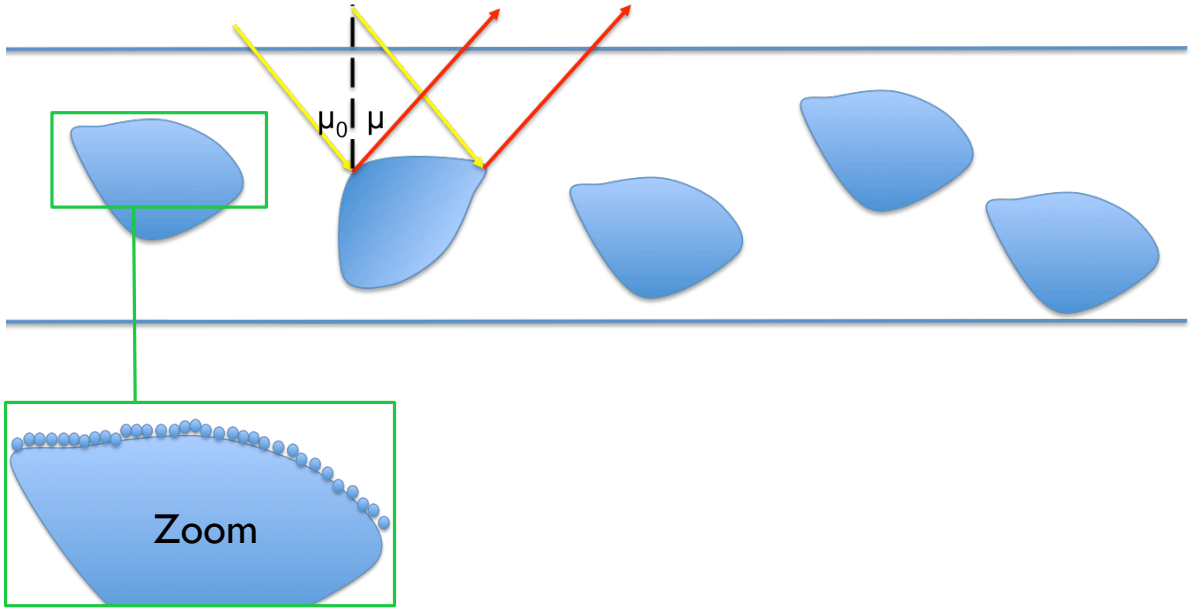

Figure 5.4: Schematic representation of the rings. Incident and emitted rays are plotted. Ciarniello et al. (2011c).

5.3 Spectral fit

5.3.1 Single scattering albedo

Single scattering albedo is computed at each wavelength following the Hapke model as in the previous sections regarding Saturn satellites. It depends on the grain size distribution of icy particles and on the abundance, type and mixing of contaminants. We investigated the usual four reddish organic compounds as contaminant, in order to produce the UV downturn in the spectra of the rings:

- Amorphous carbon (ACH2)
- Triton tholin
- Titan tholin
- Tholin from Khare et al. (1993)

Areal, intimate and intraparticle ice-contaminant mixtures have been examined with various grain size distributions: monodisperse,uniform, power law and lognormal.

5.3.2 Single particle phase function

The single particle phase function $p(g)$ is an important quantity to establish the absolute albedo level of the spectrum. Moreover it depends on wavelength. Its value can be computed through Mie theory for a spherical isolated particle. In close-packed media Mie results cannot be applied unless the forward scattering lobe due to diffraction is removed and the phase function is renormalized.This procedure is quite long and suffers the assumption of a perfect spherical shape of the grain which is not the case of a real icy particle. From the analysis on icy moons we found a positive correlation between single particle phase function and single scattering albedo when observed at intermediate phase angle ($20° - 40°$). For this reason we have derived a preliminary empirical expression for the single particle phase function, where a spectral dependence with single scattering albedo is introduced:

$$p(g_0) = 1.5\sqrt{w} \tag{5.2}$$

where g_0 is a fixed phase angle in the $20° - 40°$ range. The dependence on the root of w comes out form spectral fit attempts.

5.3.3 Optical depth

Optical depth for the investigated region of the rings has been averaged from Voyager PPS and UVS data on the Planetary Rings Node (http://pds-rings.seti.org). VIMS wavelengths are smaller than the typical size of icy chunks on the rings so optical depth values don't depend on wavelength.

5.4 Spectral fit results

5.4.1 C ring

The C ring spectrum is an average of 248 spectra for the VIS channel and 305 for the IR with the following properties:

- radial distance from Saturn center: 80000-81000 km
- average incidence: 111.6°; average emission angle: 99.9°
- average phase angle: 37.5°
- optical depth: 0.0092

The best fit is given by an intimate mixture of two species of particles: A (35%) and B (65%). A particles are an intraparticle mixture of water ice (99.8%) and Triton tholin (0.2%). B particles are an intraparticle mixture of water ice (98.7%) and amorphous carbon (1.3%). The grain size (a) distribution is a power law ($\propto a^{-q}$) with $q = 3$, minimum size $a_m = 20\ \mu m$ and maximum size $a_M = 600\ \mu m$. See fig. 5.5.

5.4.2 B ring

The B ring spectrum is an average of 285 spectra for the VIS channel and 417 for the IR with the following properties:

- radial distance from Saturn center: 102000-103000 km
- average incidence: 111.6°; average emission angle: 102.7°
- average phase angle: 27.0°

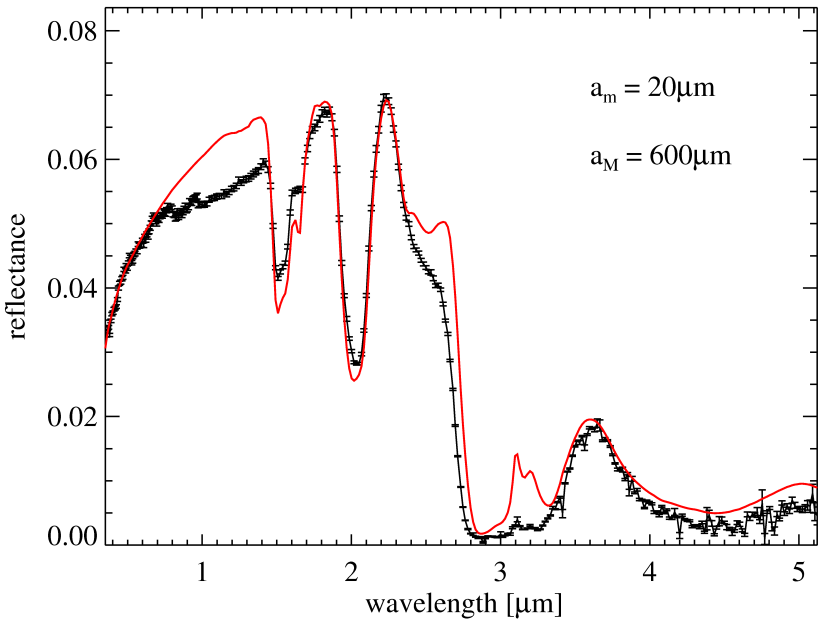

Figure 5.5: C ring spectrum (black) and best fit (red). Ciarniello et al. (2011c).

- optical depth: 1.65

The best fit is given by an intimate mixture of two species of particles: A (96.5%) and B (3.5%). A particles are an intraparticle mixture of water ice (99.5%) and Triton tholin (0.5%). B particles are made of amorphous carbon. The grain size (a) distribution is a power law ($\propto a^{-q}$) with $q = 3$, minimum size $a_m = 20\ \mu m$ and maximum size $a_M = 700\ \mu m$. See fig. 5.6.

5.4.3 Cassini Division

The Cassini Division spectrum is an average of 474 spectra for the VIS channel and 436 for the IR with the following properties:

- radial distance from Saturn center: 118000-119000 km
- average incidence: 111.6°; average emission angle: 104.2°
- average phase angle: 20.7°
- optical depth: 0.133

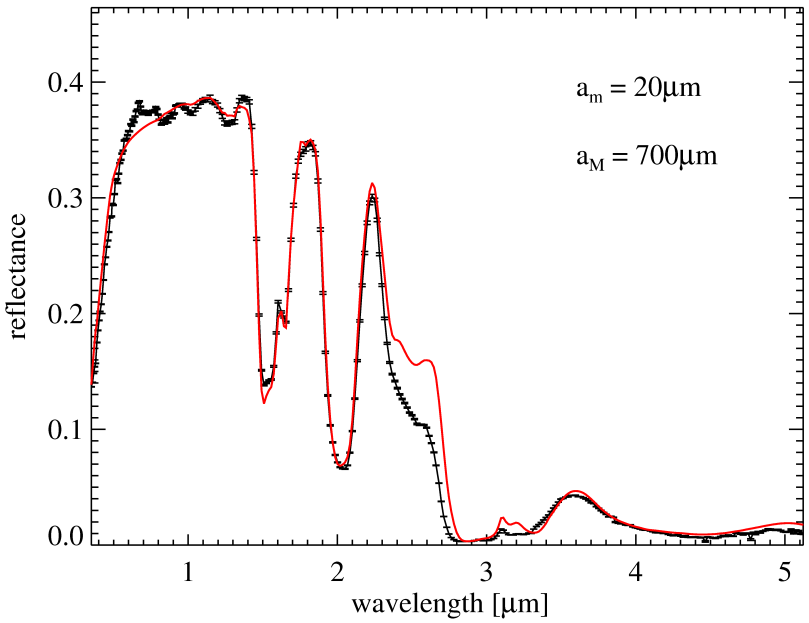

Figure 5.6: B ring spectrum (black) and best fit (red). Ciarniello et al. (2011c).

The best fit is given by an intimate mixture of two species of particles: A (75%) and B (25%). A particles are an intraparticle mixture of water ice (99.6%) and Triton tholin (0.4%). B particles are an intraparticle mixture of water ice (98.4%) and amorphous carbon (1.6%). The grain size (a) distribution is a power law ($\propto a^{-q}$) with $q = 3$, minimum size $a_m = 14\ \mu m$ and maximum size $a_M = 400\ \mu m$. See fig. 5.7.

5.4.4 A ring

The A ring spectrum is an average of 310 spectra for the VIS channel and 381 for the IR with the following properties:

- radial distance from Saturn center: 128000-129000 km
- average incidence: 111.6°; average emission angle: 105.0°
- average phase angle: 17.2°
- optical depth: 0.4185

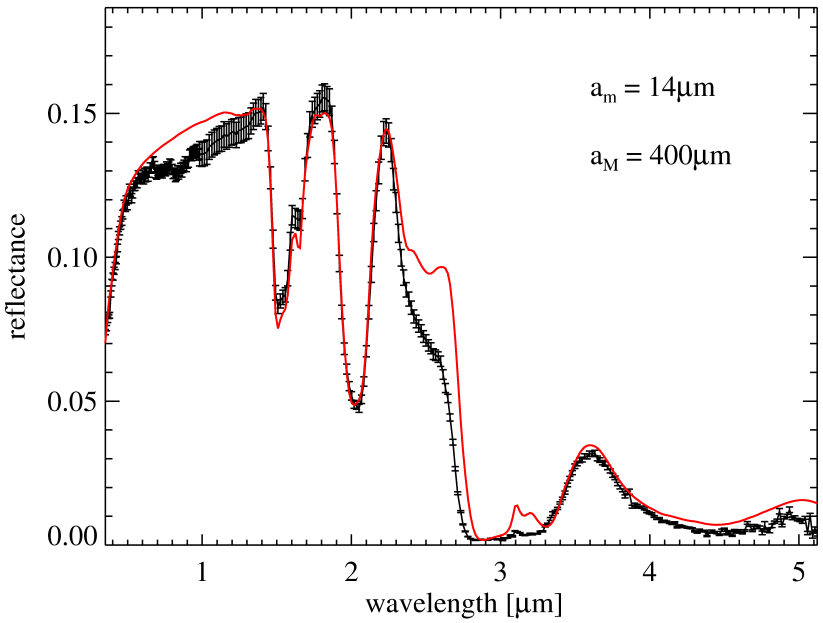

Figure 5.7: CD spectrum (black) and best fit (red). Ciarniello et al. (2011c).

The best fit is given by an intimate mixture of two species of particles: A (88%) and B (12%). A particles are an intraparticle mixture of water ice (99.6%) and Triton tholin (0.4%). B are made of amorphous carbon. The grain size (a) distribution is a power law ($\propto a^{-q}$) with $q = 3$, minimum size $a_m = 20$ μm and maximum size $a_M = 700$ μm. See fig. 5.8.

5.5 Summary and comparison with Saturn's moons spectra

Our best models of the rings are represented by intraparticle mixtures of water ice and organic contaminants with a power-law grain size distribution (fig. 5.5, 5.6, 5.7 and 5.8). The UV downturn common to all the rings is well explained by inclusions of Triton tholin in ice particles with tiny amounts ($\leq 0.5\%$). The model works better for the densest regions (A and B rings), while fails to reproduce the strong reddening around 1 μm of the C ring and Cassini division, that seem to be more contaminated. We are not able to reproduce the reflectance in the 2.5 μm region. This issue can be addressed to

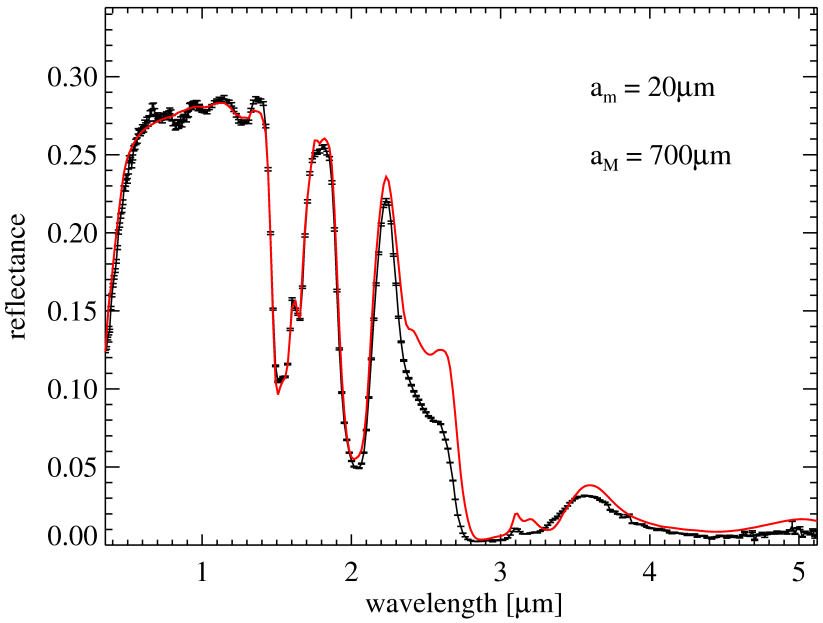

Figure 5.8: A ring spectrum (black) and best fit (red). Ciarniello et al. (2011c).

the grain size distribution but an important effect is given by the single particle phase function, whose value strongly affects the albedo level and changes with wavelength. The major effects of single-particle phase function can be seen in the Fresnel peak region, where single scattering dominates and the overestimation of $p(g)$ leads to a worse fit, particularly for the C ring and Cassini division. The results obtained for the rings can be compared with the ones obtained for Saturn's moons (sec. 3 and 4). The UV downturn is a common propriety of rings and icy satellites, and can be explained with an intraparticle mixture of water ice and Triton tholin (less than 1%). The brighter rings show a similar behavior to satellites in the region around 1 μm, while the darker rings exhibit a stronger reddening. Grain size of icy moon particles constrained by the spectral fit is smaller than the one of the rings (moreover it works fairly well with a monodisperse distribution instead of a power law). This difference in the grain size distribution is confirmed by a much less evident Fresnel peak in satellites spectra.

Chapter 6

Hapke modeling of pyroxenes

Remote sensing represents, in a large number of cases, the most effective method to retrieve information about mineralogical composition of planetary surfaces and several studies have been performed to investigate how the spectral and photometric properties of the powders can be linked to the physical and chemical state of the particles they are made of. For example one of the most sensitive parameter to infer the chemical composition and the grain size is the spectral band depth (Gaffey et al., 1990; Cloutis and Gaffey, 1991). As we will see the band depth, as each spectral signature, is influenced also by the geometry of the observation and this effect can be considered only involving a radiative transfer model. A number of works on radiative transfer modeling of powders have been produced, see for example Wilcox et al. (2006); Shepard and Helfenstein (2007, 2011); Souchon et al. (2011).

Studies on remote sensing data from space missions, which uses radiative transfer model, are aimed to infer the compositional properties of the observed targets, but often the lack of information on the photometric behavior of the endmembers used in the modelization makes the inversion process not univocal. Laboratory measurements, on the other side, have an a priori knowledge of the physical properties of the investigated media, and can constrain their photometric properties, providing relation that can be useful in the analysis of unknown media. This is what we did applying the Hapke's radiative transfer model to laboratory reflectance measures of four pyroxenes of known composition and grain size. This study aims to point out photometric properties of mineral powders which are commonly found on planetary surfaces, in order to provide a tool to interpret remote sensing data from space missions. We produced spectra in the 350 - 2500 nm range under different viewing conditions: this enabled us to

investigate both spectral and photometric characteristics of these minerals. We have studied band depth variations induced by the grain size of the sample and by the observation geometry (phase angle g) (see sec. 6.2). Since a partial phase function for these minerals was measured we applied the Hapke model to determine the photometric parameters of one of these pyroxenes (6.3). In the last section of the chapter we show how it is possible using the Hapke's derivation of single scattering albedo to compute the imaginary part of the refractive index for each material we studied (Roush et al., 2007).

6.1 Dataset and experimental setup

The dataset is composed of reflectance measurements of four pyroxenes: an orthopyroxene En88 (E), and three clinopyroxenes high in Ca, En48Wo41 (A), En45Wo50 (D) and En33Wo49 (AD). The chemistry of these minerals was determined by Electron Microprobe Analysis (CAMECA SX50, CNR-IGG laboratory, Padova) and it is summarized in table 6.2. The bidirectional reflectance spectra were measured with a Fieldspec-Pro spectrophotometer mounted on a goniometer in use at the SLAB (Spectroscopy LABoratory) at IASF-INAF, Rome (fig.6.1). The goniometer (fig. 6.2) is composed by two arms, one carrying the illuminator and one the collector. Both the arms are connected to rotating platforms which move the detector and illuminator in the same plane. Details on the angular excursion of both the arms are in table 6.1. Two optical fibers are coupled to the illuminator source (QTH lamp) and to the Fieldspec. Each fiber ends with a spherical lens which collimate the output and input beams with a max divergence of 4°. The collector is made of a bundle of three optic fibers, each one connected to one of the three detectors in the spectrophotometer, and has. The three detectors are independent grating spectrometers:

- VNIR: 350-1000 nm range
- SWIR1: 1000-1800 nm range
- SWIR2: 1800-2500 nm range .

Table 6.1: Goniometer

Maximum inclination (each arm)	65°
Minimum phase angle[a]	30°
Maximum phase angle[b]	130°

Notes: [a]the minimum phase angle is imposed by the physical dimensions of the illuminator and collector arms supports.
[b]The real maximum phase angle available is about 110° because the footprints of the collector and of the illuminator don't match anymore for larger values.

Figure 6.1: Experimental set-up at the SLAB, at IASF-INAF, Rome. On the left the goniometer. The red optical fiber connects te illuminator to the QHT lamp. The black optical fiber connect the collector to the spectrophotometer Fiedlspec-Pro.

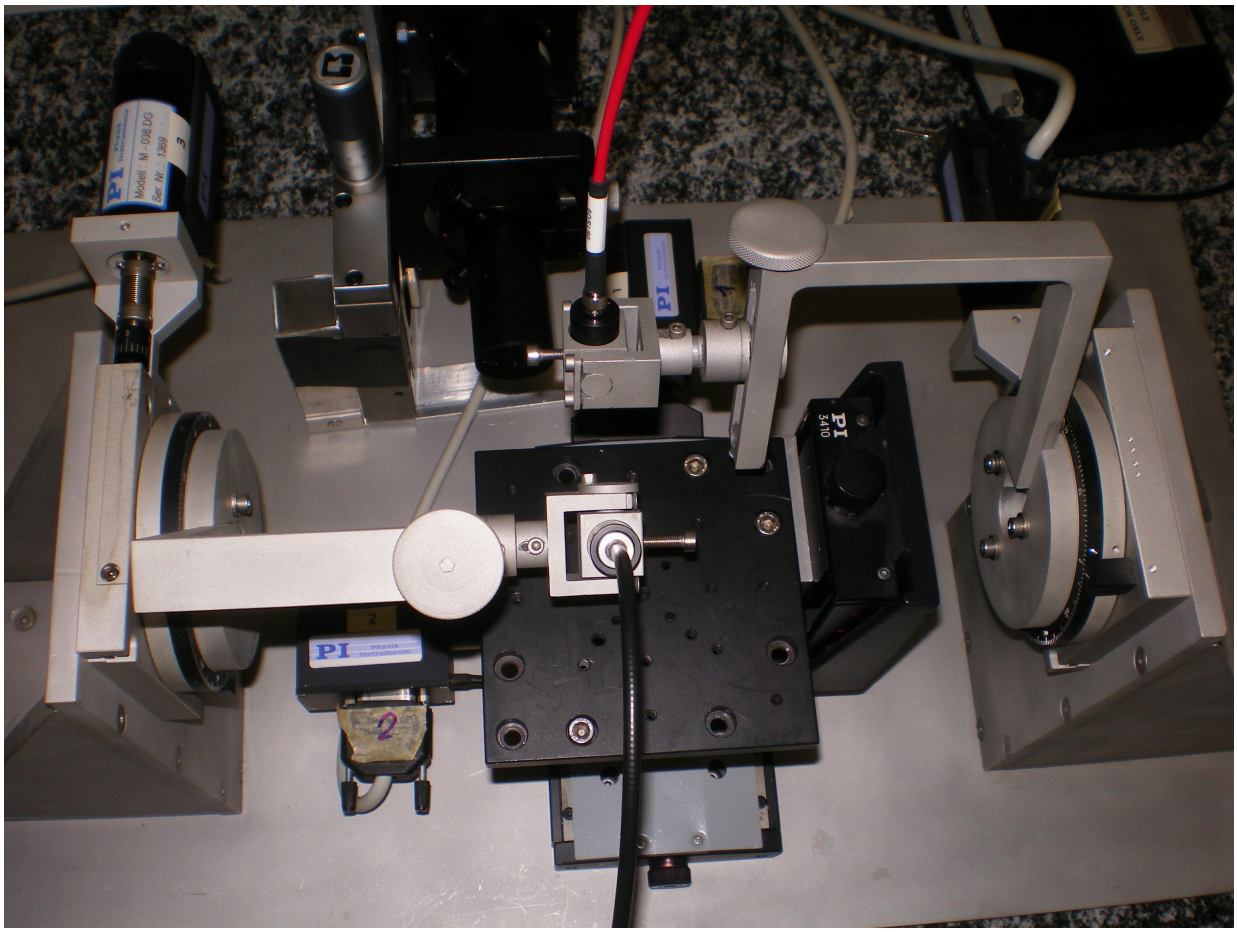

Figure 6.2: The goniometer. The two mechanical arms are visible, supporting the illuminator (red opticl fiber) and the collector (black optical fiber). The sample to be measured is placed on the black platform below the two arms.

The spectra were acquired with 1 nm spectral sampling. The illumination source was a QTH (Quartz bulb, Tungsten filament, Halogen gas) lamp (fig. 6.1) powered at 50 W. The lamp is stabilized in current thanks to a photometric control system which guarantees a constant output flux during the measurements.. The calibration was performed with Spectralon optical standard (registered trademark of Labsphere, Inc.). For all the samples with 100-125 μm grain size we have acquired spectra in the 30° - 100° phase angle range. For the case of the E sample two sets of measurements have been produced: one at variable i $(-10°, -5°, 0°, 5°, 15°, 25°, 35°, 45°, 55°,)$ and $e = 40°$ and one with variable i $(-25°, -15°, -5°, 5°, 15°, 25°, 35°, 45°)$ and $e = 55°$. Also for all the other minerals, two sets of measurements were completed: one, as for the E pyroxene, with with variable i $(-25°, -15°, -5°, 5°, 15°, 25°, 35°, 45°)$ and $e = 55°$ and one with variable e $(-10°, -5°, 0°, 5°, 15°, 25°, 35°, 45°, 55°)$ but fixed $i = 40°$.

Table 6.2: Minerals chemistry

	Enstatite %	Ferrosilite %	Wollanstonite %	$Mg\#$
E	88	12	≈ 0	0.88
A	48	11	41	0.83
D	45	5	50	0.91
AD	33	18	49	0.67

Notes: the $Mg\#$ is the ratio between Mg and $Mg + Fe$ on a molecular basis.

For all the minerals, measurements at fixed viewing geometry ($i = 30°$, $e = 0°$) have been performed for various grain sizes (< 63 μm, 100-125 μm, 125-250 μm, 250-500 μm, 500-800 μm). As an example of the entire dataset, spectra of the E sample are plotted in fig. 6.3, while in fig. 6.4 spectra of the different pyroxenes with a grain size of 125-250 μm are reported.

6.2 Band depth analysis

Orthopyroxene and clinopyroxene have well-known spectral properties (Cloutis and Gaffey, 1991) which depend on their structure and composition. Among our samples, the E type is an orthopyroxene. It exhibits the typical bands at 0.9 μm and 1.91 μm

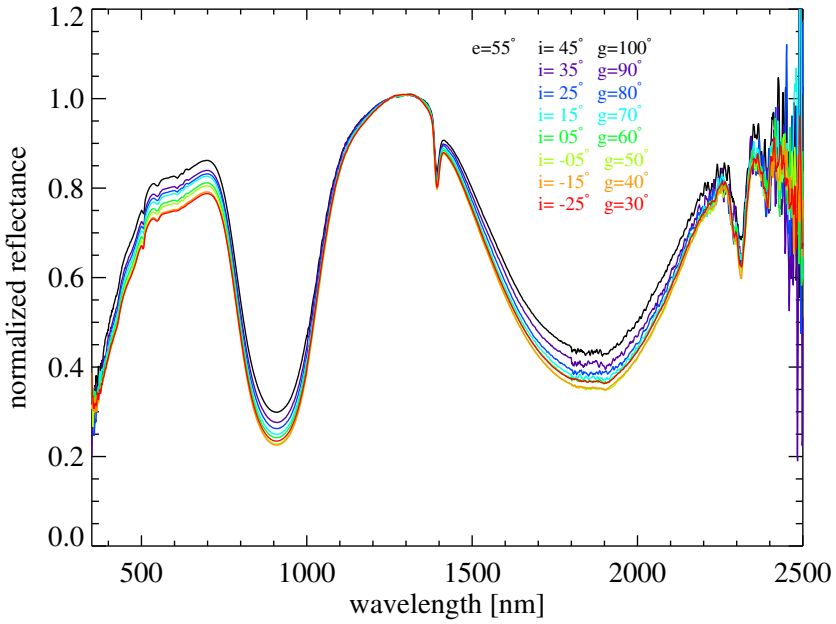

Figure 6.3: E-sample spectra (normalized @ 1250 nm) acquired at different geometries: incidence, emission and phase angles are indicated. Ciarniello et al. (2011b).

which are addressed to crystal field transitions of ferrous iron (Fe^{2+}) occupying the M2 crystallographic site (Burns, 1970; Cloutis and Gaffey, 1991). Both the bands shift to longer wavelengths with increasing iron content (Klima et al., 2007). The steep reflectance dropoff shortward of 0.5 μm is attributable to charge transfers processes.
Concerning clinopyroxenes (A, AD and D) the spectral behavior is more heterogeneous. The two extreme examples are represented by the AD and D pyroxenes. The former shows two main absorption bands at 0.98 μm and 1.16 μm that are assigned to crystal field transitions in ferrous iron in M1 site. The additional band at 0.8 μm is eventually due to $Fe^{2+} - Fe^{3+}$ charge transfer. The D clinopyroxene instead exhibits two major absorption bands at 1.05 μm and 2.33 μm, again due to crystal field transition of Fe^{2+} occupying the vacancies in M2 site left by calcium and an absorption feature at 0.74 μm addressed to $Fe^{2+} - Fe^{3+}$ charge transfer.
For all the investigated pyroxenes the depth of the most significative bands have been computed. The computation has been performed by mean of a routine written in IDL. The routine finds the local minima of the spectrum (the software can be set to recognize only bands whose width is larger than a given threshold), then it locates the wings of

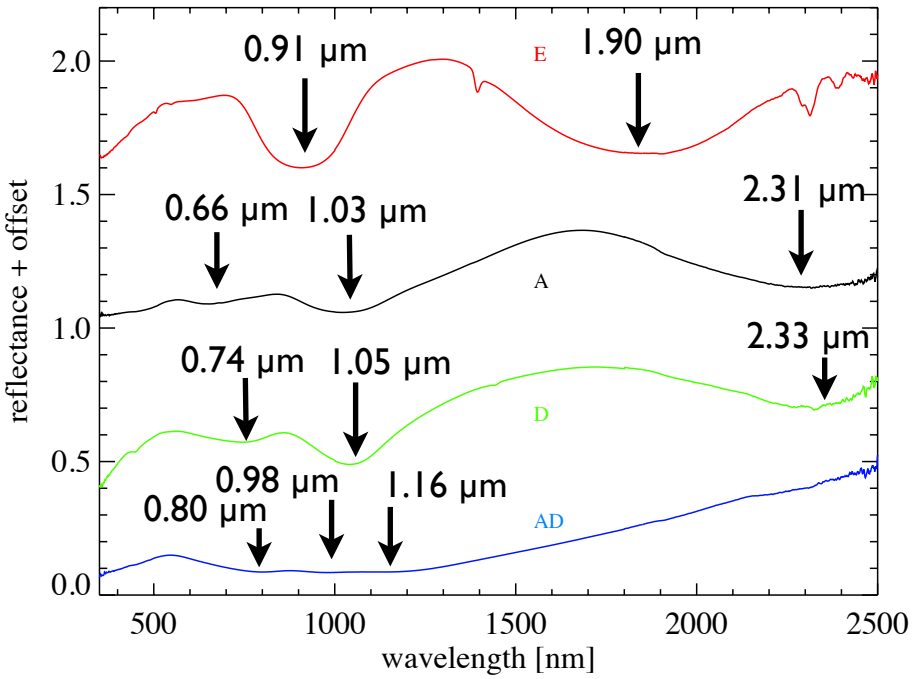

Figure 6.4: Spectra of the orthopyroxene (E) and clinopyroxenes (A, D, AD) minerals considered in this investigation for 100-125 μm grain size. An offset is added for clarity and bands of interests are indicated. Ciarniello et al. (2011b).

the band, which are the points of the spectrum closest to the band center, where the spectrum stops to grow. A linear fit is performed between the wings of the band, and the derived relation is used to compute the continuum. The band spectrum is divided by the continuum (continuum removal), and the minimum of the band (which has moved from the original position) is located again. Once the continuum is removed the band depth BD is computed with the formula $BD = 1 - B_v$, where B_v is the value of the band spectrum in the minimum position. The bands we have selected are the ones due to the crystal field transition. In the case of the AD clinopyroxene we chose to study only the 1.16 μm band, which was the most characterized.
Band depth variations (for the most of the bands indicated in fig. 6.4) induced by the grain size of the powders have been investigated for all the four minerals (fig. 6.5). The band depth increases with grain size, as expected, because light travels a longer path inside the particle and absorption is enhanced. When grain size is too large the band saturates and band depth decreases. The grain sizes we investigated do not reach the saturation regime.

Since for all the minerals two sets of measurements with variable phase angle were available (100-125 μm grain size) we measured band depth variations with geometry also (fig. 6.2).

We found, for all the studied pyroxenes, apart for not well determined bands (see for example bands at 2.31 and 2.33 μm of A and D samples respectively, which both end beyond the investigated spectral range) that band depth slowly decreases above 30° phase angle and the decrement becomes steeper towards 100°. This behavior is commonly observed in planetary surfaces, both for rocky and icy materials (Coradini et al., 2011; Filacchione et al., 2011).This effect is caused by the different scattering properties of the medium at the band center (where single scattering dominates) and at the its wings (where multiple scattering is also important) (Hapke, 1993). If we try to compute the band depth in the framework of the Hapke model, for different phase angles, only accounting for multiple scattering, we are not able to reproduce the observed behavior (fig. 6.2, bottom right panel). This means that single scattering plays an important role in this effect.
If we compare band depth variations induced by grain size with the ones produced by geometry (phase angle) we see that the effects are comparable. This is an important

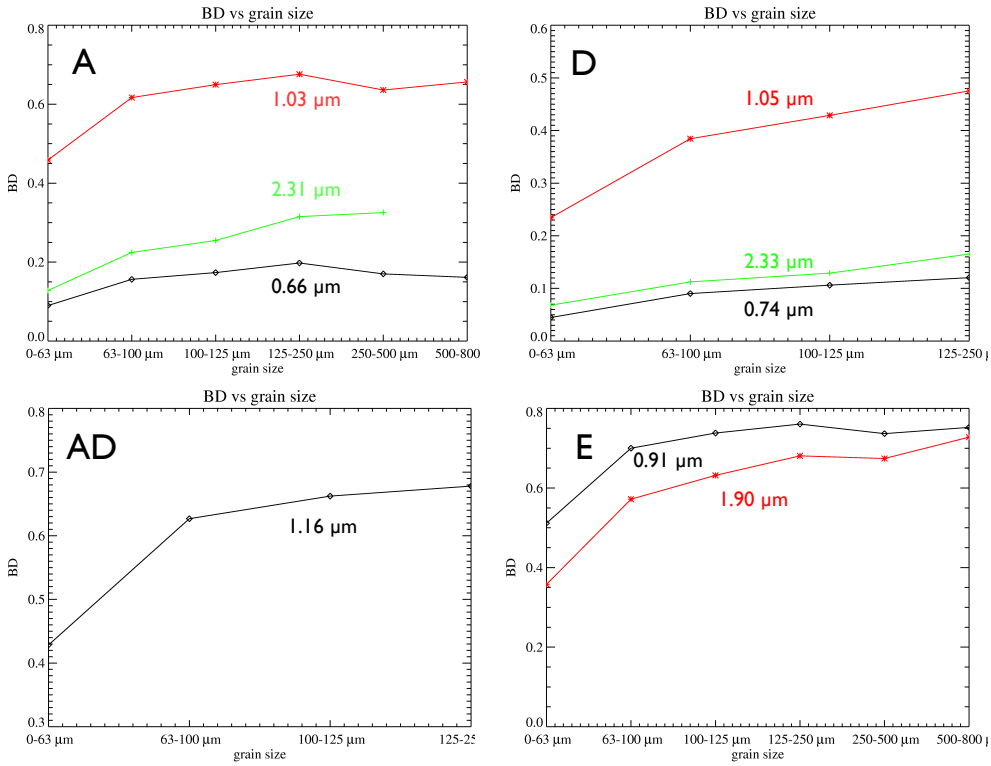

Figure 6.5: Band depth vs. grain size. Clockwise from top left: A, D, AD and E. The bands centers are indicated in the plots. Ciarniello et al. (2011b).

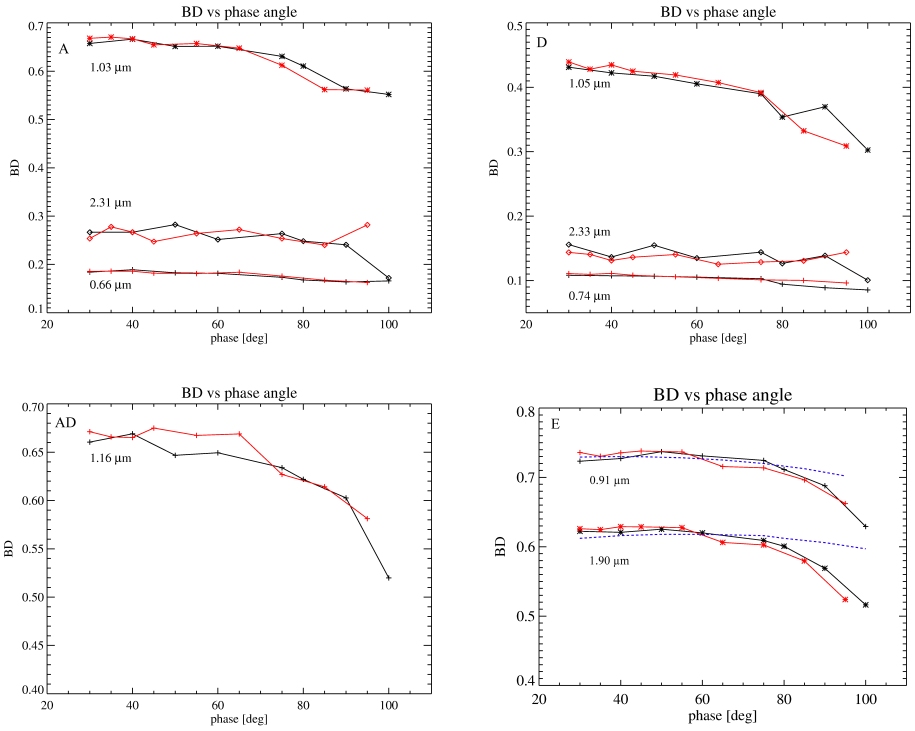

Figure 6.6: Band depth vs. phase angle. Clockwise from top left: A, D, AD and E. Two sets of measurements were available for A, D and AD minerals: one with $e = 55°$ and variable i (black curves, see text for details) and one with $i = 40°$ and variable e (red curves, see text for details). Also for the E mineral we have two sets of measurements: with $e = 55°$ and and one with $e = 40°$ and variable i (black curves and red curves respectively, see text for details). The dashed blu line in the E plot is the expected behavior of the band depth using the Hapke model and considering only multiple scattering. Ciarniello et al. (2011b).

point because typically, in spectral analysis, band depth is used as a tool to compute the grain size of the investigated medium (Jaumann et al., 2008), with the implicit assumption that normalization in the band depth calculation cancels out any geometric effect. This is obviously not true, and the consequent error in grain size determination can be up to of a factor 2.

6.3 Phase function fit

We performed a fit of the phase function for both the sets of measurements of the E mineral, respectively in the phase ranges $30° - 100°$ and $30° - 75°$, using the Hapke model (observations at 85° and 95° are not included in the following analysis because showed a large error in absolute reflectance). The Hapke equation of bidirectional reflectance (eq. 2.115) for laboratory spectra, far from the opposition surge, reduces to:

$$r(i, e, g) = \frac{1}{\mu + \mu_0} \frac{w}{4} [p(g) + H(\mu_0)H(\mu) - 1] \tag{6.1}$$

The single particle phase function $p(g)$ has been modeled with the Heyney-Greenstein formula (eq. 2.89) that we recall here:

$$p(g) = \frac{1 - \xi^2}{(1 + 2\xi \cos g + \xi^2)^{3/2}} \tag{6.2}$$

The b parameter here determines the behavior of the single particle phase function:

- $b < 0$, back-scattering
- $b > 0$, forward-scattering

The other free parameter is the single scattering albedo w.
An example of performed fits for both the sets of measurements is in fig. 6.3. Since we retrieved a couple of w and b for each wavelength of the spectral range (2151 bands) we do not show all the derived parameters in a table but we prefer to summarize the results of the fits in a figure. In fig. 6.3 the derived b values are plotted against w for the two sets of measurements.

As shown in fig. 6.3 the b and w are clearly anti-correlated. The Spearman's rank correlation coefficient ρ is -0.93 for both the sets of measures. This coefficient asses how well the relation between the two parameters can be expressed by a monotonic function. For a perfect monotonic decrescent relation the expected value should be -1, and our result is fairly close to that value. Moreover in this case it seems that the relation is close to be linear. The fact that the b values are mostly negative means that the particles are typically backscattering and the correlation with w indicates

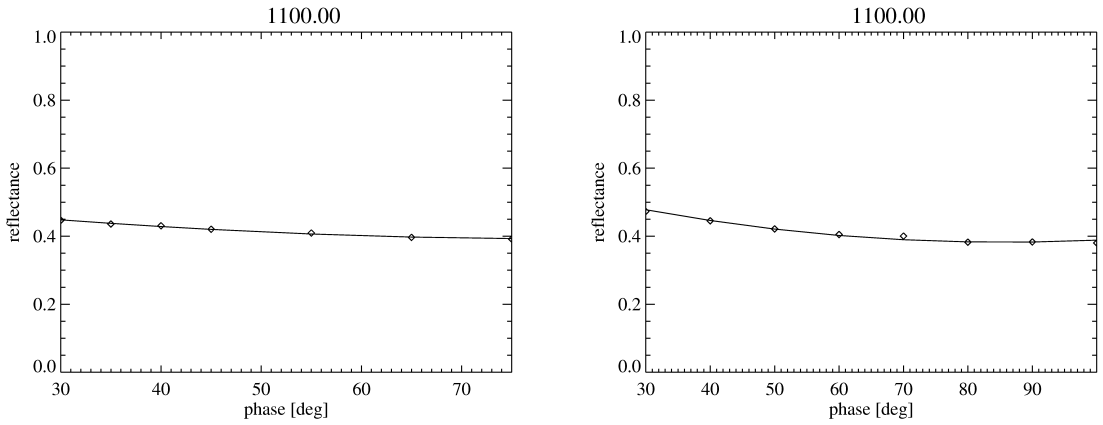

Figure 6.7: *Left panel*: phase function fit at 1100 nm (i = variable, $e = 40°$). *Right panel*: phase function fit 1100 nm (i= variable, $e = 55°$). Ciarniello et al. (2011b).

that when the particles are less absorbing the backscattering increases. This behavior reflects the one derived for the icy satellites (Rhea and Enceladus) in sec. 3 and sec. 4. This properties seems to be independent from the particle composition (ice or silicate) and appears to be driven by scattering mechanisms inside the particle itself. In fact, in absorbing particles, the photons cannot undergo multiple internal reflections. The beam crosses the particle only one time before coming out along the forward direction.

6.4 Optical constants determination

We computed the imaginary part of the refractive index k for the 4 minerals (100-125 μm), inverting the Hapke formulation of the single scattering albedo (eq. 2.116). The various terms in eq. 2.116 depends on the grain size and the real and imaginary part of the refractive index n and k. If n is fixed and the grain size is known it is possible to retrieve, estimating w, the values of k at such wavelength. Values for the real part of the refractive index in this wavelength range, where n can be considered constant, are determined using the formula in Lucey (1998) and Warrel and Davidsson (2010), which relates n to the amount of Mg-Fe in the pyroxenes:

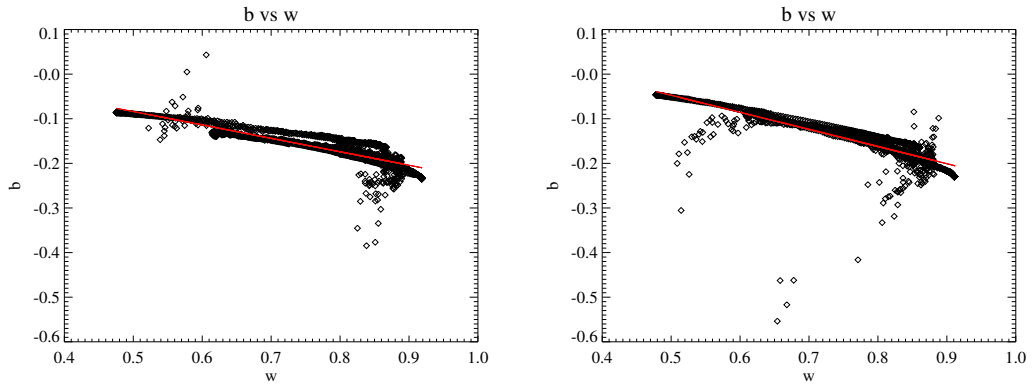

Figure 6.8: *Left panel*: b vs. w (i = variable, $e = 40°$). *Right panel*: b vs. w (i = variable, $e = 55°$). Red line in both plots is an attempt of linear fit b vs. w. Ciarniello et al. (2011b).

$$n_{opx} = 1.768 - [0.118\,(Mg\#)]$$
$$n_{cpx} = 1.726 - [0.082\,(Mg\#)] \tag{6.3}$$

where *opx* stands for orthopyroxene and *cpx* for clinopyroxene. Except for the E orthopyroxene the values of single scattering albedo are retrieved applying the eq. 6.1 to the mineral spectra ($i = 30°$ and $e = 0°$) under the assumption of isotropic single particle phase function. For the E mineral w values at each wavelength come from the phase function fit. The derived k's are plotted in fig. 6.4.

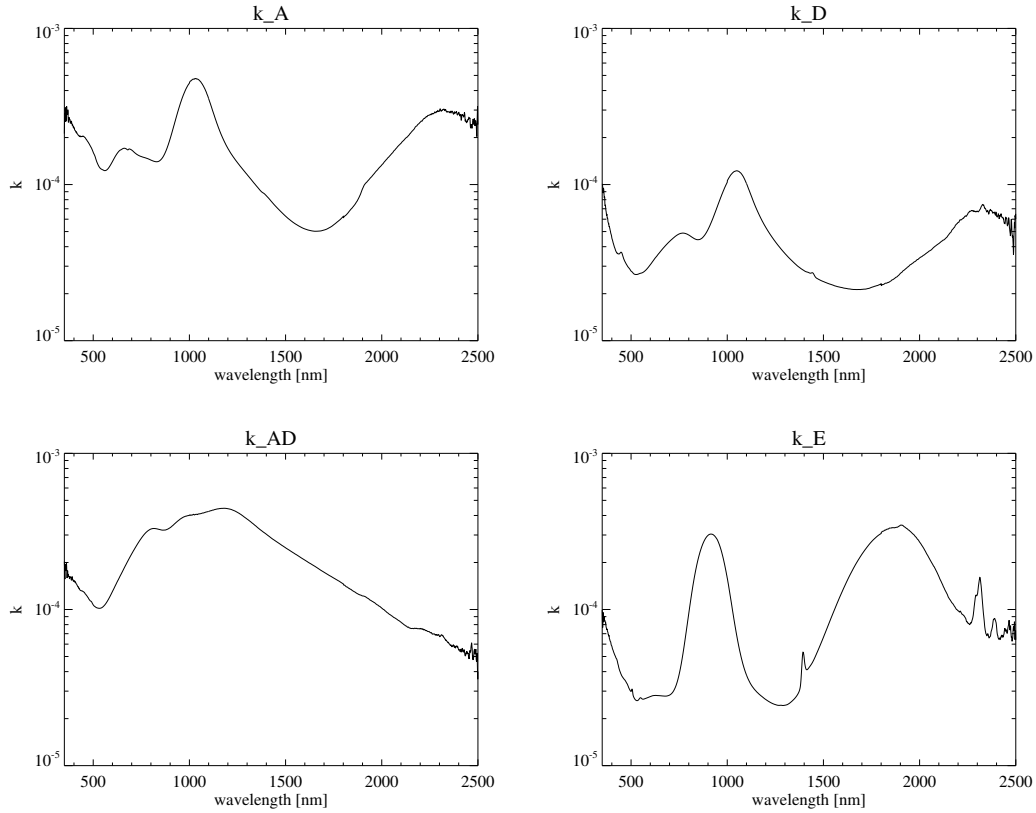

Figure 6.9: Derived imaginary part of the refractive index for the four investigate pyroxenes. Clockwise from top left: A, D, AD and E. Ciarniello et al. (2011b).

Chapter 7

A Montecarlo routine to simulate scattering in particulate media: preliminary results

Analytic solutions of radiative transfer equations have the advantage to be easy to handle and to give a clear physical picture of the scattering processes at work, however they relies on some assumptions and approximations that are not always satisfied. For example, one of the strongest assumption of the Hapke model (Hapke, 1993) is the one relative to the multiple scattering process. As shown in sec. 2.4.4 the computing of multiple scattering depends on the values of the Chandrasekhar function $H(x)$. $H(x)$, in turn, depends on the single particle phase function, and its only convenient determination is the one obtained for isotropic scattering $p(g) = 1$. In Hapke (2002) an improvement of the multiple scattering treatment is given, including the single particle phase function expressed as Legendre polynomials, but the solutions depend on infinite series, and more and more terms are needed to describe complex single particle phase functions. The necessity to develop a Montecarlo routine for the scattering in particulate media is to be able to treat any given formulation of $p(g)$. This is very important when the investigated media are not represented by single particles, but aggregates. Aggregates have a photometric behavior which is the result of the combination of single and multiple scattering processes and of other mechanisms as the opposition effect. An example of a framework where we have to deal with aggregates is represented by the Saturn's rings and by planetary rings in general. Saturn's rings are composed by

icy blocks with sizes in the $cm-m$ range. Since the wavelengths we deal with are of the order of μm's, each block can be treated as a semi-infinite medium, and the photometric output is the product of the scattering by the particles forming the regolith which covers the blocks. In sec. 5 the Hapke model developed for a semi-infinite medium has been adapted to the rings including a multiplicative term which depends on the optical depth. This term actually holds only if multiple scattering between the blocks is neglected, but this is not true in the densest regions of the rings, in particular for visible wavelengths, where ice is low absorbing and multiple scattering between blocks is enhanced.
This kind of problems raised the necessity to develop a software able to simulate photometric properties of particulate media. In the following sections our computer model will be described (sec. 7.1) and the results of some preliminary tests are presented (sec. 7.2). Application to cases of scientific interest is left as future work.

7.1 Description of the routine

Our computer model, written in IDL language, includes two stages: the production of the particulate medium and the scattering simulation.
The medium is represented by a $100 \times 100 \times 100$ tridimensional grid. Each position of the grid represents a room for one "particle" (or aggregate or block), so the model can handle up to 10^6 particles. In this approach we are implicitly assuming that each single block has cubic shape. This approximation has the advantage to make the modeling very simple. However the possibility to represents aggregates of arbitrary shape is not neglected, because more contiguous cubes can be joined to form a bigger particle. At this stage, for simplicity, we work only with single-cube blocks. The number of positions randomly occupied by the particles is related to the filling factor of the medium (which is a parameter of our model), and determines the optical depth.
The scattering process is modeled in the following way. Photons are shot from the upper side of the grid with a given direction which is individuated by the incidence angle (it is measured respect to the normal of the surface) and the azimuth angle. Rays enter the grid at quote $z = 99$ and are propagated in the same direction until they hit a particle. After the interaction the photon can be absorbed or scattered. The probability of scattering is proportional to a parameter which for simplicity we'll call particle single scattering albedo w. If $w = 0$ the photon is certainly absorbed while

if $w = 1$ the photon will be certainly scattered. If we deal with single particles (not aggregates) w is the physical single scattering albedo. If the photon is not absorbed it is scattered in a new direction. The probability that the photon is scattered in a given direction is determined by the single particle phase function $p(g)$. It determines the probability that the photon is scattered with a phase angle g respect to the original direction. The azimuth angle, which is necessary to define the new direction, calculated in a plane orthogonal to the direction of the incoming photon, is randomly assigned (this is rigorously true only in the case of spherical particles).
The photons are scattered from a particle to another until they are absorbed or leave the medium on the upper side $z = 99$ or on the bottom of the grid $z = 0$. Photons that escape the grid from lateral faces (the planes $x = 0$, $x = 99$, $y = 0$ and $y = 99$) are newly put inside the grid from the opposite side, preserving the propagation direction. This boundary condition simulates the fact that the cubic grid is not isolated, but it is a portion of an ideally infinite layer (along the x and y direction), which is the typical schematization adopted in the investigation of horizontally stratified media.

7.2 Preliminary tests

Before applying the computer model to simulate real physical situations (e.g. scattering on the ring plane) it is necessary to test the routine in order to verify if the theoretical approach we are applying is correct and if the code works properly. To do this we ran the software and computed some well-known quantities that can be easily determined in analytic way either, and compared the results.

7.2.1 Transmission factor

If we have a radiance I_0 impinging on the upper side of a thick layered medium the transmitted signal at the bottom is $I = I_0 e^{-\tau/\mu_0}$, where τ is the optical depth and μ_0 is the cosine of the incidence angle i. The above relation holds if multiple scattering is neglected. From eq. 2.25 we have that optical depth of a layer with thickness Δz is $\tau = E\Delta z$ where E is the extinction coefficient described in sec. 2.3 (for simplicity here we assume E as a constant function of z). As shown in sec. 2.3.2 the extinction

coefficient can be expressed by the eq. 2.12 that we report below

$$E = -\frac{N\langle\sigma Q_E\rangle}{\phi}\ln(1-\phi)$$

where N is the numerical density of particles, σ is the geometric cross section, Q_E is the extinction efficiency and $\phi = Nv$ is the filling factor (v is the particle volume).
The quantity we want to estimate to test our computer model is the the transmission factor $t = I/I_0 = e^{-\tau/\mu_0}$. For incidence angle $i = 0$ the cross section of the particles (cubes) is 1, as well as the volume. Q_E is 1 because we assume that particles are much larger than the wavelength. If we put this number in the expression for E we find $E = -\ln(1-\phi)$. Since our medium is 100 thick the final expression of the optical depth is $\tau = -100\ln(1-\phi)$. We produced simulations for various ϕ values and compared the derived transmission factor with the one from the expression given above. Simulations are performed with $w = 0$ in order to eliminate the contribute of multiple scattering. Results are in tab. 7.1.

Table 7.1: Transmission factors.

ϕ	t (analytic)	t (simulated)
10^{-4}	0.990	0.989
10^{-3}	0.905	0.909
10^{-2}	0.366	0.362
10^{-1}	2×10^{-5}	≈ 0

The agreement between the results of the simulations and the theory is remarkable, with differences always lower than 1%.

7.2.2 Diffusive reflectance and average scattering number

The expression of the diffusive reflectance for a semi-infinite medium of isotropic scatterers is given by:

$$r_0 = \frac{1-\gamma}{1+\gamma} \tag{7.1}$$

where $\gamma = \sqrt{1-w}$. This quantity represents an approximation of the ratio between the power emitted by the medium and the total incident power. The derivation of r_0

is not reported here and can be found in Hapke (1993). In our computer model this quantity is given by the ratio between the number of photons escaping the medium and the total number of shot photons. In our simulations photon are shot with $i = 0$ and single particle phase function is isotropic. The filling factor is $\phi = 0.3$, which is large enough to simulate the behavior of an semi-infinite medium (in the simulations transmission is found to be 0 for $\phi \geq 0.1$). The simulated values of r_0 are plotted vs. w in fig. 7.1 with the curve given by eq. 7.1

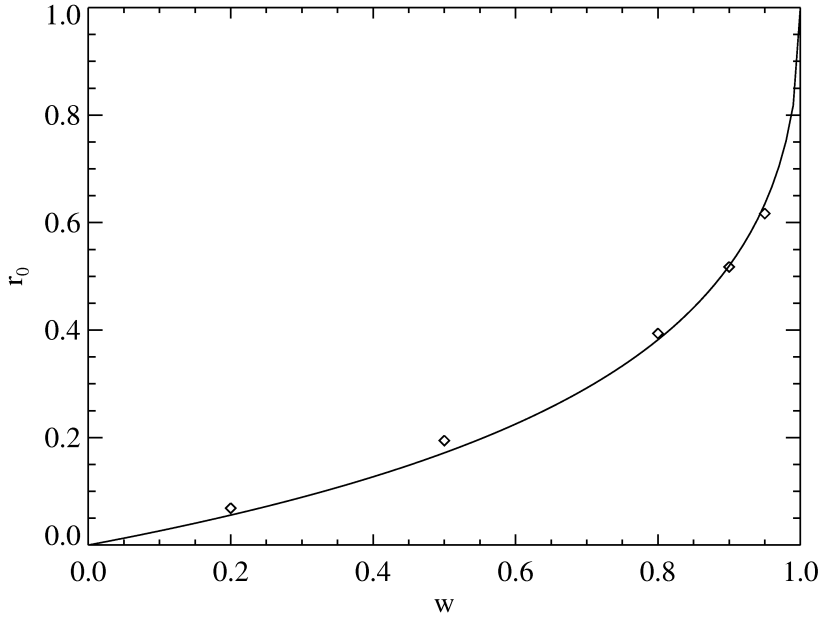

Figure 7.1: Diffusive reflectance r_0 vs w. The curve is given by the eq. 7.1 while the diamonds represent the results of computer simulations.

It can be noted that the curve is well reproduced by the results of the simulation, particularly at higher albedos.
Since r_0 is the ratio between the emitted power and the incident power, the quantity $1 - r_0$ represents the average fraction of absorbed power for a photon. The value of w, which is the probability that a photon is scattered, can be interpreted as the fraction of power scattered in each scattering. Conversely $1 - w$ represents the absorbed fraction.

Then if we compute the ratio

$$\mathcal{M} = (1 - r_0)/(1 - w) \tag{7.2}$$

we are measuring how many scatterings a photon undergoes before being absorbed or emitted by the medium. In other words we are calculating the average number of scatterings for a photon. In the routine the number of scatterings which each photon undergoes is stored in memory and the average number of scatterings can be computed. In fig. 7.2 the simulated and theoretical average number of scatterings are compared.

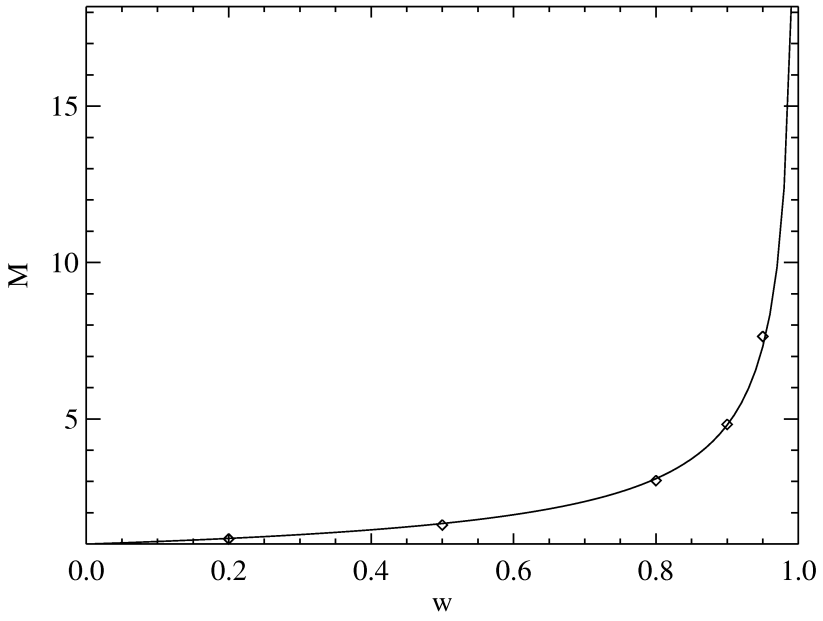

Figure 7.2: Average number of scattering $\mathcal{M}$ vs w. The curve is given by the eq. 7.2 while the diamonds represent the results of computer simulations.

The agreement between the results of simulations and computed values is remarkably good.

7.3 Applications and future works

The preliminary tests performed on the computer model we have developed show that it gives results which are consistent with theoretical predictions. This encourages to apply this kind of simulations to more complex and realistic cases, where analytical solutions of the radiative transfer equation are not applicable. One of this cases is represented by the scattering in planetary rings, where each particle is an aggregate of smaller substructures and has a complex scattering behavior. In this framework, the computer model we developed will be able to simulate multiple scattering between the aggregates, once provided a suited scattering function which describes the photometric properties of the regolith which covers each blocks. It must be pointed out that the scattering function of each aggregate is not calculated by the software, but must be given by a solution of the radiative transfer equation for the regolith, such as the bidirectional reflectance equation 2.115.

Another application of the code could be the simulation of the photometric properties of powders. In this case the particles are single grains that can be often described by a simple particle phase function and the simulation will help to evidence how the photometric output is influenced by physical parameters as the filling factor and the single scattering albedo. The comparison with a radiative transfer model could point out which are the major limitations deriving from the approximations that are commonly adopted in the analytic approach (e.g. use of the isotropic single particle phase function in the computation of multiple scattering).

The major limit of the numerical methods is the running time of the software. Depending on the physical properties of the investigated medium the simulations presented in this section required times of the order of half an hour on a common laptop and were performed with 10^6 photons. This number is enough to compute integral quantities, but if we want to retrieve the phase function of a given medium, for example simulating the observation sequence of an instrument onboard a spacecraft, which typically receives photons in a small solid angle, the number of photons to be shot need to be orders of magnitude larger, requiring proportionally a larger running time.

Another limit of our model is that it is not applicable to simulate scattering between particles whose size is of the same order (or lower than) the wavelength of light. In that case interference mechanisms occur, and they cannot be treated by our routine which propagates photons as particles, and not as electromagnetic waves.

A further development of the software will be the extension to arbitrary shaped particles (not only cubes). This will be done as stated above joining more cubes to form bigger and more complex aggregates.

Summary and conclusions

I have studied the spectrophotometric properties of particulate media in the framework of remote sensing for space missions. The analysis has started with Rhea, the largest icy satellite in the Saturnian system (Ciarniello et al., 2011a). The work has been presented at 41^{st} LPSC (Ciarniello et al., 2010c) and at the 42^{nd} DPS meeting (Ciarniello et al., 2010b). The study has been performed on spectra acquired by the instrument VIMS onboard Cassini, in the 0.35-5.12 μm spectral range, covering the $0.08° - 110°$ phase angle interval. This approach enabled us to investigate the compositional state of the ice covering the moon, the porosity of the medium and the surface roughness. The Hapke's model has been used for the analysis. As the Saturn's satellites taken into account in this study are mainly composed of water ice, only small amounts of additional compounds were needed to reproduce the observed spectral behaviour. Four different organic compounds have been investigated as water ice contaminants in order to model the UV downturn observed in the spectra. The best spectral fit in our model is represented by an intraparticle mixture of crystalline water ice (99.6%) and Triton tholin (0.4%), with a grain size (diameter) of 38 μm. Major discrepancies between the measured and fitted spectrum can be addressed to a grain size effect, because our particle diameter distribution represents only the average size of the particles and therefore neglects the contribution of grains with dimensions comparable to, or less than, the wavelength.

Once the composition of the medium has been determined it has been possible to investigate the photometric properties of the satellite fitting the full-disk phase function at each wavelength. The picture that emerges is that the dominating parameter in the scattering process is the single-scattering albedo w, showing correlation with the single-particle phase function and the opposition effect (OE). No particular dependence of OE on wavelength was found, as expected, considering that the typical grain size is larger than λ. The analysis of the OE indicates that both Shadow Hiding (SH) and

Coherent Backscattering (CB) are active, and their relative contribution depends on the single scattering albedo value. Measuring the OE angular width h in the SH regime we estimated a porosity varying between 65% and 77%.
The relatively high value of the roughness parameter ($\bar{\theta} = 33°$) is not compatible with the mean slope of surface structures like craters, depressions or other reliefs. This points to a correlation of $\bar{\theta}$ with roughness on smaller scale, possibly on the order of centimeters, confirming the Shepard and Helfenstein (2007) results, and the derived value can be interpreted as an estimation of the regolith angle of repose.

The same paradigm adopted for Rhea has been applied to Enceladus (work presented at AGU Fall Meeting 2010, Ciarniello et al. (2010a)). In this case the dataset covers the $23° - 150°$ phase angle range, with 290 full-disk images. Also for Enceladus the best spectral fit is obtained with an intraparticle mixture of water ice (99.992%) and Triton tholin (0.008%) and grain size of 63 μm. The amount of contaminants, even if minimal, is able to reproduce the weak reddening of the moon.
The study of the phase function indicates again that the single particle phase function parameters have a dependecy with the single scattering albedo. Both b and v decrease with increasing w and the final effect is that the particle phase function is more backscattering for large w.
Since in this set of observations the phase function doesn't cover the small phase angle region nothing can be concluded on the OE.
Similarly to Rhea the roughness parameter we derived ($\bar{\theta} = 29°$) is fairly high and is not compatible with the expected surface properties of a geologically active moon like Enceladus, which is frequently rejuvenated by internal processes and consequently display a low crater density over much of the surface area. This point enforces the idea that the roughness parameter in the Hapke model is sensitive to roughness on small scale rather than large scale topography.
The analysis of the phase function showed a rise in reflectance at large phase angle (150°), slowly depending on the wavelength. This has been addressed to forward scattering of small particles due to diffraction. The typical derived size of the particles producing this effect is ≈ 5 μm, which is compatible with grains produced in the active regions of Enceladus' located in the south pole area.

Spectral modeling has been performed also for the Saturn's moons Mimas, Tethys

and Dione. For these three satellites the model requires again an intraparticle mixture of water ice and Triton tholin to produce the common observed reddening. However in these cases a variable amount of amorphous carbon intimately mixed with the ice is needed to match the albedo level.

A comparative study of the spectral models produced for the five satellites indicates that the amount of tholin increases moving at larger orbital distances from Enceladus. Enceladus is thought to feed the E ring (where all the satellites orbit) with its plume activity, consequently ring particles are recollected by the surface of the moons as they orbit around Saturn. The closer the satellites to Enceladus, the larger the density of the E ring in that position and the larger the flux of fresh icy particles on the surface. On the other hand, an opposite darkening process is acting on the surfaces of the satellites: the interaction of energetic electrons driven by the Saturn's magnetic field on the satellites surface, which activate the tholin production increasing the amount of contaminant. These two processes are in competition and the final effect is that space weathering is less effective on the surfaces of the satellites closer to Enceladus, because the surface is renewed by particles from the E ring, and the resulting amount of tholin on the surface decreases.

The spectral analysis performed on the icy moons of Saturn has been extended to the rings A, B, C and the Cassini Division (AGU General Assembly 2011, Ciarniello et al. (2011c)). This new study required a modification of the Hapke model to adapt it to a finite layer of particles. Rings show a stronger reddening than the moons, nonetheless their spectral behavior has been modeled with the familiar intraparticle mixture of water ice and Triton tholin ($\leq 0.5\%$). Amorphous carbon has been added as an intimate mixture for the A and B ring, and as an intraparticle mixture for C ring and Cassini Division. The grain size distribution adopted is a power low with $q = 3$, and with diameter ranging from few tenth's to few hundreds of μm. The best match is obtained for A and B ring, while the modeling is still unsatisfactory for C ring and Cassini Division.

Another part of the present work is represented by the study of laboratory spectra of four pyroxenes (A, AD, D and E; 350-2500 μm wavelength range) (EPSC-DPS Joint Meeting 2011, Ciarniello et al. (2011b)). Spectral signatures dependence on geometry

and grain size has been investigated. We found that band depth increases with the grain size up to 800 μm (which was our largest particle diameter), while it decreases at large phase angles. The two effects are comparable, and this means that geometry effects must be taken into account in retrieving grain sizes from spectral analysis. The dependence of band depth on phase angle is not explained by multiple scattering among the particles, so it has been addressed to the dependence of the single particle phase function (which affects single scattering) on the single scattering albedo w.
This dependence is confirmed by the phase function fit (Hapke model) performed for the E orthopyroxene (enstatitic type). The derived parameter which describe the single particle phase function show that $p(g)$ is more backscattering for higher w, confirming the behavior found for the icy surfaces.
The last step of the work on the lab spectra of pyroxenes is about the application of the Hapke's model of scattering efficiency to retrieve the imaginary part of the refractive index k. This is an alternative approach to measure optical constants of unknown media by means of the reflectance spectrum. The application of the method is simple and could provide a valuable way to produce a database of k values for different minerals. In this framework I've calculated k for all the four investigated pyroxenes.

The final part of this study has been done with in mind future applications, as described in the next paragraph, and is about the development of a Montecarlo routine written in IDL to simulate scattering in particulate media. Preliminary tests have been performed to verify the accuracy of the theoretical approach and the correctness of the written procedure. We computed the transmission factor t, the diffusive reflectance r_0 and the average number of scatterings $\mathcal{M}$, and then these values have been compared to theoretical calculations. The quantities derived by the routine are in remarkable agreement with the expected values.

The analysis we presented provides various future developments. Concerning the study of the surfaces of the icy objects in the Saturnian system using VIMS data, we aim to perform a complete spectrophotometric study for all the major moons, drawing an exhaustive picture of the distribution of contaminants in the system and of the interaction of the planet environment (magnetic field and rings particles) with the surface of the satellites.
The same paradigm can be used to study the properties of the rings. Parallel to

the analytic approach, the numeric simulations produced with the IDL routine we developed can be a useful tool to investigate the photometric properties of the rings, which are made of aggregates of small particles, and are not easily handled by the Hapke theory (problem of multiple scattering between the aggregates).

Concerning the analysis of laboratory spectra we intend to study the photometric properties of mixtures of different compounds which simulate planetary surfaces. Our target is to test the capabilities of the Hapke model to retrieve the composition of a given surface (grain size and amount of the different endmembers) and to understand the limits of the inversion process.

Conclusioni

In questo lavoro mi sono occupato di studiare le proprietà spettrofotometriche di mezzi particolati nel contesto del remote sensing nelle missioni spaziali. L'analisi è iniziata con Rhea, il più grande satellite ghiacciato nel sistema di Saturno (Ciarniello et al., 2011a). Il lavoro è stato presentato al 41^{mo} LPSC (Ciarniello et al., 2010c) e al 42^{mo} DPS meeting (Ciarniello et al., 2010b). Lo studio è stato effettuato utilizzando spettri acquisiti dallo strumento VIMS a bordo della sonda Cassini, nell'intervallo spettrale 0.35-5.12 μm, coprendo l'intervallo di angoli di fase $0.08° - 110°$. Questo approccio ha permesso di investigare la composizione dello strato di ghiaccio che riveste il satellite, la porosità del mezzo e la rugosità superficiale. L'analisi è stata svolta utilizzando il modello di Hapke. Poichè Rhea, come la quasi totalità dei satelliti di Saturno, è composto primariamente di ghiaccio d'acqua, una piccola quantità di materiale contaminante è sufficiente a riprodurre gli spettri osservati. Quattro differenti composti organici sono stati investigati come contaminanti del ghiaccio d'acqua allo scopo di riprodurre il forte assorbimento nella regione ultravioletta dello spettro. Il fit spettrale migliore è stato ottenuto con una mistura "intraparticle" di ghiaccio d'acqua (99.6%) e Triton tholin (0.4%), con una dimensione delle particelle pari a 38 μm. Le maggiori differenze tra lo spettro simulato e quello osservato possono essere dovute a problemi che riguardano la corretta determinazione del diametro dei grani. In particolare la distribuzione della dimensione dei grani che abbiamo adottato rappresenta solo il diametro medio delle particelle e quindi non considera il contributo di grani con dimensioni comparabili o minori della lunghezza d'onda.

Un volta che la composizione del mezzo è stata determinata è stato possibile investigare le proprietà fotometriche del satellite eseguendo un fit della funzione di fase full-disk per ogni lunghezza d'onda del range spettrale. Il disegno che emerge è che il parametro dominante nel processo di scattering è l'albedo di singolo scattering w, che appare correlato alla funzione di fase della singola particella e all'effetto d'opposizione

(OE). Nessuna dipendenza dell'OE dalla lunghezza d'onda è stata riscontrata, come d'altronde ci si aspettava, considerando che la dimensione tipica dei grani è maggiore di λ. L'analisi dell'OE indica che sia lo Shadow Hiding (SH) che il Coherent Backscattering (CB) sono attivi, e che il loro contributo relativo dipende dal valore dell'albedo di singolo scattering. Misurando la larghezza angolare h dell'OE in regime di SH è stata stimata la porosità che varia tra il 65% e il 77%.
Il valore relativamente alto del parametro di rugosità ($\bar{\theta} = 33°$) non è compatibile con la pendenza media di strutture superficiali quali crateri, depressioni o altri rilievi. Questo indica una correlazione di $\bar{\theta}$ con rugosità su scala più piccola, all'incirca dell'ordine di qualche centimetro, confermando i risultati di Shepard and Helfenstein (2007), e il valore che è stato derivato può essere interpretato come una stima dell'angolo di riposo della regolite.

Lo stesso paradigma applicato a Rhea è stato adottato per Encelado (lavoro presentato all'AGU Fall Meeting 2010, Ciarniello et al. (2010a)). In questo caso il dataset copre angoli di fase che vanno da 23°a 150°, con 290 immagini full-disk. Anche per Encelado il miglior fit spettrale è ottenuto con una mistura "intraparticle" di ghiaccio d'acqua (99.992%) e Triton tholin (0.008%) con particelle di 63 μm. L'abbondanza di contaminante, seppur minima, è in grado di riprodurre il debole arrossamento del satellite. Anche in questo caso lo studio della funzione di fase indica che i parametri relativi alla funzione di fase della singola particella sono collegati al valore dell'albedo di singolo scattering. Sia b che v diminuiscono all'aumentare di w e l'effetto risultante è che la funzione di fase della particella privilegia il back-scattering per alti w.
Purtroppo il dataset disponibile non si spinge ad angoli di fase minori di 23° e quindi non si può concludere nulla sull'OE.
In maniera simile a quanto trovato per Rhea il parametro di rugosità che abbiamo derivato è particolarmente alto ($\bar{\theta} = 29°$) e non è compatibile con le proprietà superficiali attese per un oggetto geologicamente attivo quale Encelado, per il quale i processi di ringiovanimento superficiale, legati all'attività endogena, determinando una bassa densità di crateri. Questo fatto rafforza l'idea che il parametro di rugosità nel modello di Hapke sia sensibile alla rugosità su piccola scala.
L'analisi della funzione di fase ha mostrato un aumento di riflettanza a grandi angoli di fase ($g = 150°$), dipendente dalla lunghezza d'onda. Questo è stato imputato al forward scattering prodotto dalle particelle più piccole a causa della diffrazione. La di-

mensione stimata di queste particelle è dell'ordine di 5 μm ed è compatibile con quella dei grani emessi dalle regioni attive di Encelado.

La modellizzazione spettrale è stata eseguita per altre tre lune di Saturno: Mimas, Tethys e Dione. Anche per questi satelliti il modello prevede una mistura "intraparticle" di ghiaccio d'acqua e Triton tholin per riprodurre l'arrossamento dello spettro. Tuttavia in questi casi una quantità variabile di carbone amorfo, tramite una mistura intima ("sale e pepe") con il ghiaccio, è necessaria per ottenere il giusto livello di albedo.

Uno studio comparativo dei modelli spettrali prodotti per questi cinque satelliti indica che l'abbondanza di tolina aumenta allontanandosi da Encelado.
Ciò è spiegabile con l'osservazione che i tre satelliti considerati orbitano tutti all'interno dell'anello E generato dalla attività criovulcanica di Encelado. Pertanto, più vicino un satellite è ad Encelado, maggiore è la densità dell'anello in quella posizione e maggiore il flusso di particelle di ghiaccio sulla superficie. Allo stesso tempo, però, l'interazione degli elettroni energetici guidati dal campo magnetico di Saturno sulla superficie dei satelliti, attiva la produzione di composti organici (come le toline) aumentando l'abbondanza di contaminante. I due processi competono e l'effetto finale è che lo space weathering (produzione di composti organici in seguito all'interazione con le particelle energetiche) è meno efficace sulle superfici dei satelliti più vicini ad Encelado, poichè la superficie subisce un processo di ringiovanimento grazie alle particelle di ghiaccio provenienti dall'anello E, facendo diminuire l'ammontare relativo di toline.

L'analisi spettrale eseguita sulle lune ghiacciate di Saturno è stata estesa agli anelli A,B,C e alla Divisione di Cassini (AGU General Assembly 2011, Ciarniello et al. (2011c)). Questo studio richiede una modifica del modello di Hapke, per adattarlo ad uno strato finito di particelle. Gli anelli mostrano un arrossamento maggiore rispetto ai satelliti, tuttavia questo è stato riprodotto nel modello con la consueta mistura "intraparticle" di ghiaccio d'acqua e Triton tholin ($\leq 0.5\%$). Del carbone amorfo è stato aggiunto come mistura intima per gli anelli A e B, e come mistura "intraparticle" per l'anello C e la Divisione di Cassini. La distribuzione della dimensione dei grani adottata è una legge di potenza con $q = 3$, nella quale il diametro delle particelle varia da qualche decina fino ad alcune centinaia di μm. Il miglior accordo è stato ottenuto per gli anelli A e B, mentre il fit è ancora insoddisfacente per l'anello C e la Divisione di

Cassini.

Un'altra parte del lavoro è rappresentata dallo studio di spettri di laboratorio di quattro pirosseni (qui indicati come A, AD, D and E; intervallo spettrale 350-2500 μm) (EPSC-DPS Joint Meeting 2011, Ciarniello et al. (2011b)). È stata studiata la dipendenza delle segnature spettrali rispetto alla dimensione dei grani e alla geometria dell'osservazione. Si è determinato che la profondità di banda aumenta con la dimensione delle particelle fino a 800 μm (che rappresenta anche il diametro massimo dei nostri campioni), mentre diminuisce all'aumentare della fase. I due effetti sono confrontabili, e ciò implica che gli effetti dovuti alla geometria dell'osservazione devono essere sempre considerati nelle analisi spettrali per effettuare una corretta interpretazione. La dipendenza della profondità di banda dall'angolo di fase non è giustificata dallo scattering multiplo tra le particelle che compongo il mezzo e quindi è stata imputata alla dipendenza della funzione di fase della singola particella (che influenza lo scattering singolo) dall'albedo di singolo scattering w.
Questa dipendenza è confermata dal fit della funzione di fase (modello di Hapke) effettuato sull'ortopirosseno E (tipo enstatitico). I parametri relativi alla funzione di fase della singola particella che sono stati derivati mostrano che $p(g)$ privilegia il backscattering per valori alti di w, confermando il trend rilevato per le superfici ghiacciate.
L'ultimo sviluppo dello studio sugli spettri di laboratorio di pirosseni riguarda l'applicazione del modello di Hapke, nella parte di derivazione dell'efficienza di scattering della particella, per determinare la parte immaginaria dell'indice di rifrazione k del mezzo analizzato. Questo rappresenta un approccio alternativo per calcolare le costanti ottiche a partire da misure di riflettanza dello spettro. L'applicazione del metodo è relativamente semplice e potrebbe fornire un valido strumento per produrre un dataset di costanti ottiche di differenti minerali. In questo contesto ho calcolato k per i quattro pirosseni analizzati.

Nell'ultima fase del lavoro di tesi ho sviluppato una procedura Montecarlo scritta in IDL per simulare lo scattering nei mezzi particolati. . Questo approccio permette di studiare in dettagli gli effetti dello scattering multiplo e si presta a sviluppi futuri molto interessanti, come descritto nel prossimo paragrafo. Sono stati eseguiti dei test preliminari per verificare la correttezza dellÕapproccio teorico ed il funzionamento del codice. Sono stati calcolati il fattore di trasmissione t, la riflettanza diffusiva r_0 e il nu-

mero medio di scattering $\mathcal{M}$, e questi valori sono stati confrontati con i calcoli previsti dalla teoria. Le quantità derivate dalle simulazioni sono in ottimo accordo con i valori aspettati.

Il lavoro svolto in questa tesi apre la strada ad una serie di sviluppi futuri. Per quel che riguarda lo studio dei corpi ghiacciati del sistema di Saturno utilizzando dati dallo strumento VIMS, l'intenzione è quella di completare uno studio spettrofotometrico per tutte le lune maggiori, ottenendo quindi un quadro il più possibile completo della distribuzione ed origine dei contaminanti nel sistema dei satelliti e dell'interazione di questi con l'ambiente esterno (il campo magnetico di Saturno e le particelle degli anelli).
Lo stesso paradigma può essere utilizzato nello studio delle proprietà degli anelli. Parallelamente all'approccio analitico, le simulazioni numeriche prodotte con la procedura IDL che è stata sviluppata rappresentano uno strumento utile per investigare le proprietà fotometriche degli anelli, che sono composti da aggregati di particelle, i quali non sono gestiti facilmente all'interno della teoria di Hapke (problema dello scattering multiplo tra gli aggregati).

Per quanto riguarda l'analisi degli spettri di laboratorio si intende investigare le proprietà fotometriche di misture che simulino composizioni superficiali di oggetti planetari del sistema solare. Lo scopo è quello di verificare le capacità del modello di Hapke nel derivare la composizione di una data superficie (dimensione dei grani e abbondanze dei vari componenti) e capire quali sono i limiti del processo di inversione.

Appendix A. Fit procedure

Performing an inversion of a model with several free parameters is a challenging task. The most common problem is to discriminate between different solutions that give similar results. Fitting algorithms are able to find minima in the parameters space but it is difficult to discriminate between local and absolute ones. To overcome this problem we adopted a very simple and transparent method. We determined a grid in the parameter space through a quantization of the parameters over the full range of variability. For each point of the grid (a single combination of the parameters) we calculated the model prediction and compared it to the data. The best prediction represents the final results of the fit. This method correctly finds the absolute minimum if the parameters space is sufficiently sampled. The quantization we chose is related to the degree of precision needed by the fit. At the same time the variability range for unbounded parameters has been fixed considering a range of values with physical sense. Concerning the spectral fit we chose a quantization for the particle diameter a_m of 1 μm in a range extending from 10 to 100 μm; we knew from previous analysis that higher values where unnecessary and that diameter values lower than 10 μm would have broken the limits given by geometric optics in Hapke model. The water ice mixing percentage range changes corresponding to the different mixtures, and in any case p was ≤ 1. The quantization "step" of the parameters has been chosen as the minimum variation that could create an appreciable change in the output, consequently the fitted value can be assumed with an uncertainty of half "step". For the phase function fit

the various parameters have been quantized in the following way:

$$
\begin{aligned}
B_0 &\in [0;2],\ B_{0i} = i \cdot 0.1,\ i = 0,1,2,...,10 \\
h &\in [0.0001;0.1],\ h_i = 10^{-4+0.15 \cdot i},\ i = 0,1,2,...,30 \\
b &\in [0;0.9],\ b_i = i \cdot 0.1,\ i = 0,1,2,...,9 \\
v &\in [-1;1],\ v_i = -1 + i \cdot 0.1,\ i = 0,1,2,...,20 \\
\bar{\theta} &\in [10^\circ;35^\circ],\ \bar{\theta}_i = i,\ i = 10^\circ, 11^\circ, 12^\circ, ..., 35^\circ
\end{aligned}
$$

Bibliography

Ambartsumian, V., 1958. The theory of radiative transfer in planetary atmospheres. In: Ambartsumian, V. (Ed.), Theoretical Astrophysics. Pergamon Press, New York, pp. 550–64.

Berreman, D., 1970. Resonant reflectance anomalies: effect of shape of surface irregularities. Phys. Rev. B1, 381–389.

Bowell, E., Hapke, B., Domingue, D., Lumme, K., Peltoniemi, J., Harris, A. W., 1989. Application of photometric models to asteroid. In: Binzel, R. P., Gehrels, T., Matthews, M. S. (Eds.), Asteroids II. Uniersity of Arizona Press, Tucson, pp. 524–556.

Brown, R. H., Baines, K. H., Bellucci, G., Bibring, J. P., Buratti, B. J., Capaccioni, F., Cerroni, P., Clark, R. N., Coradini, A., Cruikshank, D. P., Drossart, P., Formisano, V., Jaumann, R., Langevin, Y., Matson, D. L., McCord, T. B., Mennella, V., Miller, E., Nelson, R. M., Nicholson, P. D., Sicardy, B., Sotin, C., 2004. The Cassini Visual and Infrared Mapping Spectrometer (VIMS) investigation. Space Sci. Rev. 115 (1-4), 111–168.

Buratti, B. J., 1985. Application of radiative transfer models to bright icy satellites. Icarus 61, 208–217.

Buratti, B. J., Hicks, M. D., 2003. The Dark Side of Iapetus: a model that finally works? Bull. Am. Astron. 35, 915 (abstract).

Buratti, B. J., Hicks, M. D., Soderblom, L. A., Britt, D., Oberst, J., Hillier, J. K., 2004. Deep space photometry of the nucleus of comet 19P/Borrelly. Icarus 167, 16–29.

Buratti, B. J., Mosher, J. A., Nicholson, P. D., McGhee, C. A., G, F. R., 1998. Near-infrared photometry of the Saturnian satellites during ring plane crossing. Icarus 136, 223–231.

Burns, R. G., 1970. Minearalogical Applications of Crsytal Field Theory. Cambridge University Press, New York.

Chandrasekhar, S., 1960. Radiative transfer. Dover, New York.

Ciarniello, M., Capaccioni, F., Filacchione, G., Clark, R., Cruikshank, D., Cerroni, P., Coradini, A., Brown, R., Buratti, B., Tosi, F., Stephan, K., 2011a. Hapke modeling of Rhea surface properties through Cassini-VIMS spectra. Icarus 214, 541–555.

Ciarniello, M., Capaccioni, F., Filacchione, G., Clark, R. N., Cruikshank, D. P., Cerroni, P., Coradini, A., Brown, R. H., Buratti, B. J., Tosi, F., Stephan, K., 2010a. Spectrophotometric Modeling of Enceladus Surface Properties and Composition from Vims Data. In: American Geophysical Union, Fall Meeting. pp. #P33A–1558, (abstract).

Ciarniello, M., Capaccioni, F., Filacchione, G., Clark, R. N., Cruikshank, D. P., Cerroni, P., Coradini, A., Brown, R. H., Buratti, B. J., Tosi, F., Stephan, K., 2010b. Spectrophotometric Modeling of Rhea's Surface form VIMS Data. In: American Astronomical Society, DPS meeting #42 (abstract).

Ciarniello, M., Capaccioni, F., Filacchione, G., Coradini, A., Cerroni, P., Tosi, F., 2010c. Spectrophotometric Analysis of Rhea Surface Scattering Properties. Lunar Planet. Sci XLI, 1643 (asbstract).

Ciarniello, M., Capaccioni, F., Filacchione, G., Coradini, A., Cerroni, P., Tosi, F., Stephan, K., 2010d. VIS-IR spectral modeling of Rhea and Enceladus. EGU General Assembly 2010, 6177 (abstract).

Ciarniello, M., Capaccioni, F., Sgavetti, M., 2011b. Hapke modeling of pyroxenes: effects of phase angle, grain size and mixture composition. In: EPSC-DPS Joint Metting (abstract).

Ciarniello, M., Filacchione, G., Nicholson, P. D., Clark, R. N., Coradini, A., Brown, R. H., Buratti, B. J., Hedman, M. M., 2011c. Saturn's rings spectrophotometric modeling by CASSINI-VIMS data. In: EGU General Assembly (abstract).

Clark, R. N., 1999. Spectroscopy of rocks and minerals and principles of spectroscopy. In: Rencz, A. N. (Ed.), Manual of Remote Sensing. John Wiley and Sons, New York, pp. 3–58 (Chapter 1).

Clark, R. N., Carlson, R., Grundy, W., Noll, K., 2011. Observed ices in the Solar System. In: Gudipati, M. (Ed.), Solar System Ices, in press.

Clark, R. N., Curchin, J. M., Jaumann, R., Cruikshank, D. P., Brown, R. H., Hoefen, T. M., Stephan, K., Moore, J. M., Buratti, B. J., Baines, K. H., Nicholson, P. D., Nelson, R. M., 2008. Compositional mapping of Saturn's satellite Dione with Cassini VIMS and implications of dark material in the Saturn system. Icarus 193 (2), 372 – 386, saturn's Icy Satellites from Cassini.
URL http://www.sciencedirect.com/science/article/pii/S0019103507003740

Clark, R. N., et al., 2011. The composition of Iapetus: Mapping results from Cassini VIMS, submitted for publication.

Clark, R. N., Lucey, P. G., 1984. Spectral properties of ice-particulate mixtures and implication for remote sensing. I - intimate mixtures. J .Geophys. Res. 89, 6341–6348.

Clark, R. N., Owensby, P. D., 1981. The infrared spectrum of rhea. Icarus 46 (3), 354 – 360.
URL http://www.sciencedirect.com/science/article/pii/001910358190138X

Cloutis, E. A., Gaffey, M. J., 1991. Pyroxene Spectroscopy Revisited: Spectral-Compositional Correlation and Relationship to Geothermometry. J .Geophys. Res. 96 (E5), 809–822.

Coradini, A., De Sanctis, M. C., Ammanito, E., Capaccioni, F., Capria, M. T., Carraro, F., Cartacci, M., Filacchione, G., Fonte, S., Magni, G., Noschese, R., Tosi, F., Barucci, A., Federico, C., Frigeri, A., Fulchignoni, M., Langevin, Y., Marchi, S., Palomba, E., Turrini, D., McCord, T. B., McFadden, L. A., Pieters, C., Raymond, C. A., Russell, C. T., TEAM, D., 2011. Vesta Mineralogy: VIR maps Vesta's surface. EPSC-DPS Joint Meeting abstracts 6 (740).

Cruikshank, D. P., Ore, C. M. D., Roush, T. L., Geballe, T. R., Owen, T. C., de Bergh, C., Cash, M. D., Hartmann, W. K., 2001. Constraints on the Composition of Trojan

Asteroid 624 Hektor. Icarus 153 (2), 348 – 360.
URL http://www.sciencedirect.com/science/article/pii/S001910350196703X

Cruikshank, D. P., Owen, T. C., Ore, C. D., Geballe, T. R., Roush, T. L., de Bergh, C., Sandford, S. A., Poulet, F., Benedix, G. K., Emery, J. P., 2005. A spectroscopic study of the surfaces of Saturn's large satellites: H_2O ice, tholins, and minor constituents. Icarus 175 (1), 268 – 283.
URL http://www.sciencedirect.com/science/article/pii/S0019103504002970

Cruikshank, D. P., Roush, T. L., Bartholomew, M. J., Geballe, T. R., Pendleton, Y. J., White, S. M., Bell, J. F., Davies, J. K., Owen, T. C., de Bergh, C., Tholen, D. J., Bernstein, M. P., Brown, R. H., Tryka, K. A., Ore, C. M. D., 1998. The Composition of Centaur 5145 Pholus. Icarus 135 (2), 389 – 407.
URL http://www.sciencedirect.com/science/article/pii/S0019103598959978

Cuzzi, J. N., Estrada, P. R., 1998. Compositional Evolution of Saturn's Rings Due to Meteoroid Bombardment. Icarus 132 (1), 1 – 35.
URL http://www.sciencedirect.com/science/article/pii/S0019103597958632

Davidsson, B. J., GutiÈrrez, P. J., Rickman, H., 2009. Physical properties of morphological units on Comet 9P/Tempel 1 derived from near-IR Deep Impact spectra. Icarus 201 (1), 335 – 357.
URL http://www.sciencedirect.com/science/article/pii/S0019103509000025

Domingue, D., Verbiscer, A., 1997. Re-Analysis of the Solar Phase Curves of the Icy Galilean Satellites. Icarus 128 (1), 49 – 74.
URL http://www.sciencedirect.com/science/article/pii/S0019103597957304

Domingue, D. L., Denevi, B. W., Ernst, C. M., Holsclaw, G. M., Izenber, N. R., McClintock, W. E., Murchie, S. L., Robinson, M. S., 2009. Regional color photometry of Mercury's surface. Lunar Planet. Sci XL, 1301 (asbtract).

Domingue, D. L., Lockwood, G., Thompson, D., 1995. Surface textural properties of icy satellites: a comparison between Europa and Rhea. Icarus 115, 228–249.

Drossart, P., 1993. Optics on a fractal surface and the photometry of the regoliths. Planetary and Space Science 41 (5), 381 – 393.
URL http://www.sciencedirect.com/science/article/pii/003206339390072A

Emery, J. P., Burr, D. M., Cruikshank, D. P., Brown, R. H., Dalton, J. B., 2005. Near-infrared (0.8-4.0 μm) spectroscopy of Mimas, Enceladus, Tethys, and Rhea. Astron. Astrophys 435, 353–362.

Esposito, L. W., 1986. Structure and evolution of saturn's rings. Icarus 67, 345–357.

Esposito, L. W., 2006. Planetary Rings. Cambridge Planetary Science.

Filacchione, G., Capaccioni, F., Ciarniello, M., Nicholson, P. D., Hedman, M. M., Clark, R. N., Brown, R. H., Cerroni, P., 2011. VIS-IR spectrograms of Saturn's rings retrieved from Cassini-VIMS radial mosaics. EPSC-DPS Joint Meeting abstracts 6 (293).

Filacchione, G., Capaccioni, F., Clark, R., Cuzzi, J., Cruikshank, D., Coradini, A., Cerroni, P., Nicholson, P., McCord, T., Brown, R., Buratti, B., Tosi, F., Nelson, R., Jaumann, R., Stephan, K., 2010. Saturn's icy satellites investigated by Cassini-VIMS: II. Results at the end of nominal mission. Icarus 206 (2), 507 – 523, cassini at Saturn.
URL http://www.sciencedirect.com/science/article/pii/S0019103509004461

Filacchione, G., Capaccioni, F., McCord, T., Coradini, A., Cerroni, P., Bellucci, G., Tosi, F., D'Aversa, E., Formisano, V., Brown, R., Baines, K., Bibring, J., Buratti, B., Clark, R., Combes, M., Cruikshank, D., Drossart, P., Jaumann, R., Langevin, Y., Matson, D., Mennella, V., Nelson, R., Nicholson, P., Sicardy, B., Sotin, C., Hansen, G., Hibbitts, K., Showalter, M., Newman, S., 2007. Saturn's icy satellites investigated by Cassini-VIMS: I. Full-disk properties: 350-5100 nm reflectance spectra and phase curves. Icarus 186 (1), 259 – 290.
URL http://www.sciencedirect.com/science/article/pii/S0019103506002715

Gaffey, M. J., W, S. D. G., Lambert, S. J. L., 1990. Metal Silicate Mixtures: Spectral Properties and Applications to Asteroid Taxonomy. J .Geophys. Res. 95 (B6), 8323–8338.

Grundy, W., 2009. Is the missing ultra-red material colorless ice? Icarus 199 (2), 560 – 563.
URL http://www.sciencedirect.com/science/article/pii/S0019103508003849

Hapke, B., 1993. Theory of reflectance and emittance spectroscopy. Topics in Remote Sensing, 3. Cambridge University Press, Cambridge, UK.

Hapke, B., 2002. Bidirectional Reflectance Spectroscopy: 5. The Coherent Backscatter Opposition Effect and Anisotropic Scattering. Icarus 157 (2), 523 – 534.
URL http://www.sciencedirect.com/science/article/pii/S0019103502968533

Hapke, B., 2008. Bidirectional reflectance spectroscopy: 6. Effects of porosity. Icarus 195 (2), 918 – 926.
URL http://www.sciencedirect.com/science/article/pii/S0019103508000419

Hapke, B., Nelson, R., Smythe, W., 1998. The Opposition Effect of the Moon: Coherent Backscatter and Shadow Hiding. Icarus 133 (1), 89 – 97.
URL http://www.sciencedirect.com/science/article/pii/S0019103598959073

Hapke, B. W., Shepard, M. K., Nelson, R. M., Smythe, W. D., Piatek, J. L., 2009. A quantitative test of the ability of models based on the equation of radiative transfer to predict the bidirectional reflectance of a well-characterized medium. Icarus 199 (1), 210 – 218.
URL http://www.sciencedirect.com/science/article/pii/S0019103508003266

Heyney, L. G., Greenstein, J. L., 1941. Diffuse radiation in the Galaxy. Astrophys. J. 93, 70–83.

Hudson, R. S., Ostro, S. J., 1999. Physical Model of Asteroid 1620 Geographos from Radar and Optical Data. Icarus 140 (2), 369 – 378.
URL http://www.sciencedirect.com/science/article/pii/S0019103599961420

Iess, L., Rappaport, N. J., Tortora, P., Lunine, J., Armstrong, J. W., Asmar, S. W., Somenzi, L., Zingoni, F., 2007. Gravity field and interior of Rhea from Cassini data analysis. Icarus 190 (2), 585 – 593, deep Impact Mission to Comet 9P/Tempel 1, Part 2.
URL http://www.sciencedirect.com/science/article/pii/S0019103507001522

Ishimaru, A., Kuga, Y., 1982. Attenuation of a coherent field in a dense distribution of particles. J. Opt. Soc. Amer. 72, 1317–20.

Jacobson, R. A., Antreasian, P. G., Bordi, J. J., Criddle, K. E., Ionasescu, R., Jones, J. B., Mackenzie, R. A., Meek, M. C., Parcher, D., Pelletier, F. J., Owen, Jr., W. M., Roth, D. C., Roundhill, I. M., Stauch, J. R., 2006. The Gravity Field of the Saturnian System from Satellite Observations and Spacecraft Tracking Data. The Astronomical Journal 132, 2520–2526.

Jaumann, R., Stephan, K., Hansen, G. B., Clark, R. N., Buratti, B. J., Brown, R. H., Baines, K. H., Newman, S. F., Bellucci, G., Filacchione, G., Coradini, A., Cruikshank, D. P., Griffith, C. A., Hibbitts, C. A., McCord, T. B., Nelson, R. M., Nicholson, P. D., Sotin, C., Wagner, R., 2008. Distribution of icy particles across Enceladus' surface as derived from Cassini-VIMS measurements. Icaruscarus 193, 407–419.

Kempf, S., Beckmann, U., Moragas-Klostermeyer, G., Postberg, F., Srama, R., Economou, T., Schmidt, J., Spahn, F., Grün, E., Feb. 2008. The E ring in the vicinity of Enceladus. I. Spatial distribution and properties of the ring particles. Icarus 193, 420–437.

Khare, B. N., Sagan, C., Arakawa, E. T., Suits, F., Callcott, T. A., Williams, M. W., 1984. Optical constants of organic tholins produced in a simulated Titanian atmosphere: From soft x-ray to microwave frequencies. Icarus 60 (1), 127 – 137.
URL http://www.sciencedirect.com/science/article/pii/0019103584901428

Khare, B. N., Thompson, W. R., Cheng, L., Chyba, C., Sagan, C., Arakawa, E. T., Meisse, C., Tuminello, P. S., 1993. Production and Optical Constants of Ice Tholin from Charged Particle Irradiation of (1:6) C_2H_6/H_2O at 77 K. Icarus 103 (2), 290 – 300.
URL http://www.sciencedirect.com/science/article/pii/S0019103583710717

Klima, R. L., Pieters, C. M., Dyar, M. D., 2007. Spectroscopy of synthetic Mg-Fe pyroxenes I: Spin-allowed and spin-forbidden crystal field bands in the visible and near-infrared. Meteoritics and Planetary Science 42 (2), 235–253.

Kortum, G., 1969. Reflectance Spectroscopy. New York: Springer-Verlag.

Lucey, P. G., 1998. Model near-infrared optical constants of olivine pyroxene as a function of iron content. J. Geophys. Res. 103, 1703–1713.

Lumme, K., Bowell, E., 1981. Radiative transfer in the surfaces of atmosphereless bodies. I Theory. Astron. J. 86, 1694–1704.

MacKintosh, F. C., Sajeev, J., 1988. Coherent backscattering of light in the presence of time-reversal-noninvariant and parity-nonconserving media. Phys. Rev. B 37, 1884–1897.

Mallama, A., Wang, D., Howard, R. A., 2002. Photometry of Mercury from SOHO/LASCO and Earth: The Phase Function from 2° to 170°. Icarus 155 (2), 253 – 264.
URL http://www.sciencedirect.com/science/article/pii/S0019103501967235

Mallet, P., Guérin, C. A., Sentenac, A., 2005. Maxwell-Garnett mixing rule in the presence of multiple scattering: Derivation and accuracy. Phys. Rev. B 72, doi:10.1103/PhysRevB.72.014205.

Mastrapa, R., Bernstein, M., Sandford, S., Roush, T., Cruikshank, D., Ore, C. D., 2008. Optical constants of amorphous and crystalline H_2O-ice in the near infrared from 1.1 to 2.6 μm. Icarus 197 (1), 307 – 320.
URL http://www.sciencedirect.com/science/article/pii/S0019103508001735

Mastrapa, R., Sandford, S. A., Roush, T. L., Cruikshank, D. P., Ore, C. M. D., 2009. Optical constants of amorphous, crystalline H_2O-ice: $2.5-22\ \mu m$ $(4000-455\ cm^{-1})$ optical constants of H_2O-ice. Astrophys. J. 701, 1347–1356.

Maxwell-Garnett, J., 1904. Colours in metal glasses and in metallic films. Philos. Trans. R. Soc. Lon. Ser. A 203, 385–420.

McCord, T., Coradini, A., Hibbitts, C., Capaccioni, F., Hansen, G., Filacchione, G., Clark, R., Cerroni, P., Brown, R., Baines, K., Bellucci, G., Bibring, J.-P., Buratti, B., Bussoletti, E., Combes, M., Cruikshank, D., Drossart, P., Formisano, V., Jaumann, R., Langevin, Y., Matson, D., Nelson, R., Nicholson, P., Sicardy, B., Sotin, C., 2004. Cassini VIMS observations of the Galilean satellites including the VIMS calibration procedure. Icarus 172 (1), 104 – 126, cassini-Huygens at Jupiter.
URL `http://www.sciencedirect.com/science/article/pii/S0019103504002143`

McDonald, G. D., Thompson, W. R., Heinrich, M., Khare, B. N., Sagan, C., 1994. Chemical Investigation of Titan and Triton Tholins. Icarus 108 (1), 137 – 145.
URL `http://www.sciencedirect.com/science/article/pii/S0019103584710463`

McGuire, A. F., Hapke, B. W., 1995. An Experimental Study of Light Scattering by Large, Irregular Particles. Icarus 113 (1), 134 – 155.
URL `http://www.sciencedirect.com/science/article/pii/S0019103585710123`

Mie, G., 1908. Beiträge zur Optik trüber Medien, speziell kolloidaler Metallösungen. An. Phys. 377-445.

Miller, E., Klein, G., Juergens, D., Mehaffey, K., Oseas, J., Garcia, R., Giandomenico, A., Irigoyen, R., Hickok, R., Rosing, D., Sobel, H., Bruce, C., Flamini, E., DeVidi, R., Reininger, F., Dami, M., Soufflot, A., Langevin, Y., G.Huntzinger, 1996. The Visual and Ifrared Mapping Spectrometer for Cassini. SPIE 2803, 206.

Mishchenko, M., Dlugach, J., Yanovitskij, E., Zakharova, N., 1999. Bidirectional reflectance of flat, optically thick particulate layers: an efficient radiative transfer solution and applications to snow and soil surface. J. Quant. Spectrosc. Radiat. Transfer 63, 409–432.

Mishchenko, M. I., Liu, L., Mackowski, D. W., Cairns, B., Videen, G., 2007. Multiple scattering by random particulate media: exact 3D results. Optics Express 15 (6), 2822–2836.

O'Donnell, K., Mendez, E., 1987. Experimental study of scattering from characterized random surfaces. J. Opt. Soc. Amer. A4 (1194-1205).

Pitman, K. M., Buratti, B. J., Mosher, J. A., 2010. Disk-integrated bolometric Bond albedos and rotational light curves of saturnian satellites from Cassini Visual and Infrared Mapping Spectrometer. Icarus 206, 537–560.

Porco, C. C., Helfenstein, P., Thomas, P. C., Ingersoll, A. P., Wisdom, J., West, R., Neukum, G., Denk, T., Wagner, R., Roatsch, T., Kieffer, S., Turtle, E., McEwen, A., Johnson, T. V., Rathbun, J., Veverka, J., Wilson, D., Perry, J., Spitale, J., Brahic, A., Burns, J. A., Del Genio, A. D., Dones, L., Murray, C. D., Squyres, S., 2006. Cassini Observes the Active South Pole of Enceladus. Science 311, 1393–1401.

Poulet, F., Cruikshank, D. P., Cuzzi, J. N., Roush, T. L., G, F. R., 2003. Compositions of Saturn's rings A, B, and C from high resolution near-infrared spectroscopic observations. Astron. Astrophys. 412, 305–316.

Poulet, F., Cuzzi, J. N., Cruikshank, D. P., Roush, T. L., Dalle Ore, C. M., 2002. Comparison between the shkuratov and hapke scattering theories for solid planetary surfaces: Application to the surface composition of two centaurus. Icarus 160, 313–324.

Reininger, F., Dami, M., Paolinetti, R., Pieri, S., Falugiani, S., 1994. Visible infrared mapping spectrometer-visible channel (VIMS-VIS). Instrumetation in Astronomy, SPIE 2198, 239–250.

Roatsch, T., Jaumann, R., Stephan, K., Thomas, P. C., 2009. Cartographic Mapping of the Icy Satellites Using ISS and VIMS Data. In: Dougherty, M. K., Esposito, L. W., Krimigis, S. M. (Eds.), Saturn from Cassini-Huygens. Springer Netherlands, pp. 763–781.

Roush, T. L., 1994. Charon:more than water ice? Icarus 108 (243-254).

Roush, T. L., Esposito, F., Rossman, G. R., Colangeli, L., 2007. Estimated optical constants of gypsum in the regions of weak absorptions: Application of scattering theories and comparisons to independent measurements. J .Geophys. Res. 112, E10003.

Schenk, P., Hamilton, D. P., Johnson, R. E., McKinnon, W. B., Paranicas, C., Schmidt, J., Showalter, M., 2011. Plasma, plumes and rings: Saturn system dynamics as recorded in global color patterns on its midsize icy satellites. Icarus 211, 740–757.

Shafer, D. R., 1978. Four-mirror unobscured anastigmatic telescopes with all-spherical surfaces. Applied Optics 17 (7), 1072–1074.

Shepard, M. K., Helfenstein, P., 2007. A test of the Hapke photometric model. J. Geophys. Res. 112, doi:10.1029/2005JE002625.

Shepard, M. K., Helfenstein, P., 2011. A laboratory study of the bidirectional reflectance from particulate samples. Icarus 215, 526–533.

Shkuratov, Y., Kreslavsky, M. A., Ovcharenko, A. A., Stankevich, D. G., Zubko, E. S., Pieters, C., Arnold, G., 1999a. Opposition effect from Clementine data and mechanisms of backscatter. Icarus 141 (132-155).

Shkuratov, Y., Starukhina, L., Hoffmann, H., Arnold, G., 1999b. A model of spectral albedo of particulate surfaces: implications for optical properties of the Moon. Icarus 137, 235–246.

Shkuratov, Y. G., Stankevich, D. G., Petrov, D. V., Pinet, P. C., Cord, A. M., Daydou, Y. H., Chevrel, S. D., 2005. Interpreting photometry of regolith-like surfaces with different topographies: shadowing and multiple scattering. Icarus 173, 3–15.

Souchon, A. L., Pinet, P. C., Chevrel, S. D., Daydou, Y. H., Baratoux, D Kurita, K., Shepard, M. K., Helfenstein, P., 2011. An experimental study of Hapke's modeling of natural granular surface samples. Icarus 215, 313–331.

Spahn, F., Albers, N., Hörning, M., Kempf, S., Krivov, A. V., Makuch, M., Schmidt, J., Seiß, M., Sremčević, M., 2006. E ring dust sources: Implications from Cassini's dust measurements. Planetary and Space Science 54 (9-10), 1024 – 1032.

Spencer, J. R., Denk, T., 2010. Formation of Iapetus' extreme albedo dichotomy by exogenically triggered thermal ice migration. Science 327, 432.

Stankevich, D., Shkuratov, Y., 2004. Monte carlo ray-tracing simulation of light scattering in particulate media with optically contrast structure. Journal of Quantitative Spectroscopy and Radiative Transfer 87 (3-4), 289 – 296.
URL http://www.sciencedirect.com/science/article/pii/S0022407303003947

Thomas, P. C., Helfenstein, P., Veverka, J., Burns, J., Porco, C., Denk, T., Turtle, E., 2006. Sizes, shape, relaxation states and interior configurations of icy saturnian satellites. Bull. Am. Astron. Soc. 38 (621 (abstract)).

Torrance, K., Sparrow, E., 1967. Theory for off-specular reflection from roughned surfaces. J. Opt. Soc. Amer. 57, 1105–1114.

Tosi, F., Turrini, D., Coradini, A., Filacchione, G., 2010. Probing the origin of the dark material on Iapetus. Mon. Not. R. Astron. Soc. 403, 1113–1130.

Verbiscer, A., French, R. G., Showalter, M., Helfenstein, P., 2007. Enceladus: Cosmic Graffiti Artist Caught in the Act. Science 315, 5813–5815.

Verbiscer, A., Veverka, J., 1989. Albedo dichotomy of Rhea: Hapke analysis of Voyager photometry. Icarus 82, 164–178.

Warrel, J., Davidsson, B. J. R., 2010. A Hapke model implementation for compositional analysis of VNIR spectra of Mercury. Icarus 209, 164–178.

Warren, S. G., 1984. Optical constants of ice from the ultraviolet to the microwave. Appl. Opt. 23, 1206–1225.

Wilcox, B., Lucey, P. G., Haawke, B. R., 2006. Radiative transfer modeling of compositions of lunar pyroclastic deposits. J .Geophys. Res. 111, CiteID E09001.

Zerull, R., Giese, R., 1974. Microwave analogue studies. In: Gehrels, T. (Ed.), Planets Stars and Nebulae Studied with Photopolarimetry. University of Arizona Press, Tucson, pp. 901–915.

Zubko, V. G., Mennella, V., Colangeli, L., Bussoletti, E., 1996. Optical constants of cosmic carbon analogue grains – I. Simulation of clustering by a modified continuous distribution of ellipsoids. Mon. Not. R. Astron. Soc 282, 1321–1329.